



APPLICATIONS OF PEROVSKITE OXIDE  
THIN FILMS:  
MICROCANTILEVERS, SUPERCONDUCTING  
DEVICES AND DIELECTRIC  
INTERCONNECTIONS

by

Giuseppe Vasta

A thesis submitted to the  
School of Electrical and Electronic Engineering of  
the University of Birmingham  
for the degree of

DOCTOR OF PHILOSOPHY

November 2011

Copyright Giuseppe Vasta

**UNIVERSITY OF  
BIRMINGHAM**

**University of Birmingham Research Archive**

**e-theses repository**

This unpublished thesis/dissertation is copyright of the author and/or third parties. The intellectual property rights of the author or third parties in respect of this work are as defined by The Copyright Designs and Patents Act 1988 or as modified by any successor legislation.

Any use made of information contained in this thesis/dissertation must be in accordance with that legislation and must be properly acknowledged. Further distribution or reproduction in any format is prohibited without the permission of the copyright holder.

# Contents

<b>Abstract</b>	<b>iv</b>
<b>Acknowledgements</b>	<b>v</b>
<b>Publications</b>	<b>vi</b>
<b>Introduction</b>	<b>vii</b>
<b>1 Piezoelectricity and device description</b>	<b>1</b>
1.1 General properties of ferroelectric materials . . . . .	1
1.2 Piezoelectricity and equations of state . . . . .	8
1.3 <i>BaTiO<sub>3</sub></i> properties . . . . .	9
1.4 Device and material descriptions . . . . .	13
1.5 Summary . . . . .	17
<b>2 Mechanical properties</b>	<b>18</b>
2.1 Mechanical model . . . . .	19
2.2 Model for a piezoelectric generator . . . . .	31
2.3 Cantilever design principles . . . . .	36
2.3.1 Design of simple beam cantilevers . . . . .	41
2.3.2 Design of u-shape cantilevers . . . . .	49
2.4 Summary . . . . .	54
<b>3 Apparatus and methods</b>	<b>56</b>
3.1 Pulsed Laser Deposition setup . . . . .	57
3.2 X-ray diffraction . . . . .	63
3.2.1 Sample surface alignment . . . . .	66
3.2.2 $\varphi$ and $\theta - 2\theta$ scans . . . . .	68
3.3 Device patterning and milling . . . . .	69
3.4 Critical point drying . . . . .	70
3.5 Wirebonding . . . . .	72
3.6 Electrical Measurements . . . . .	73

3.7 Other Measurements . . . . .	77
3.8 Summary . . . . .	78
<b>4 Fabrication process of the cantilevers</b>	<b>80</b>
4.1 Introduction to the fabrication procedure . . . . .	81
4.2 Fabrication process for the 31 mode cantilevers . . . . .	84
4.3 Fabrication process for the 33 mode cantilevers . . . . .	94
4.4 <i>MgO</i> as sacrificial layer . . . . .	99
4.5 Summary . . . . .	101
<b>5 Characterization of the multi-layers</b>	<b>103</b>
5.1 X-ray diffraction analysis . . . . .	104
5.2 Nano-indentation measurements . . . . .	114
5.3 Summary . . . . .	118
<b>6 Residual stress analysis</b>	<b>120</b>
6.1 Experimental method . . . . .	121
6.2 Theoretical values of the residual stress . . . . .	135
6.3 Discussion . . . . .	142
6.4 A refinement of our analysis . . . . .	146
6.5 Summary . . . . .	147
<b>7 Electrical characterization</b>	<b>150</b>
7.1 Resistivity of the <i>SrRuO<sub>3</sub></i> layer . . . . .	151
7.2 Measured impedance of the <i>BaTiO<sub>3</sub></i> based capacitors . . . . .	152
7.2.1 Device modeling . . . . .	152
7.2.2 Analysis of <i>BaTiO<sub>3</sub></i> capacitive structures grown directly on <i>SrTiO<sub>3</sub></i> substrate . . . . .	156
7.2.3 Analysis of <i>BaTiO<sub>3</sub></i> capacitive structures grown on the sacrificial layer . . . . .	161
7.2.4 Discussion on the impedance measurements . . . . .	168
7.3 Hysteresis loop measurements . . . . .	171
7.4 Summary . . . . .	174
<b>8 Conclusions and future developments</b>	<b>178</b>
<b>I Appendixes</b>	<b>199</b>
<b>A Mechanics</b>	<b>200</b>
A.1 Basic concepts . . . . .	200
A.2 Mechanical behaviour of cantilevers . . . . .	205

<b>B Unusual cantilevers</b>	<b>221</b>
B.1 Design of beams with different width connected in series . . . . .	221
B.2 Design of tuning fork cantilevers . . . . .	224
<b>C Impedance measurement data</b>	<b>230</b>
<b>D Superconductive devices</b>	<b>236</b>
D.1 Supercond. and Josephson junctions . . . . .	236
D.1.1 Fundamentals about superconductivity . . . . .	236
D.1.2 Josephson junctions . . . . .	240
D.1.3 SQUIDs: superconductive quantum interference devices	243
D.1.4 Conventional and unconventional superconductivity .	246
D.1.5 Superconductive devices and qubit applications . . . . .	249
D.1.6 $Nb/Au/YBa_2Cu_3O_7$ ramp type Josephson junctions .	251
D.2 Equipment and experimental methods . . . . .	257
D.2.1 Pulsed Laser Deposition system . . . . .	257
D.2.2 Photholithography and Milling . . . . .	258
D.2.3 Susceptibility measurements . . . . .	258
D.2.4 AFM investigation . . . . .	262
D.2.5 Current-Voltage (I-V) and Resistance versus Temperature (R-T) measurements . . . . .	263
D.3 Device Fabrication . . . . .	274
D.3.1 Introduction to the fabrication process . . . . .	275
D.3.2 $SrTiO_3/YBa_2Cu_3O_7$ bilayer deposition . . . . .	277
D.3.3 Pads and ramp patterning . . . . .	286
D.3.4 Ramp cleaning, interlayer deposition, and gold top elec- trode definition . . . . .	290
D.3.5 Summary . . . . .	301
D.4 Measurements and Results . . . . .	303
D.4.1 Electrical measurements on the $Au/YBa_2Cu_3O_7$ ramp type contacts . . . . .	303
D.4.2 Conclusions . . . . .	320
<b>E <math>LaYbO_3</math> dielectric layer</b>	<b>322</b>
<b>F Copies of the publications</b>	<b>330</b>
<b>II Bibliography</b>	<b>331</b>

# Abstract

The aim of this Phd is to investigate the properties of micro-cantilevers, containing  $BaTiO_3$  based capacitors on their top and verify if they can be used as energy harvesting devices.  $SrRuO_3/BaTiO_3$  systems behaving as high quality (i.e. with an impedance phase between  $-80^\circ$  and  $-90^\circ$ ) capacitive structures, in the frequency range  $6\text{ KHz} - 50\text{ KHz}$  and with a residual polarization equal to  $2.5\text{ }\mu\text{C/cm}^2$  have been fabricated on  $400\text{ nm}$  thick  $MgO$  sacrificial layer. These structures allow to design microcantilevers with a minimum resonance frequency of  $6\text{ KHz}$ .

Two piezoelectric modes are generally used in energy harvesting devices, they are the 33 and the 31 piezoelectric mode. X-ray diffraction analysis shows that the polar axis of  $BaTiO_3$  is perpendicular to the surface of the film when this layer is grown on  $SrRuO_3$  and  $SrTiO_3$ . This configuration fits the 31 energy harvesting mode. When  $BaTiO_3$  is grown on  $MgO$  the polar axis is parallel to the surface of the film so this configuration fits the 33 energy harvesting mode.

Micro-cantilevers employing  $YBa_2Cu_3O_7$  and  $MgO$  sacrificial layers have been fabricated with a technology developed for the fabrication of  $Nb/Au/YBa_2Cu_3O_7$  ramp type Josephson junctions.

# Acknowledgements

When I first came to the UK to have my Phd interview, I did not understand people well and my English was not great. However I accepted the position which was offered me with enthusiasm, and during these three years and a half I worked with the maximum dedication.

If this has been possible I have to say thanks to my wife Oriana who followed and supported me into this adventure and to my family who always believed in what I was doing.

Then I have to thank Dr. Edward Tarte, he offered me the Phd position at the University of Birmingham and he always believed in my scientific skills. Another important mentor who supported my scientific work has been Dr. Tim Jackson, he always helped me with extremely good suggestions.

Other people who helped me to fill at home are: Christian Schuppler, Duncan Burker, Andreas Frommhold, Samia Benmerah, Richard Barret, Donna Johnson, Charanjit Panesar, Alan Islas Cital, Robert Davies, Nick Bassett, and David Webb.

Thanks to everyone for this great experience in the UK.

# Publications

## Accepted

- G. Vasta, T. J. Jackson, J. Bowen, E. Tarte, "New Multilayer Architectures for Piezoelectric BaTiO<sub>3</sub> Cantilever Systems" MRS Proceedings Volume 1325/mrss11-1325-e08-05 DOI:10.1557/opl.2011.970 (2011);
- G. Vasta, Timothy J. Jackson, Andreas Frommhold, James Bowen, Edward J. Tarte "Residual stress analysis of all perovskite oxide cantilevers" Journal of Electroceramics (accepted for publication) DOI: 10.1007/s10832-011-9663-6 (2011);
- G. Vasta, T. J. Jackson, E. Tarte "Electrical properties of BaTiO<sub>3</sub> based ferroelectric capacitors grown on oxide sacrificial layers for micro-cantilevers applications" Thin Solid Films (accepted for publication) DOI: 10.1016/j.tsf.2011.11.032 (2011).

## In preparation

- "Dielectric properties of SrRuO<sub>3</sub>/LaYbO<sub>3</sub>/SrRuO<sub>3</sub> capacitors" to submit to Thin Solid Films.

# Introduction

In recent years, the need of autonomous micro-systems like self-supportive sensors for environmental monitoring purposes [1], led to investigations on energy scavenging from the surrounding environment. An interesting way to harvest energy from the environment is represented by the conversion of the parasitic mechanical vibrations into electrical energy [2]. Piezoelectric materials are the perfect candidate for such conversion because they can efficiently convert mechanical strain into the separation of electrical charge and hence potential difference [1]. Furthermore the simplicity of the piezoelectric micro-generator is particularly attractive for use in MEMS structures [3].

Studies on energy harvesting devices based on  $Pb(Zr, Ti)O_3$  have been widely performed [1, 4, 5], powers ranging from few  $\mu W$  up to few  $mW$  have been extracted from these devices [5]. However the environmental problems associated with lead have stimulated this Phd focusing on the use of a lead free piezoelectric material like  $BaTiO_3$ . Furthermore the Directive 2002/95/EC of the European Parliament [9] restricts the use of hazardous substances like lead in the manufacture of various types of electronic and electrical equipment.

$Pb(Zr_{1-x}Ti_x)O_3$  (PZT) and related compositions have been the main-

stay for high performance actuators and transducers, owing to their superior piezoelectric coefficients. The maximum value of the  $d_{33}$  and  $g_{33}$  piezoelectric coefficients in PZT are  $520 \text{ pC/N}$  and  $71 \cdot 10^{-3} \text{ Vm/N}$  respectively reached for  $x = 0.48$  [8]. For  $\text{BaTiO}_3$  the values of the  $d_{33}$  and  $g_{33}$  piezoelectric coefficients are  $85.6 \text{ pC/N}$  and  $57.5 \cdot 10^{-3} \text{ Vm/N}$  [6]. The smaller values of the  $\text{BaTiO}_3$  piezoelectric coefficients lead to a reduction of the performances achievable with the devices employing  $\text{BaTiO}_3$  as piezoelectric layer.

To harvest energy from the vibrations present in the environment, a capacitive structure containing a piezoelectric material is usually integrated on the top of a micro-cantilever [1, 4, 5]. The maximum power is extracted at the resonance frequency of the micro-cantilever, so it is necessary to tune the fabricated devices with the frequencies of the vibrations present in the environment. Usually the vibrations present in the environment have frequencies ranging from few hertz to few kilo-hertz. Jeon et al. [4] produced a PZT micro-cantilever with a resonance frequency of  $13.9 \text{ KHz}$ . It is desirable to have devices with resonance frequencies ranging from few hertz to few kilo-hertz, in this frequency range the impedance phase of the piezoelectric capacitors integrated on the micro-cantilevers should be equal to  $-90^\circ$ . An impedance phase bigger than  $-90^\circ$  indicates the presence of resistive losses in the piezoelectric layer. We consider good quality capacitors all the devices with an impedance phase comprised between  $-80^\circ$  and  $-90^\circ$ .

The aim of this Phd is to investigate the properties of micro-cantilevers, containing  $\text{BaTiO}_3$  based capacitors on their top and verify if they can be used as energy harvesters. To do that a fabrication process which allow to fabricate suspended micro-cantilever has to be designed. Then it is neces-

sary to fabricate devices which behave as high quality capacitors (with an impedance phase between  $-80^\circ$  and  $-90^\circ$ ) at the micro-cantilever working frequency.

To fabricate the capacitive structure  $SrRuO_3$  is chosen as electrode layer, eventually  $Au$  can be used to replace the top  $SrRuO_3$  electrode. With the exception of gold, only oxides are used for the fabrication of the micro-cantilevers. Different layer sequences fitting the 31 and the 33 piezoelectric mode are deposited on the top of an oxide sacrificial layer, they are:

- $SrRuO_3/BaTiO_3/SrRuO_3$  (31 piezoelectric mode);
- $SrRuO_3/BaTiO_3/MgO/SrTiO_3$  (33 piezoelectric mode);

when  $YBa_2Cu_3O_7$  is used as sacrificial layer, and

- $SrRuO_3/BaTiO_3/SrRuO_3$  (31 piezoelectric mode);
- $SrRuO_3/BaTiO_3$  (33 piezoelectric mode);

when  $MgO$  is used as sacrificial layer. The choice of an oxide sacrificial layer and the use of all oxide materials allow the epitaxial growth of one layer on top of the other so the epitaxy is maintained through the stack.

These structures are fabricated by Pulsed Laser Deposition and contact photolithography techniques, the employed technological process is similar to that one employed for the fabrication of the  $Nb/Au/YBa_2Cu_3O_7$  ramp type Josephson junctions [10, 11]. This technological process has been chosen because investigations on  $Au/YBa_2Cu_3O_7$  ramp contacts have been performed during the first part of this Phd. A discussion on the fabrication process and the properties of these devices is reported in Appendix D.

During this Phd the same technology has been used also for the deposition of  $LaYbO_3$  thin films in  $SrRuO_3/LaYbO_3/SrRuO_3$  capacitive structures. Thin films of  $LaYbO_3$  find application as high-k dielectric, the properties of this kind of devices, fabricated during this Phd, are reported in Appendix E.

In the main body of the thesis, chapter 1 reports some basic concepts of ferroelectricity, the properties of  $BaTiO_3$  and the description of the multilayer structures which are used for the fabrication of the 31 and 33 mode piezoelectric cantilevers.

In chapter 2 the mathematical model describing the mechanical properties of microcantilevers together with the design rules employed for the design of the proposed suspended structures are discussed. Furthermore a mathematical model which takes into account the presence of a piezoelectric capacitor integrated on the top of the cantilevers and the fact that the structures are used as power source for a resistive load is discussed. Finally the properties of the designed simple beam and u-shape cantilevers are reported.

Chapter 3 is about the experimental methods used for the fabrication and the characterization of the multi-layer structures, here the Pulsed Laser Deposition system, the photolithography techniques, the critical point drying and the wirebonding system used for the fabrication of the mico-cantilever devices are described. In this chapter also the X-ray diffraction techniques together with the methods used for the electrical characterization of the capacitors are reported. Finally the nano-indentation method employed to measure the Young's modulus of each film in the multi-layer stacks is discussed.

Chapter 4 reports the fabrication process of the 31 and 33 mode piezo-

electric micro-cantilevers. Here the reasons which lead to the introduction of each step in the fabrication process are explained. In this chapter the use of the  $YBa_2Cu_3O_7$  film as sacrificial layer is discussed.  $YBa_2Cu_3O_3$  is easy to etch in weak acid solutions like 0.1%  $HNO_3$ , such weak acid solutions do not damage the other thin film layers present in the stack.

Chapter 5 presents the results of the X-ray diffraction analysis performed on different multi-layer sequences containing  $BaTiO_3$ ,  $SrRuO_3$ ,  $MgO$ ,  $SrTiO_3$  and  $YBa_2Cu_3O_7$  thin films. This analysis shows that epitaxy is maintained through stacks containing a combination of the previous layers. The analysed works on energy harvesting micro-cantilevers [1, 4, 5] do not report which is the orientation of the polar axis in the piezoelectric film respect to the position of the electrodes of the capacitive structure. This aspect is quite important as the charge collected between the electrodes of the piezoelectric capacitor depends on the orientation of the polar axis in the piezoelectric film. The performed X-ray diffraction analysis shows that the polar axis of  $BaTiO_3$  is perpendicular to the surface of the film when this layer is grown on  $SrRuO_3$  and  $SrTiO_3$ . This configuration fits the 31 energy harvesting mode. When  $BaTiO_3$  is grown on  $MgO$  the polar axis is parallel to the surface of the film so this configuration fits the 33 energy harvesting mode. At the end of the chapter the results of the nano-indentation measurements are discussed. The measured values of the Young's modulus are sensibly higher than the values of the Young's modulus of  $Pb(Zr,Ti)O_3$  and  $SiO_2$  used for the fabrication of energy harvesting cantilevers by Jeon et al. [4]. This is useful to reduce the residual stress in the suspended structures after their release.

Chapter 6 reports a method to evaluate the residual stress on the top surface of the fabricated micro-cantilevers. In previous works the residual stress in micro-cantilevers was caculated by measuring the deflection of the free end in the case of small deflections [12, 13], or by using the Stoney formula [4, 14]. In our multilayer cantilevers the Stoney formula does not apply because some of the hypothesis necessary for the application of this method are not fulfilled [15]. Furthermore deflections of the free end equal to  $40 \mu m$  for cantilever having lengths of  $180 \mu m$  have been measured, so also the hypothesis of small deflection of the free end does not apply.

In this method the mathematical expression of the curve approximating the deflection of the cantilever is calculated by measuring the deflection of the suspended structures at different distances from the anchor point. This enables the calculation of the radius of curvature of the structure and so of the residual stress.

In chapter 7 the results of the electrical characterization of the capacitive structures are reported and analysed. The influence of the  $YBa_2Cu_3O_7$  and  $MgO$  sacrificial layers on the electrical properties of the  $SrRuO_3/BaTiO_3/SrRuO_3$  capacitors is discussed. It is shown that the presence of particulate on the surface of the sacrificial layer increases the resistive losses in the capacitors. Piezoelectric capacitors grown on an oxide sacrificial layer in an oxygen environment at a pressure of  $20 Pa$  present resistive losses, the capacitive behaviour is recovered for deposition pressures equal or lower than  $8 Pa$  hovewer the residual polarization of the  $BaTiO_3$  is reduced at values smaller than  $2.5 \mu C/cm^2$  for deposition pressures smaller than  $8 Pa$ .

Finally chapter 8 reports the conclusion and the future developments of

the project.

The major contributions of this thesis are:

- $YBa_2Cu_3O_7$  can be used as sacrificial layer to suspend micro-cantilevers containing  $BaTiO_3$  and  $SrRuO_3$  based capacitive structures, the use of all oxide materials allows to maintain the epitaxy through the stack;
- when the  $BaTiO_3$  is grown on  $SrRuO_3$ , the  $BaTiO_3$  polar axis is perpendicular to the surface of the film, this configuration can be used to fabricate energy harvesting devices using the 31 piezoelectric mode;
- when the  $BaTiO_3$  is grown on  $MgO$ , the  $BaTiO_3$  polar axis is parallel to the surface of the film this configuration can be used to fabricate energy harvesting devices using the 33 piezoelectric mode;
- the properties of  $SrRuO_3/BaTiO_3/SrRuO_3$  piezoelectric capacitors grown on  $YBa_2Cu_3O_7$  sacrificial layers are degraded by the particulates present on the surface of the sacrificial layer itself;
- a reduction of the deposition pressure (below 8 Pa) during the growth of  $BaTiO_3$  thin films reduces the resistive losses in  $BaTiO_3$  based capacitors, however also the value of the  $BaTiO_3$  residual polarization is reduced below  $2.5 \mu C/cm^2$ ;
- $SrRuO_3/BaTiO_3/SrRuO_3$  capacitive structures fabricated on  $MgO$  sacrificial layer at a  $BaTiO_3$  deposition pressure equal to 8 Pa and at a growing temperature of  $780^\circ C$  present an impedance phase between  $-80^\circ C$  and  $-90^\circ$  over 6 KHz and a  $BaTiO_3$  residual polarization of  $2.5 \mu C/cm^2$ .

# Chapter 1

## Piezoelectricity and device description

Section one and section two of this chapter provide an overview on ferroelectricity and piezoelectricity. In section three the crystal structure and the properties of  $BaTiO_3$  crystals are reported. Finally in section four the materials and the structures of the micro-cantilevers employed for the fabrication of energy harvesting devices are discussed.

### 1.1 General properties of ferroelectric materials

The properties of dielectric media, including those ones of piezoelectric materials, can be described by their **polarization**. The polarization values measured in normal dielectrics after the application of experimentally achievable fields are usually small. Some crystals show polarization values which are

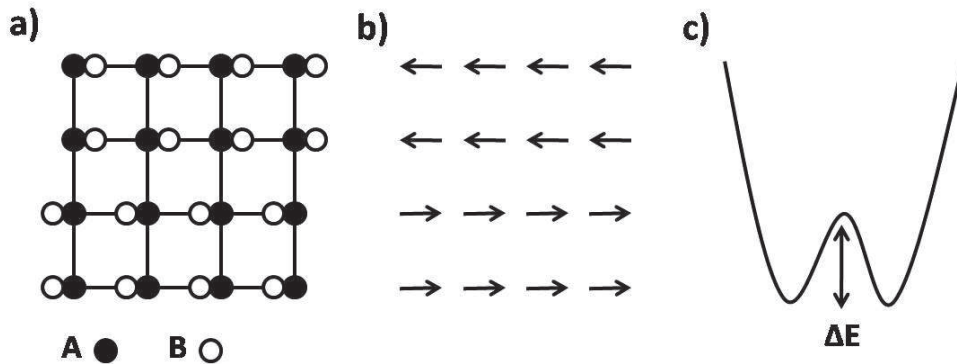


Figure 1.1: a) Two dimensional fictitious crystal with chemical formula  $AB$ . b) Uniform polarized domains in the two dimensional crystal. c) Potential between two adjacent  $A$  ions.

many orders of magnitude larger than those observed in most dielectrics. These materials are classified as **ferroelectric**. The reason of this name is due to the similarity of the ferroelectric phenomenon with that of ferromagnetism. Ferroelectric crystals show a spontaneous electric polarization and hysteresis effect in the relation between dielectric displacement and electric field. In ferroelectric materials the values of the spontaneous polarization vary from  $10^{-7} C/cm^2$  to about  $10^{-4} C/cm^2$ , in normal dielectrics such high values of polarization could theoretically be attained only with electric fields from  $10^5 V/cm$  to  $10^8 V/cm$  [16].

To explain the basic features of ferroelectricity it is possible to introduce a simplified two dimensional crystal having the chemical formula  $AB$  and the fictitious structure of fig.1.1a.

The  $A$  ions are assumed to carry a negative charge, they are located on the lattice points of a simple square structure. The  $B$  ions, carrying the

positive charge, are located on the horizontal lines joining the *A* ions. Their equilibrium position are such that they always lie closer to one of the two adjacent *A* ions. This is possible if the potential between the two adjacent *A* ions is like that one shown in fig.1.1c. There are two equilibrium positions, with the same minimum value of the energy, for a *B* ion on the line joining two *A* ions. The *B* ions can jump from one equilibrium position to the other but in order to do so they must receive the energy necessary to overcome the energy barrier  $\Delta E$ .

If at a certain given temperature  $T$ , all *B* ions are close to the *A* ions on the left side, every *AB* group can be thought as an electric dipole and the structure on the square lattice can be represented by an assembly of dipoles pointing all in the same direction, as in the two bottom rows of fig.1.1b. The crystal is said to be **spontaneously polarized**. The **spontaneous polarization** is measured in terms of the charge induced on the surfaces perpendicular to the polarization as charge per unit area.

The crystals having spontaneous polarization are called **pyroelectric** and the direction of the spontaneous polarization is called **polar axis**. Pyroelectrics exhibit spontaneous polarization at any temperature (provided that the crystalline state persist). In ferroelectrics this effect is only observable in certain temperature ranges.

Alignment of the electric dipoles may extend only over a region of the crystal, while in another region the direction of the spontaneous polarization may be reversed, as in the upper part of fig.1.1b. The regions of uniform polarization are called **domains**.

Suppose now that an electric d.c. field is applied in the horizontal direc-

tion of fig.1.1. The dipoles already oriented in the direction of the field will remain so aligned, but those which are oriented in the direction antiparallel to the field tend to reverse their orientation. If the applied field is sufficiently large, the B ions of the simplified model will be able to overcome the barrier  $\Delta E$ , and in doing so will cause the corresponding dipole to switch into the direction of the field. This phenomenon of polarization reversal takes place by way of a nucleation process and domain-wall motion.

There are a number of fundamental inaccuracies in the description of the previous model, in spite of the fact that it helps to account for the general properties of ferroelectric crystals.

In the first place, pairs of atoms have been arbitrarily chosen, and a dipole moment, defined as the product between the charge and the separation, has them been attributed. This procedure is not legitimate in a real structure. It is true that in a ferroelectric crystal every unit cell carries a dipole moment, but it is not possible to attribute this dipole moment to a specific pair of atoms in the unit cell.

What it is possible to say is that given a charge distribution  $\rho(r)$  within a given crystal the electric moment with respect to an arbitrary origin,

$$\vec{P}(\vec{r}) = \int \int \int \rho(\vec{r}) \vec{r} dv \quad (1.1)$$

is different from zero and the value of this volume integral is independent of the choice of the origin.

A second important point is that the dipole moment of each unit cell does not consist only of ionic charges (displacement of ionic sublattices).

Eventually, charge separation may arise from the distortion of the electronic cloud of a given atom. So the charge distribution  $\rho(r)$  within the crystal involves both ionic and electronic charges.

Suppose now that the crystal of fig.1.1a is initially composed of an equal number of positive and negative domains (i.e. domains oriented to the right and domains oriented to the left fig.1.1b). This means that the overall polarization of the crystal is equal to zero. If a small electric field directed in the positive direction is applied, for small values of the field  $\vec{E}$ , a linear relationship between the polarization  $\vec{P}$  and the applied field is observed.

$$\vec{P}(\vec{E}, t) = \epsilon_0 \chi \vec{E}(t) \quad (1.2)$$

Where  $\epsilon_0$  is the permittivity of free space,  $\chi$  is the electric susceptibility of the crystal and  $t$  is time. This happens because the field is not large enough to switch any of the domains and the crystal will behave like a normal dielectric. In the plot  $\vec{P}$  vs.  $\vec{E}$ , fig.1.2 the portion  $OA$  of the curve is obtained.

When the electric field is increased, a number of negative domains change their orientation to positive and the polarization increase rapidly (portion  $AB$ ), until a state in which all the domains are aligned in the positive direction is reached. This is a state of saturation (portion  $BC$ ) and the crystal consists of a single domain. If the applied electric field is decreased, the polarization does not return to zero but it follows the path  $CD$ . When the applied field is reduced to zero some of the domains will remain aligned in the positive direction and the crystal will exhibit a **residual polarization**  $\vec{P}_r$  whose magnitude is equal to the length of the segment  $OD$ . The extra-

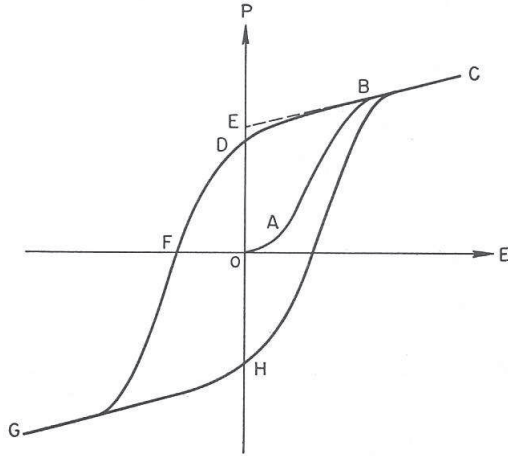


Figure 1.2: Ferroelectric hysteresis loop [16].

pulation of the linear portion  $BC$  of the curve back to the polarization axis represents the value of the **spontaneous polarization**  $\vec{P}_s$  whose magnitude is equal to the segment  $OE$ .

In order to cancel the overall polarization of the crystal, it is necessary to apply an electric field in the opposite (negative) direction. The value of the field required to reduce the polarization to zero is called **coercive field**  $\vec{E}_c$ , its magnitude is equal to the segment  $OF$ . Further decrease of the field will cause a complete alignment of the dipoles in the negative direction (portion  $FG$ ), and the cycle can be completed by reversing the field direction once again ( $GH$ ).

The relation between the polarization  $\vec{P}$  and the applied electric field  $\vec{E}$  is so represented by an **hysteresis loop** ( $CDGHC$ ), and can be expressed as follows,

$$\vec{P}(\vec{E}, t) = \epsilon_0 \chi \vec{E}(t) + \vec{P}_d(\vec{E}, t) \quad (1.3)$$

where  $\vec{P}_d$  is the contribution to the polarization due to the switching dipoles [17].

The most important property of a ferroelectric is the reversibility of the spontaneous polarization. An electric field can cause the polarization to alter its orientation. In terms of the two dimensional fictitious crystal, fig.1.1 it means that the shift of the  $B$  ions is small, and this small relative shift turns the crystal into its electrical twin. If the energy barrier  $\Delta E$  is so low as to be accessible with the help of an electric field, then it may also be affected by other factors, such as temperature changes.

With increasing temperature, the thermal motion of the atoms in the lattice may increase and the  $B$  ions may be able to overcome the energy barrier  $\Delta E$  without the help of an external field and jump from one equilibrium position to another. Here the statistical distribution of the  $B$  ions is symmetrical with respect to the  $A$  ions. Another possibility is that the shape of the potential curve between adjacent  $A$  ions changes and  $\Delta E$  becomes equal to zero. In this case there is only one equilibrium position for the  $B$  ions. In both cases the crystal is no longer polar, and it will behave as a normal dielectric material.

The temperature at which such a transition from the polar into the non-polar state occurs is referred as **Curie temperature**. Almost all ferroelectric crystals have a Curie temperature, and those which do not have it simply decompose before such a temperature is reached [16].

## 1.2 Piezoelectricity and equations of state

Piezoelectricity is a reciprocal phenomenon, this means that there are **direct** and **converse** piezoelectric effects. Such effect is observed in crystals in which permanent dipole moments have no center of symmetry in their arrangement. The piezoelectric effect must not be confused with electrostriction exhibited by common dielectrics. In both cases we are dealing with the effect of an electric field on the shape or dimensions of the material, electrostriction is quadratic and the (converse) piezoelectric effect is linear in the field.

The **direct piezoelectric effect** is the appearance of electrical charges on the faces of a crystal which is being subjected to a mechanical stress. The **converse piezoelectric effect** is the change of the dimensions of a material caused by an external electric field [18].

Piezoelectric phenomena are described by a system of two equations. There are four equivalent systems which correspond to four equivalent descriptions, the differences between the four systems consist in the initial thermodynamic potential chosen for the derivation. The four equivalent systems describing the piezoelectric phenomena are:

$$\begin{aligned} \textbf{h-form : } & d\sigma_i = c_{ij}^{D,T} dx_j - h_{in}^{T*} dD_n \\ & dE_m = -h_{mj}^T dx_j + \kappa_{mn}^{x,T} dD_n \end{aligned} \tag{1.4}$$

$$\begin{aligned} \textbf{g-form : } & dx_i = s_{ij}^D d\sigma_j + g_{in}^* dD_n \\ & dE_m = -g_{mj} d\sigma_j + \kappa_{mn}^\sigma dD_n \end{aligned} \tag{1.5}$$

$$\begin{aligned} \textbf{d-form : } \quad dx_i &= s_{ij}^E d\sigma_j + d_{in}^* dE_n \\ dD_m &= -d_{mj} d\sigma_j + \epsilon_{mn}^\sigma dE_n \end{aligned} \quad (1.6)$$

$$\begin{aligned} \textbf{e-form : } \quad d\sigma_i &= c_{ij}^E dx_j - e_{in}^* dE_n \\ dD_m &= e_{mj} dx_j + \epsilon_{mn}^x dE_n \end{aligned} \quad (1.7)$$

they form the elastic and dielectric **linear equations of state**. In these equations the symbol  $*$  indicates the transpose of the matrix,  $\epsilon$  represent the dielectric permittivity tensor,  $\kappa$  is its reciprocal tensor,  $d, e, h, g$  represent the tensors of piezoelectric compliances,  $c$  is the tensor of elastic stiffnesses and  $s$  is the tensor of elastic compliances. The  $\epsilon$  and  $\kappa$  tensors are  $(3 \times 3)$  matrices, the  $d, e, h$  and  $g$  tensors are  $(3 \times 6)$  matrices and the  $d^*, e^*, h^*$  and  $g^*$  are  $(6 \times 3)$  matrices [19, 20] [19].

The h-form, g-form, d-form and e-form equation systems represent four equivalent ways to describe piezoelectric media, each system differs from the others in the choice of the independent variables.

### 1.3 *BaTiO<sub>3</sub>* properties

The aim of the project concerning the piezoelectric devices, developed during the second part of this Phd, is to construct energy harvesting structures based on lead free piezoelectric materials. For such purpose *BaTiO<sub>3</sub>* has been chosen as piezoelectric medium. The main reason is that thin films of such material can be deposited by our Pulsed Laser Deposition system, furthermore the characteristics of such films, like the crystal structure, well fit the other materials used for the fabrication of our devices.

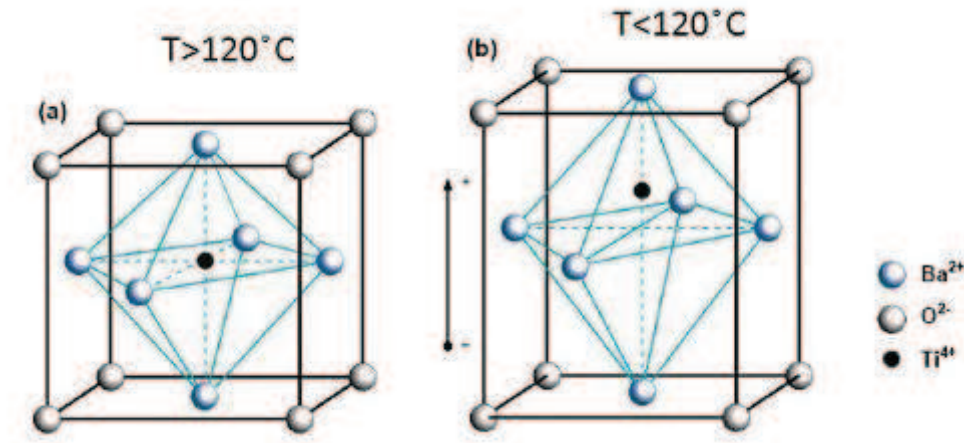


Figure 1.3: a) Above 120°C the  $BaTiO_3$  unit cell has cubic structure.  
b) Below 120°C and above 5°C the  $BaTiO_3$  unit cell has tetragonal structure [21].

Barium Titanate belongs to the perovskite material family, its Curie temperature is 120°C. Above the Curie temperature  $BaTiO_3$  is stable in its cubic phase fig. 1.3a, due to the symmetry of such phase the material is not piezoelectric. Below the Curie temperature and above 5°C the crystal structure is tetragonal fig. 1.3b, in this phase the cube edge which is parallel to one of the original cubic (100) directions is elongated fig. 1.4b, such axis is called **polar axis**. The other two cube edges are instead compressed. Below 5°C and above -90°C a new phase appears which has orthorombic symmetry, this phase is still ferroelectric and the direction of the spontaneous polarization is parallel to one the original cubic (110) directions fig. 1.4c. At -90°C a third transition from orthorhombic to rhombohedral occurs. The polar axis lies along one of the original cubic (111) directions fig. 1.4d.

The phase of interest in our application is the tetragonal one. In this

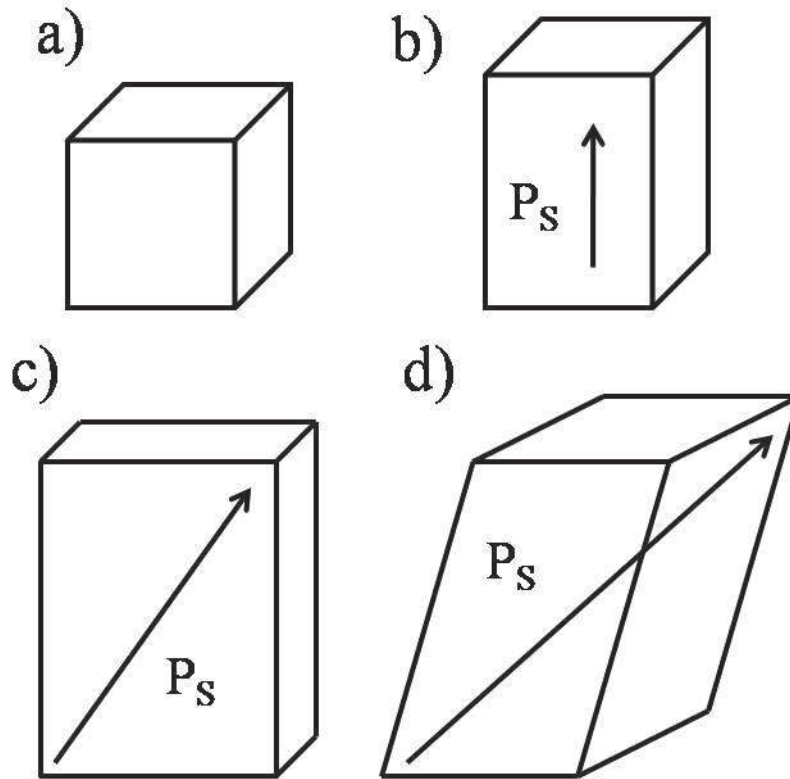


Figure 1.4: Unit cells of the four phases of  $BaTiO_3$ , the dotted lines delineate the original cubic cell. The arrows indicate the direction of the spontaneous polarization  $P_s$  in each phase. a) Cubic phase stable above  $120^\circ C$ . b) Tetragonal phase stable between  $120^\circ C$  and  $5^\circ C$ . c) Orthorhombic phase stable between  $5^\circ C$  and  $-90^\circ C$ . d) Rhombohedral phase stable below  $-90^\circ C$ . [16].

phase the unit cell dimensions are [16]:

$$a = 3.992 \text{ \AA} \quad c = 4.036 \text{ \AA} \quad (1.8)$$

In the polar phases the dipole moment is generated by a shift of the  $Ti^{4+}$  and of the  $Ba^{2+}$  cations with respect to the  $O^{2-}$  anions. In the tetragonal

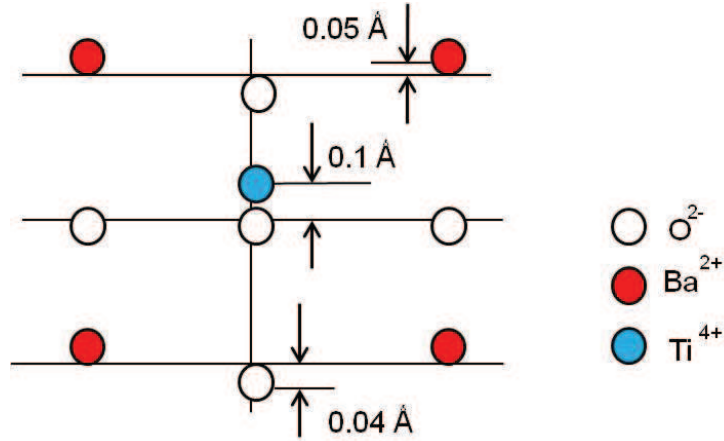


Figure 1.5: Shift between the  $Ti^{4+}$  and  $Ba^{2+}$  cations with respect to the  $O^{2-}$  anions in the  $BaTiO_3$  tetragonal structure at  $18^\circ C$  [16].

phase the shift between the  $Ti^{4+}$  cations and the  $O^{2-}$  anions is equal to  $0.1 \text{ \AA}$  instead the shift between the  $Ba^{2+}$  cations and the  $O^{2-}$  anions assumes values of  $0.05 \text{ \AA}$  and  $0.04 \text{ \AA}$ , fig. 1.5. These shifts are also responsible for the high values of the dielectric constant which are typical in ferroelectric materials.

The  $BaTiO_3$  in its cubic phase has only one dielectric constant, this is due to the symmetry of the cubic structure. In the tetragonal phase there are two dielectric constants denoted by  $\epsilon_a$  and  $\epsilon_c$ . The values for such constants are [16]:

$$\epsilon_a = 160 \quad \epsilon_b = 4100 \quad (1.9)$$

the dielectric constants exhibits pronounced anomalies at the transitions from one phase to another. The spontaneous polarization for  $BaTiO_3$  in the tetragonal phase is [16]:

$$P_s \approx 16 \frac{\mu C}{cm^2} \quad (1.10)$$

<i>Material</i>	<i>Structure</i>	<i>Lattice parameter [Å]</i>
$BaTiO_3$	tetragonal (*)	$a = b = 3.992$ $c = 4.036$
$SrTiO_3$	cubic	$a = b = c = 3.905$
$MgO$	cubic	$a=b=c=4.211$
$SrRuO_3$	orthorhombic (**) $\gamma = 89.6^\circ$	$a = 5.670$ $b = 5.5304$ $c = 7.8446$
$YBa_2Cu_3O_7$	orthorhombic	$a = 3.82$ $b = 3.88$ $c = 11.68$

Table 1.1: Lattice parameters of the materials used in the multilayer [16, 25, 26].  
(\*) At room temperature. (\*\*) Usually treated as a pseudo-cubic perovskite ( $a = 3.93\text{\AA}$ ).

however an higher value for the residual polarization in  $BaTiO_3$  equal to  $26 \mu C/cm^2$  is reported in [22].

## 1.4 Device and material descriptions

As already stated in sec. 1.3, the goal of the project is the fabrication of piezoelectric lead free devices for micro-scale energy generation. The idea is to fabricate multi-layer cantilevers of different size and shape, containing a capacitive structure, in order to convert the vibrations present in the environment into electrical energy.

Table 1.1 reports the materials employed for the fabrication of the micro-cantilevers. Only oxides are used in our devices, two of these oxide materials,  $SrTiO_3$  and  $BaTiO_3$ , belong to the perovskite family. The general formula of the compounds belonging to this family is  $ABO_3$ , where  $A$  is a monovalent,

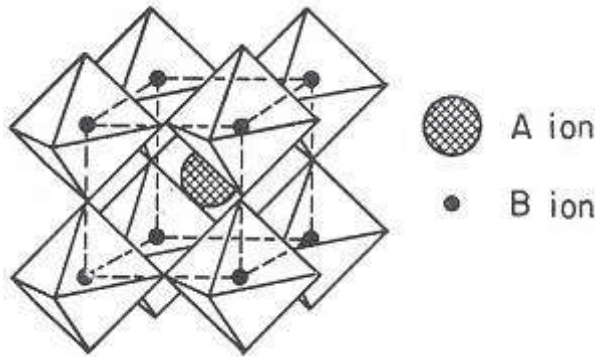


Figure 1.6: Perovskite structure  $ABO_3$  considered as a three-dimensional frame-work of  $BO_6$  octahedra [16].

divalent or trivalent metal and  $B$  is a trivalent, tetravalent or pentavalent element. The traditional view of the perovskite lattice is that it consists of small  $B$  cations within oxygen octahedra, and larger  $A$  cations with twelve coordinated oxygens fig.1.6 [24]. As already stated in sec. 1.3, at room temperature, the  $BaTiO_3$  has a tetragonal unit cell while the  $SrTiO_3$  has cubic unit structure.

The other materials used in our multilayers are  $YBa_2Cu_3O_7$ ,  $SrRuO_3$  and  $MgO$ . The  $YBa_2Cu_3O_7$  and the  $SrRuO_3$  oxides present an orthorhombic unit cell. The  $YBa_2Cu_3O_7$  cell can be seen as three perovskite unit cells stacked upon each other, the  $SrRuO_3$  has orthorhombic structure but it can be also seen as a pseudocubic perovskite [25]. The  $MgO$  has a cubic unit cell with the  $Mg$  atom within oxygen octahedra [27].

These materials have been chosen because they have a crystal structure which allow the epitaxial growth of a layer on top of the other. The lattice parameters of the different materials are reported in tab.1.1.

In the multilayers which have been developed  $SrRuO_3$  is used as an electrode layer and the  $BaTiO_3$  is the piezoelectric film, both layers are used in the 33 and in the 31 structures. Alternatively a gold film can be used as top electrode in both structures. The  $MgO$ , as will be discussed in chap 5 changes the orientation of the  $BaTiO_3$  polar lattice, making it parallel to the surface of the film. The  $YBa_2Cu_3O_7$  is used as sacrificial layer to suspend the multilayer structure. The thin films have been epitaxially grown on (001) oriented  $SrTiO_3$  substrates by Pulsed Laser Deposition.

There are two piezoelectric modes which are commonly used in suspended cantilevers containing a piezoelectric film, they are the 31 and the 33 modes, fig. 1.7 [4, 1, 5, 23].

In the 31 mode the developed electric field  $\vec{E}$  is perpendicular to the applied input stress  $\sigma_{xx}$ , while in the 33 mode the electric field is parallel to the input stress. The 31 mode has separate top and bottom electrode, the 33 mode eliminates the need for a bottom electrode by employing an interdigitated conductive layer on its top. The 33 design presents also the advantage to produce an higher open circuit voltage than the 31 design, in fact the 33 design produces the following output open circuit voltage:

$$V_{33} = \sigma_{xx} L g_{33} \quad (1.11)$$

where  $L$  is the spacing between the fingers of the interdigitated electrode and  $g_{33}$  [ $Vm/N$ ] is the piezoelectric constant. In the 31 design the output open circuit voltage is:

$$V_{31} = \sigma_{xx} t g_{31} \quad (1.12)$$

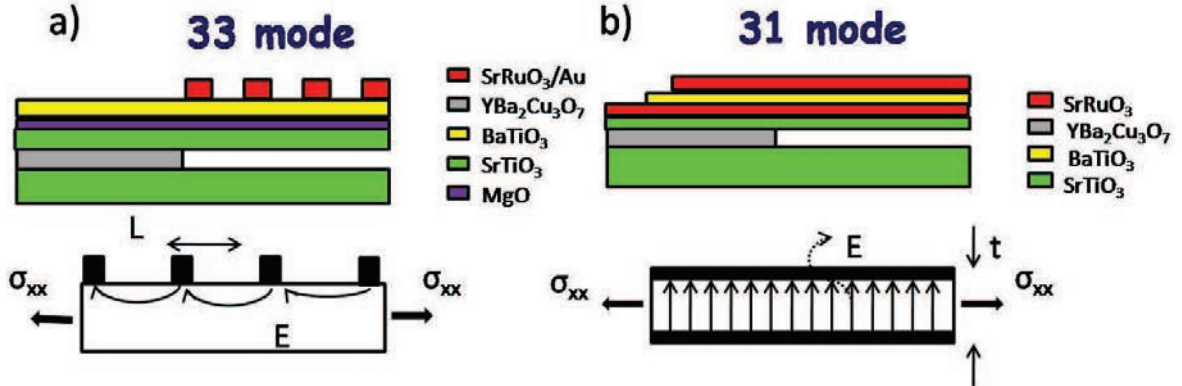


Figure 1.7: a) Multilayer structure fitting the 33 mode design. The  $YBa_2Cu_3O_7$  is the sacrificial layer used to obtain suspended structures, the  $SrTiO_3$  functions as buffer layer, the  $MgO$  film changes the growing orientation of the  $BaTiO_3$  polar axis making it parallel to the surface of the film, the  $BaTiO_3$  is the piezoelectric layer, the  $SrRuO_3$  and the  $Au$  work as electrode. b) Multilayer structure fitting the 31 mode design. The  $YBa_2Cu_3O_7$  is the sacrificial layer used to obtain suspended structures, the  $SrTiO_3$  functions as buffer layer, the  $BaTiO_3$  is the piezoelectric layer and the  $SrRuO_3$  works as electrode.

where  $t$  is the distance between the top and the bottom electrode and  $g_{31}$  [Vm/N] is the piezoelectric constant. In the  $BaTiO_3$  the following relation is valid [6],

$$g_{33} > g_{31} \quad (1.13)$$

with

$$g_{33} = 57.5 \cdot 10^{-3} \text{ Vm/N} \quad (1.14)$$

and

$$g_{31} = -23.0 \cdot 10^{-3} \text{ Vm/N} \quad (1.15)$$

[6]. Furthermore for the two structures

$$L > t \quad (1.16)$$

hence the 33 mode can be expected to provide a much larger output voltage than the 31 mode [4, 1].

## 1.5 Summary

In this chapter the basic concepts of ferroelectricity and the properties of  $BaTiO_3$  have been discussed. The materials which are going to be used for the fabrication of the micro-cantilevers and their crystal structures have been introduced. They are:  $BaTiO_3$ ,  $SrRuO_3$ ,  $SrTiO_3$ ,  $MgO$ ,  $YBa_2Cu_3O_7$  and  $Au$ . The structures working with the 31 and 33 piezoelectric modes have been analysed and it has been shown how an higher output voltage is expected from devices using the 33 piezoelectric mode.

# Chapter 2

## Mechanical properties and cantilever design

In this chapter the mechanical model and the design criteria for multi-layer cantilevers with different shapes and with a seismic mass constructed on their free end will be discussed. The basic theory and the description of the mechanical behaviour of a suspended beam with a clamped end is reported in Appendix A. Here the cantilevers and their seismic masses will be modeled as a *spring mass damper system* [4, 5, 28, 29, 30, 31], the damping will be divided into two contributions [5]: the *mechanical damping* due mainly to the air resistance [28, 30], and the *electrical damping* [4] due to the dissipation in the piezoelectric layer contained in the cantilever.

First a purely mechanical model which does not take into account the fact that the cantilever is used as micro-generator will be developed. The model for a cantilever used as micro-generator will be developed in sec. 2.2.

Finally the design adopted for our suspended structures and its effect on

the parameters of the mechanical model is discussed.

## 2.1 Mechanical model for suspended multi-layer cantilevers

Let us consider the system of axis reported in fig. 2.1a, and assume the positive sign for the directions of the forces and of the bending moments indicated in fig. 2.1a. Furthermore it is assumed that the cantilever is oriented parallel to the  $x$  axis with the free end, point (1), coinciding with the origin of the reference system, fig. 2.1.

When the cantilever free end moves in the  $z$  direction (fig. 2.1b) after the application of a force  $F_{1-z}$ , and/or a bending moment  $M_{1-y}$ , the total displacement is the sum of a **linear displacement**  $u_{1-z}$  and of a **rotation**  $\theta_{1-y}$ , [30].

In the case that a force  $F_{z-1}$  and a moment  $M_{1-y}$  are applied to the free end (point 1) of the cantilever, the linear displacement  $u_{1-z}$  can be thought as the sum of two effects, one due to the force  $F_{1-z}$  and the other due to the bending moment  $M_{1-y}$ . In the same way also the rotation  $\theta_{1-y}$  is the sum of two effects one due to the force along the  $z$  axis and the other due to the moment around the  $y$  axis. This is summarized by the system 2.1:

$$\left\{ \begin{array}{l} u_{1-z} = C_{u_z-F_z} F_{1-z} + C_{u_z-M_y} M_{1-y} \\ \theta_{1-y} = C_{\theta_y-F_z} F_{1-z} + C_{\theta_y-M_y} M_{1-y} \end{array} \right. \quad (2.1)$$

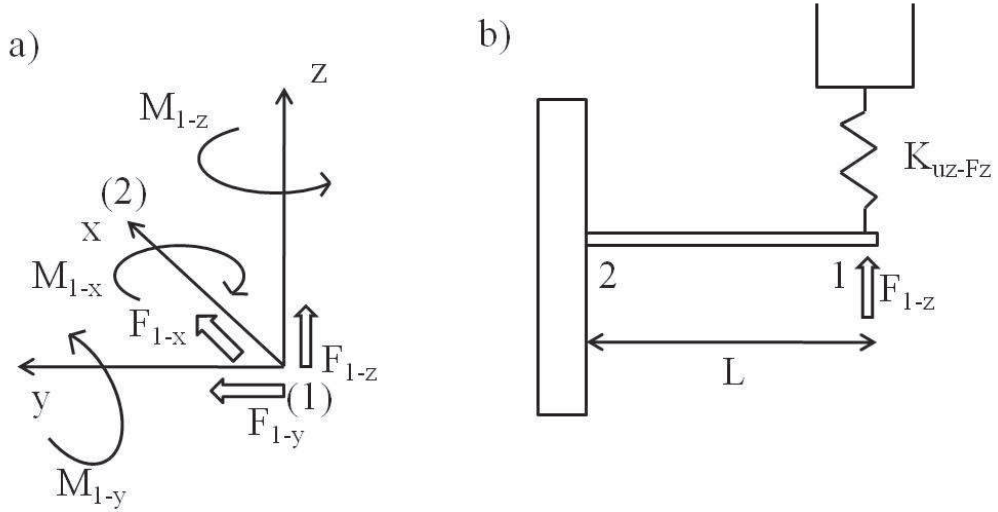


Figure 2.1: a) Reference system showing the convention adopted for the forces and the bending moments. Point 1 and point 2 correspond to the free and to the built in end of the cantilever, this means that the cantilever will be oriented with the long side parallel to the  $x$  axis. b) The elastic behaviour of a cantilever with a free end is modelled with a spring having elastic constant equal to  $K_{uz-Fz}$ .

where  $C_{u_z-F_z}$ ,  $C_{u_z-M_y}$ ,  $C_{\theta_y-F_z}$  and  $C_{\theta_y-M_y}$  are the elements of the compliance matrix. When the forces and the bending moments are written as a function of the rotation and of the linear displacement, the elements of the matrix of the elastic constants appear in the two equations, system 2.2.

$$\left\{ \begin{array}{l} F_{1-z} = K_{F_z-u_z} u_{1-z} + K_{F_z-\theta_y} \theta_{1-y} \\ M_{1-y} = K_{M_y-u_z} u_{1-z} + K_{M_y-\theta_y} \theta_{1-y} \end{array} \right. \quad (2.2)$$

It is now clear that the deflection of the free end of a cantilever can be modelled with a linear deflection plus a rotation. The model for the linear

deflection is a spring with elastic constant  $K_{u_z-F_z}$  fig. 2.1b, but there is no model for the rotation  $\theta_{1-y}$  [30].

We are now interested in finding the elastic constants in the case of a displacement parallel to the  $z$  axis. This means that we are interested in the displacement  $u_{1-z}$  and to the rotation  $\theta_{1-y}$ . The values of the calculated elastic constants will be used to build the equivalent model of the suspended cantilever. Considering eq. A.51 (see appendix A), which gives the contribution of the force  $F_{1-z}$  and of the bending moment  $M_{1-y}$  to the total deflection of the cantilever in the case of a constant cross section, the elements of the compliance matrix  $C_{u_z-F_z}$  and  $C_{u_z-M_y}$  can be easily derived. In the case of a variable cross section they are:

$$C_{u_z-F_z} = \frac{1}{K_{F_z-u_z}} = \frac{u_{1-z}}{F_{1-z}} = \frac{1}{\tilde{E}} \int_0^L \frac{x^2}{I_y(x)} dx \quad (2.3)$$

and:

$$C_{u_z-M_y} = \frac{1}{K_{M_y-u_z}} = \frac{u_{1-z}}{M_{1-y}} = \frac{1}{\tilde{E}} \int_0^L \frac{x}{I_y(x)} dx \quad (2.4)$$

where [30]:

$$C_{u_z-M_y} = C_{\theta_y-F_z} \quad ; \quad K_{F_z-\theta_y} = K_{M_y-u_z}. \quad (2.5)$$

Considering eq. A.42, the coefficient  $C_{\theta_y-M_y}$  can be written as:

$$C_{\theta_y-M_y} = \frac{1}{\tilde{E}} \int_0^L \frac{1}{I_y(x)} dx \quad (2.6)$$

where  $I_y(x)$  is the moment of inertia of the cantilever cross section eq. A.34,

$\tilde{E}$  is the Young Modulus of the material which constitutes the cantilever and  $L$  is the length of the beam.

It has been anticipated that the model of a cantilever with a built in end is that one of a spring mass damper system, in this model the elastic constant of the spring is chosen equal to  $K_{u_z-F_z}$ . This is a simplification of the problem because the rotation of the free end is neglected, however this implies an error of only 10% [30]. In this way the elastic constant of a suspended beam with a free end and an uniform cross section is [28]:

$$K = K_{u_z-F_z} = \frac{3\tilde{E}I_y}{L^3}. \quad (2.7)$$

A more accurate expression for the elastic constant, which takes into account the rotation of the free end, can be calculated by using the Castigliano theorems, however one of the main reasons for which the equivalent model of the cantilever is calculated, is the evaluation of the beam resonant frequency. The expression of the elastic constant to use in the calculation of the resonant frequency is that one reported in eq. 2.7, [28, 30].

In section 1.4 it has been showed that the fabricated cantilever are not made of only one material but they are multi-layer cantilevers. In appendix A and in the initial part of this section only homogeneous beams have been discussed, now the case of a multi-layer cantilever will be treated.

According the theory of the *transformed section* [32], the section of a multi-layer cantilever is transformed into an equivalent homogeneous (made of only one material) section [28, 30, 32, 33]. From a mathematical point of view this means that the relationships which have been found in the case of

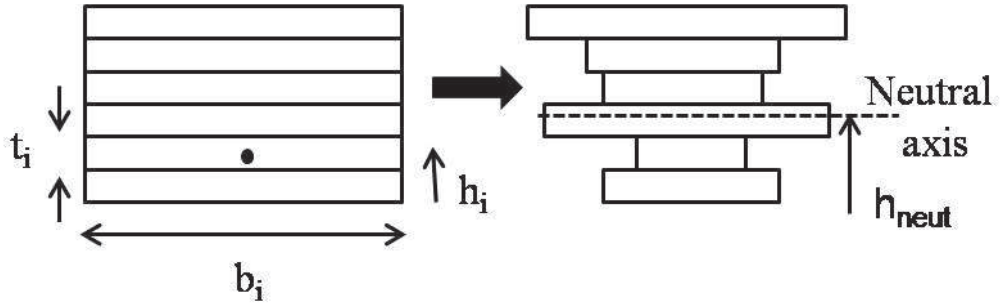


Figure 2.2: Equivalent section model of an heterogeneous multilayer cantilever according to the equivalent section theory;  $b_i$  is the width of the layer  $i$ ,  $t_i$  is the thickness of the layer  $i$ ,  $h_i$  indicates the distance between the baricenter of the layer  $i$  and the (bottom) base of the cross-section, finally  $h_{neut}$  indicates the distance between the neutral axis and the (bottom) base of the cross-section.

the homogeneous beam can be used.

In fig. 2.2 the cross section of a multi-layer cantilever is shown, to find the equivalent cross section, the Young modulus of each layer  $\tilde{E}_i$  has to be normalized with respect to the maximum Young Modulus  $\tilde{E}_{max}$ . The width of each layer  $b_i$  can be transformed into a new width  $b_{i,n}$ , according to the following relation:

$$b_{i,n} = b_i \frac{\tilde{E}_i}{\tilde{E}_{max}} \quad (2.8)$$

this new layer with different width has the Young Modulus equal to the maximum Young Modulus. When this is repeated for each film present in the stack, the result is an homogeneous cross section made of layers with different shapes [30, 33, 32]. Now as we are dealing with an homogeneous beam, the position of the neutral axis (look section A.2 in Appendix A) can

be calculated by knowing the baricenter of each layer eq. 2.9:

$$h_{neut} = \frac{\sum_i (t_i b_{i,n}) h_i}{\sum_i (t_i b_{i,n})} \quad (2.9)$$

$h_{neut}$  indicates the position of the neutral axis,  $t_i$  is the thickness of the layer  $i$ ,  $h_i$  is the position of the baricenter of the layer  $i$  and  $b_{i,n}$  is the normalized width of the layer  $i$  [30, 33].

The next step is the understanding of the elastic response of the equivalent cross section when an external force or an external bending moment is applied. In order to do that the expression of the moment of inertia of the equivalent cross section has to be found. In Appendix A, with eq. A.34, the cross-sectional moment of inertia for a rectangular cross section has been evaluated. Here we are interested to the moment of inertia respect to the neutral axis; considering the equivalent cross section of fig. 2.2, the moment of inertia of each layer present in the stack is:

$$I_i = I_{i,g} + (b_{i,n} t_i) (h_{neut} - h_i)^2 \quad (2.10)$$

where:

$$I_{i,g} = \frac{b_{i,n} t_i^3}{12} \quad (2.11)$$

the moment of inertia of the whole cross section,  $I_{cs}$ , is the sum of the moments of inertia of each layer eq. 2.12.

$$I_{cs} = \sum_i I_i \quad (2.12)$$

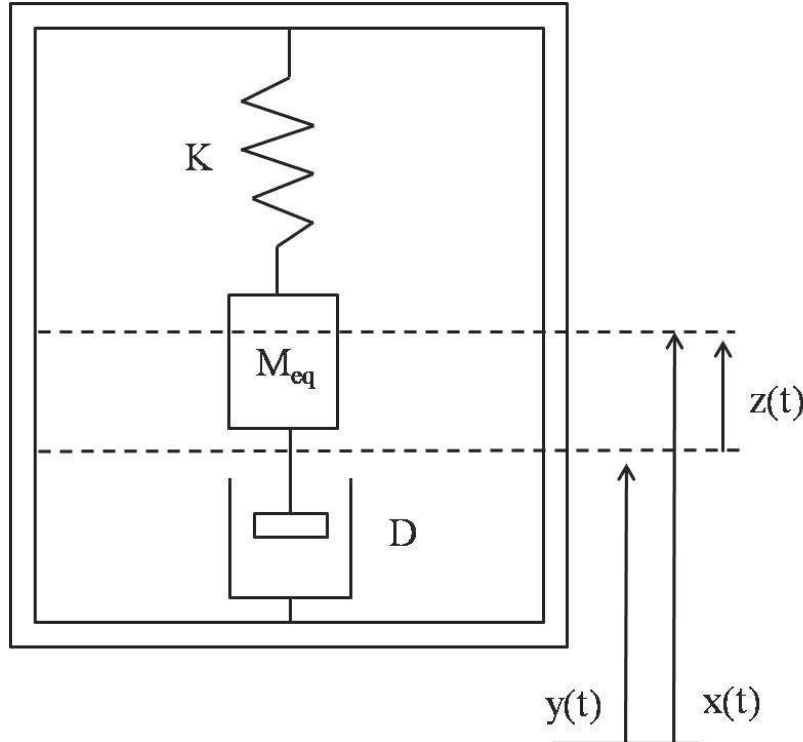


Figure 2.3: Lumped element model of a cantilever with a built in end and a seismic mass on the free end. The cantilever is modelled as a spring mass damper system, where  $K$  is the spring constant,  $M_{eq}$  is the equivalent mass and  $D$  is the damping coefficient. The frame takes into account the presence of a package and the fact that the device is fabricated on a substrate,  $y(t)$  is the motion of the frame respect to an inertial reference,  $x(t)$  is the motion o the mass respect to an inertial reference and  $z(t)$  is the relative motion of the mass respect to the housing frame.

Fig. 2.3 reports the lumped element model of the micro-cantilever piezoelectric generator with its housing frame, this model is constituted by a spring mass damper system [2, 3, 5, 29, 34, 35]. What we want to do is to write the mathematical expression of the spring constant, the damping coefficient

and the mass of the lumped model. The expression of the elastic constant which has to be used is that one reported in eq. 2.7. In the case of a multi-layer structure the maximum Young Modulus  $\tilde{E}_{max}$  and the total moment of inertia of the cross section  $I_{cs}$  eq. 2.12, have to be inserted in eq. 2.7 [28, 30].

The damping coefficient is modeled as the displacement of a plane with surface  $S$  and thickness  $T$ ,  $S$  is the total surface of the cantilever and  $T$  its total thickness, in the case of the multilayer cantilever of fig. 2.2  $T$  is:

$$T = \sum_i t_i \quad (2.13)$$

the damping coefficient  $D$  is [28]:

$$D = \mu_{air} \frac{S}{T} \quad (2.14)$$

with:

$$\mu_{air} = 1.85 \cdot 10^{-5} \left[ \frac{Kg}{ms} \right] \quad (2.15)$$

being the air dissipation factor.

The mass  $M_{eq}$  which has to be used, is the value of the mass that placed in the point where the force is applied, point 1 in fig. 2.1, produces a bending moment equal to that one of the applied force [30]. For the applied force gravity can be considered.

The fabricated cantilevers have lengths bigger than  $30 \mu m$ , to calculate the equivalent mass of the designed cantilevers, each structure has been divided in blocks having a length of  $30 \mu m$  and then the following formula has

been applied [30]:

$$M_{eq} = \sum_i^{n-1} \left( \frac{M_i d_i}{d_n} \right) + M_n \quad (2.16)$$

$M_i$  represents the mass on the block  $i$  and  $d_i$  is the distance between the anchor and the centroid of the block  $i$ . To experimentally calculate the equivalent mass of a suspended cantilever the resonance frequency of the structure can be measured and then eqs. 2.21, 2.22 and 2.24 can be used [28]. This represents a method to verify the accuracy of eq. 2.16.

All the parameters of the equivalent lumped model of fig. 2.3 have been derived whether in the case of an homogeneous beam or in the case of a multi-layer cantilever. The equation governing the movement of the mass in the generator is:

$$M_{eq} \frac{d^2 z}{dt^2} = -K(z - z_0) - D \frac{dz}{dt} + F_{ext} \quad (2.17)$$

$z(t)$  is the motion of the mass respect to the housing frame ( $z = x - y$ ) [2, 3, 5, 29, 34, 35],  $K(z - z_0)$  represents the reaction of the spring, the term  $-Kz_0$  takes into account the initial deformation after the release of the structure due to the residual stress,  $-D(dz/dt)$  represent the dissipation (mainly due to the air resistance) and  $F_{ext}$  is the applied external force, it can be expressed in the following way:

$$F_{ext} = -M_{eq} \frac{d^2 y}{dt^2} \quad (2.18)$$

$y(t)$  is the vibration of the housing frame.

If the reference system is chosen in a way that:

$$z_0 = 0 \quad (2.19)$$

in Laplace domain eq. 2.17 can be written as [28, 30]:

$$H(s) = \frac{z(s)}{F_{ext}(s)} = \frac{1}{K} \frac{1}{s^2 \frac{M_{eq}}{K} + s \frac{D}{K} + 1} \quad (2.20)$$

$H(s)$  is the transfer function of the system, in this case the position of the tip  $z(s)$  represents the system output and the applied force  $F_{ext}(s)$  is the system input. Equations 2.17 and 2.20 allow parameters of the system like natural frequency  $\omega_n$ , damping factor  $\xi$ , resonant frequency  $\omega_r$  and quality factor  $Q$  to be calculated. These parameters are reported in the following equations [5, 28, 29, 30].

$$\omega_n = \sqrt{\frac{K}{M_{eq}}} \quad (2.21)$$

$$\xi = \frac{D}{2\sqrt{KM_{eq}}} \quad (2.22)$$

$$Q = \frac{1}{2\sqrt{1 - 2\xi^2}}. \quad (2.23)$$

$$\omega_r = \omega_n \sqrt{1 - 2\xi^2} \quad (2.24)$$

Eq. 2.24 gives the expression of the resonant frequency in the case of an underdamped system.

Now we want to understand which is the power dissipated per cycle in the damper, when a vibrating force is applied to the system. When a sinusoidal

force is applied to the frame, the motion of the frame  $y(t)$  is sinusoidal:

$$y(t) = Y_0 \sin(\omega t) \quad (2.25)$$

the force applied to the spring mass damper system is calculated according eq. 2.18. With this input force, the steady state solution of eq. 2.17 (when  $z_0 = 0$ ) is [34]:

$$z(t) = \frac{Y_0 \left( \frac{\omega}{\omega_n} \right)^2}{\sqrt{\left[ 1 - \left( \frac{\omega}{\omega_2} \right)^2 \right]^2 + \left( 2\xi \frac{\omega}{\omega_n} \right)^2}} \sin(\omega t - \phi) \quad (2.26)$$

where:

$$\phi = \arctan \left( \frac{\omega D}{K - \omega^2 M_{eq}} \right) = \arctan \left( \frac{2\xi \frac{\omega}{\omega_n}}{1 - \left( \frac{\omega}{\omega_n} \right)^2} \right). \quad (2.27)$$

Every cycle, as an effect of the damping force, a certain amount of energy  $W_d$  is dissipated into the system. The energy lost per cycle can be expressed as [34]:

$$W_d = \oint D \frac{dz(t)}{dt} dz = \oint D \left( \frac{dz}{dt} \right)^2 dt \quad (2.28)$$

substituting the value of  $z(t)$  found in eq. 2.26, the energy dissipated in one cycle can be written as [34]:

$$W_d = 2\xi M_{eq} \frac{\pi}{\omega} \frac{Y_0^2 \left( \frac{\omega}{\omega_n} \right)^3 \omega^3}{\left[ 1 - \left( \frac{\omega}{\omega_n} \right)^2 \right]^2 + \left[ 2\xi \frac{\omega}{\omega_n} \right]^2} \quad (2.29)$$

this imply that the power dissipated in one cycle is given by the following expression [5, 29, 35].

$$P_d = \xi M_{eq} Y_0 \frac{\left(\frac{\omega}{\omega_n}\right)^3 \omega^3}{\left[1 - \left(\frac{\omega}{\omega_n}\right)^2\right]^2 + \left[2\xi\frac{\omega}{\omega_n}\right]^2} \quad (2.30)$$

For a cantilever containing a piezoelectric layer the total damping can be divided into a mechanical damping  $D$  and into an electrical damping  $D_e$ . This means that two dissipation factors can be considered,  $\xi$  which takes into account the air resistance, and  $\xi_e$  which is the damping factor due to the piezoelectric transduction mechanism [35]. If  $\xi$  is replaced by  $\xi_e$  in eq. 2.30, the generated electrical power  $P_e$  is obtained [5, 35], looking at eq. 2.30 the maximum electrical power is generated at the natural frequency of the system, furthermore the generated power increases when the swinging amplitude  $Y_0$  and the seismic mass increase. That is why a seismic mass is usually integrated on the tip of a cantilever used as energy harvester.

Cantilevers containing a PZT piezoelectric layer and a seismic mass with lengths ranging from hundreds of microns to few millimeters and resonance frequencies from few hertz to kilo-hertz have been produced in recent years [4, 1, 5], the generated output power at the resonance frequency varies between few  $\mu W$  to few  $mW$  [5].

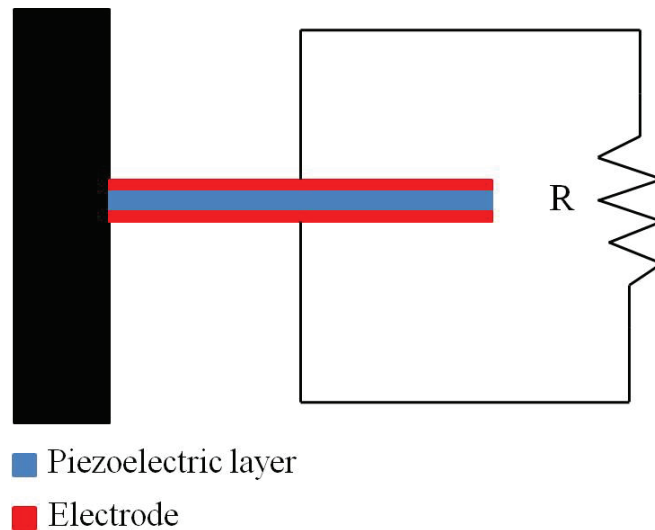


Figure 2.4: Cantilever containing a piezoelectric layer used as generator and connected to an  $RC$  load.

## 2.2 Our model for a piezoelectric generator connected to an $RC$ load

The mechanical model found in the previous section, will now be extended to the case of a cantilever containing a piezoelectric layer and connected to an  $RC$  load fig. 2.4, where the capacitive contribution is given by the intrinsic capacitance  $C_p$  across the piezoelectric film [3]. When a vibrational force is applied to the cantilever, it will start swinging and a stress is applied to the piezoelectric layer. The applied stress generates an electric field across the piezoelectric film which results in a current flowing through the load connected to the piezoelectric generator. Such current produces a voltage drop across the load, due to the converse piezoelectric effect, this voltage drop produces a deformation into the piezoelectric layer which acts like an

extra force applied to the cantilever. Considering eq. 2.17, and choosing the reference system in such a way that  $z_0 = 0$  it is possible to write:

$$M_{eq} \frac{d^2 z}{dt^2} = -Kz - D \frac{dz}{dt} + F_{ext} + k_{me} V \quad (2.31)$$

where  $k_{me}$  is the coupling coefficient [3], and  $V$  is the voltage drop across the load. In Laplace domain, with zero initial conditions, eq. 2.31 becomes:

$$M_{eq} s^2 z = -Kz - Dsz + F_{ext} + k_{me} V. \quad (2.32)$$

The next step is to find the relation between the voltage drop  $V$  and the input vibrational force, in order to do that the piezoelectric equations can be used. Let us consider the g-form of the piezoelectric equations, eqs. 1.5, and in particular the equation where the electric field is the dependant variable. In the case of the 31 and of the 33 energy harvesting mode, section 1.4, such equation can be written in a scalar form:

$$E_3 = -g_{31}\sigma_1 + \kappa_{33}^\sigma D_3 \quad (2.33)$$

for the 31 mode and:

$$E_3 = -g_{33}\sigma_3 + \kappa_{33}^\sigma D_3 \quad (2.34)$$

for the 33 mode. To simplify the notation the following form of such equations will be considered:

$$E = -g\sigma + \kappa D \quad (2.35)$$

then if we are considering a 31 or a 33 device the right subscripts will be

added.

The relation between the current density  $\vec{J}(t)$  and the electric displacement  $\vec{D}(t)$  is:

$$\vec{J}(t) = \frac{\partial \vec{D}(t)}{\partial t} \quad (2.36)$$

in Laplace domain eq. 2.36 becomes:

$$\vec{D}(s) = \frac{I(s)}{sA} \quad (2.37)$$

where  $A$  is the electrode area of the piezoelectric generator. The voltage drop across the load is equal to the voltage generated with the cantilever and for the electric field across the piezoelectric layer it is possible to write:

$$\vec{E}(s) = \frac{V(s)}{\delta} \quad (2.38)$$

$\delta$  represents the spacing between the electrodes. Substituting the expression for the electric displacement and the electric field in eq. 2.35 the voltage drop can be written in the following form:

$$\begin{aligned} V(s) &= \delta \left[ -g \frac{F_{ext}}{A} + \kappa \frac{V(s)}{sAz^*} \right] \Rightarrow \\ &\Rightarrow V(s) = -g\delta F_{ext} \frac{s z^*}{sAz^* - \delta\kappa} \end{aligned} \quad (2.39)$$

where:

$$z^* = \frac{R}{sC_p R + 1} \quad (2.40)$$

is the total impedance and takes into account the capacitance contribution

$C_p$  of the piezoelectric generator.

Substituting the expression for  $z^*$  in eq. 2.39, and eq. 2.39 in eq. 2.32, the transfer function of the system can be written as follow:

$$\begin{aligned} H(s) &= \frac{z(s)}{F_{ext}(s)} = \frac{s(\delta\kappa C_p R + k_{me}\delta g R - AR) + \delta\kappa}{(M_{eq}s^2 + Ds + K)[s(\delta\kappa C_p R - AR) + \delta\kappa]} = \\ &= \frac{s \frac{k_{me}gR}{\kappa} + 1}{(M_{eq}s^2 + Ds + K)}. \end{aligned} \quad (2.41)$$

Now we want to find out an expression for the coupling coefficient  $k_{me}$ . When a deflection  $\Delta z$  is applied to the cantilever, a charge  $Q$  is generated on the electrodes, the coupling coefficient can be expressed as [3]:

$$k_{me} = \frac{Q}{\Delta z}. \quad (2.42)$$

Let us consider the d-form of the piezoelectric equations, eqs 1.6, and in particular the equation linking the strain  $x$  and the electric field  $E$  when the applied stress is zero. Again in the case of the 31 and 33 devices this equation can be written into two simplified forms:

$$x_1 = d_{31}E_3 \quad (2.43)$$

and:

$$x_3 = d_{33}E_3 \quad (2.44)$$

to simplify the notation the following form of such equation will be considered:

red:

$$x = dE \quad (2.45)$$

then depending on the device mode the right subscripts will be added. Considering eq. A.3 and expressing the electric field across the piezoelectric layer as the electric field between the two electrodes of a parallel face capacitor,  $E = Q/\delta C_p$ , eq. 2.45 becomes:

$$\frac{Q}{\Delta l} = k_{me} = \frac{C_p \delta}{dl}. \quad (2.46)$$

Now eq. 2.45 says that a strain is produced when a voltage is applied across the piezoelectric layer. The voltage is applied between the two electrodes of the cantilever so the spacing between the electrodes changes by an amount equal to  $\Delta l$ . This means that in eq. 2.46  $\delta = l$  and the coupling coefficient is then:

$$k_{me} = \frac{C_p}{d} \quad (2.47)$$

substituting the expression for  $k_{me}$  in eq. 2.41, and taking into account the relationship between the piezoelectric constants [36]:

$$g = \frac{d}{\kappa} \quad (2.48)$$

(in the general case eq. 2.48 is a relationship between tensors) the transfer function of the cantilever connected to a resistor assumes the following form:

$$H(s) = \frac{z(s)}{F_{ext}(s)} = \frac{sC_p R + 1}{(M_{eq}s^2 + Ds + K)} \quad (2.49)$$

eq. 2.49 is valid when the piezoelectric layer sandwiched between two electrode behaves as an ideal capacitor, this means that no losses are present in the piezoelectric film.

Let us assume the case of an underdamped system (2 complex and conjugate poles), from the last equation it is clear that the resonance frequency of the system is still given by eq. 2.24, what might change is the amplitude of the resonance. In fact the presence of a zero in the transfer function modifies the transient response of the system. If the zero occurs at a frequency higher than the frequency of the two complex poles, the frequency response of the system is qualitatively the same as that for a system with only two complex poles. If the zero is at a frequency equal or lower than the the frequency of the two complex poles, the amplitude of the resonance is bigger than that one of a system with only two complex poles [37].

## 2.3 Cantilever design principles

In this section the attention is focused on the cantilever design principles and on the properties of cantilevers with different shapes.

Equation 2.30 reveals that the maximum power which can be dissipated in the damper, and thus converted into electrical energy, is given at the natural frequency. Limitations to the maximum working frequency come from the vibration sources present in the environment. Suitable vibrations can be found in applications like household goods (fridges, washing machines, microwave ovens etc.), industrial plant equipment, moving structures such as automobiles, aeroplanes, buildings and bridges [5]. All these applications

suggest working frequencies ranging from few hertz to few kilo-hertz, these frequencies values impose some conditions on the size of the devices.

For the design of such structures, it is important to understand how the parameters of the lumped model vary with the cantilever dimensions. If eqs. 2.7 and 2.21 are considered and taking into account the fact that the equivalent mass is proportional to the length of the beam, for the natural frequency of the system it is possible to write:

$$\omega_n \propto \frac{1}{L^2} \quad (2.50)$$

so the natural frequency of the system decreases with the square of the length of the cantilever. This suggests that working with a long beam is beneficial for low frequency applications, however considering also eqs. 2.22 and taking into account that the damping coefficient  $D$ , and the equivalent mass  $M_{eq}$ , are both proportional to the length of the device, for the damping factor the following dependance is found:

$$\xi \propto L^2 \quad (2.51)$$

this means that an increase in the length of the beam will increase the damping factor of the system.

To have a resonance peak in the frequency response of an underdamped system, the following condition has to be satisfied [37, 38].

$$\xi < 0.7 \quad (2.52)$$

When damping factor is larger than 0.7, for example in the case of long beams, it can be reduced with the addition of an appropriate seismic mass. A low damping factor is desirable in energy harvesting applications because the lower the damping factor, the higher the swinging amplitude and the output power at the resonance frequency.

Now the effect of the cantilever thickness  $T$  on the natural frequency and on the damping factor of the system will be analyzed. Taking into account eqs. 2.7, 2.11 and 2.12 the dependance of the elastic constant  $K$  on the cantilever thickness is:

$$K \propto T^3 \quad (2.53)$$

considering eq. 2.21 and the fact that the mass of the cantilever is proportional to its thickness relation 2.54 is found.

$$\omega_n \propto T \quad (2.54)$$

The natural frequency of the system increases when the thickness of the beam increases, considering also eq. 2.14, we have:

$$\xi \propto \frac{1}{T^3} \quad (2.55)$$

the damping factor scales down with the cube of the cantilever thickness and this is desirable to increase the output power of the device as previously explained.

For the dependance of the natural frequency and of the damping factor on the cantilever width, eqs. 2.7, 2.11 and 2.12 suggest that the elastic constant

of the beam is directly proportional to its width, however also the mass of the cantilever is directly proportional to the cantilever width, with the help of eq. 2.21 it is clear that the natural frequency of the beam does not depend on its width. Using eq. 2.22 it is found that also the damping factor does not depend on the cantilever width.

Swinging cantilevers containing a piezoelectric layer produce an alternated output voltage, usually this output voltage needs to be rectified in order to power low consumption electronic components. This implies that the peak of the output voltage has to overcome the threshold voltage of the rectifying diodes [4]. Eqs. 1.11 and 1.12 suggest that the generated output voltage is proportional to the distance between the electrodes, so to rise the generated output voltage the electrode distance can be increased. In the case of a 31 device an increase in the electrode distance produces an increase in the thickness of the device bringing to an higher natural frequency and to a lower damping factor. In the case of a 33 device an increase in the electrode distance produces a lower resonance frequency and an higher damping factor. In the expressions of the generated output voltages, eqs. 1.11 and 1.12, the longitudinal stress  $\sigma_{xx}$  appears; for small deflections of the cantilever the longitudinal stress can be calculated by using eqs. A.27 and A.28.

All these dependances constitute the design criteria for a piezoelectric cantilever used as an energy harvester. Depending on the specifications of interest like resonant frequency, damping factor, minimum output power etc., a certain design flow will be adopted. Such a design flow depends also on the available technology, for example a minimum thickness might be requested for each film present in the multilayer beam, such minimum thickness guarantees

<i>Material</i>	<i>Film Thickness [nm]</i>	<i>Density [g/cm<sup>3</sup>]</i>
<i>BaTiO<sub>3</sub></i>	150	6.02
<i>SrTiO<sub>3</sub></i>	220	5.12
<i>MgO</i>	60	3.58
<i>Au</i>	70	19.3

Table 2.1: Film thicknesses used for the design of the 33 devices and density of the used materials [21, 39, 40, 41].

the conservation of the properties of that layer. Other limitations might come from photolithography resolution, film deposition technique etc..

Structures with different shapes like simple beams, u-shape cantilevers, cantilevers made of two beams with different width connected in series and tuning fork cantilevers have been designed during this Phd. Such designs do not have to be intended as an attempt aimed to produce the devices in their final form, but they are a way to investigate the behaviour and the performances of the different layers when they are put together and patterned with a certain geometry.

The design of the cantilevers has been done for the 33 mode structures having the layer sequence: *Au/BaTiO<sub>3</sub>/MgO/SrTiO<sub>3</sub>*, sec. 1.4; the reason for that is due to the theoretical higher output voltages which can be delivered by this kind of devices as opposite to the 31 structures. The geometries designed for the 33 devices are going to be used also for the fabrication of the cantilevers using the 31 mode having the layer sequence: *SrRuO<sub>3</sub>/BaTiO<sub>3</sub>/SrRuO<sub>3</sub>*. It has to be pointed out that the gold top electrode of a 33 device can be replaced with a *SrRuO<sub>3</sub>* electrode, however the

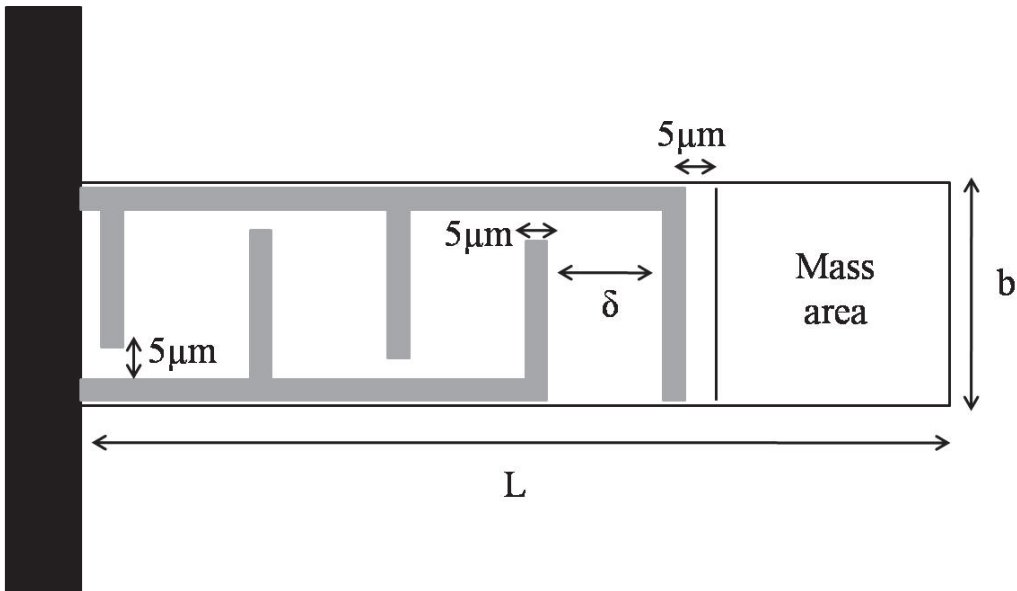


Figure 2.5: Top view of a 33 mode simple beam cantilever, the area near the free end, labeled as *Mass area*, represents the part of the beam where the seismic mass will be housed,  $\delta$  is the spacing between the fingers of the electrode,  $L$  is the cantilever length and  $b$  is the cantilever width. The lines of the interdigitated electrode (in gray) are  $5\mu m$  wide, the black area represents the anchor of the cantilever.

design has been performed considering a gold electrode. The thicknesses of the layers used for the design of the suspended beams and the densities of the used materials [21, 39, 40, 41] necessary to calculate the equivalent mass  $M_{eq}$ , are reported in tab. 2.1.

### 2.3.1 Design of simple beam cantilevers

The properties and the modeling of single beam cantilevers have been widely discussed throughout the chapter. With reference to fig. 2.1 such type of cantilevers can vibrate in response to the forces  $F_{1-z}$  and  $F_{1-y}$ . In the first

<i>Device</i>	<i>L</i> [ $\mu m$ ]	<i>b</i> [ $\mu m$ ]	$\delta$ [ $\mu m$ ]	<i>Mass area</i> [ $\mu m \times \mu m$ ]	$K_{1-z}$ [ $N/m$ ]	<i>Seismic mass</i> [ $Kg$ ]	<i>Gold thickness</i> [ $\mu m$ ]	$M_{eq}$ [ $Kg$ ]
dev.1	130	30	10	$30 \times 30$	0.06	/	0.07	$4.84 \cdot 10^{-12}$
dev.2	130	30	10	$30 \times 30$	0.06	$17.37 \cdot 10^{-12}$	1	$22.21 \cdot 10^{-12}$
dev.3	135	30	20	$30 \times 30$	0.039	/	0.07	$6.82 \cdot 10^{-12}$
dev.4	135	30	20	$30 \times 30$	0.039	$7.47 \cdot 10^{-12}$	0.5	$14.32 \cdot 10^{-12}$
dev.5	135	30	20	$30 \times 30$	0.039	$16.15 \cdot 10^{-12}$	1	$23 \cdot 10^{-12}$
dev.6	260	30	20	$30 \times 50$	0.0056	/	0.07	$12.78 \cdot 10^{-12}$
dev.7	260	30	20	$30 \times 50$	0.0056	$28.95 \cdot 10^{-12}$	1	$41.73 \cdot 10^{-12}$
dev.8	270	30	30	$30 \times 50$	0.005	/	0.07	$13.03 \cdot 10^{-12}$
dev.9	270	30	30	$30 \times 50$	0.005	$28.93 \cdot 10^{-12}$	1	$41.98 \cdot 10^{-12}$
dev.10	440	30	30	$30 \times 80$	0.0013	/	0.07	$21.32 \cdot 10^{-12}$
dev.11	440	30	30	$30 \times 80$	0.0013	$92.64 \cdot 10^{-12}$	2	$113.96 \cdot 10^{-12}$
dev.12	440	50	30	$50 \times 80$	0.0022	/	0.07	$35.17 \cdot 10^{-12}$
dev.13	440	50	30	$50 \times 80$	0.0022	$154.3 \cdot 10^{-12}$	2	$189.57 \cdot 10^{-12}$
dev.14	500	30	30	$30 \times 105$	$7.8 \cdot 10^{-4}$	/	0.07	$24.71 \cdot 10^{-12}$
dev.15	500	30	30	$30 \times 105$	$7.8 \cdot 10^{-4}$	$182.38 \cdot 10^{-12}$	3	$207.1 \cdot 10^{-12}$
dev.16	500	30	50	$30 \times 105$	$7.8 \cdot 10^{-4}$	/	0.07	$24.5 \cdot 10^{-12}$
dev.17	500	30	50	$30 \times 105$	$7.8 \cdot 10^{-4}$	$243.18 \cdot 10^{-12}$	4	$267.68 \cdot 10^{-12}$
dev.18	500	30	50	$30 \times 275$	$7.9 \cdot 10^{-4}$	/	0.07	$28.05 \cdot 10^{-12}$
dev.19	500	30	50	$30 \times 275$	$7.9 \cdot 10^{-4}$	$318.45 \cdot 10^{-12}$	2	$346.5 \cdot 10^{-12}$

Table 2.2: Length  $L$ , width  $b$ , electrode spacing  $\delta$ , mass area, elastic constant  $K_{1-z}$ , seismic mass, gold thickness and equivalent mass  $M_{eq}$  of the designed 33 mode simple beam cantilevers. The symbol "/" in the seismic mass column indicates that there is no seismic mass integrated on the tip of the micro-cantilever.

case the cantilever will vibrate in a plane parallel to the  $yz$  plane while in the second case the vibration is parallel to the  $xy$  plane. In the case of vibrations parallel to the  $xy$  plane the expressions of the cross sectional moment of inertia, of the elastic constant and of the damping factor are still valid provided that the cantilever thickness becomes the cantilever width and the cantilever width becomes the cantilever thickness.

Fig. 2.5 shows the top view of a 33 mode simple beam cantilever, the

<i>Device</i>	$f_n$ [KHz]	$\xi$	$f_r$ [KHz]	$V_{out}$ [V]
dev.1	17.72	0.13	17.43	11.43
dev.2	8.28	0.063	8.24	11.43
dev.3	12	0.14	11.78	21
dev.4	8.31	0.1	8.23	21
dev.5	6.56	0.079	6.52	21
dev.6	3.33	0.54	2.15	5.75
dev.7	1.84	0.3	1.67	5.75
dev.8	3.12	0.59	1.72	8
dev.9	1.74	0.33	1.54	8
dev.10	1.24	1.47	/	3
dev.11	0.537	0.63	0.244	3
dev.12	1.26	1.4	/	3
dev.13	0.541	0.6	0.287	3
dev.14	0.895	2	/	2.3
dev.15	0.309	0.69	0.068	2.3
dev.16	0.898	2	/	3.9
dev.17	0.272	0.61	0.138	3.9
dev.18	0.839	1.68	/	3.9
dev.19	0.240	0.53	0.159	3.9

Table 2.3: Natural frequency  $f_n$ , damping factor  $\xi$ , resonance frequency  $f_r$  and generated output voltage  $V_{out}$  of the designed 33 mode simple beam cantilevers. The output voltage has been calculated assuming a deflection of the free end equal to  $5\mu m$ . The symbol "/" in the resonance frequency column indicates that there is no resonance for those devices.

area near the free end, labeled as *Mass area*, represents the part of the beam where the seismic mass will be housed,  $\delta$  is the spacing between the fingers of the electrode,  $L$  is the cantilever length and  $b$  is the cantilever width. The lines of the interdigitated electrode are  $5\mu m$  wide.

Tabs. 2.2 and 2.3 show the performances of cantilevers with a range of

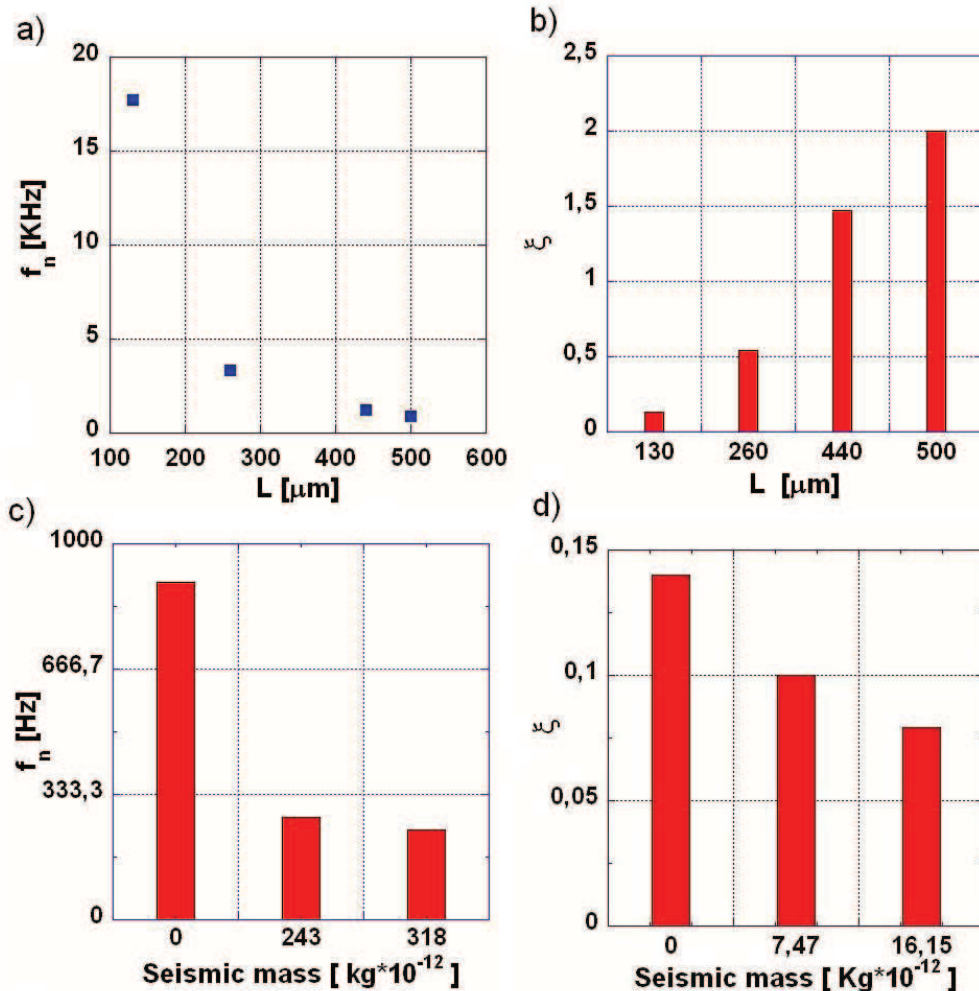


Figure 2.6: a) Natural frequency as function of the cantilever length for the designed devices. The values reported in the graph are relative to the devices 1, 6, 10 and 14 of tabs. 2.2 and 2.3. b) Damping factor as function of the cantilever length, the data in the graph are relative to the devices 1, 6, 10 and 14 of tabs. 2.2 and 2.3. c) Natural frequency as function of the seismic mass, the data in the graph are relative to the devices 16, 17 and 19 of tabs. 2.2 and 2.3. d) Damping factor as function of the seismic mass, the data in the graph are relative to the devices 3, 4 and 5 of tabs. 2.2 and 2.3.

dimensions. As previously stated, such devices should resonate from few  $Hz$  up to few  $KHz$ . This can be achieved with cantilever lengths of order of a few  $mm$  but as the length increases so does the damping. In addition, after the undercut of the sacrificial layer (see chap. 4), very long cantilevers will suffer the problem of the free end curling, consequence of the residual stress (see chap. 6). This despite the fact that the employed materials present a Young's Modulus higher than the materials which are usually employed for the realisation of this kind of devices [4, 1, 23].

Figs. 2.6a and b report the natural frequency and the damping factor as function of the cantilever length, the values in the graph are relative to the cantilevers without seismic mass.

Another way to reduce the resonance frequency is to use relatively heavy seismic masses (fig. 2.6c reports the natural frequency as function of the seismic mass), this will also results in a reduction of the damping factor fig 2.6d. In order to do that, gold seismic masses have been assumed. The advantage of using a gold seismic mass is the high gold density, tab. 2.1, the disadvantage is due to its cost. Another solution would be the use of seismic masses made with perovskites structure materials, but here the density is three times lower, so masses having a bigger volume are required. As the seismic masses are grown by Pulsed Laser Deposition an extremely long growth time is required in order to have masses with a weight comparable to the gold ones. For the construction of a prototype, a seismic gold mass should be used, if the fabrication of a bigger number of devices is requested, seismic masses of other materials should be employed.

Devices with lengths ranging from  $135\ \mu m$  to  $500\ \mu m$  have been designed,

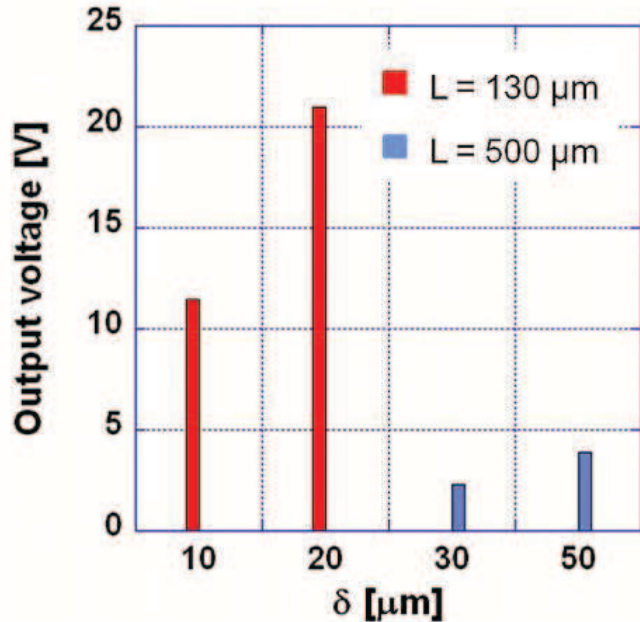


Figure 2.7: Output voltage as function of the spacing between the fingers of the interdigitated electrode  $\delta$  for two couples of devices with different length. The data in the graph are relative to the devices 1, 3, 14, and 16

their theoretical resonance frequencies are in the range  $159\text{ Hz} - 17.43\text{ KHz}$ .

Tab. 2.3 also reports the theoretical output voltage generated with a deflection of the free end  $\Delta_z$  equal to  $5\mu m$ . Such voltage levels are not surprising as for cantilevers with similar size employing  $PZT$ ,  $100\text{ V}$  are required in order to have a free end deflection of  $30\mu m$  [23]. It has to be emphasized that the generated output voltages have been calculated assuming the following value for the piezoelectric coefficient [6]:

$$g_{33} = 57.5 \cdot 10^{-3} \left[ \frac{Vm}{N} \right] \quad (2.56)$$

however due to the presence of defects and other not ideal structures present in the deposited  $BaTiO_3$  films such coefficient can exhibits a different value.

Considering eqs. 1.11, A.4 and A.27 the maximum output voltage for a 33 mode cantilever is

$$V_{33} = E_{BTO} \cdot \frac{\Delta_z}{\rho} \cdot g_{33} \cdot \delta \quad (2.57)$$

where  $E_{BTO}$  is the Young's modulus of the  $BaTiO_3$  and  $\rho$  is the radius of curvature of the deflected cantilever. The output voltage as function of the spacing between the fingers of the interdigitated electrode  $\delta$  is shown in fig. 2.7.

The output voltage of the designed micro-cantilevers has been analysed. However these structures should be used as energy scavenging devices, so it is important to understand the amount of power which they can supply. To take advantage of the separation of charges which takes place in the piezoelectric layer when an input stress is applied, capacitors are integrated on the top of the suspended beams. The energy  $W_d$  stored in a capacitive structure is [42]:

$$W_d = \frac{1}{2}CV^2 \quad (2.58)$$

where  $C$  is the capacitance and  $V$  is the output voltage. Equation 2.58 shows that a device design aimed to maximaze the output voltage of the structure, also maximize the energy stored in the capacitor. The output power  $P_d$  can be expressed as [34]:

$$P_d = W_d \cdot \nu \quad (2.59)$$

where  $\nu$  is the frequency of the mechanical solicitation applied to the can-

tilever. Equation 2.59 shows that the extracted power increases when the working frequency of the device increases. The devices of tables 2.2 and 2.3 have resonance frequencies with order of magnitude  $10^2 \text{ Hz} - 10^4 \text{ Hz}$  and their output voltages are in the range  $2.3 \text{ V} - 21 \text{ V}$ . In chap. 7 the impedance measurements of the capacitive structures integrated on the microcantilevers are reported; 31 and 33 mode capacitors having parallel plate or interdigitated area equal to  $95 \mu\text{m} \times 30 \mu\text{m}$ ,  $105 \mu\text{m} \times 30 \mu\text{m}$ ,  $205 \mu\text{m} \times 30 \mu\text{m}$  and  $215 \mu\text{m} \times 30 \mu\text{m}$  have been fabricated. For  $\text{BaTiO}_3$  thicknesses in the range  $200 \text{ nm} - 400 \text{ nm}$  capacitance value with orders of magnitude  $10^{-12} \text{ F} - 10^{-10} \text{ F}$  have been measured.

With these values, according eqs. 2.58 and 2.59, the maximum power (at resonance) is extracted for resonance frequencies of  $10^4 \text{ Hz}$ , output voltages with order of magnitude  $10^1 \text{ V}$  and capacitances of  $10^{-10} \text{ F}$ . The extracted power has order of magnitude:

$$P_d \approx 10^2 \mu\text{W}. \quad (2.60)$$

For resonance frequencies of  $10^2 \text{ Hz}$ , output voltages of  $2 \text{ V}$  and capacitances of  $10^{-12} \text{ F}$  the minimum power (at resonance) results:

$$P_d \approx 10^{-1} \text{nW}. \quad (2.61)$$

So from this devices powers in the range  $0.1 \text{ nW} - 100 \mu\text{W}$  can be extracted. In the case of PZT, extracted power in the range  $\mu\text{W} - \text{mW}$  has been reported [5] however in this case cantilevers with lengths and widths of few

millimeters have been fabricated. The power extracted from the  $BaTiO_3$  based micro-cantilevers is expected to be smaller than the power extracted from PZT micro-cantilevers having the same area, this is due to the superior piezoelectric coefficients of PZT. However with our design theoretical powers up to  $10^2 \mu W$  can be extracted, furthermore the available power can be increased by using capacitors with a bigger area.

In principle on top of the interdigitated electrode a further piezoelectric film and a further electrode can be grown, this in theory would allow to harvest twice the power generated with a device containing only a piezoelectric film. However it would be really challenging to grow a further good quality piezoelectric film on the top of the device, the reasons for that will be explained in sec. 7.2.

### 2.3.2 Design of u-shape cantilevers

U-shape cantilevers consist of two *arms* supporting the area where the seismic mass will be housed fig. 2.8. The purpose for such design is again the reduction of the natural and of the resonance frequencies. In the previous section the reduction of these frequencies has been reached by reducing the elastic constant of the cantilever, in this section the reduction of the resonance frequency is obtained by increasing the seismic mass. In fact compared to a simple beam, the u-shape cantilever contains a much bigger area where it is possible to integrate the seismic mass, this is the reason which brings to the choice of such design. Another advantage is due to the fact that on an u-shape cantilevers two capacitive structures are integrated, one for each

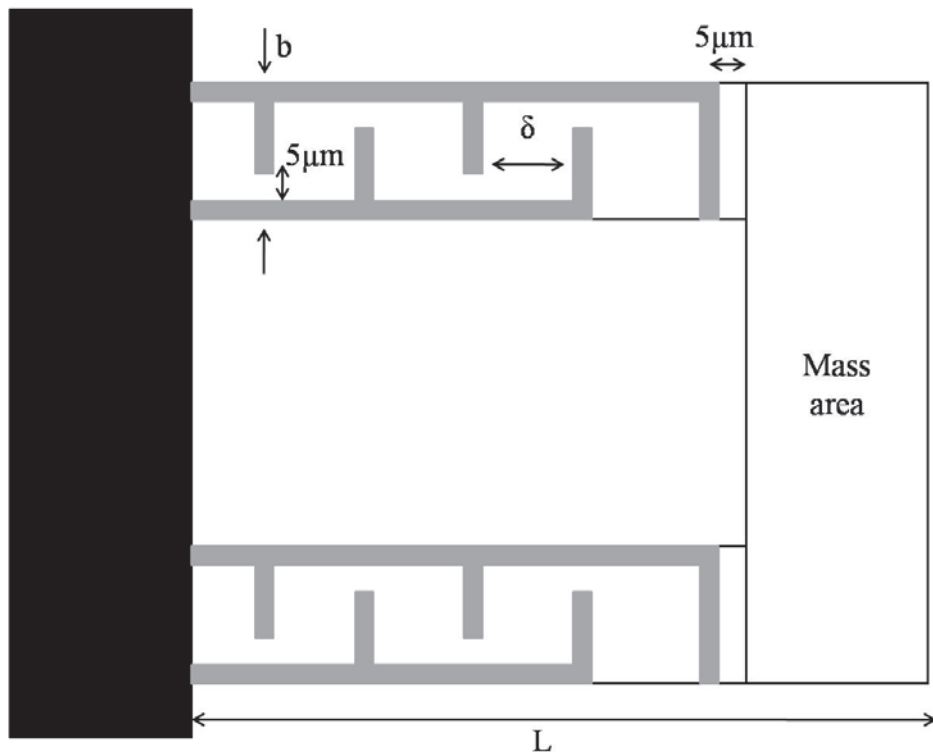


Figure 2.8: U-shape cantilever using the 33 mode, the area near the free end, labeled as *Mass area*, represents the part of the beam where the seismic mass will be housed,  $\delta$  is the spacing between the fingers of the electrode,  $L$  is the cantilever length and  $b$  is the width of the single arm of the cantilever. The lines of the interdigitated electrode (in gray) are  $5\mu\text{m}$  wide, the black area represents the anchor of the cantilever.

arm. According to eq. 2.58 the energy stored in these structures is twice the energy stored in a simple beam cantilever having the dimensions equal to those of a single arm of the u-shape cantilever. However the reduction of the resonance frequency in the u-shape cantilever leads to a reduction in the extracted power.

The U-shape cantilever is mechanically equivalent to a simple cantilever

<i>Device</i>	<i>L</i> [ $\mu m$ ]	<i>b</i> [ $\mu m$ ]	$\delta$ [ $\mu m$ ]	<i>Mass area</i> [ $\mu m \times \mu m$ ]	$K_{1-z}$ [N/m]	<i>Gold mass</i> [Kg]	<i>Seismic thickness</i> [ $\mu m$ ]	$M_{eq}$ [Kg]
dev.1	130	30	10	$30 \times 120$	0.09	/	0.07	$19.9 \cdot 10^{-12}$
dev.2	130	30	10	$30 \times 120$	0.09	$69.48 \cdot 10^{-12}$	1	$89.38 \cdot 10^{-12}$
dev.3	135	30	20	$25 \times 120$	0.08	/	0.07	$20.64 \cdot 10^{-12}$
dev.4	135	30	20	$25 \times 120$	0.08	$28.95 \cdot 10^{-12}$	0.5	$49.60 \cdot 10^{-12}$
dev.5	135	30	20	$25 \times 120$	0.08	$61.95 \cdot 10^{-12}$	1	$74.44 \cdot 10^{-12}$
dev.6	260	30	20	$50 \times 120$	0.011	/	0.07	$36.35 \cdot 10^{-12}$
dev.7	260	30	20	$50 \times 120$	0.011	$115.8 \cdot 10^{-12}$	1	$152.15 \cdot 10^{-12}$
dev.8	270	30	30	$50 \times 120$	0.0098	/	0.07	$32.47 \cdot 10^{-12}$
dev.9	270	30	30	$50 \times 120$	0.0098	$115.8 \cdot 10^{-12}$	1	$148.27 \cdot 10^{-12}$
dev.10	440	30	30	$80 \times 150$	0.0023	/	0.07	$77.28 \cdot 10^{-12}$
dev.11	440	30	30	$80 \times 150$	0.0023	$463.2 \cdot 10^{-12}$	2	$540.48 \cdot 10^{-12}$
dev.12	500	30	30	$105 \times 170$	0.0016	/	0.07	$90.94 \cdot 10^{-12}$
dev.13	500	30	30	$105 \times 170$	0.0016	$1033.52 \cdot 10^{12}$	3	$1124.45 \cdot 10^{-12}$
dev.14	500	30	50	$105 \times 200$	0.0016	/	0.07	$102 \cdot 10^{-12}$
dev.15	500	30	50	$105 \times 200$	0.0016	$1318 \cdot 10^{-12}$	3	$1318 \cdot 10^{-12}$
dev.16	500	30	50	$160 \times 200$ 2 ( $30 \times 115$ )	0.0016	/	0.07	$136.63 \cdot 10^{-12}$
dev.17	500	30	50	$160 \times 200$ 2 ( $30 \times 115$ )	0.0016	$1501 \cdot 10^{-12}$	2	$1638 \cdot 10^{-12}$

Table 2.4: Length  $L$ , width  $b$ , electrode spacing  $\delta$ , mass area, elastic constant  $K_{1-z}$ , seismic mass and equivalent mass  $M_{eq}$  of the designed 33 mode u-shape cantilevers. Devices 16 and 17 contains two values in the column labeled as *Mass area* because a certain area on each arm of the u-shape cantilever has been used as mass area. The symbol "/" in the seismic mass column indicates that there is no seismic mass integrated on the tip of the micro-cantilever.

with a beam width equal to twice the real one [28]. This implies that the same design principles used to design a simple beam cantilever can be employed in the design of the u-shape beams.

Tabs. 2.4 and 2.5 contain the dimensions and the parameters of the designed u-shape cantilevers.

<i>Device</i>	$f_n$ [KHz]	$\xi$	$f_r$ [KHz]	$V_{out}$ [V]
dev.1	10.71	0.13	10.53	11.43
dev.2	5.05	0.063	5.03	11.43
dev.3	9.91	0.14	9.71	21
dev.4	6.35	0.093	6.35	21
dev.5	5.19	0.076	5.15	21
dev.6	2.72	0.54	1.79	5.75
dev.7	1.35	0.27	1.25	5.75
dev.8	2.27	0.63	1.26	8
dev.9	1.29	0.29	1.18	8
dev.10	0.869	1.28	/	3
dev.11	0.329	0.48	0.242	3
dev.12	0.667	2.02	/	2.3
dev.13	0.189	0.57	0.111	2.3
dev.14	0.630	2.	/	3.9
dev.15	0.175	0.57	0.104	3.9
dev.16	0.545	2.1	/	3.9
dev.17	0.157	0.6	0.083	3.9

Table 2.5: Natural frequency  $f_n$ , damping factor  $\xi$ , resonance frequency  $f_r$  and generated output voltage  $V_{out}$  of the designed 33 u-shape cantilevers. The output voltage has been calculated assuming a deflection of the free end equal to  $5\mu m$ . The symbol "/" in the resonance frequency column indicates that there is no resonance for those devices.

Let us now compare a simple beam cantilever with an u-shape cantilever, in order to do that the single beam cantilever labeled as dev.2 is compared with the u-shape cantilever having the same label, tabs. 2.2, 2.3, 2.4 and 2.5. Both devices have a length equal to  $130\mu m$  and in both cases the two seismic masses correspond to a gold layer having a thickness of  $1\mu m$ . The single beam cantilever presents a resonance frequency  $f_r$  equal to  $8.24 KHz$

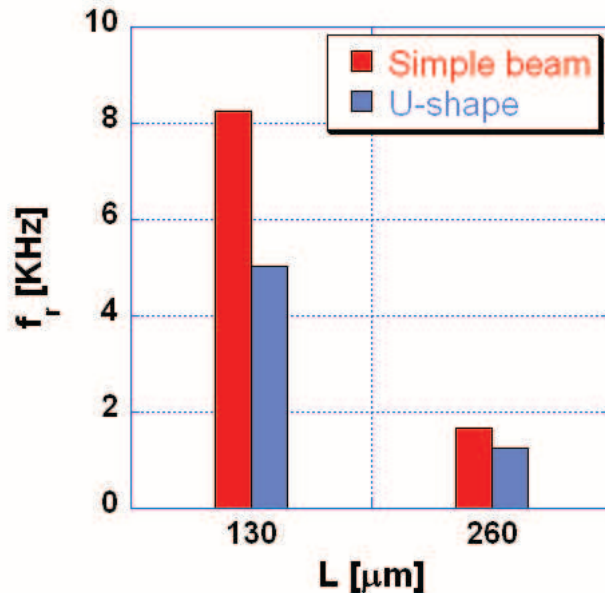


Figure 2.9: Resonant frequency as function of the cantilever length for two simple beam cantilevers and two u-shape cantilevers. For all the devices a gold seismic mass with a thickness of  $1\mu m$  has been assumed.

while the resonance frequency of the u-shape structure is  $5.03KHz$ , so the difference is more than  $3KHz$ , fig. 2.9. There is no difference instead in the value of the damping factor because it is true that the u-shape cantilever presents a bigger equivalent mass but it also presents a bigger surface which balances the effect of the big mass. The same happens for the other devices.

This demonstrates that compared to a simple beam, the u-shape structure presents the advantage of having a lower resonance frequency without increasing the damping factor.

As shown by tabs. 2.4 and 2.5 devices with a length ranging from  $130\mu m$

to  $500\mu m$  have been designed, their resonance frequencies varies between  $10.53 KHz$  and  $83 Hz$ . Also in this case the generated output voltage has been calculated considering a deflection of the free end equal to  $5\mu m$ . The power extracted from these devices is still in the range  $10^{-1} nW - 10^2 \mu W$

## 2.4 Summary

In this chapter the basic relationships which allow to model a multi-layer micro-cantilever as a spring mass damper system are reported, sec. 2.1. In sec. 2.2 this mathematical model is extended to the case of a micro-cantilever connected to a resistive load. It is shown that in this case the model is that one of a second order system with a zero.

In sec. 2.3 the design principles employed for the design of our cantilevers have been discussed. It has been shown that an increase of the cantilever length reduces the value of the resonance frequency but it also increases the damping factor of the structure. On the other side an increase of the cantilever thickness increases the resonance frequency of the cantilever but it also reduces its damping factor.

In subsec. 2.3.1 the dimensions and the key parameters of the designed simple beam cantilevers are reported, our structures have lengths ranging from  $100\mu m$  to  $500\mu m$  and widths of  $30\mu m$  and  $50\mu m$ . For these devices resonance frequencies in the range  $20 KHz - 100 Hz$ , output voltages in the range  $2 V - 20 V$  and output powers in the range  $0.1 nW - 100 \mu W$  have been calculated with output voltages in the range  $2 V - 20 V$ .

In subsec. 2.3.2 the dimensions and the key parameters of the cantilevers

having u-shape geometry are reported. This geometry brings to a reduction of the resonance frequency which this time is in the range  $10\text{ KHz} - 80\text{ Hz}$ . The power which can be extracted from these devices is still in the range  $10^{-1}\text{ nW} - 10^2\text{ }\mu\text{W}$ .

During this Phd tuning fork cantilevers and cantilevers composed of two beams with different sections connected in series have been also designed, these kinds of cantilevers have not been fabricated during this project, their design is discussed in appendix B.

# Chapter 3

## Apparatus and methods

In this chapter an overview of the experimental methods and equipment used for the fabrication and the characterization of the thin films is provided. In section 3.1 the Pulsed Laser Deposition system employed for the growth of the thin films together with its important parts are described. Section 3.2 is about the X-ray diffraction equipment and the experimental method used to investigate the crystal structure of the deposited films. Sections 3.3, 3.4 and 3.5 report an explanation of the patterning, milling, crytical point dry-ing and wirebonding techniques. They are necessary to define the geometry of the micro-cantilevers, remove the etchant from the sample without stiction, and connect the devices to run electrical measurements. In section 3.6 the impedance and hysteresis loop measurement techniques employed to characteize the  $BaTiO_3$  based capacitive structures are discussed. Finally section 3.7 report a discussion on the Atomic Force Microscope (AFM) and nano-indentation techniques.

### 3.1 Pulsed Laser Deposition setup

The thin films employed in our devices were grown by **Pulsed Laser Deposition** (PLD). This method employs a focused laser beam to eject atoms from a target, made of the deposition material, by irradiation. The ejected atoms leave the target and form a luminous cloud called **plume** in which a large number of molecular and atomic collisions take place. The atoms finally arrive on a substrate glued on a sample-holder placed facing the target and heated to a certain temperature. The arrival of atoms from the target material to the substrate produces the growth of a thin film on the substrate itself. The advantages of this deposition technique are the possibility to deposit high melting point materials, supposing that they absorb the laser light, while maintaining stoichiometry. The target composition is entirely transferred to the deposited film because of the non-thermal mechanism of removal from the target (ablation). The disadvantage of PLD consists in the high number of droplets of submicron size which are often seen on the surface of the grown films [44, 45].

To control the deposition temperature a solid state heater is used as substrate holder. The deposition is run inside a vacuum chamber, fig. 3.1 connected to a roughing and to a turbo pump which allows control of the deposition pressure.

A Lambda Physik LPX 210i KrF (krypton-fluorine) excimer laser with a wavelength of  $248\text{ nm}$  and a laser pulse duration of  $20\text{ ns}$  was used. The laser beam travels along a laser path formed by four mirrors before entering the deposition chamber through a vacuum sealed  $\text{CaF}_2$  window and strikes

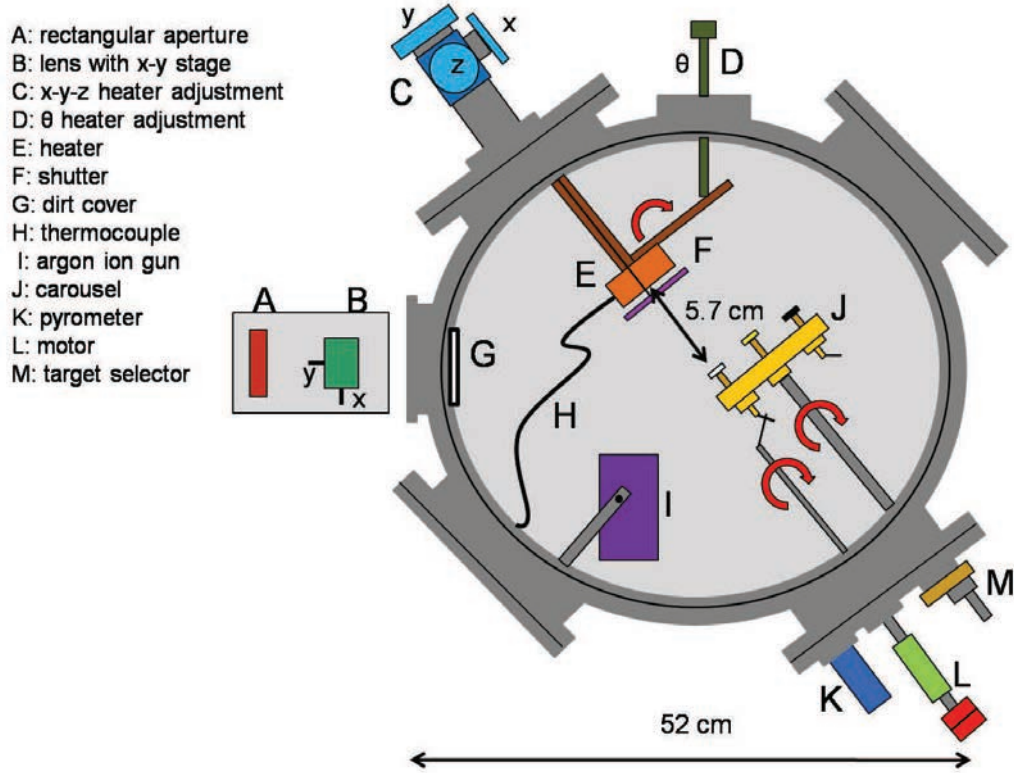


Figure 3.1: Top sketch view of the inside of the deposition chamber with its important parts.

the ablation target. During this path, the laser beam passes first through an attenuator, an aperture and a lens of  $30\text{ cm}$  focal length which is on an adjustable  $x - y$  stage fig. 3.2.

The output energy of an excimer laser is influenced by the voltage applied across its electrodes. It is possible to apply a voltage in the range  $16\text{ KV} - 24\text{ KV}$ . The higher the applied voltage, the more stable is the energy. With high voltages, the energy measured inside the deposition chamber might exceed the value of  $81\text{ mJ}$  which is the optimum energy value for our deposition, see sec. D.3.2. On the other hand if the energy is reduced by

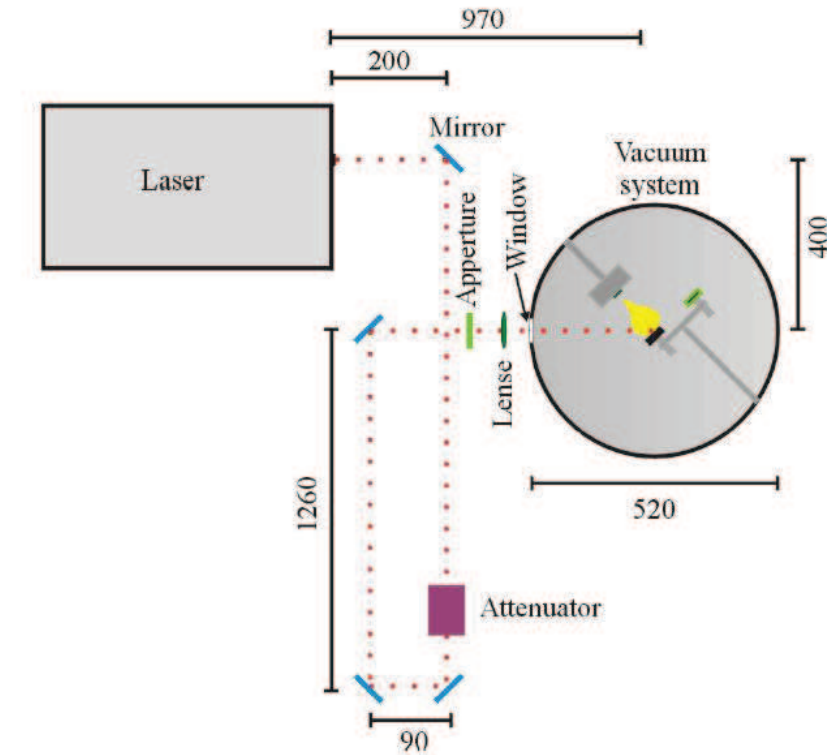


Figure 3.2: Sketch (top view) of pulsed laser deposition system including laser, beam path with optical components and vacuum chamber. The reported distances are in millimeters [11].

applying less voltage to the electrodes, energy fluctuations might be present and the laser energy will not be constant during the film growth. The solution to the problem is the introduction of an attenuator along the laser beam path which allows setting of the desired energy of the beam even if the voltage applied to the laser electrodes would otherwise produce an energy which is too high for the film deposition.

In PLD applications, it is desirable to have an homogeneous intensity profile across the laser spot on the target. This ensures a pure material

ablation and not a mixture of ablation and unwanted thermal evaporation. Due to this reason there is a rectangular aperture which selects the central part of the beam, where the beam intensity is roughly constant, just before the focusing lens. This results in a rectangular-shaped laser spot profile on the ablation target, where the laser fluence is almost the same in each point of the profile. The laser spot size can be varied by adjusting the distance between the target material and the focusing lens.

Fig. 3.1 shows a top view sketch of the deposition chamber with its important parts. Before the laser beam enters the chamber it passes through a rectangular aperture (A) and a focusing lens (B) mounted on an adjustable  $x - y$  stage. The chamber entrance window is protected from the ablated material with a  $0.5\text{ mm}$  thick quartz slide (G), this can be replaced when it is so dirty as to significantly reduce the beam energy. A heater (E) is mounted on a  $x - y - z$  adjustable vacuum sealed stage (C) with a shutter (F) placed in front of it. A vacuum sealed mechanism made of two shafts and one spring (D) was added to the heater in order to rotate it around an axis perpendicular to the plane of the picture. This allows to place the heater in front of a Kaufman argon ion gun (I). The chamber also contains a K-type thermocouple (H) attached to the heater and controlled by a Eurotherm 818 temperature controller and a three-target carousel (J). One of the three targets can be selected facing the heater in ablation position via vacuum-sealed rod (M). A motor (L) is used to rotate the target during the ablation. The target rotation spreads the laser beam damage so as to eliminate changes in composition between the film and the target [46]. Pre-ablation to clean the surface of the targets is performed with the shutter (F)

in front of the substrate. Additional control over temperature is provided by an infrared radiation pyrometer (K). The pyrometer has been introduced because the K-type thermocouple measures the temperature of the heater while the substrate is glued on the heater with silver paint. The silver paint is responsible for a good thermal contact but the amount of silver paint used will be different from gluing to gluing, therefore altering this thermal contact. Additionally, silver paint gets less viscous over time which also has an impact on the gluing process and hence on its thermal properties. Therefore an optical temperature measurement sensitive to the surface of the substrate is desirable. The pyrometer is equipped with a vacuum proof lens which is located in the deposition chamber. An in built laser pointer ensures that the pyrometer always detects radiation from the desired object. A shutter placed in front of the lens protects it from coating during the ablation.

Fig. 3.3 shows a side view of the outside of the vacuum system. An Edwards *E2M12* rotary vacuum pump serves as fore-pump for a Leybold Turbovac *361C* turbo-molecular pump via an Edwards speedy valve. The turbo pump itself is separated via a gate valve from the vacuum chamber. A bypass valve connects the Edwards fore-pump directly to the system. The venting of the chamber is performed with a Swagelok venting valve. A *MKS 1159B* mass flow-meter controls the argon flow to the argon ion gun. Additionally, a Swagelok valve separates the vacuum chamber from the argon gas cylinder. Argon ions are used for the soft and hard etches of the  $YBa_2Cu_3O_7$  ramp and for the growth of the gold top electrode in the project of the Josephson junction devices, see secs. D.3.4. The system is also connected to an oxygen gas cylinder through a Swagelok valve, it is necessary because all the thin

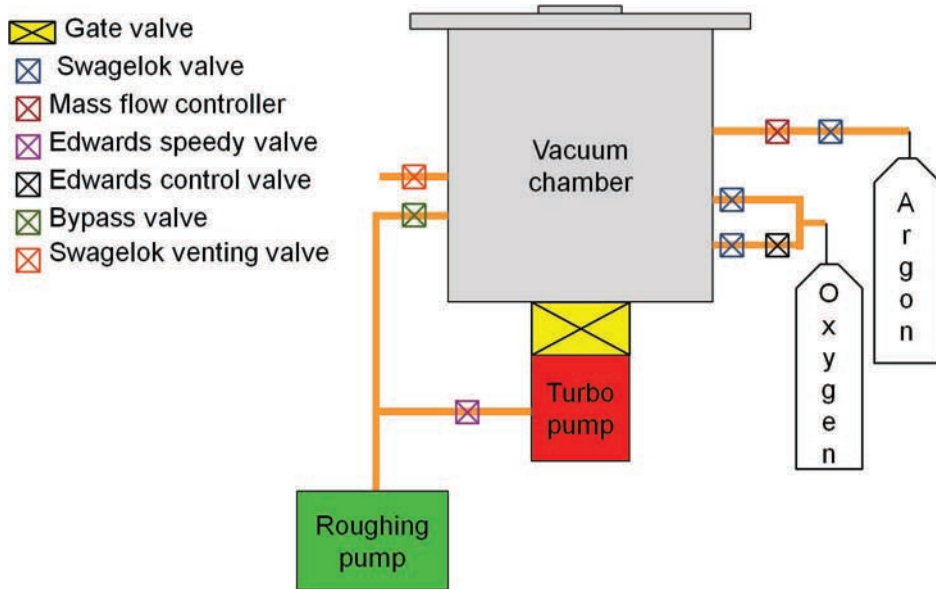


Figure 3.3: Side view of the vacuum system. An argon and an oxygen cylinder are connected to the system. The argon is used to operate the argon ion gun, furthermore an argon flow can be set through the chamber. The oxygen cylinder is necessary because all the thin oxide films are grown in oxygen environment.

oxide films are grown in an oxygen flow environment. In parallel, an oxygen flow can be established through an Edwards *DM20* control valve driven by an Edwards 1501*B* Datametrics pressure controller while the rotary pump is pumping the chamber through the by-pass valve. This parallel oxygen line can also be completely shut off with a Swagelok valve.

Pressure from  $10^5 \text{ Pa}$  to  $100 \text{ Pa}$  is measured by an Edwards *CG16K* capsule dial gauge. The pressure range from  $13.33 \text{ Pa}$  to  $0.13 \text{ Pa}$  is measured by an Edwards capacitance manometer. An Edwards penning gauge covers the pressure range from 1 to  $10^{-5} \text{ Pa}$  [11].

## 3.2 X-ray diffraction

X-ray diffraction analysis was used to evaluate the crystalline quality of the grown films.

A Siemens D5000 X-ray Diffractometer was used. The basic components of a diffractometer are the X-ray source, the X-ray detector and the goniometer which rotates the sample with high angular precision. The D5000 diffractometer has a fixed copper cathode which generates X-rays at three different wavelengths from three electronic level transitions,  $1.54056 \text{ \AA}$  called  $CuK\alpha_1$ ,  $1.54429 \text{ \AA}$  called  $CuK\alpha_2$  and at  $1.39222 \text{ \AA}$  called  $CuK\beta$ . The intensity of the  $\lambda_{CuK\alpha 2}$  is about two times weaker than the intensity of the  $\lambda_{CuK\alpha 1}$  radiation and the intensity of  $\lambda_{CuK\beta}$  is orders of magnitude smaller. However, diffraction peaks from all three of them may appear in studies of high quality single crystals. To cut out the  $\lambda_{CuK\beta}$  radiation a filter made with a thin film of nickel can be inserted in front of the X-ray source. To shape the beam, diaphragms or collimating slits can be placed in front of the X-ray source and in front of the X-ray detector. It is possible to use slits with different apertures. For the characterization of the films  $2 \text{ mm}$ ,  $1 \text{ mm}$  and  $0.2 \text{ mm}$  collimating slits were used. The smaller the slit the higher the accuracy of the measurements and the lower the intensity of the diffracted beam. It must be kept in mind that the detector saturates at rates close to and higher than  $180 \cdot 10^3$  counts per second and such high rates should be avoided. When the intensity of the diffracted beam is near to the detector saturation value, an attenuator can be placed in front of the X-ray source.

It is possible to think a crystal in terms of reflecting planes of atoms

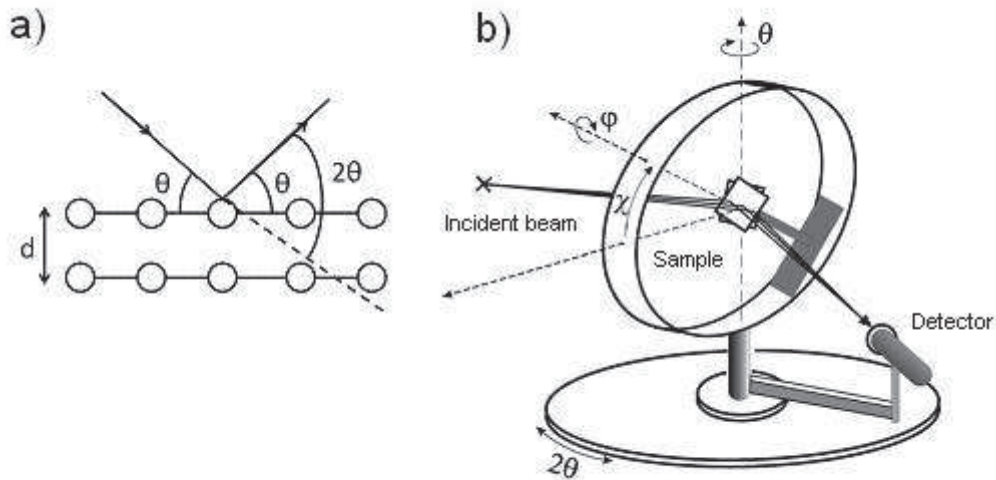


Figure 3.4: a) The fundamental Bragg law of diffraction, the detector of a diffractometer has to be kept at an angle equal to  $2\theta$  relative to the incoming beam. b) Four circle Euler cradle with variable angles  $2\theta$ ,  $\theta$ ,  $\varphi$  and  $\chi$  [48].

the reflected beam is always much weaker than the incident beam. Strong reflected beams are produced when the path differences between reflections from successive planes is equal to a whole number of wavelengths. This approach provides a simple expression for the analysis of crystal structures:

$$n\lambda = 2d_{hkl} \sin\theta \quad (3.1)$$

where  $\lambda$  is the wavelength of the incident radiation,  $n$  is the order of the reflection,  $d_{hkl}$  is the lattice plane spacing and  $\theta$  is the angle of incidence to the planes [47].

An X-ray diffractometer register the angle  $\theta$  at which diffracted beams

appear as peaks in the graph "*detected intensity vs. angle*". The sample is mounted on a goniometer which sweeps the angle  $\theta$  within some range while keeping the detector at  $2\theta$  relative to the incoming beam to satisfy the Bragg law fig. 3.4a,b.

The tube, the detector and the point of incidence on the sample define a plane called diffraction plane. In the D5000 this plane is horizontal and consequently the lattice planes which cause the diffraction must be positioned vertically. The crystal lattice planes causing diffraction might not coincide with the sample surface since the surface might be cut along other crystallographic planes. This means that many motion degrees of freedom are necessary to find the desired diffraction geometry. This is achieved by the use of four sample rotation circles. The mechanical device capable of performing those movements is called Euler cradle fig. 3.4b. The D5000 cradle has the following physical move ranges:

*angle  $2\theta$  from  $0^\circ$  to  $168^\circ$ ; angle  $\theta$  from  $0^\circ$  to  $84^\circ$ ;*

*angle  $\varphi$  from  $0^\circ$  to  $360^\circ$ ; angle  $\chi$  from  $0^\circ$  to  $90^\circ$ .*

In addition, the cradle is mounted on a translation stage with two linear movements, to raise/lower the sample position relative to the beam (vertically) and to shift the sample left or right relative to a zero point (horizontally), the ranges here a  $+/- 10\text{ mm}$ .

The D5000 diffractometer operation is controlled by the *SPEC X-ray diffraction software*.

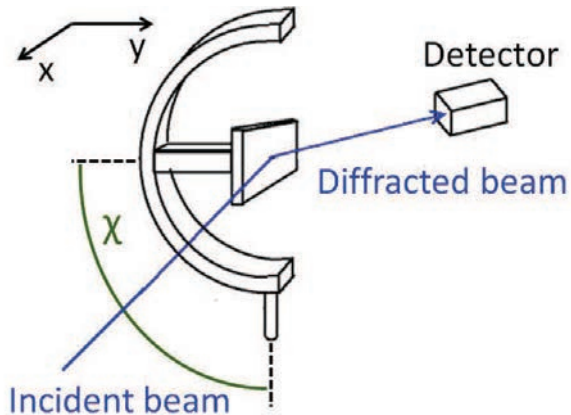


Figure 3.5: During the alignment the sample is mounted on a columnar stage and  $\chi$  is set to  $90^\circ$ .

### 3.2.1 Sample surface alignment

The sample surface alignment is an important step in the diffraction measurement. The sample under investigation is mounted on a pillar stage. As previously stated the diffraction plane is horizontal, so the sample has to be set in a vertical position, in order to do that  $\chi$  is moved to  $90^\circ$  fig. 3.5. To perform a precise alignment the linear translation stage moves the sample along the  $x$  and  $y$  direction completely independently of the Euler cradle angles fig. 3.5.

A typical y-scan obtained for the sample called *GV10(P)* (where *P* means that the sample was fabricated for the piezoelectric device project) is shown in fig. 3.6a. When the y-position is below 4.5 mm, the sample is below the beam and the intensity measured by the detector is high, when the y-position is over 4.7 mm the sample is fully obstructing the detector and the measured intensity is roughly zero. The sample has to be positioned at the

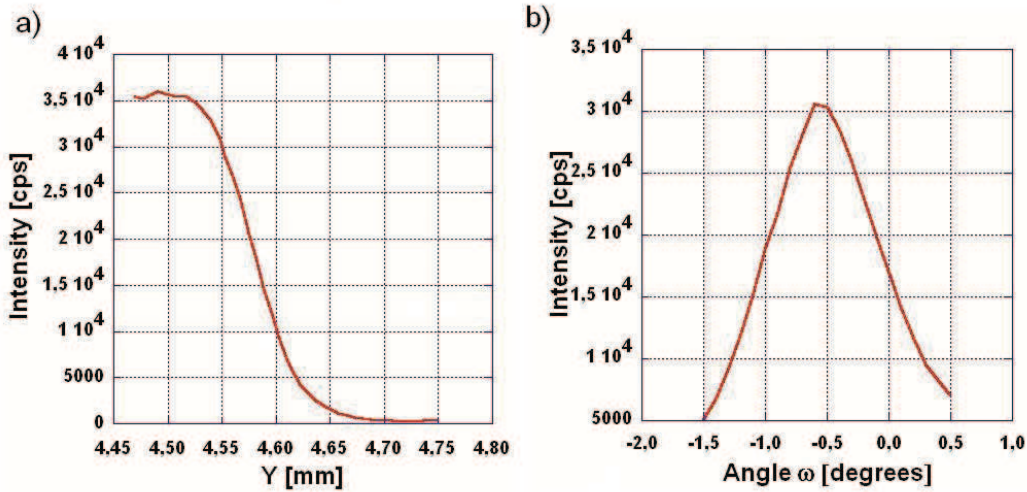


Figure 3.6: a) Y-scan graph during the sample surface alignment, for the sample called  $GV10(P)$ . b) Rocking curve or  $\omega$ -scan during the sample surface alignment, for the sample called  $GV10(P)$ .

half-intensity point, this indicates that the sample is exactly at the center of the beam.

The next step is to take a **rocking curve**, in this case the angle between the incoming beam and the sample is denoted as  $\omega$  which is different from  $\theta$  over the whole scan range with the exception of the point  $\omega = 2\theta/2$ ; there, the detector is fixed in a point where the angle between the incoming beam and the reflected beam is  $2\theta$ . The circle holding the sample is moved independently to "rock" the sample around its position and sweep the angle  $\omega$  within the range  $\theta \pm \Delta\theta$ . This kind of scan it is also called the  $\omega$ -*scan*.

A typical rocking curve is shown in fig. 3.6b. The peak will appear when the sample surface is parallel to the beam because any tilt results in increased obstruction of the beam path by the sample. The peak point is

shifted to about  $-0.6^\circ$ , indication of a sample tilted relatively to the cradle zero geometry.

The next step is the compensation of the sample tilting, this is achieved by setting the intensity peak of the rocking curve as the  $\omega$ -zero position.

### 3.2.2 $\varphi$ and $\theta - 2\theta$ scans

After the sample alignment, it is possible to start searching for the Bragg peaks. All the deposited films have been grown on (001) oriented  $SrTiO_3$  substrates. In this case only the  $(00l)$  planes give diffraction peaks when  $\chi = 90^\circ$ .

The *SPEC X-ray diffraction software* allows the user to enter the theoretical lattice constants, the lattice structure, the reflection planes and the order of the reflection under investigation. It will return the values of  $2\theta$ ,  $\theta$ ,  $\phi$  and  $\chi$  at which the diffracted intensity peaks are expected.

The crystal structure of our deposited films is either cubic or tetragonal. As our films have been grown on (001) oriented  $SrTiO_3$  substrates, the family planes  $(00l)$  of the film will be parallel to the top surface of the sample. However it is unknown if the directions  $(h00)$  or  $(0k0)$  are parallel to the side surfaces of the substrate. In order to find these epitaxial orientations it is necessary to run what is called a  $\phi$ -scan.

A  $\phi$ -scan is equivalent to a rotation of the sample around the axis perpendicular to its surface. It might have many applications and the simplest one is to confirm experimentally the symmetry of the crystal under investigation. If the  $2\theta$  angle is fixed to register the reflection from a  $(hkl)$  plane of a cubic

lattice and the sample is rotated within the entire  $360^\circ$  range of  $\phi$ , four peaks separated by  $90^\circ$  from each other will appear. That is due to the symmetry of the cube. In the case of a tetragonal structure where the longest lattice parameter is perpendicular to the rotation axis, two peaks separated by  $180^\circ$  will appear.

At this point the  $\phi$  value corresponding to one of these peaks is chosen and a  $\theta - 2\theta$  scan can be run. In a  $\theta - 2\theta$  scan the X-ray source and the X-ray detector with their collimating slits are set in a way that the incident and the reflected beams make equal angles to the sample surface fig. 3.4a. This is achieved by rotating the detector at twice the angular velocity of the sample rotation.

The angles corresponding to the diffracted peaks are then recorded and the lattice geometry of the material under investigation can be constructed.

### 3.3 Device patterning and milling

To transfer the desired device geometry on the deposited films, contact photolithography and argon ion beam milling have been used.

*S1813* photoresist was used to define the geometry of the different devices on the substrate. The *S1813* is spun on the sample using a Headway Research. Inc. 1 – *EC101D – R790* spinner. The spinning speed for this kind of photoresist can vary between  $7000 \text{ rpm}$  and  $2000 \text{ rpm}$ . The thickness of the spun resist is  $800 \text{ nm}$  when the spinning speed is  $7000 \text{ rpm}$ , and  $1500 \text{ nm}$  when the spinning speed is  $2000 \text{ rpm}$ . The resist resolution is  $0.48 \mu\text{m}$  [50].

Contact photolithography is used to transfer the device geometry on the

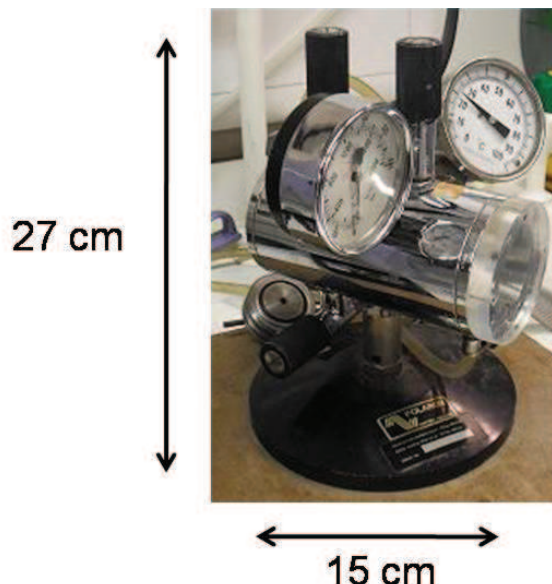


Figure 3.7: Critical point dryer used in this project.

deposited films by using a 104851 Karl Suss Mask aligner. After the exposure the sample is developed in *MF319* developer.

An Oxford Applied Research *IM150* Ion milling system was used to transfer the patterned geometry on the sample. The milling profile is real time controlled by an *HAL 301 s/2* mass spectrometer which is connected to the milling system.

### 3.4 Critical point drying

The last step of the fabrication process, necessary to produce suspended cantilevers, consists in the undercutting of the sacrificial layer. To stop the undercut the sample is rinsed in water. After rinsing, the water must be dried from the surface of the sample. If a freestanding structure overhangs

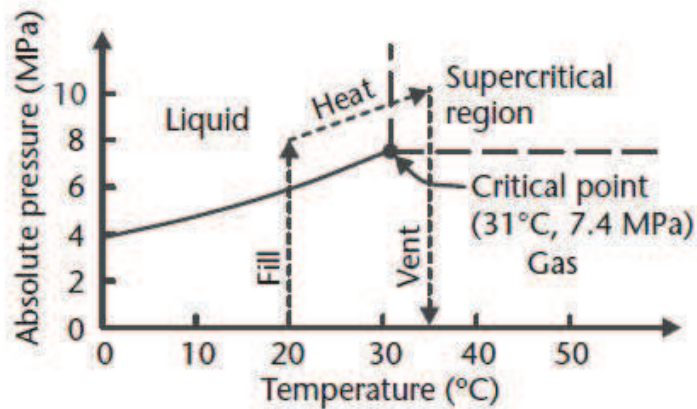


Figure 3.8: Path of the carbon dioxide pressure-temperature phase diagram during critical point drying [51].

the substrate, the surface tension traps some water between the substrate and the suspended structure. As the water dries, its volume and hence its thickness decreases. The suspended structure, due to the surface tension, is pulled down until it contacts the substrate. If a sufficiently large, smooth area of the structure makes contact with the substrate it can stick to the substrate. This phenomenon is known as **stiction** in the micromachining community [51].

A solution to avoid stiction is to use a critical point drying. The sample is immersed in ethanol after its rinsing in distilled water, then it is placed inside a pressure chamber fig. 3.7. Liquid carbon dioxide is introduced in the chamber at a pressure of  $7.5 \text{ MPa}$  and the ethanol is drained from the bottom. When only carbon dioxide remains inside the chamber the system is heated to about  $35^\circ\text{C}$ , this will also produce an increase in pressure. The carbon dioxide has now surpassed its critical point [ $31.1^\circ\text{C}$ ;  $7.39 \text{ MPa}$ ] fig.

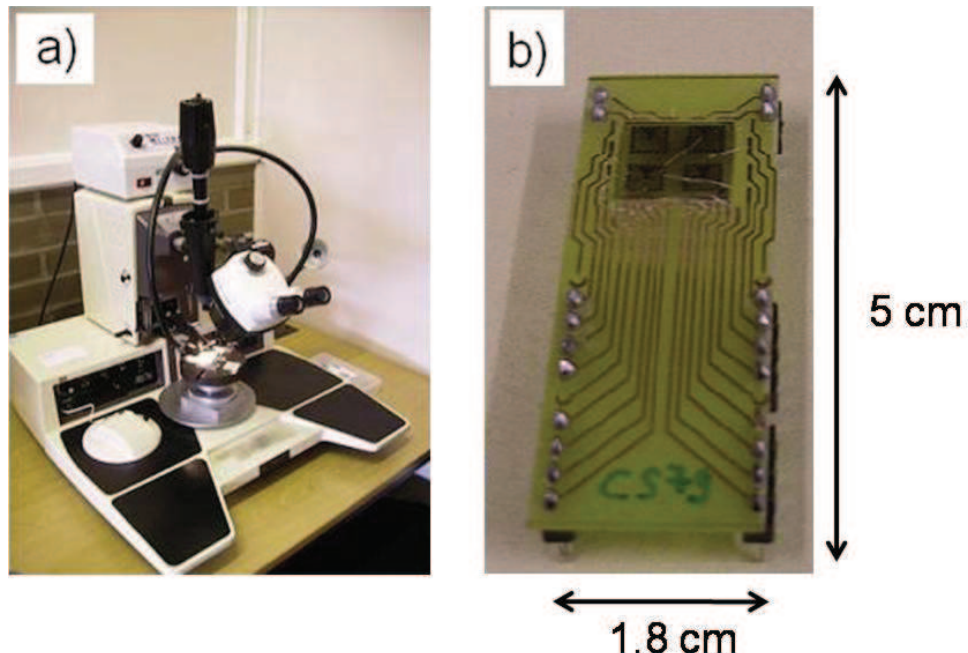


Figure 3.9: a) Wirebonding machine used during this project. b) Chip-carrier with a connected sample on its top.

3.8, in such condition there is no apparent difference between the liquid and the gas state, the surface tension between the ethanol and suspended structure is then reduced to zero. Finally the carbon dioxide is vented off and the sample is taken out from the chamber [51]. This process allow the production of suspended structure without the developing of surface tension between the liquid and the fabricated devices, avoiding in this way the problem of stiction.

### 3.5 Wirebonding

Wirebonding was used to connect the pads of the capacitors which are integrated on the top of the cantilevers. First the sample is attached to a chip

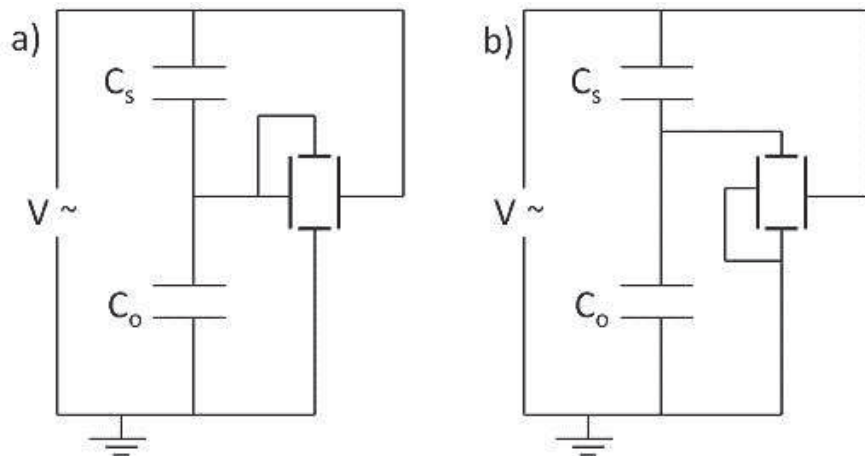


Figure 3.10: a) Schematic circuit for the observation of ferroelectric hysteresis loop according to Sawyer and Tower,  $C_s$  is the ferroelectric capacitor while  $C_0$  is the linear sense capacitor [16]. b) Modified version of the Sawyer and Tower circuit.

carrier using nail varnish. Fig. 3.9 shows the wirebonder, it contains a needle, through which an aluminum wire of diameter of  $25 \mu m$  passes. When the needle is moved onto the desired pad, an ultrasonic vibration is applied to melt the wire and form a connection. Connections are made between the contact pads on the sample and copper tracks on the chip-carrier, fig. 3.9b.

### 3.6 Electrical Measurements

Impedance measurements were performed on the fabricated capacitors by using an Agilent 4294A Precision Impedance Analyzer with a source voltage of  $1 V$  over the frequency range of  $50 Hz - 50 KHz$ . This frequency range has been chosen because the micro-cantilevers are suppose to operate around their resonance frequencies which are in the range  $100 Hz - 20 KHz$  chap.

2, so good electrical properties are also expected in this range.

Hysteresis loop measurements were also run on the capacitors. For this purpose a modified version of the Sawyer and Tower circuit was used. Fig. 3.10a shows the classical circuit for the observation of the hysteresis loop according to Sawyer and Tower. The voltage across the ferroelectric crystal  $C_s$  is applied to the horizontal plates of the oscilloscope while the voltage across the linear capacitor, which is proportional to the crystal polarization is applied to the vertical plates of the oscilloscope [16].

The channels of the modern oscilloscopes share the same ground, so the modern version of the Sawyer and Tower circuit is that one shown in fig. 3.10b.

An alternating voltage, usually a sine-wave or a triangular-wave, is applied to the ferroelectric and linear capacitors which are connected in series. The applied voltage will force a charge on the top plate of the ferroelectric capacitor, the same amount of charge will leave the bottom plate of the ferroelectric capacitor and will be collected on the top plate of the linear capacitor [52]. The voltage across the capacitor  $C_0$  is therefore proportional to the polarization of the ferroelectric crystal. When the input voltage is equal zero, the voltage across  $C_0$  represents the residual polarization of the ferroelectric crystal.

In the case of lossy ferroelectric capacitors the contribution of the dielectric losses,  $Q(t)_{loss}$ , needs to be added to the switching charge, eq. 3.2

$$Q(t)_{loss} = \sigma E(t)At \quad (3.2)$$

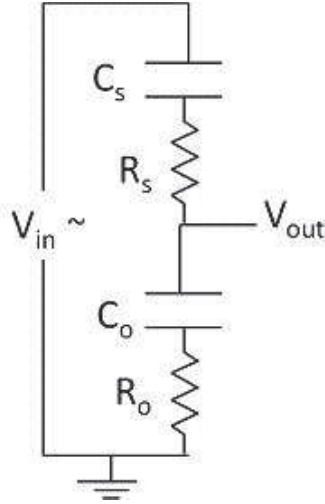


Figure 3.11: Schematic of the compensated circuit for the observation of ferroelectric hysteresis loop,  $C_s$  is the ferroelectric capacitor,  $R_s$  models the dielectric losses in the ferroelectric capacitor,  $C_0$  is the linear sense capacitor and  $R_0$  is the compensation resistor.

where  $\sigma$  is the electrical conductivity representing the dielectric losses,  $E(t)$  the applied field and  $t$  the measuring time [53]. The total charge is so given by eq. 3.3

$$Q(t)_{tot} = P_r A + \sigma E(t) A t \quad (3.3)$$

where  $P_r$  is the residual polarization and  $A$  the area of the ferroelectric capacitor.

The impedance of a lossy ferroelectric capacitor contains a real part and an imaginary part, and it can be modelled with a resistor and a capacitor in parallel or in series. If the series model is chosen, the circuit of fig. 3.11 describes the hysteresis loop measurements. In this circuit the resistance  $R_s$  models the losses in the ferroelectric layer, while  $R_0$  is a resistor which has been added to the base circuit.

The transfer function of the circuit in fig. 3.11 is:

$$G(s) = \frac{V(s)_{out}}{V(s)_{in}} = C_s \frac{s C_0 R_0 + 1}{s(C_s C_0 R_s + C_s C_0 R_0) + C_s + C_0}. \quad (3.4)$$

Its phase is:

$$\angle G(s) = \arctan(C_0 R_0) - \arctan\left(\frac{C_s C_0 R_s + C_s C_0 R_0}{C_s + C_0}\right). \quad (3.5)$$

This transfer function has a pole at frequency  $\omega_p$  and a zero at frequency  $\omega_z$  given by:

$$\omega_p = \frac{C_s + C_0}{C_s C_0 R_s + C_s C_0 R_0} \quad (3.6)$$

and

$$\omega_z = \frac{1}{C_0 R_0}. \quad (3.7)$$

The value of the resistor  $R_0$  can be chosen in such a way that both the pole and zero are at the same frequency, eq. 3.8.

$$\omega_p = \omega_z \implies R_0 = \frac{C_s}{C_0} R_s \quad (3.8)$$

By doing so the contribution to the phase shift of the pole and of the zero will cancel each other and the phase of eq. 3.5 will be equal zero. The result is that in a  $V_{out}$  vs  $V_{in}$  plot the loop will be only due to the switching charge and the contribution of the dielectric losses will be cancelled. A similar approach is valid when the model of a resistor and a capacitor connected in parallel is chosen.

To run hysteresis loop measurements a Tektronic TDS 1002B oscilloscope

and a TTi TG210 function generator were used.

### 3.7 Other Measurements

Other instruments which were used to investigate the quality of the deposited thin films were an AFM (Atomic Force Microscope) and a Nano-indentation tool.

AFM scans of the surface of the deposited thin films were performed to verify the presence of particulates and outgrowths and to measure the average roughness of the surfaces. AFM scans were run in contact mode on an area of  $10 \mu m \times 10 \mu m$  at a scan frequency of  $0.4 Hz$ . More details of this technique are reported in sec. D.2.4.

Nano-indentation measurements were performed on multi-layers to evaluate the Yong's Modulus of each film. The nano-indentation technique consists in the measurement of the movement of a diamond probe in contact with the surface of the thin film. In order to do that an increasing load is applied and the probe indents the contact surface [54].

Nano-indentation measurements allow the measurement of the Reduced Modulus  $\tilde{E}_r$  of the material. The reduced modulus takes into account the effect of non-rigid indenters during the probe displacement [55]. The relation linking the Young's Modulus to the reduced modulus is [54, 55]:

$$\frac{1}{E_r} = \frac{1 - \nu^2}{\tilde{E}} + \frac{1 - \nu_i^2}{\tilde{E}_i} \quad (3.9)$$

where  $\tilde{E}$  and  $\nu$  are the Young's modulus and the Poisson Ratio of the material

under investigation and  $\tilde{E}_i$  and  $\nu_i$  are the same parameter for the indenter probe. In our case a diamond probe having [54]:

$$\tilde{E}_i = 1141 \text{GPA} \quad (3.10)$$

and

$$\nu_i = 0.07. \quad (3.11)$$

was used. Nano-indentation measurements were performed by Dr. James Bowen [56].

### 3.8 Summary

In this chapter the following techniques have been discussed:

- Pulse Laser Deposition;
- contact photolithography and argon ion beam milling;
- critical point drying;
- X-ray diffraction;
- nano-indentation;
- impedance measurements;
- hysteresis loop measurements;
- atomic force microscope (AFM) investigation.

Pulse laser deposition, contact photolithography and argon ion beam milling are used for the fabrication of the micro-cantilevers having a  $BaTiO_3$  based capacitive structure on their top. The device fabrication procedure is described in chap. 4.

The results of the X-ray diffraction and nano-indentation measurements are reported in chap. 5, while the results of the impedance, hysteresis loop and AFM measurements are discussed in chap. 7.

# Chapter 4

## Fabrication process of the cantilevers

This chapter describes the fabrication process of the 31 and 33 mode piezoelectric cantilevers. The reasons which leads to the introduction of each step in the fabrication procedure are introduced and explained.

In section 4.1 an overview of the fabrication processes employed for the 31 and the 33 mode micro-cantilevers is presented. In section 4.2 a detailed description of the fabrication process for the devices using the 31 piezoelectric mode together with the reasons which lead to the employed process parameters are reported. Section 4.3 presents a detailed description of the fabrication process adopted for the devices working with the 33 piezoelectric mode. Finally sec. 4.4 shows how the fabrication process changes when a  $MgO$  rather than a  $YBa_2Cu_3O_7$  film is used as sacrificial layer in the proposed multi-layers.

## 4.1 Introduction to the fabrication procedure

Figs. 4.1 and 4.2 report the main steps of the fabrication procedure employed for the 31 and the 33 mode cantilevers.

As already mentioned in chap. 1, besides the electrode and the piezoelectric layers other thin film layers have been introduced in the stack. The details of the fabrication process for each type of cantilever will be further discussed in the next sections of this chapter, here only a general introduction to the fabrication procedure is given.

The main steps illustrated in figs. 4.1 and 4.2 are:

- deposition of the sacrificial layer plus deposition of the bottom electrode layer for the 31 mode devices, fig. 4.1a, the 33 mode structures do not have bottom electrode so during the first step of the fabrication process the sacrificial layer and other thin films can be grown fig. 4.2a;
- patterning of the bottom electrode by argon ion beam milling and contact photolithography fig. 4.1b, this step is only present in the fabrication of the 31 mode cantilevers;
- deposition of the  $BaTiO_3$  piezoelectric film and of the top electrode layer fig. 4.1c, this step is only present in the fabrication of the 31 mode cantilevers;
- patterning by contact photolithography and argon ion beam milling of the top electrode figs. 4.1d and 4.2b;
- opening of windows through the piezoelectric layer to contact the bottom electrode fig. 4.1e, this step is only present in the fabrication of

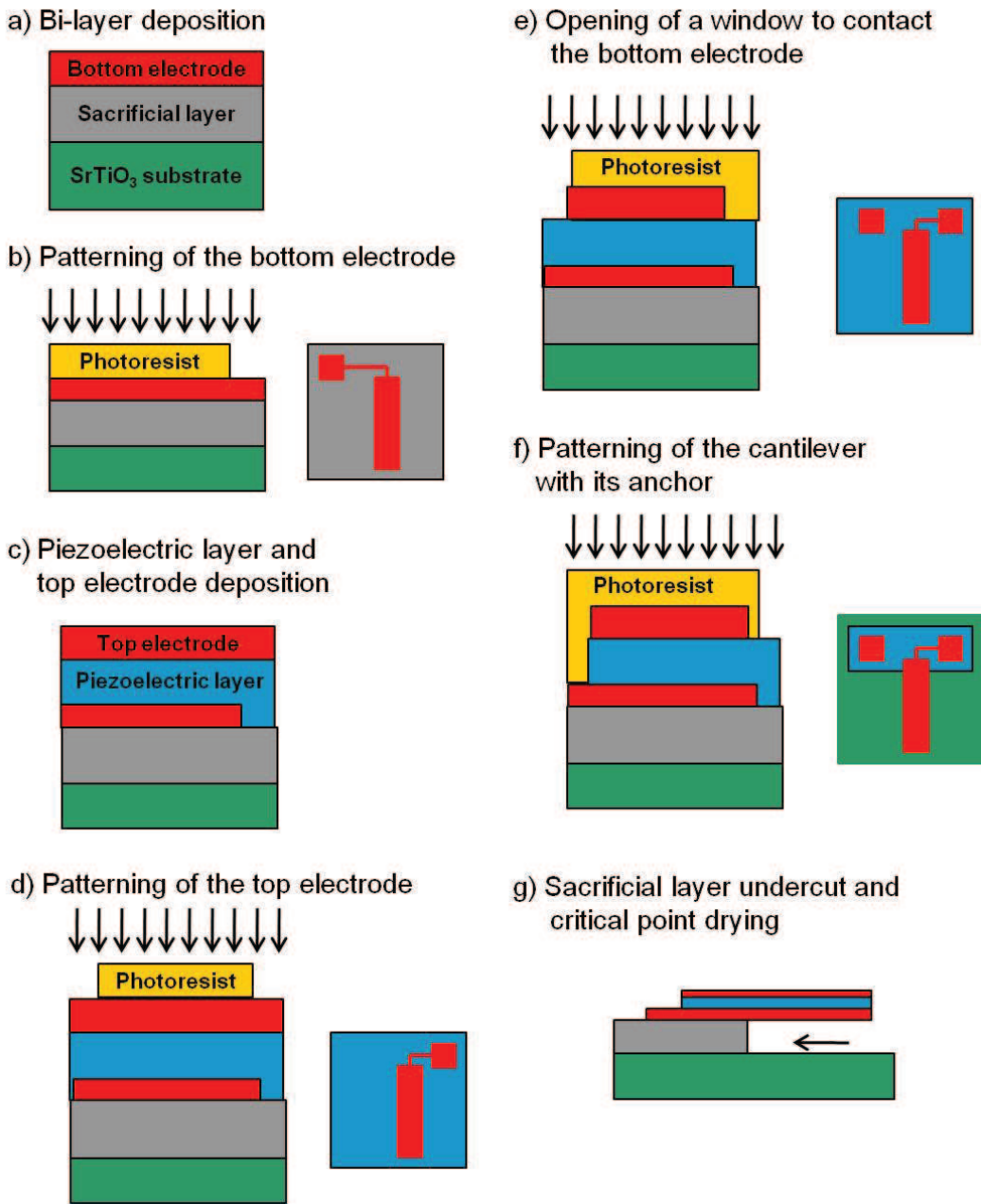


Figure 4.1: Main steps for the fabrication process of the 31 mode cantilevers.

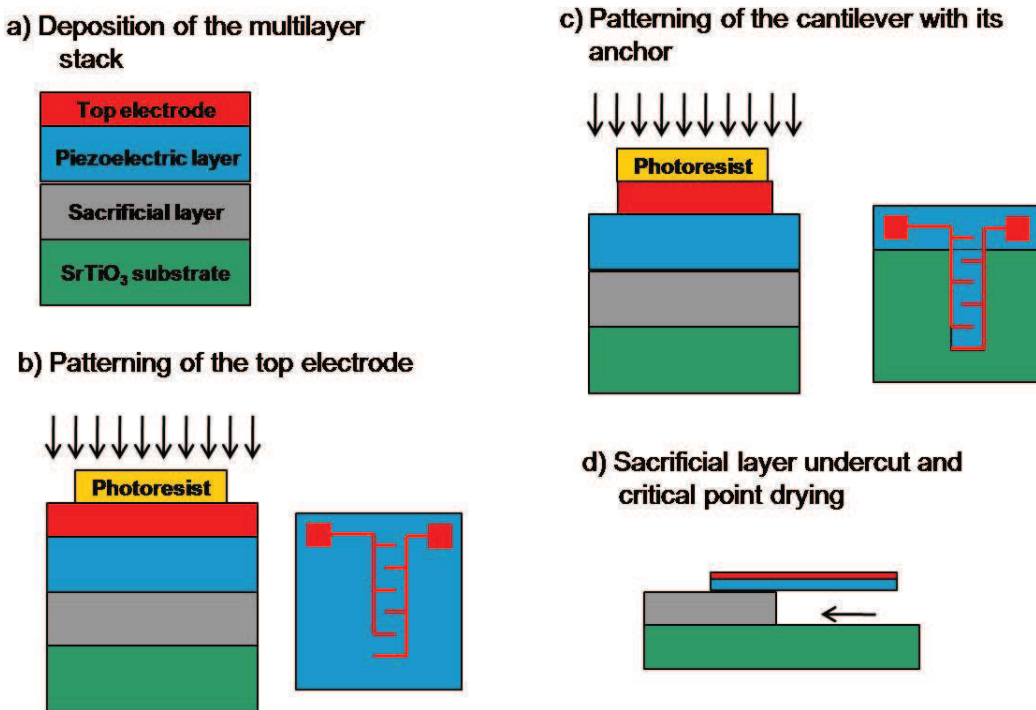


Figure 4.2: Main steps for the fabrication process of the 33 mode cantilevers.

the 31 mode cantilevers;

- patterning by contact photolithography and argon ion beam milling of the cantilever structure with its anchor figs. 4.1f and 4.2c;
- undercut of the sacrificial layer and critical point drying figs. 4.1g and 4.2d.

## 4.2 Fabrication process for the 31 mode cantilevers

The top-down layer sequences which have been used for the fabrication of the 31 mode piezoelectric cantilevers are  $SrRuO_3/BaTiO_3/SrRuO_3/YBa_2Cu_3O_7$  and  $SrRuO_3/BaTiO_3/SrRuO_3/SrTiO_3/YBa_2Cu_3O_7$ . The  $YBa_2Cu_3O_7$  is used as sacrificial layer because it is easy to etch in weak nitric acid solutions [57] like 0.1%  $HNO_3$  and because  $BaTiO_3$ ,  $SrRuO_3$  and  $SrTiO_3$  layers can be epitaxially grown on its top. The  $BaTiO_3$  film is the piezoelectric layer while the  $SrRuO_3$  acts as an electrode, a  $SrTiO_3$  buffer layer can be introduced between the  $YBa_2Cu_3O_7$  sacrificial layer and the  $SrRuO_3$  bottom electrode to improve the interface between the two films. The  $SrRuO_3$  film used for the fabrication of the top electrode can be also replaced with a gold layer.

Let us consider the  $SrRuO_3/BaTiO_3/SrRuO_3/YBa_2Cu_3O_7$  stack, the first step in the fabrication process is the deposition of the  $SrRuO_3/YBa_2Cu_3O_7$  bilayer on a (001) oriented  $SrTiO_3$  substrate. The  $SrTiO_3$  substrates used in this project, have an area of  $1\text{ cm}^2$ , a thickness of  $1\text{ mm}$  and are supplied by Crystal [58]. The ablation targets employed for the deposition of the thin films are supplied by Praxair [59].

A single crystal (001) oriented  $SrTiO_3$  substrate is glued with silver paint onto the thermocoax heater, the silver paint is dried for at least 30 minutes at room temperature then the heater is placed inside the deposition chamber. The target of the materials which are going to be deposited, in this case  $YBa_2Cu_3O_7$  and  $SrRuO_3$ , are cleaned by using acetone and sand paper,

then they are mounted inside the vacuum deposition chamber. The laser energy is set to have the desired energy level on the target, the energy is also measured outside the vacuum chamber, in this way the laser beam can be set to the right energy during the deposition.

The laser spot size is checked before to enter the deposition chamber by using photo-sensitive paper, then its size on the target is measured. The spotsize has to be uniform and with a well define edge, this ensures an uniform laser fluence  $U$  (measured in  $[J/cm^2]$ ) on the area of the target hit by the laser. These steps take the name of *pre-ablation* or *ablation preparation*.

The deposition chamber is then closed and pumped down over night by using a roughing pump and a turbo pump, on the next day, inside the vacuum chamber, a pressure of  $2 \cdot 10^{-5} Pa$  is reached. The energy of the beam is then set to the energy level measured during the ablation preparation, this ensures the desired fluence on target inside the chamber. It follows an in-situ cleaning step of the ablation targets at room temperature and in oxygen flow at the pressure which will be used during the film deposition, which reduces the oxygen deficiency on the surface of the target [60]. During the cleaning and the film depositions the targets are rotated to ensure uniform erosion [61]. The cleaning is performed with 1200 pulses at the repetition rate of  $4 Hz$ , the same rate used during the film growth.

The substrate is then heated to  $740^\circ C$  in vacuum at a rate of  $35^\circ C/min$  and at this temperature a  $400 nm$  or  $500 nm$  thick  $YBa_2Cu_3O_7$  film is grown in oxygen flow at a pressure of  $20 Pa$  and with a pulse rate of  $4 Hz$ , the  $YBa_2Cu_3O_7$  ablation parameters are reported in table 4.1. These ablation parameters have been set equal to the values which minimize the roughness

<i>Material (heater)</i>	<i>P</i> [Pa]	<i>T</i> [°C]	<i>d<sub>TS</sub></i> [cm]	<i>U</i> [J/cm <sup>2</sup> ]	<i>Spotsizes</i> [mm <sup>2</sup> ]	<i>f</i> [Hz]	<i>dep. rate</i> Å/pulse
<i>YBa<sub>2</sub>Cu<sub>3</sub>O<sub>7</sub></i>	20	740	5.7	3.39	2.39	4	0.21
<i>SrTiO<sub>3</sub></i>	28	740	5.7	3.77	2.15	4	0.17
<i>BaTiO<sub>3</sub></i>	20	740	5.7	3.44	2.35	4	0.18
<i>BaTiO<sub>3</sub></i>	8	780	5.7	3.44	2.35	4	0.14
<i>SrRuO<sub>3</sub></i>	40	780	5.7	3.37	2.40	4	0.12
<i>MgO</i>	27	740/780	5.7	3.54	2.29	4	0.10
<i>Au</i>	$5 \cdot 10^{-5}$	<i>RT</i>	5.7	4.28	2.40	4	0.07

Table 4.1: Laser ablation condition for the *YBa<sub>2</sub>Cu<sub>3</sub>O<sub>7</sub>*, *SrTiO<sub>3</sub>*, *BaTiO<sub>3</sub>*, *SrRuO<sub>3</sub>*, *MgO* and *Au*, two different growing conditions are reported for the *BaTiO<sub>3</sub>*. Also shown are: the oxygen pressure *P* during the film deposition, the deposition temperature *T*, the target-sample distance *d<sub>TS</sub>*, the fluence on target *U*, the spotsize on target, the pulse frequency *f* and the deposition rate, *RT* stands for room temperature.

and the number of particulates on the top surface of the *YBa<sub>2</sub>Cu<sub>3</sub>O<sub>7</sub>* film, as will be further discussed in sec. D.3.2.

After the sacrificial layer deposition, the sample is kept for 30 minutes at the *YBa<sub>2</sub>Cu<sub>3</sub>O<sub>7</sub>* ablation conditions, this is important to thermally stabilize the species on the surface of the sacrificial layer and reduce the number of outhgrowth which may occur when the temperature of the sample is further increased [62].

The sample is then heated to 780°C at a rate of 3°/min and a 150 nm thick *SrRuO<sub>3</sub>* film is grown at a pressure of 40 Pa in oxygen flow, in order to provide a bottom electrode for our *BaTiO<sub>3</sub>* based ferroelectric capacitors. The ablation conditions used for the growth of the *SrRuO<sub>3</sub>* ensure the deposition of films having a resistivity near to its minimum value (see sec. 7.1)

[25]. The ablation parameters for the  $SrRuO_3$  films together with the ablation parameters of the other layers grown for the fabrication of piezoelectric cantilevers are reported in table 4.1; the target to sample distance has been set equal to  $5.7\text{ cm}$  and the pulse repetition rate used is equal to  $4\text{ Hz}$ .

After the deposition of the bilayer the sample is cooled in  $90 \cdot 10^3\text{ Pa } O_2$  static environment, with dwells of 15 minutes at  $600^\circ C$  and of 30 minutes at  $450^\circ C$  during cooling to fully oxygenate the  $YBa_2Cu_3O_7$  layer [10]. When room temperature is reached the sample is detached from the heater with the help of a scalpel and the silver paint on the back side of the substrate is carefully removed with sandpaper.

A  $SrTiO_3$  buffer layer can be introduced between the  $YBa_2Cu_3O_7$  sacrificial layer and the  $SrRuO_3$  bottom electrode. The buffer layer is important for the devices employing the 33 piezoelectric mode, see sec. 4.3. However the presence of the buffer layer seems to improve the  $SrRuO_3/YBa_2Cu_3O_7$  interface, the introduction of the  $SrTiO_3$  film in the 31 mode stack allows the 97% of the structures to be suspended by undercut, without buffer layer the yield is reduced to 77% (see tab. 4.2 in sec. 4.3). The ablation parameters for the  $SrTiO_3$  used as buffer layer in the 31 and 33 mode cantilevers are reported in table 4.1

The sample is then processed in the clean room for the patterning of the bottom electrode with its contact pads. The substrate is first cleaned in an ultrasonic bath with acetone and isopropanol, dried with nitrogen and baked at  $100^\circ C$  on a hot plate for 1 minute. Next Shipley Microposit S1813 photoresist is spun on the sample at a spinning speed of  $4000\text{ rpm}$  for 30 seconds this produces a resist layer with a thickness of approximately  $1.3\text{ }\mu\text{m}$

on the sample [63], the sample is baked again at  $100^{\circ}C$  for 1 minute and 30 seconds in order to harden the resist layer.

Next the sample is exposed in contact mode to the UV light for 30 seconds through the edge mask, fig. 4.3a, in a *MJB3* Karl Suss mask aligner at a power of  $295\text{ W}$  and developed for about 30 seconds in Shipley Microposit *MF – 319* developer.

The edge mask allows the removal of the resist at the edge of the sample, since during the spinning a resist hump is formed at the edge, which would reduce the resolution of the photolithography [11].

Then follows the definition of the bottom electrode geometry. The sample is exposed in contact mode to the UV light for 10 seconds through the bottom electrode mask fig. 4.3b and the resist is then developed for 25 seconds in *MF – 319*. The sample is now inserted in the vacuum chamber of an Oxford Applied Research (OAR) *IM150* argon ion milling system where it is milled with an argon beam incident at  $45^{\circ}$  respect to the sample surface. The sample is kept under rotation and milled at a beam energy of  $500\text{ eV}$ . The end point of the milling is detected with the help of a Hiden mass spectrometer.

Next the sample is cleaned in an ultrasonic bath with acetone and isopropanol, brought to the laser ablation facilities and glued on the heater to undergo the deposition of the  $\text{BaTiO}_3$  piezoelectric film and the  $\text{SrRuO}_3$  top electrode layer. Then follows the pre-ablation procedure previously described.

The sample is heated to  $780^{\circ}C$  in oxygen flow at a pressure  $20\text{ Pa}$ , fig. 4.4, it is not heated in vacuum to avoid the decomposition of the  $\text{YBa}_2\text{Cu}_3\text{O}_7$  sacrificial layer, (see chap. D.3). At  $740^{\circ}C$  the annealing step already per-

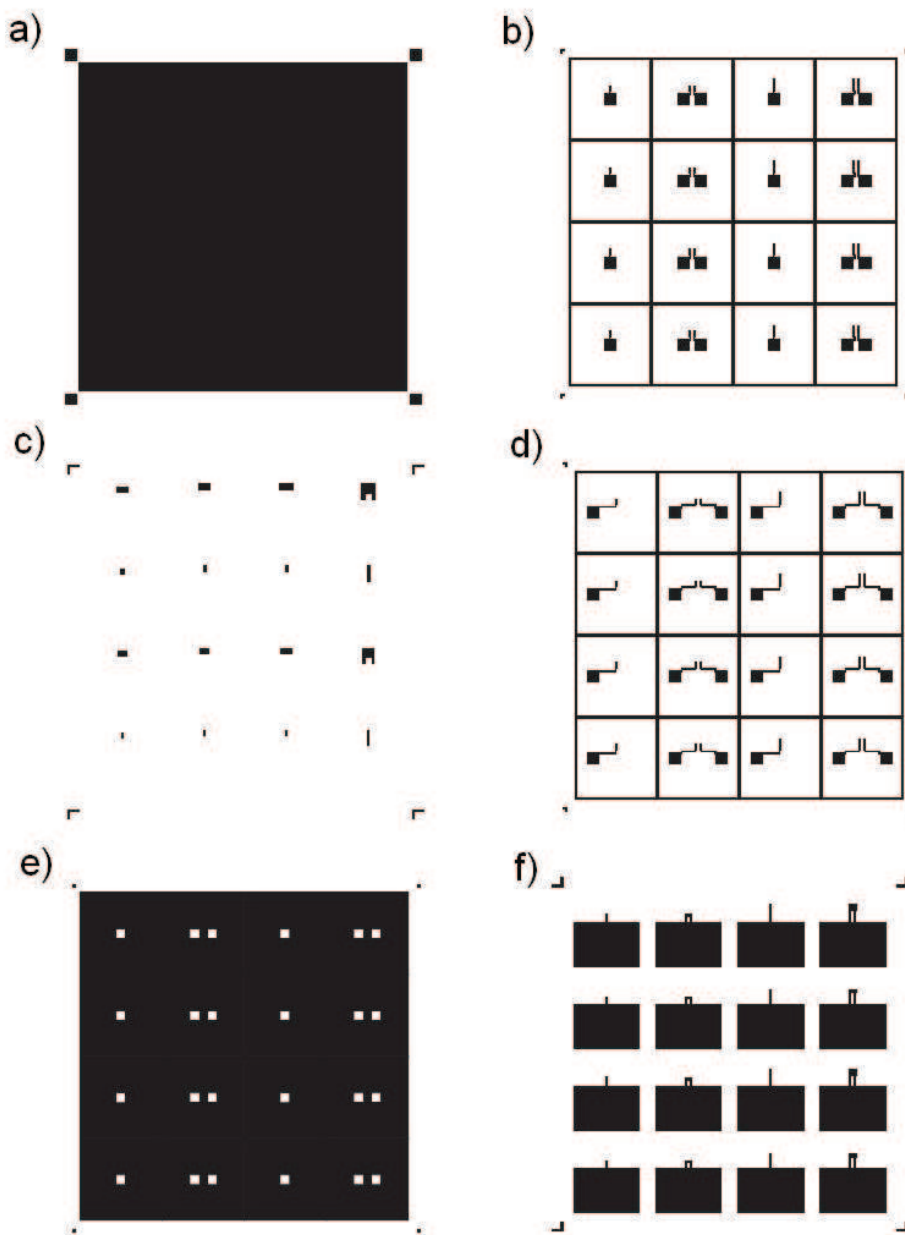


Figure 4.3: Masks used for the fabrication of the 31 mode piezoelectric cantilever: a) edge mask, b) bottom electrode mask, c) seismic mass mask, d) top electrode mask, e) pad mask and f) cantilever mask. The masks have been designed by A. Frommhold [64].

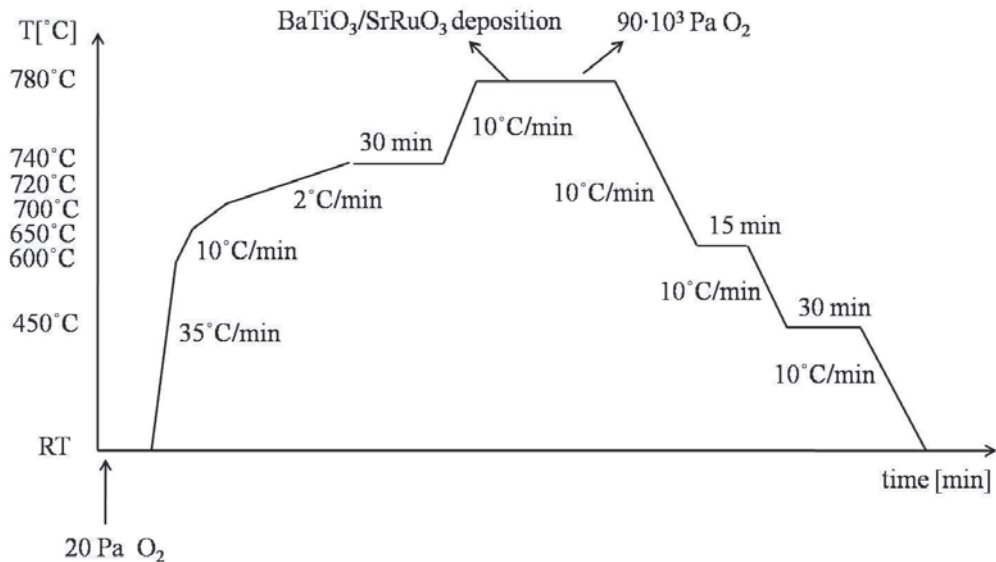


Figure 4.4: Heating process before the  $SrRuO_3/BaTiO_3$  deposition and subsequent cooling down procedure.

formed during the sacrificial layer and the bottom electrode deposition is repeated.

Then follows the deposition of a  $200 - 400\text{ nm}$  thick  $BaTiO_3$  film at a temperature of  $780^\circ\text{C}$  in oxygen flow. Different pressures have been used during the deposition of the piezoelectric layer. Initially the  $BaTiO_3$  was grown at a pressure of  $20\text{ Pa}$ . Different works [65, 66] reported pulsed laser deposition of  $BaTiO_3$  grown at oxygen pressures in the range  $13 - 20\text{ Pa}$ , however our  $BaTiO_3$  based capacitors grown in this pressure range present resistive losses (see sec. 7.2). To reduce the losses present in the capacitive structures the growing pressure has been reduced to  $8\text{ Pa}$ . The lower background pressure reduces the energy lost by the atomic species in the ablation plume [61] in this way the clusters of atoms which arrive on the surface of

the sample have higher mobility and so also a longer diffusion length on the substrate which is useful during the crystal growth. Resistive losses are reduced in the  $BaTiO_3$  films grown at lower background pressures, a detailed discussion on this aspect is presented in sec. 7.2. The ablation parameters used for the deposition of the  $BaTiO_3$  are reported in table 4.1,  $BaTiO_3$  films have been also grown at pressures of 0.40, 0.27 and 0.01  $Pa$  the reasons which led to these choices are discussed in chap. 7.

Next a 100 nm thick  $SrRuO_3$  layer is deposited using the ablation parameters reported in table 4.1, after the deposition of the top electrode layer the chamber is filled with oxygen up to a pressure of  $90 \cdot 10^3 Pa$ , the sample is then cooled in  $90 \cdot 10^3 Pa O_2$  static environment with dwells of 15 minutes at  $600^\circ C$  and of 30 minutes at  $450^\circ C$  during cooling to fully oxygenate the  $YBa_2Cu_3O_7$  layer, fig. 4.4 [10] and to maintain consistency with the oxygenation of the  $BaTiO_3$  film [67].

After the deposition of the top electrode layer, the sample is brought again to the clean room facilities for the definitions of the top electrode, pad and cantilever geometries.

The definition of the top electrode, fig. 4.3d, is done with the same photolithography process used for the patterning of the bottom electrode, the sample is then milled at  $45^\circ$  and under rotation. These photolithography and milling steps are repeated to open some windows through the piezoelectric layer and contact the bottom electrode pads. The mask layout used in this case is shown in fig. 4.3e, here the UV exposure time and the time necessary for the developing of the photoresist have been set equal to 30 seconds.

Finally the cantilever structure and its anchor are defined. The milling

process is run through the thin film stack until the  $SrTiO_3$  substrate is reached. The sacrificial layer has a thickness of  $400 - 500\text{ nm}$  and the piezoelectric layer is  $300 - 400\text{ nm}$  thick. To etch these relative thick layers a milling time up to two hours is necessary, so to avoid the milling through the photoresist, two resist layers are spun on the sample, then it is exposed to the UV light through the cantilever mask for 120 seconds and developed in  $MF - 319$  for 45 seconds. The mask layout used for the definition of the cantilever and its anchor geometry is shown in fig. 4.3f.

After the definition of the cantilever geometry the sacrificial layer which is under the patterned structures is undercut in  $0.1\% HNO_3$ , the etching time varies between 2 and 6 minutes and depends on the size of the devices which are going to be suspended. The sample is then rinsed in distilled water, immersed in ethanol and dried using critical point drying to avoid the breakage of the structure due to stiction [68] (see sec. 3.4). A schematic of the final structure is shown in fig. 1.7b.

The milling of the cantilever structure proceeds all the way to the  $SrTiO_3$  substrate in order to obtain a well defined cantilever geometry. Fig. 4.5a shows a  $BaTiO_3/SrTiO_3$ ,  $300\text{ }\mu\text{m}$  long,  $20\text{ }\mu\text{m}$  wide u-shape cantilever, the  $BaTiO_3$  is  $120\text{ nm}$  thick and the  $SrTiO_3$  is  $500\text{ nm}$  thick. The bilayer has been grown on a  $400\text{ nm } YBa_2Cu_3O_7$  sacrificial layer, the device belongs to the sample labeled as  $GV08(P)$ . The  $YBa_2Cu_3O_7$  layer in this case has been removed by wet etching only the ion milling is stopped when the sacrificial layer is reached. This produced a much less well defined cantilever compared to the case where wet etching plus argon ion beam milling was used fig. 4.5b. The device of fig. 4.5b is a  $SrRuO_3/BaTiO_3/SrRuO_3$ ,  $234\text{ }\mu\text{m}$  long,  $20\text{ }\mu\text{m}$

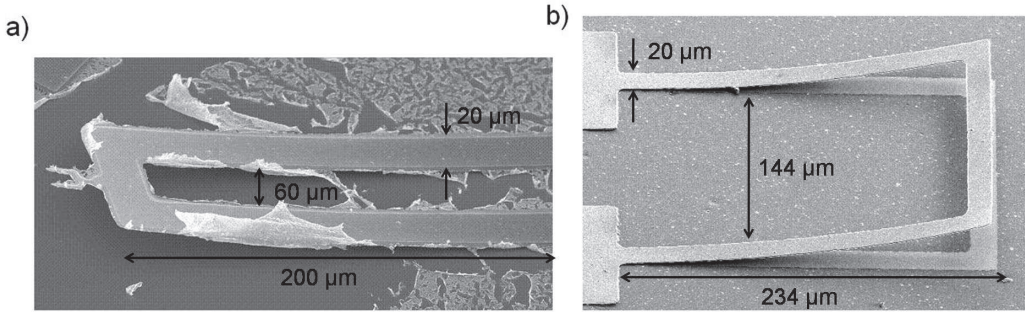


Figure 4.5: a)  $BaTiO_3$  (120 nm)/ $SrTiO_3$  (500 nm), 300  $\mu m$  long u-shape cantilever grown on 400 nm  $YBa_2Cu_3O_7$ , the device belongs to the sample labeled as  $GV08(P)$ . The  $YBa_2Cu_3O_7$  layer in this case was removed by wet etching, rather than ion-beam milling, which has produced a much less well defined cantilever compared with ion milling. b)  $SrRuO_3$  (50 nm)/ $BaTiO_3$  (100 nm)/ $SrRuO_3$  (350 nm), 234  $\mu m$  long, 20  $\mu m$  wide u-shape cantilever grown on 400 nm  $YBa_2Cu_3O_7$ , the device belongs to the sample labeled as  $GV21(P)$ . In this case the sacrificial layer is removed by argon ion beam milling and wet etching resulting in a well defined structure.

wide u-shape cantilever grown on 400 nm  $YBa_2Cu_3O_7$ , the device belongs to the sample labeled as  $GV21(P)$ .

As already stated in sec. 2.3 the fabrication process allows the deposition of a second piezoelectric film on the top of the second  $SrRuO_3$  layer followed by the deposition of a third  $SrRuO_3$  electrode. This in theory would allow one to harvest twice the power generated with a device containing only a single piezoelectric film. The higher the number of piezoelectric layer in the stack the higher the generated power. However with increasing number of piezoelectric films and electrode layers the thickness of the cantilever is increased and so also its resonant frequency sec. 2.3, furthermore the challenge in this stackable approach is represented by the quality of the piezoelectric

film, in fact as will be discussed in sec. 7.2 the  $BaTiO_3$  is more lossy when the thickness of the underlying layers is increased or other layers are added underneath the  $BaTiO_3$  film.

In sec. 2.1 it has been stated that the output power of suspended cantilevers, used as energy harvesting devices, can be increased with the integration of a seismic mass on the cantilever free end. If a seismic mass has to be included on the free end of the cantilever, another layer has to be grown after the deposition of the top electrode, the mask to use for the definition of the mass geometry is shown in fig. 4.3c.

### 4.3 Fabrication process for the 33 mode cantilevers

The top-down layer sequence which has been used for the fabrication of the 33 mode cantilevers is:  $SrRuO_3/BaTiO_3/MgO/SrTiO_3/YBa_2Cu_3O_7$ . The  $SrRuO_3$  works as electrode and can also be replaced with a gold film, the  $BaTiO_3$  is the piezoelectric layer, the  $MgO$  is used to orientate the polar axis of the  $BaTiO_3$  parallel to the surface of the film, the  $SrTiO_3$  is a buffer layer used to improve the  $MgO/YBa_2Cu_3O_7$  interface and the  $YBa_2Cu_3O_7$  is again used as sacrificial layer.

The first step in the fabrication of the 33 mode structures is the deposition of the  $MgO/SrTiO_3/YBa_2Cu_3O_7$  three-layer, the pre-ablation and the target cleaning procedures are equal to those ones described in sec. 4.2 and are not repeated here, also in this case the multilayer is grown on a (001)

oriented  $SrTiO_3$  substrate.

The substrate is heated in vacuum up to a temperature of  $740^\circ C$  at a rate of  $35^\circ C/min$ . At this temperature a  $400\text{ nm}$  or  $500\text{ nm}$  thick  $YBa_2Cu_3O_7$  sacrificial layer is grown in oxygen flow and at a pressure of  $20\text{ Pa}$ . The ablation parameters are reported in table 4.1. Then follows a 30 minutes annealing step at the  $YBa_2Cu_3O_7$  growing conditions to thermally stabilize the species on the surface of the sacrificial layer, then the  $SrTiO_3$  and the  $MgO$  films are grown, their ablation parameters are reported in table 4.1. Buffer layers with thicknesses ranging from  $50\text{ nm}$  to  $1\text{ }\mu m$  have been fabricated, the thickness of the grown  $MgO$  film is around  $25\text{ nm}$ . The tri-layer is cooled in  $90 \cdot 10^3\text{ Pa } O_2$  static environment, with dwells of 15 minutes at  $600^\circ C$  and of 30 minutes at  $450^\circ C$  during cooling to fully oxygenate the  $YBa_2Cu_3O_7$  sacrificial layer [10].

As previously stated, the  $SrTiO_3$  film functions as a buffer layer, and is introduced in the stack to improve the interface quality between the  $YBa_2Cu_3O_7$  and the  $MgO$  film. Fig. 4.6 shows secondary ion mass spectroscopy (SIMS) data during the milling of two samples, one with the  $SrTiO_3$  buffer layer and one without. The  $SrTiO_3/YBa_2Cu_3O_7$  interface, fig. 4.6b, is better defined than the  $MgO/YBa_2Cu_3O_7$  interface, fig. 4.6a, with a sharp transition between layers evidenced by the SIMS signal. Wu et al. [69] studied the atomic configurations of  $YBa_2Cu_3O_7/MgO$  interfaces, they reported that diffusion induced interstitial or substitutional  $Mg$  atoms in the first  $YBa_2Cu_3O_7$  layers. This phenomenon is mainly observed in films grown by liquid phase epitaxy, however it can also occurs in thin films prepared by pulse laser deposition.

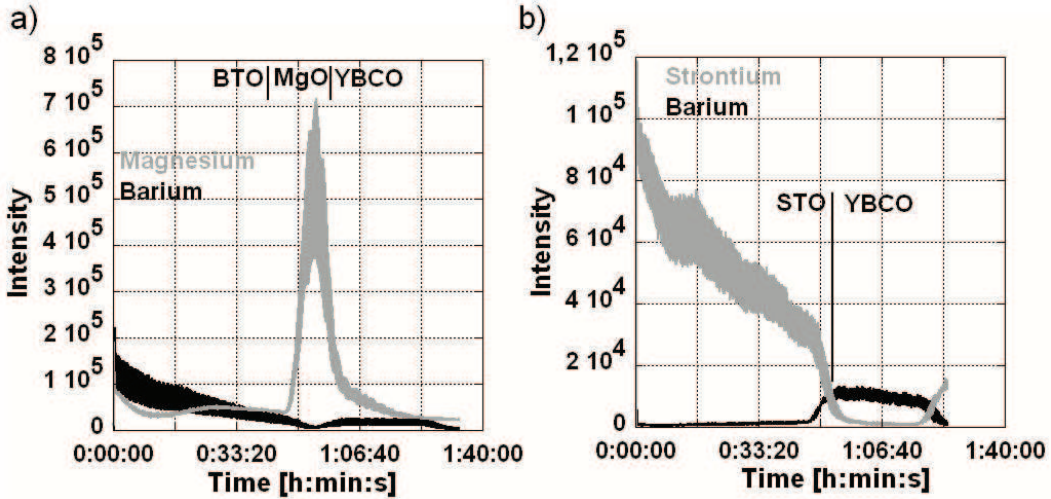


Figure 4.6: Secondary Ion beam spectroscopy of a milling step: a)  $BaTiO_3$  (500 nm)/ $MgO$  (70 nm)/ $YBa_2Cu_3O_7$  (400 nm) tri-layer, sample labeled as  $GV17(P)$  and b)  $SrTiO_3$  (500 nm)/ $YBa_2Cu_3O_7$  (400 nm) bilayer

Without a well defined interface, it was difficult to undercut the  $YBa_2Cu_3O_7$  and suspend the structure. Tab. 4.2 reports the number of suspended devices for the 33 and 31 mode layer sequences, the stacks containing the  $SrTiO_3$  buffer layer show an higher number of suspended devices.

After the first deposition step, the sample is prepared for the deposition of a second three-layer having as top-down layer sequence:

$SrRuO_3/BaTiO_3/MgO$ . The ablation of all the films belonging to the 33 mode stack is not performed in one go as our deposition systems allows the deposition of only three different material in situ. During the deposition of the second three-layer another thin  $MgO$  layer is deposited on the existing  $MgO$  film, this is done to provide a fresh ablated seed layer to the  $BaTiO_3$  film.

<i>Sample name</i>	<i>Layer sequence</i>	<i>Piezoelectric mode</i>	<i>Total number of devices</i>	<i>Number of suspended devices</i>
<i>GV10(P)</i>	<i>BaTiO<sub>3</sub>(100 nm)/MgO(60 nm)/SrTiO<sub>3</sub>(500 nm)/YBa<sub>2</sub>Cu<sub>3</sub>O<sub>7</sub>(400 nm)</i>	33	30	28
<i>GV16(P)</i>	<i>BaTiO<sub>3</sub>(100 nm)/MgO(60 nm)/YBa<sub>2</sub>Cu<sub>3</sub>O<sub>7</sub>(400 nm)</i>	33	30	1
<i>GV21(P)</i>	<i>SrRuO<sub>3</sub>(50 nm)/BaTiO<sub>3</sub>(100 nm)/SrRuO<sub>3</sub>(350 nm)/YBa<sub>2</sub>Cu<sub>3</sub>O<sub>7</sub>(400 nm)</i>	31	30	23
<i>GV22(P)</i>	<i>SrRuO<sub>3</sub>(100 nm)/BaTiO<sub>3</sub>(200 nm)/SrRuO<sub>3</sub>(100 nm)/SrTiO<sub>3</sub>(100 nm)/YBa<sub>2</sub>Cu<sub>3</sub>O<sub>7</sub>(400 nm)</i>	31	30	29

Table 4.2: Number of suspended structures for two stacks containing the *SrTiO<sub>3</sub>* buffer layer and two without.

The ablation preparation and the target cleaning are performed as described in sec. 4.2 then the sample is heated to 740°C, as shown in fig. 4.4 and at this temperature the 30 minutes *YBa<sub>2</sub>Cu<sub>3</sub>O<sub>7</sub>* annealing step is repeated. The sample is then heated to 780°C where a 25 nm *MgO* seed layer, a 200 – 400 nm *BaTiO<sub>3</sub>* piezoelectric film and a 100 nm *SrRuO<sub>3</sub>* top electrode layer are grown. Again, after the deposition of the top electrode, the chamber is filled with oxygen up to a pressure of  $90 \cdot 10^3$  Pa and the sample is then cooled in  $90 \cdot 10^3$  Pa *O<sub>2</sub>* static environment with dwells of 15 minutes at 600°C and of 30 minutes at 450°C.

The sample is then detached from the heater and cleaned as described in sec. 4.2, it is then brought to the clean room facilities for the patterning of the top electrode. The sample is first processed as described in the previous section, after the UV exposure through the edge mask, it is exposed to the UV light through the top electrode mask, fig. 4.7, for 10 seconds and it is then

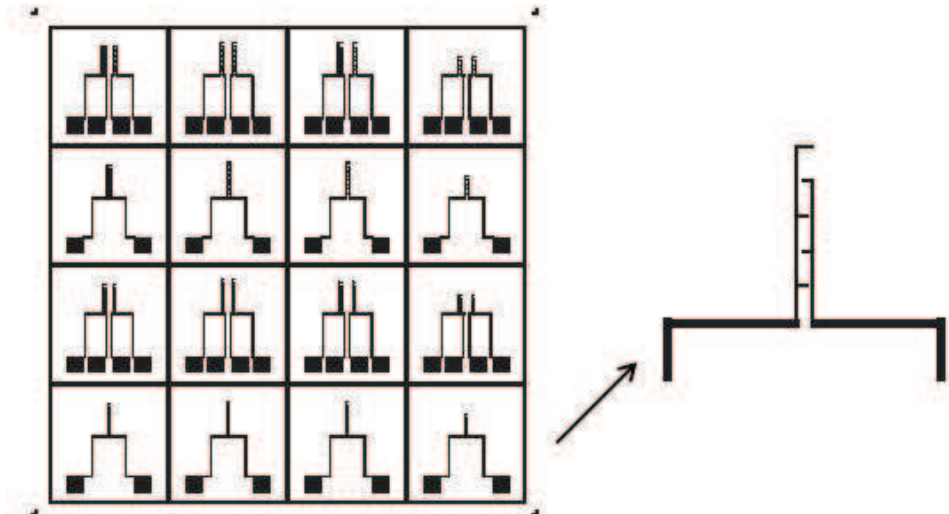


Figure 4.7: Top electrode mask used for the 33 mode piezoelectric devices.

milled at  $45^\circ$  under rotation. Then follows the patterning of the cantilever and of the anchor structures which is done with a further photolithography and milling step in the way which has been described in the previous section.

The cantilevers have been released by undercutting the sacrificial layer in 0.1%  $HNO_3$ , the etching time varies between 2 and 6 minutes. The sample is then rinsed in distilled water and dried by using critical point drying to avoid stiction problems. Like the  $YBa_2Cu_3O_7$ , the  $MgO$  can be etched in  $HNO_3$  [70], however due to the low acid concentration and to the relatively short etching time no undercut is observed in the  $MgO$  layer in this case.

Fig. 1.7a shows the schematic of the structure obtained with this fabrication process. A thickness of 50 nm for the buffer and for the seed layer is enough to allow to these films the performing of their tasks, however the

thicknesses of these layers can be varied to fit the required specification like the value of the resonant frequency and so on.

For the integration of the seismic mass into the structure a further layer has to be grown and patterned after the deposition of the top electrode.

Also in this case a further piezoelectric and electrode layers can be grown on the top of the existing structure, again the advantage is that one to increase the harvested energy however the disadvantages of a thicker cantilever like lossy  $BaTiO_3$  layers (see sec. 7.2) could be present.

#### 4.4 $MgO$ as sacrificial layer

Impedance measurements on the fabricated capacitors revealed the presence of resistive losses in the  $BaTiO_3$  film grown in stacks containing  $YBa_2Cu_3O_7$  sacrificial layers, a detailed discussion on these aspects is postponed to chap. 7. This led to the choice of  $MgO$  as sacrificial layer, with its introduction in the stack a reduction of the resistive losses in the piezoelectric film is measured, sec. 7.2.

One of the advantages into the use of the  $MgO$  sacrificial layer is the reduction in the number of layers necessary for the fabrication of the 33 mode stack which becomes  $SrRuO_3/BaTiO_3/MgO$  (top-down layer sequence). This tri-layer can be grown in one go with our deposition system.

The top-down layer sequence for 31 mode multilayer using  $MgO$  sacrificial layer is:  $SrRuO_3/BaTiO_3/SrRuO_3/SrTiO_3/MgO$ . The  $SrTiO_3$  buffer layer is maintained into the layer sequence because after the patterning of the  $SrRuO_3$  bottom electrode some regions of the sample have  $SrRuO_3$  on

their top, on other areas  $MgO$  is present. As will be discussed in sec. 5.1 the  $BaTiO_3$  grows with the polar axis perpendicular to the surface of the film on  $SrRuO_3$  and on  $SrTiO_3$  while it grows with the polar axis parallel to the surface of the film on  $MgO$ . The use of the  $SrTiO_3$  layer allows the growth of  $BaTiO_3$  with the polar axis out of plane all over the sample after the patterning and the milling of the  $SrRuO_3$  bottom electrode.

There are two main disadvantages related to the use of the  $MgO$  sacrificial layer, the first is that higher  $HNO_3$  concentrations are necessary for the undercut of the sacrificial layer, the second is the long etching time associated with the  $MgO$  undercut.

The etching of the  $MgO$  sacrificial layer has been performed in a solution of 20%  $HNO_3$  for 8 hours. In order to increase the  $MgO$  etch rate the solution has been kept in motion with the use of a magnetic stirrer. After 8 hours in 20%  $HNO_3$  only the simple beam cantilevers were released, to suspend the larger u-shape cantilever an even longer etching time is necessary.

Due to the higher acid concentration and to the long etching time some damage is visible in the  $SrRuO_3$  top layer. This problem can be easily solved by leaving the resist layer on the top of the fabricated structures after the patterning of the cantilever and its anchor. The photoresist protects the top layer during the  $MgO$  undercut when the structures are released, then the sample is rinsed in acetone to remove the resist from the top of the cantilevers. Finally the sample is rinsed in water immersed in ethanol and critical point dried.

## 4.5 Summary

In this chapter the fabrication processes used for the 31 and 33 modes cantilevers have been described. It is possible to use  $YBa_2Cu_3O_7$  or  $MgO$  as sacrificial layers, the  $YBa_2Cu_3O_7$  is easy to etch in weak acid solutions like 0.1%  $HNO_3$ , in this case, the etching time necessary to suspend a cantilever of area  $200\ \mu m \times 30\ \mu m$  varies between 6 and 8 minutes. When the  $MgO$  is used as sacrificial layer stronger acid solutions like 20%  $HNO_3$  are necessary. In this case to suspend a beam with an area of  $200\ \mu m \times 30\ \mu m$  8 hours are requested.

To obtain a well defined geometry the sacrificial layer is removed by a combination of argon ion beam milling and wet etching, if only wet etching is used a much less well defined cantilever is produced.

The stacks used to produce 31 mode structures are:

$SrRuO_3/BaTiO_3/SrRuO_3/YBa_2Cu_3O_7$  and

$SrRuO_3/BaTiO_3/SrRuO_3/SrTiO_3/YBa_2Cu_3O_7$ ; the multilayer used for the 33 mode devices is  $SrRuO_3/BaTiO_3/MgO/SrTiO_3/YBa_2Cu_3O_7$ .

The  $BaTiO_3$  is the piezoelectric film, the  $SrRuO_3$  works as electrode, the  $MgO$  is used in the 33 mode cantilevers to change the growing orientation of the  $BaTiO_3$ , the  $SrTiO_3$  is used as buffer layer and the  $YBa_2Cu_3O_7$  is the sacrificial layer.

At the beginning the suspended structures have been release by undercutting a  $YBa_2Cu_3O_7$  sacrificial layer. The presence of resistive losses in the  $BaTiO_3$  film, (see chap. 7) led to the introduction of a  $MgO$  sacrificial layer. This simplifies the 33 mode layer sequence which becomes:

$SrRuO_3/BaTiO_3/MgO$  and such three-layer can be deposited in situ. The 31 mode multilayer, with the introduction of the  $MgO$  sacrificial layer, present the same number of thin films, its top-down layer sequence is:

$SrRuO_3/BaTiO_3/SrRuO_3/SrTiO_3/MgO$ .

# Chapter 5

## Characterization of the multi-layers

This chapter is about the characterization of the 33 and 31 mode multi-layers, in particular X-ray diffraction investigations and nanoindentation measurements are discussed and analysed. In section 5.1 X-ray diffraction measurements performed on different multilayer combinations which fit the 31 and the 33 piezoelectric modes are presented. Particular emphasis is placed on the growing orientation of  $BaTiO_3$  on  $SrTiO_3$ ,  $SrRuO_3$  and  $MgO$ , furthermore a discussion on the critical thickness of each layer employed in the multi-layer is reported. Section 5.2 presents the results of the nano-indentation measurements performed on the multi-layers used for the X-ray diffraction characterization.

## 5.1 X-ray diffraction analysis

X-ray diffraction has been used to evaluate the crystal structures and the lattice parameters of the grown films, the employed setup and the experimental methods have been described in sec. 3.2.

The measured data have been processed with the unit cell refinement software called Lapod [71], this software allows the calculation of the lattice parameters of the deposited films from the  $2\theta$  values corresponding to the positions of several diffracted peaks. The lattice parameters have been calculated considering the second, third and fourth order reflections of different diffractions planes. To validate the software results some lattice parameters have been hand calculated by considering only the second orders reflections, the obtained values agreed well with the software results.

X-ray diffraction analysis has been performed on  $BaTiO_3$ ,  $MgO$  and  $SrRuO_3$ . X-ray scans have not been run on the  $SrTiO_3$  films because all the multi-layers have been grown on  $SrTiO_3$  substrates, which means that it is not possible to distinguish between the diffraction peaks of the film and of the substrate because they overlap. During the investigations, peaks associated with the  $YBa_2Cu_3O_7$  (002) planes have been measured, however an accurate investigation on the  $YBa_2Cu_3O_7$  films has not been possible as the X-ray source of our diffractometer stopped working.

Table 5.1 reports the lattice parameters of the  $BaTiO_3$ ,  $MgO$  and  $SrRuO_3$  films in different multilayer sequences. The  $MgO$  film is (001) oriented when it is grown on both the  $SrTiO_3$  substrate and on the  $YBa_2Cu_3O_7$  sacrificial layer, also the  $SrRuO_3$  electrode layer is (001) oriented when grown on

Sample label	Material [Top-down layer sequence]	In plane a axis measured [ $\text{\AA}$ ] (bulk [ $\text{\AA}$ ])	In plane b axis measured [ $\text{\AA}$ ] (bulk [ $\text{\AA}$ ])	Out of plane c axis measured [ $\text{\AA}$ ] (bulk [ $\text{\AA}$ ])
<i>GV03(P)</i>	<b>BaTiO<sub>3</sub></b> [BaTiO <sub>3</sub> (126 nm)/SrTiO <sub>3</sub> (500 nm)/ YBa <sub>2</sub> Cu <sub>3</sub> O <sub>7</sub> (400 nm)]	<b>3.996 ± 0.006</b> (3.992)	<b>3.996 ± 0.006</b> (3.992)	<b>4.015 ± 0.003</b> (4.036)
<i>GV16(P)</i>	<b>BaTiO<sub>3</sub></b> [BaTiO <sub>3</sub> (100 nm)/MgO (60 nm)/ YBa <sub>2</sub> Cu <sub>3</sub> O <sub>7</sub> (400 nm)]	<b>4.002 ± 0.003</b> (3.992)	<b>4.002 ± 0.003</b> (3.992)	<b>3.997 ± 0.002</b> (4.036)
<i>GV10(P)</i>	<b>BaTiO<sub>3</sub></b> [BaTiO <sub>3</sub> (100 nm)/MgO (60 nm)/ SrTiO <sub>3</sub> (500 nm)/YBa <sub>2</sub> Cu <sub>3</sub> O <sub>7</sub> (400 nm)]	<b>4.028 ± 0.008</b> (3.992)	<b>4.028 ± 0.008</b> (3.992)	<b>3.985 ± 0.010</b> (4.036)
<i>GV21(P)</i>	<b>BaTiO<sub>3</sub></b> [SrRuO <sub>3</sub> (50 nm)/BaTiO <sub>3</sub> (100 nm)/ SrRuO <sub>3</sub> (350 nm)/YBa <sub>2</sub> Cu <sub>3</sub> O <sub>7</sub> (400 nm)]	<b>3.951 ± 0.002</b> (3.992)	<b>3.951 ± 0.002</b> (3.992)	<b>4.069 ± 0.002</b> (4.036)
<i>GV09(P)</i>	<b>MgO</b> [MgO (80 nm)]	4.220 ± 0.005 (4.211)	4.220 ± 0.005 (4.211)	4.220 ± 0.005 (4.211)
<i>GV15(P)</i>	<b>MgO</b> [MgO (150 nm)/YBa <sub>2</sub> Cu <sub>3</sub> O <sub>7</sub> (150 nm)]	4.211 ± 0.004 (4.211)	4.211 ± 0.004 (4.211)	4.211 ± 0.004 (4.211)
<i>GV14(P)</i>	<b>SrRuO<sub>3</sub></b> [SrRuO <sub>3</sub> (500 nm)/YBa <sub>2</sub> Cu <sub>3</sub> O <sub>7</sub> (400 nm)]	5.529 ± 0.06 (5.567)	5.519 ± 0.06 (5.530)	7.825 ± 0.06 (7.845)

Table 5.1: Lattice parameters of the BaTiO<sub>3</sub>, MgO and SrRuO<sub>3</sub> in different multi-layer sequences.

YBa<sub>2</sub>Cu<sub>3</sub>O<sub>7</sub>.

The measured lattice parameters of the MgO and SrRuO<sub>3</sub> films are very close to bulk values. The theory predicts that any epitaxial layer having a lattice parameter mismatch  $f$  with the substrate of less than 9% would grow elastically strained to the same interatomic spacing of the substrate up to some critical thickness  $d_c$ . Beyond  $d_c$  misfit dislocations are introduced, the misfit strain is released and the initially strained film relaxes [72, 73].

In a thin film multi-layer the lattice mismatch or lattice misfit of the layer  $n$  grown on the layer  $n - 1$  is defined as:

$$f = \frac{a_{n-1} - a_n}{a_n} \quad (5.1)$$

where  $a_n$  and  $a_{n-1}$  are the unstrained lattice parameters of the layers  $n$  and

$n - 1$ , for the grown films the unstrained lattice parameters are reported in table 1.1. The expression of the critical film thickness  $d_c$  is:

$$d_c = \frac{b}{8\pi(1+\nu)f} \ln \left( \frac{d_c}{b} + 1 \right) \quad (5.2)$$

where  $\nu$  is the Poisson's ratio,  $b$  is the dislocation Burgers vector and  $f$  is the lattice misfit of the film [72]. To calculate the value of the critical thickness  $d_c$  of each film present in the analysed stacks rather than the modulus of the Burgers vector, to first approximation it is possible to consider the spacing between the (001) planes of the different crystal structures. The values of the Poisson's ratios for the deposited films are reported in table 5.2, they have been taken from published results [25, 74, 75, 76, 77].

When the  $MgO$  is grown on orthorhombic  $YBa_2Cu_3O_7$  the misfit between the unstrained  $MgO$  lattice parameter and the  $a$  axis of the  $YBa_2Cu_3O_7$  is equal to 9.3% while the misfit between the  $MgO$  lattice constant and the  $YBa_2Cu_3O_7$   $b$  axis is equal to 7.86%. In both cases the calculated critical thickness is smaller than  $1 \text{ \AA}$ , in agreement with the relaxed lattice parameters which have been measured.

Also in the case of  $MgO$  films grown on (001) oriented  $SrTiO_3$  substrates an unstrained lattice parameter has been measured, the lattice misfit of the  $MgO/SrTiO_3$  system is equal to 7.3%, this results in a critical thickness equal to zero which is consistent with measurements. The growth of epitaxial  $MgO$  on (001) oriented  $SrTiO_3$  substrates has been studied by Chern [78], he used molecular beam epitaxy to prepare his  $MgO$  films. Also in that case (001) oriented  $MgO$  films have been observed, with a relaxation along the

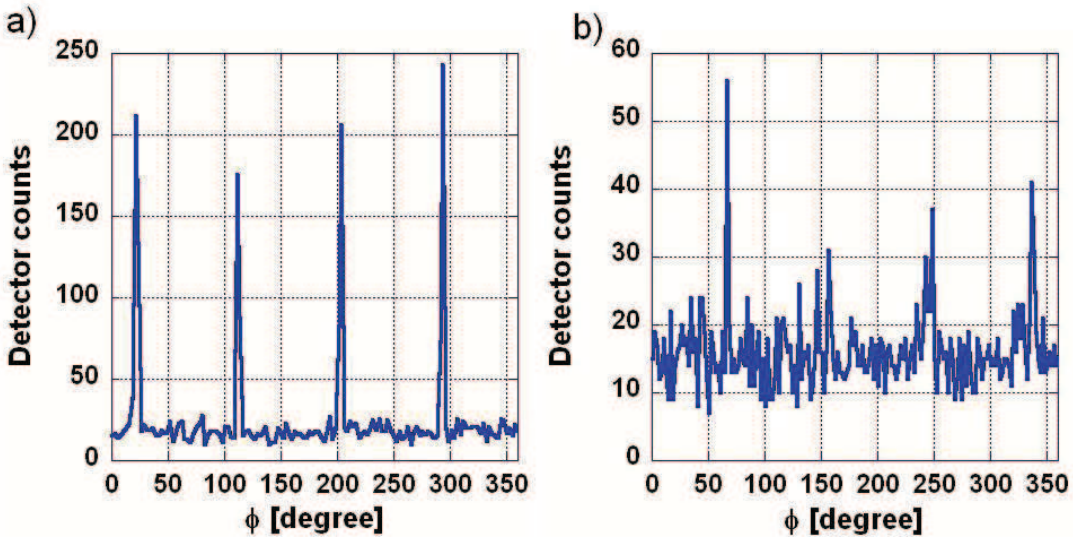


Figure 5.1:  $\phi$  scan around the  $(-202)$  plane of the  $SrRuO_3$  lattice, for the sample labeled  $GV14(P)$  when a) an orthorhombic crystal structure is assumed (the heights of the peaks are not equal because of the non perfect alignment) b) a pseudocubic crystal structure with lattice constant  $a = 3.93 \text{ \AA}$  is assumed.

out of plane direction.

$SrRuO_3$  films have been grown on the top of the  $YBa_2Cu_3O_7$  sacrificial layers,  $SrRuO_3$  has an orthorhombic unit cell, however it can be treated as a pseudocubic perovskite structure having a lattice constant  $a = 3.93 \text{ \AA}$  [25] this has been confirmed by the X-ray diffraction investigations on these films.

Fig. 5.1a shows a  $\phi$  scan around the  $(-202)$  plane of the  $SrRuO_3$  film when the orthorhombic structure is assumed, the diffraction peaks are sharp and this is an indication of a good crystal structure, a broadening of the diffraction peaks is in fact related to the presence of imperfections in the lattice [47]. Fig. 5.1b shows a  $\phi$  scan around the  $(-202)$  lattice plane of the

$SrRuO_3$  when the pseudocubic cristal structure is assumed, the diffraction peaks have lower intensity and are broader than the previous measurement. This happens because the software controlling the diffractometer assumes a cubic structure for the  $SrRuO_3$  and it looks for peaks at values of  $\vartheta$  which do not correspond to those having the maximum intensity. In fact the pseudocubic lattice, approximates the  $SrRuO_3$  crystal structure, however the real structure of the film is orthorhombic, so the diffracted peaks have their maximum intensity at diffracted angles  $\vartheta$  which slightly differ from those ones of a cubic lattice. The pseudocubic lattice with a lattice constant  $a = 3.93 \text{ \AA}$  is assumed for the  $SrRuO_3$  film, this simplifies the calculation of the lattice misfit and of the critical thickness. The  $\phi$  angles at which the diffracted peaks are found are not equal for the two scans of fig. 5.1 as a different  $\phi = 0$  has been chosen in the two cases.

As in the case of the  $MgO$  layers, also the grown  $SrRuO_3$  films show lattice constants near to the bulk values given in table 5.1, calculations of the  $SrRuO_3$  critical thickness on the  $YBa_2Cu_3O_7$  sacrificial layer return a value slightly smaller than  $1 \text{ \AA}$ , so no strain is observed for the measured lattice parameters. The difference between measurements and bulk values in the  $a$  and  $b$  lattice parameter of the  $SrRuO_3$  is attributed to the instrument error and to imperfections in the crystal structure of the film.

X-ray analysis on the  $BaTiO_3$  films reveals that  $BaTiO_3$  grows (001) oriented which means with the polar axis perpendicular to the surface of the film on  $SrTiO_3$  and on  $SrRuO_3$ , table 5.1 and fig. 5.2a-b, while it grows with the polar axis parallel to the surface of the film on  $MgO$ , table 5.1 and fig. 5.2c-d. The (002) reflection of sample  $GV03(P)$  corresponds to a  $BaTiO_3$  c

axis having a length of  $4.015\text{ \AA}$  while the (002) reflection of sample  $GV21(P)$  corresponds to a  $c$  axis with a length of  $4.069\text{ \AA}$ , so in this cases the  $c$  axis is associated with the polar axis. The (002) reflections of samples  $GV16(P)$  and  $GV10(P)$  correspond to a  $c$  axis with a length of  $3.997\text{ \AA}$  and  $3.985\text{ \AA}$  respectively, here the  $c$  axis does not correspond to the  $BaTiO_3$  polar axis.

When the polar axis is perpendicular to the plane of the film, the polarization can be easily accessed by a parallel plate capacitor fig. 1.7b, so  $BaTiO_3$  grown on  $SrRuO_3$  can be used to produce 31 mode cantilevers. When the polar axis is parallel to the surface of the film, the polarization can be accessed by using an interdigitated capacitor fig. 1.7a, so an  $MgO$  film is introduced as seed layer to orientate the  $BaTiO_3$  in a way that fits the 33 piezoelectric mode.

As previously stated when the  $BaTiO_3$  is grown on  $SrTiO_3$  the polar axis is equal to  $4.015\text{ \AA}$ , this is smaller than the value reported in bulk materials. Kim et al. [79] reported that in  $SrTiO_3/BaTiO_3$  superlattices the  $c$  axis lattice parameter decreases from  $4.12\text{ \AA}$  to  $4.06\text{ \AA}$  when the oxygen pressure during the deposition is increased from  $1.33 \cdot 10^{-3}\text{ Pa}$  to  $0.133\text{ Pa}$ . The  $BaTiO_3$  of the investigated sample has been grown at an oxygen pressure of  $20\text{ Pa}$  so this can explain the shorter value measured. A deeper investigation on this aspect could not be possible because of the problems which occurred with the X-ray diffraction equipment, however the two layer sequences proposed for the fabrication of microcantilevers do not have  $BaTiO_3$  layers grown directly on  $SrTiO_3$  films.

The in plane lattice parameters of  $BaTiO_3$  films grown on  $SrTiO_3$  layers have a value similar to that one reported for bulk materials.

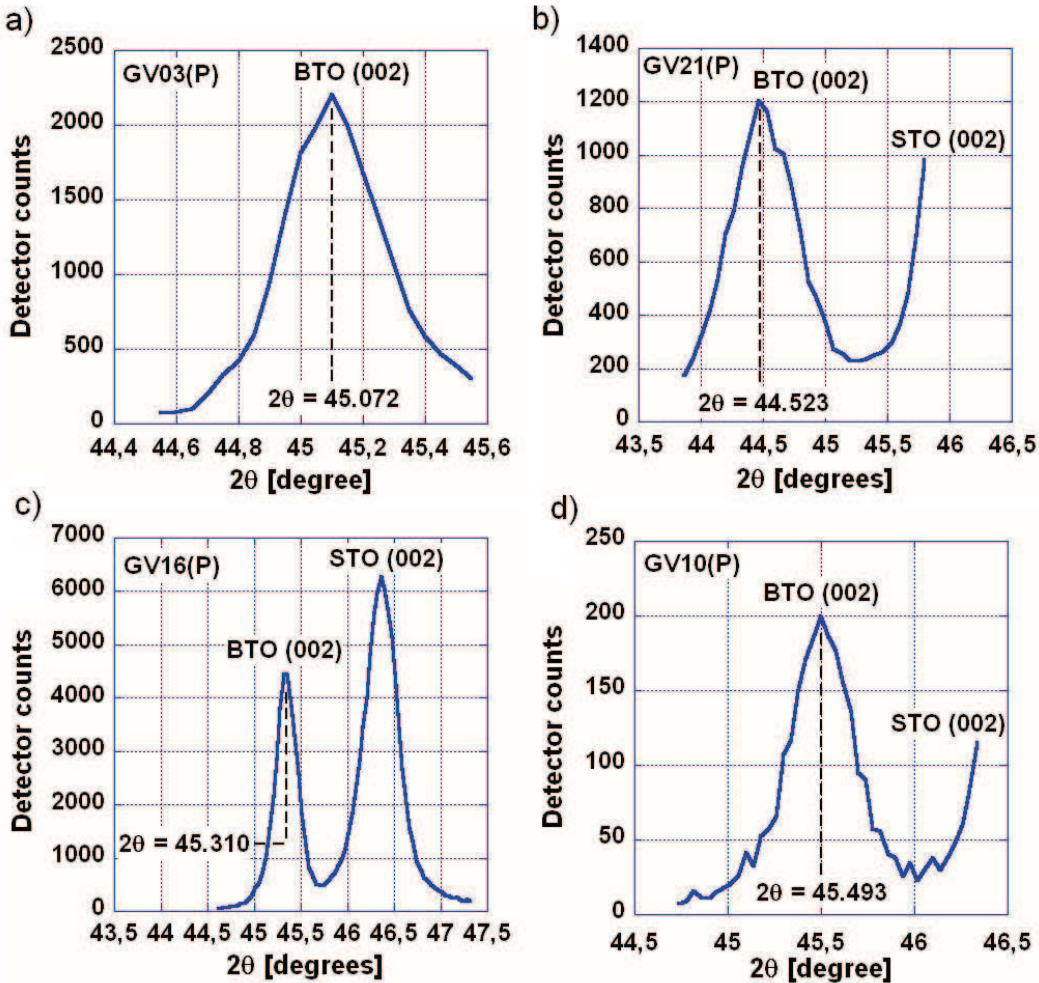


Figure 5.2:  $BaTiO_3 \vartheta - 2\vartheta$  scan of the (002) plane for: a)  $BaTiO_3$  (126 nm)/ $SrTiO_3$  (500 nm)/ $YBa_2Cu_3O_7$  (400 nm) sample labeled  $GV03(P)$ ; b)  $SrRuO_3$  (50 nm)/ $BaTiO_3$  (100 nm)/ $SrRuO_3$  (350 nm)/ $YBa_2Cu_3O_7$  (400 nm) sample labeled  $GV21(P)$ ; c)  $BaTiO_3$  (500 nm)/ $MgO$  (60 nm)/ $YBa_2Cu_3O_7$  (400 nm) sample labeled  $GV16(P)$ ; d)  $BaTiO_3$  (500 nm)/ $MgO$  (60 nm)/ $SrTiO_3$  (500 nm)/ $YBa_2Cu_3O_7$  (400 nm) sample labeled  $GV10(P)$ .

Calculations of the critical thickness for  $BaTiO_3$  films grown on  $SrTiO_3$  layers return a value around  $2.5 \text{ \AA}$ , this is smaller than the  $BaTiO_3$  lattice

parameters, so a relaxed  $BaTiO_3$  layer is expected to grow on  $SrTiO_3$ . This is consistent with observations.

$BaTiO_3$  grown on  $SrRuO_3$  also has a polar axis perpendicular to the surface of the film, here an elongation of the polar axis equal to 0.83% respect to bulk materials is observed. This is highlighted by a shift of  $-0.5^\circ$  for the diffraction peak of the  $BaTiO_3$  relative to the (002) plane respect to the same peak on  $SrTiO_3$ , fig. 5.2b. The measured polar axis is equal to  $4.069 \text{ \AA}$ , table 5.1, this value is in excellent agreement with that one reported by Choi et. al [22]. The elongation of the polar axis is attributed to the in plane biaxial stress experienced by the  $BaTiO_3$  layer. Calculations of the critical thickness for the  $BaTiO_3/SrRuO_3$  system gives a value equal to  $9 \text{ nm}$  this suggests that the first layers of the  $BaTiO_3$  grow elastically strained and the in plane biaxial stress produces an elongation of the polar axis, this is in agreement with observations. The in plane lattice constants as consequence of the biaxial stress have a value equal to  $3.951 \text{ \AA}$ , table 5.1.

The measured polar lattice parameter represents an average value over the film thickness, in fact after the first  $9 \text{ nm}$  the thin film relaxes as consequence of the introduction of dislocations and the  $BaTiO_3$  lattice constants assumes the bulk values. Choi et. all [22] have grown a  $200 \text{ nm}$   $BaTiO_3$  layer on  $100 \text{ nm}$  thick  $SrRuO_3$  and they reported a partially relaxed  $BaTiO_3$  film. Sample  $GV21(P)$  has a  $100 \text{ nm}$  thick  $BaTiO_3$  layer sandwiched between two  $SrRuO_3$  electrodes, in the residual stress analysis which is developed in chap. 6 a relaxation of the  $100 \text{ nm}$  piezoelectric film after the first  $10 \text{ nm}$  has been assumed, such assumption led to an agreement between theory and measurements for the residual stresses in suspended cantilevers. It is

important to point out that eq. 5.2 represents an approximation [72] so critical thicknesses larger than those ones suggested by the theory could be present in the grown films. However the fact that an elongation of the polar axis measured when the theoretical critical thickness has a finite value and the agreement between theory and results in the residual stress analysis, see chap. 6, suggests the correctness of this treatment. Furthermore Choi et. al [22] claimed an increase of the remanent polarization for  $BaTiO_3$  on  $SrRuO_3$  as consequence of the stress induced in the film, this has not been measured in the fabricated ferroelectric capacitors (see sec. 7.3) and confirms the relaxation of the piezoelectric films after few nanometers.

Thin film stacks where the  $BaTiO_3$  thin films have been grown on an  $MgO$  layer are present in the samples  $GV10(P)$  and  $GV16(P)$ , in both cases the polar axis lies parallel to the plane of the film, table 5.1. This is confirmed by the  $\vartheta - 2\vartheta$  scans relative to the (002) plane of  $BaTiO_3$  films fig. 5.2c-d. The smaller lattice mismatch between the  $c$  axis of  $BaTiO_3$  and the  $MgO$  lattice parameter is the reason for such orientation [66, 67].

According to eq. 5.2 the critical thickness of  $BaTiO_3$  on  $MgO$  is negligible so unstrained lattice parameters should be measured in the plane of the film. Despite that the measured polar lattice parameter appears smaller than the bulk value, this happens because the measurements provide an average value, in fact there are two possible orthogonal orientations when the polar axis is in the plane of the substrate and a non polar axis must also lie in plane.

The measured in plane lattice parameters are not equal for the samples  $GV10(P)$  and  $GV16(P)$ , there is a difference of  $0.026 \text{ \AA}$  between the two values. A difference in the measured lattice parameters may arise by differ-

ences in the alignment of the two samples, however we think that this not the only reason for such a difference. Sample *GV10(P)* contains an  $SrTiO_3$  buffer layer between the  $MgO$  and the  $YBa_2Cu_3O_7$  sacrificial layer. As will be discussed in secs. 7.2 and D.3.2, particulates and outgrowths might be present on the surface of the  $YBa_2Cu_3O_7$  films even after the recalibration of the  $YBa_2Cu_3O_7$  ablation parameters aimed to reduce the roughness of the  $YBa_2Cu_3O_7$  top surface, see fig. D.21. These outgrowths and particulates, which are off-stoichiometric, may have heights in the orders on hundreds of nm while the  $MgO$  seed layer is only 60 nm thick, so they might reduce the quality of the seed layer and have an influence on the  $BaTiO_3$  piezoelectric layer. This is confirmed by sample *GV10(P)* where the 500 nm  $SrTiO_3$  buffer layer, introduced between the  $YBa_2Cu_3O_7$  and the  $MgO$  films, covers the outgrowths of the sacrificial layer, leading to a better seed layer and to a  $BaTiO_3$  film having a polar lattice parameter near to that one showed in bulk materials, table 5.1.

In the fabrication process described in chap. 4, the 31 mode and the 33 mode stacks are not grown in one go but the the film deposition is performed in two steps, this has also been done for the preparation of the multilayer used for the X-ray diffraction analysis. As will be discussed in chap. 7 in order to reduce the losses in the  $BaTiO_3$  layers the  $BaTiO_3$  deposition pressure has been reduce from 20 Pa to 8 Pa. Due to problems with the diffractometer no X-ray analysis has been performed on the films grown at lower pressure, however in literature an elongation of the lattice parameters for low growing pressure is reported [22], furthermore Wang et all [67] for  $BaTiO_3$  grown on  $MgO$  at a pressure of 5 Pa report a polar axis longer than the bulk value .

<i>Material</i>	<i>Thermal expansion coefficient</i> [ $10^{-6}1/K$ ]	<i>Young Modulus</i> [GPa]	<i>Poisson ratio</i>
$YBa_2Cu_3O_7$	13.4	129	0.3
$SrRuO_3$	8	190	0.3
$BaTiO_3$ (on $MgO$ or $SrRuO_3$ )	11.3	175	0.35
$BaTiO_3$ (on $SrTiO_3$ )	11.3	79	0.35
$MgO$	8	233	0.18
$SrTiO_3$	9.4	130	0.25

Table 5.2: Thermal expansion coefficient [85, 86, 87, 88, 89], Poisson's ratio [25, 74, 75, 76, 77] and Young's Modulus of the deposited films. The Young's Modulus has been measured by nanoindentation technique.

The most important information derived from the X-ray diffraction analysis is that the out of plane  $BaTiO_3$  polar axis in the  $SrRuO_3/BaTiO_3/SrRuO_3$  capacitive structure fits the 31 piezoelectric mode while the in plane  $BaTiO_3$  polar axis in the  $SrRuO_3/BaTiO_3/MgO$  layer sequence fits the 33 piezoelectric mode.

## 5.2 Nano-indentation measurements

Nano-indentations measurements have been performed on the deposited multi-layers to evaluate the Young's modulus of each film, such measurements have been run by Dr. J. Bowen [56]. As already reported in sec. 3.7 this technique allows the evaluation of the reduced modulus of the materials, the Young's modulus is then calculated according eq. 3.9.

The measurements have been performed on multi-layers deposited on  $YBa_2Cu_3O_7$  sacrificial layer in the way described in chap. 4. The values of the reduced modulus measured near the top surface of the stack or at the interface between two layers have not been used to calculate the Young's modulus of the grown films. Measurements of the reduced modulus reveal that in the first  $10\text{ nm}$  or  $15\text{ nm}$  from the top surface of the stack, or from the interface between two layers, the reduced modulus assumes values which are not constant and are not compatible with the bulk Young's modulus of the same material. After the first  $10\text{ nm}$  or  $15\text{ nm}$  the reduced modulus approaches a value compatible with the Young's modulus measured in the bulk of the same material; such a value is maintained through the thickness of the film until the next interface is reached. However if the values measured in the first  $10\text{ nm} - 15\text{ nm}$  are considered, they alter the average Young's modulus by less than 10%

Indentations were performed from the top surface down to the desired depth through the multilayer. The indenter was held at load for 60 seconds, then retracted from the sample at a rate of  $0.5\text{ nm/s}$ . Each indentation was separated by  $50\text{ }\mu\text{m}$ , to avoid any influence of the previous measurement.

The values reported in table 5.2 represent the Young's Modulus averaged over the film thickness over a minimum of 25 measurements.

Fig. 5.3 show a nanoindentation across a  $BaTiO_3$  layer around a depth of  $100\text{ nm}$  from the substrate. For this sample the average value of the Young's modulus is equal to  $163\text{ GPa}$  deviations up to 20% from the central value are present in the measurement.

Indentations measurements on  $BaTiO_3$  grown on a  $SrTiO_3$  layer have

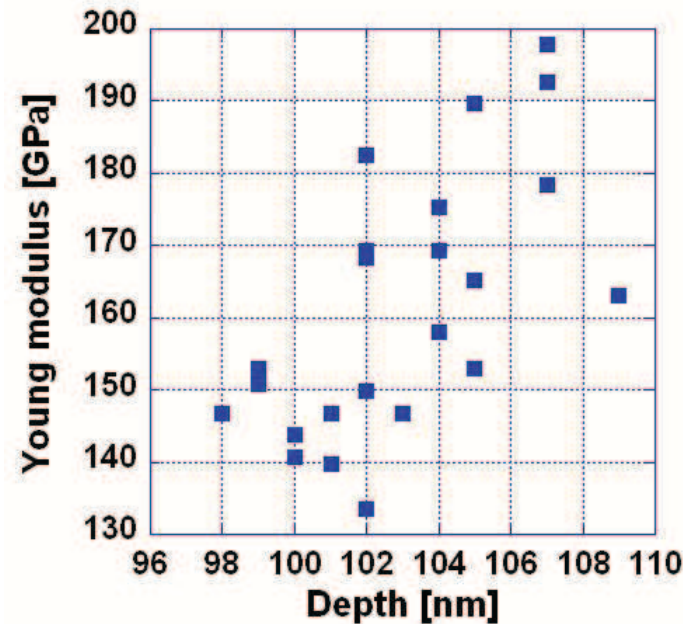


Figure 5.3: Nanoindentation scan for a  $BaTiO_3$  film belonging to the stack  $BaTiO_3(200\text{ nm})/SrRuO_3(200\text{ nm})/YBa_2Cu_3O_7(100\text{ nm})$ .

been run on the sample labeled as  $GV03(P)$ , such sample has top down layer sequence:  $BaTiO_3/SrTiO_3/YBa_2Cu_3O_7$ ; this three-layer has been grown in situ. In this sample the measured value of the Young's modulus is smaller than the value measured in the case of  $BaTiO_3$  films grown on  $SrRuO_3$  or on  $MgO$  layers. The smaller value of the Young's modulus equal to  $79\text{ GPa}$  is in agreement with that one reported in [81]. It is known that  $MgO$  and  $SrRuO_3$  are stiffer than  $SrTiO_3$ , so an influence of the underlying layer on the Young's modulus of the  $BaTiO_3$  can not be excluded. Furthermore it has to be highlighted that in sample  $GV03(P)$  all the thin films are deposited in situ, while for the 33 and 31 mode stacks, used to evaluate the Young's modulus of  $BaTiO_3$  on  $MgO$  and on  $SrRuO_3$ , this is not possible because our deposition

system allows the deposition of only three layers *in situ*. In the 33 and 31 mode multi-layers before the deposition of the  $BaTiO_3$  the thin film stacks are heated up in oxygen at the deposition temperature and annealed for about 30 minites before the beginning of the ablation. The annealing step can improve the quality of the top surface of the film stack which acts as a seed for the  $BaTiO_3$  deposition, however a further investigation it is necessary to understand the origin of such mismatch. The measured Young's modulus for the  $SrRuO_3$  and the  $MgO$  well agreed with the value reported in literature [82, 83] while the measured value for the  $SrTiO_3$  film is smaller than  $265\text{ GPa}$  reported in [84]. The Young's modulus measured on the  $SrTiO_3$  substrate is equal to  $191\text{ GPa}$  which is still smaller than the value reported in literature, however the  $SrTiO_3$  substrate supplier [58] does not report the Young's modulus of the substrate in the datasheet.

The Young's modulus of the materials used here are sensibly higher than the Young's modulus of  $PZT$  ( $63\text{ GPa}$ ) and  $SiO_2$  ( $69\text{ GPa}$ ), these materials have been used for the fabrication of energy harvesting cantilevers by Jeon et al. [4]. They introduced a  $SiN_x$  buffer layer in their film stack to reduce the curling of the beam after its release. The Young's modulus measured for the thin films employed in our stack are high enough to not require the use of an additional buffer layer.

Table 5.2 also reports the Poisson's ratio [25, 74, 75, 76, 77], and the thermal expansion coefficients [85, 86, 87, 88, 89] for the materials used in this project.

### 5.3 Summary

In this chapter it is shown that the  $BaTiO_3$  grows with the polar axis perpendicular to the surface of the film on  $SrRuO_3$  and  $SrTiO_3$  while it grows with the polar axis parallel to the surface of the film on  $MgO$ . When the polar axis is perpendicular to the surface of the film the 31 piezoelectric mode can be used to produce energy harvesting devices, instead with the polar axis parallel to the surface of the film it is possible to fabricate devices using the 33 piezoelectric mode.

When the  $BaTiO_3$  is grown on  $SrTiO_3$  the polar axis has a length of  $4.015 \text{ \AA}$ , which is smaller than the value reported in bulk materials. This is believed to be the effect of the oxygen pressure during the growth of the  $BaTiO_3$  film [79]. In our case an oxygen pressure of  $20 \text{ Pa}$  has been used during the growth of  $BaTiO_3$ .

For  $BaTiO_3$  grown on  $SrRuO_3$  the polar axis has a length of  $4.069 \text{ \AA}$ , in this case the elongation of the polar axis is attributed to the in plane biaxial stress experienced by the  $BaTiO_3$  layer when grown on  $SrRuO_3$ . This is confirmed by a critical thickness of  $9 \text{ nm}$  for  $BaTiO_3$  on  $SrRuO_3$ .

The polar axis of  $BaTiO_3$  is parallel to the surface of the film when it is grown on  $MgO$ . The smaller lattice mismatch between the  $c$  axis of  $BaTiO_3$  and the  $MgO$  lattice parameter is the reason for such orientation. The polar axis lengths measured in this case are  $4.002 \text{ \AA}$  and  $4.028 \text{ \AA}$ , both of them are smaller than the value measured in bulk materials. This happens because the measurements provide an average value for the length of the polar axis, in fact there are two possible orthogonal orientations when the

polar axis is in the plane of the substrate and a non polar axis must also lie in plane.

Nanoindentation measurements have been run on the grown multilayers, the measured Young's modulus are high enough (130 - 233 GPa) to avoid the introduction of an additional buffer layer necessary to reduce the curling of the cantilevers after their release.

The Young's modulus of the  $BaTiO_3$  is equal to 175 GPa when it is grown on  $SrRuO_3$  and  $MgO$ , and to 79 GPa when it is grown on  $SrTiO_3$ , a further investigation is necessary to understand the reasons of such mismatch.

# Chapter 6

## Residual stress analysis for suspended cantilevers

In this chapter an experimental method useful to determine the residual stresses at the top surface of thin film multi-layer cantilevers is discussed. The method consists into the measuring of the cantilever deflection at different distances from the anchor point, in this way the radius of curvature of the structure and so also the residual stress at the cantilever top surface can be evaluated.

In previous works the residual stress in microcantilevers was caculated by measuring the deflection of the free end in the case of small deflections [12, 13], or by using the Stoney formula [4, 14]. In our multilayer cantilevers the Stoney formula does not apply because some of the hypothesis necessary for the application of this method are not fulfilled [15]. Furthermore deflections of the free end equal to  $40 \mu m$  for cantilever having lengths of  $180 \mu m$  have been measured, so also the hypothesis of small deflection of the free end does

not apply.

The proposed method is applicable either in the case of large deflections of the free end or when the Stoney formula does not apply, the deflections of the cantilevers are measured by using SEM and interferometry techniques.

In section 6.1 the proposed experimental method is discussed and applied to the fabricated micro-cantilevers, furthermore an error analysis is developed on the experimental values of the radius of curvature and of the residual stresses. In section 6.2 the causes which produce the residual stress in the micro-cantilevers are analyzed and the theoretical values of the residual stresses are compared with the experimental ones. Section 6.3 presents a discussion on the experimental results and explains why in some cases the measured values deviate from those predicted by the theory. Finally section 6.4 reports a refinement of the proposed method.

## 6.1 Experimental method

Let us consider a thin film stack grown on a  $YBa_2Cu_3O_7$  sacrificial layer, when the sacrificial layer is undercut and the cantilever is released, it usually results in a curved structure rather than straight. The bending of the cantilever is due to the so called **residual stress** which may arise by: a mismatch of the thermal expansion coefficients between the different layers, a mismatch of lattice constants between the epitaxially grown films, atomic diffusion through the film thicknesses and interstitial or substitutional defects into the layers [90].

The understanding and the control of the residual stress is important to

avoid cracking and unwanted deformations of the structures which might lead to deviations from the expected behaviours [91]. To control the curvature of a suspended beam, an understanding of the stresses into the beam is required, this can be obtained from the beam theory, see appendix A.1.

The expression of the longitudinal stress in an homogeneous deflected beam is [32]:

$$\sigma_x = \frac{\tilde{E}h_y}{\rho} \quad (6.1)$$

where  $\tilde{E}$  is the Young's modulus of the beam,  $h_y$  is the distance from the neutral axis and  $\rho$  is the radius of curvature. In a multi-layer eq. 6.1 is valid for each individual film. The longitudinal stress assumes its maximum value at the bottom and top surface of the cantilever.

In previous works [12, 13], the radius of curvature  $\rho$  of a deflected beam has been evaluated by measuring the deflection at the cantilever free end and then the following equation has been used.

$$y = \frac{l^2}{2\rho} \quad (6.2)$$

This formula is an approximation valid for small deflections, for larger deflections another method has to be followed.

To estimate the longitudinal stress at the top surface of the cantilevers the deflection curve has been calculated by measuring the deflection of the beam at different distances from the anchor point, in this way the radius of

curvature at the cantilever free end can be calculated by using eq 6.3.

$$\frac{1}{\rho} = - \frac{\frac{d^2y}{dx^2}}{\left[1 + \left(\frac{dy}{dx}\right)^2\right]^{\frac{3}{2}}} \quad (6.3)$$

The stress at the top surface of the cantilever is calculated with eq. 6.1 applied to an equivalent homogeneous cantilever derived from the multi-layer structure according to the transformed section theory (see sec. 2.1) [32].

The deflection of the beam at different distances from the anchor has been measured with SEM and interferometry techniques.

The measurement of the deflection profile has been used by Kalb et al. [14] to estimate the curvature of suspended beams containing phase-change materials. In that work the Stoney equation was used to calculate the elastic strain at the interface between a thick cantilever and a thin film grown on its top. The expression of the Stoney formula is [15]:

$$\frac{1}{\rho} = \frac{6f(1 - \nu_s)}{h_s^2 \tilde{E}_s} \quad (6.4)$$

$f$  is the force experienced by the film,  $E_s$ ,  $h_s$  and  $\nu_s$  are the Young's modulus the thickness and the Poisson's ratio of the substrate.

Such a treatment is only valid if the film thickness is negligible compared with the cantilever thickness [14, 15]. This restriction does not apply to the method proposed in this work, furthermore we demonstrate the effectiveness of the method in multilayers to which the Stoney equation would not directly apply.

The proposed analysis has been performed on  $SrRuO_3/BaTiO_3/SrRuO_3$

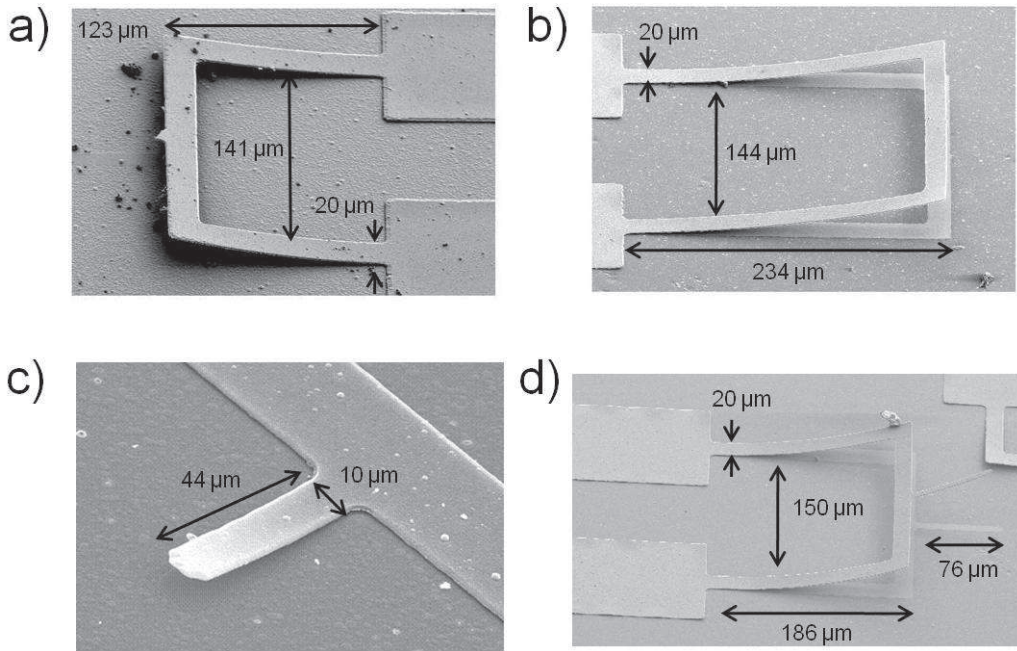


Figure 6.1: SEM pictures of 4 investigated devices: a)  $123\text{ }\mu\text{m}$  long,  $20\text{ }\mu\text{m}$  wide  $\text{BaTiO}_3/\text{MgO}/\text{SrTiO}_3$  (IP) U-shape cantilever, the  $\text{SrTiO}_3$  film is  $500\text{ nm}$  thick, the  $\text{MgO}$  layer is  $50\text{ nm}$  thick and the  $\text{BaTiO}_3$  film is  $120\text{ nm}$  thick; b)  $234\text{ }\mu\text{m}$  long,  $20\text{ }\mu\text{m}$  wide  $\text{SrRuO}_3/\text{BaTiO}_3/\text{SrRuO}_3$  (OP) U-shape cantilever, the bottom  $\text{SrRuO}_3$  layer is  $350\text{ nm}$  thick, the  $\text{BaTiO}_3$  film is  $100\text{ nm}$  thick and the  $\text{SrRuO}_3$  top layer is  $50\text{ nm}$  thick; c)  $44\text{ }\mu\text{m}$  long,  $10\text{ }\mu\text{m}$  wide  $\text{BaTiO}_3/\text{SrTiO}_3$  (Bi) cantilever, the  $\text{SrTiO}_3$  is  $500\text{ nm}$  thick and the  $\text{BaTiO}_3$  is  $120\text{ nm}$  thick; d)  $186\text{ }\mu\text{m}$  long,  $20\text{ }\mu\text{m}$  wide u-shape cantilever with in series a  $76\text{ }\mu\text{m}$  long,  $8\text{ }\mu\text{m}$  simple beam the cantilever, the top-down layer sequence of the structure is  $\text{SrRuO}_3/\text{BaTiO}_3/\text{SrRuO}_3$  (OP), the bottom  $\text{SrRuO}_3$  layer is  $350\text{ nm}$  thick, the  $\text{BaTiO}_3$  film is  $100\text{ nm}$  thick and the  $\text{SrRuO}_3$  top layer is  $50\text{ nm}$  thick.

(sample  $\text{GV21}(P)$ ) u-shape cantilevers,  $\text{BaTiO}_3/\text{MgO}/\text{SrTiO}_3$   
 (sample  $\text{GV10}(P)$ ) u-shape cantilevers and on  $\text{BaTiO}_3/\text{SrTiO}_3$  (sample  
 $\text{GV07}(P)$ ) simple beam cantilevers.

As already discussed in sec. 5.2 the  $\text{BaTiO}_3$  polar axis is perpendicular

to the surface of the film or out of plane (OP) when it is grown on  $SrRuO_3$  so the  $SrRuO_3/BaTiO_3/SrRuO_3$  multi-layer will be labeled as OP stack. For the same reason the  $BaTiO_3/MgO/SrTiO_3$  layer sequence is called IP (in plane) stack while the  $BaTiO_3/SrTiO_3$  cantilevers are called Bi (bi-layer) devices.

At the beginning of the project, the idea was to deposit a gold top electrode on the top of the IP stack. However, as already reported in secs. 2.3 and 4.3, if a further piezoelectric layer has to be grown on the top of the structure, due to the compatibility with the high temperature ablation process,  $SrRuO_3$  has to be used as electrode layer. Structures containing only one piezoelectric layer can use gold as top electrode. Gold is deposited at room temperature so it does not influence the thermal stress analysis which is developed in this section. In the future the proposed residual stress analysis can be extended to the  $SrRuO_3/BaTiO_3/MgO/SrTiO_3$  stack.

The SEM analysis has been performed with a Philips XL30S FEG, fig. 6.1 shows the SEM pictures of four of the investigated structures.

When the cantilever is undercut it leaves a trace on the substrate fig. 6.2. The deflection of the beam measured with SEM technique was evaluated by measuring the distance between the trace on the substrate and the top surface of the cantilever. Measurements uncertainties of  $300\text{ nm}$  in the  $y$  direction and of  $1\text{ }\mu\text{m}$  in the  $x$  direction have been estimated.

To validate the SEM measurements, the deflection of the cantilevers has been also measured with a MicroXAM2 interferometer (Omniscan, UK). The interferometer was operated in phase mode employing light of wavelength  $510\text{ nm}$ , and at a magnification of  $100X$ . Interferograms were found to be

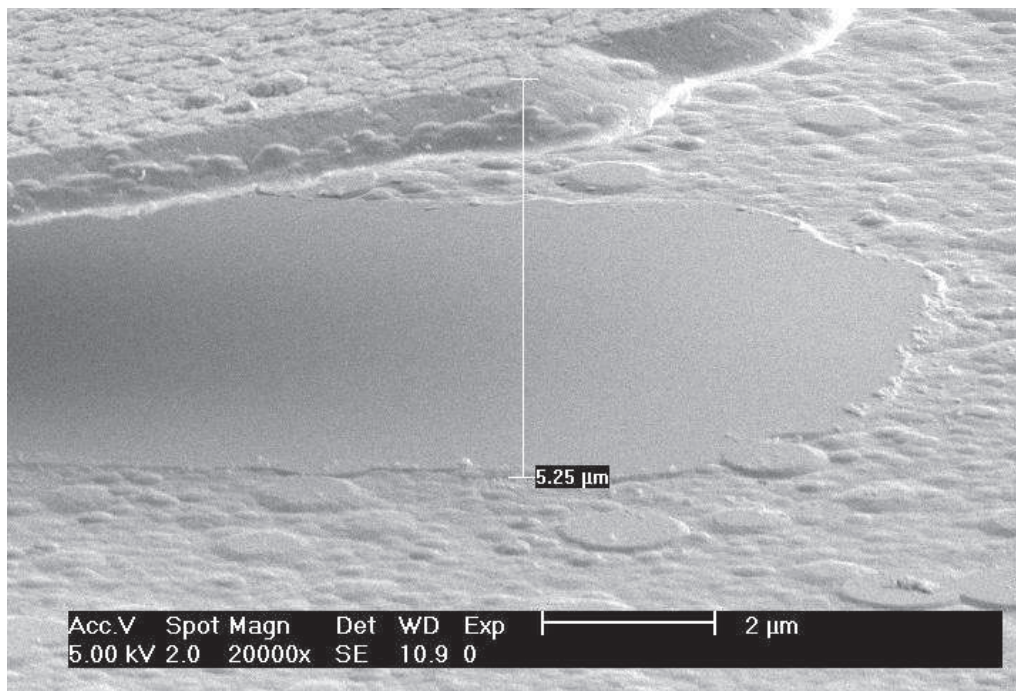


Figure 6.2: SEM pictures showing the measurements of the deflection for a  $BaTiO_3/SrTiO_3$  cantilever (Bi device) at  $32\mu m$  from the anchor. An angle of few degree is present between the substrate and the detector, the value of this angle has been taken into account for the measurement of the beam deflection.

unreliable, due to differences in the reflectivities of the various materials. Instead, the interferometer was operated manually, employing a motorised  $x$ ,  $y$ ,  $z$  stage with  $\pm 0.1\mu m$  resolution. The interferometric fringes were focused on the sample surface and the position of peak light intensity was considered to be the  $x$  position of interest, whose position could be determined with approximately  $\pm 3\mu m$  accuracy due to the manual positioning involved. The corresponding  $y$ -position ( $\pm 3\mu m$  accuracy) was recorded for each surface location assessed. These measurements have been run by dr. James Bowen

[56].

In order to determine the residual stresses in a cantilever, we must consider the forces distributed over its cross section. These represent a system equivalent to a couple and the resultant of these forces in the  $x$  direction must be equal to zero fig. A.7, (see appendix A.1) [32].

Equation 6.5:

$$\tilde{E}\hat{I} \frac{d^2y}{dx^2} = M \quad (6.5)$$

is the differential equation describing the deflection curve of the cantilever, it implies that such curve is described by a parabola:

$$y = ax^2 + bx + c. \quad (6.6)$$

To find the curve which better approximates the cantilevers, the deflections of the structures have been measured at five different distances ( $A; B; C; D; E$ ) from the anchor. Then the parabola passing through the points  $A, C$  and  $E$  has been calculated.

Five different points have been measured, however only three points are necessary to calculate the expression of a parabola, this means that ten different parabolas can be calculated.

The parabola which better approximates the deflection of the cantilevers is usually that one passing through the points ( $A; C; E$ ), this parabola has been used to calculate the radius of curvature of the suspended structures. The radius of curvature has been calculated using eq. 6.3.

The deflections measured using the SEM and the interferometer techniques, the calculated parabolas and radius of curvatures for the analysed

<i>Device</i>	<i>Cantilever type</i>	<i>Length [μm]</i>	<i>Width [μm]</i>	<i>SEM coordinates (A; B; C; D; E) (x[μm], y[μm])</i>	<i>Interferometer coordinates (A; B; C; D; E) (x[μm], y[μm])</i>	<i>SEM Parabola (Interferometer parabola)</i> $y = ax^2 + bx + c$	<i>Radius of curvature (SEM) [μm]</i>	<i>Radius of curvature (interf.) [μm]</i>
OP	U-shape	120 μm	20 μm	(0, 1.74); (20, 3.35); (50, 8.44); (90, 19.5); (118, 30.5);	(0, 1.5); (20, 3.5); (50, 8.2); (90, 18); (118, 31);	$y = 1620x^2 + 0.053x + 1.74 \cdot 10^{-6}$ ( $y = 1706x^2 + 0.0487x + 1.5 \cdot 10^{-6}$ )	$-403 \pm 7.15$	-390
OP	U-shape	128 μm	20 μm	(0, 0.828); (20, 2.07); (50, 6.62); (90, 15.9); (120, 26.5);	(0, 1.2); (20, 2.8); (50, 6.3); (90, 15.4); (118, 26);	$y = 1400.8x^2 + 0.0458x + 0.828 \cdot 10^{-6}$ ( $y = 1590x^2 + 0.0225x + 1.2 \cdot 10^{-6}$ )	$-448 \pm 38$	-405
OP	U-shape	234 μm	20 μm	(0, 1.24); (50, 3.97); (100, 10.06); (150, 17.4); (225, 37.6);	(0, 1); (50, 3.7); (100, 9.6); (150, 17); (225, 36.3);	$y = 546x^2 + 0.039x + 1.24 \cdot 10^{-6}$ ( $y = 567x^2 + 0.0293x + 10^{-6}$ )	$-1038 \pm 406$	-999
IP	U-shape	120 μm	20 μm	(0, 1.02); (20, 2.3); (50, 5.72); (90, 13.5); (122, 21.6);	(0, 2); (20, 3.6); (50, 5.8); (90, 12.3); (118, 18.6);	$y = 1040x^2 + 0.042x + 1.02 \cdot 10^{-6}$ ( $y = 834x^2 + 0.0343x + 2 \cdot 10^{-6}$ )	$-551 \pm 37$	-612
IP	U-shape	122 μm	20 μm	(0, 0.911); (20, 2.7); (50, 6.82); (90, 15.8); (119, 24.2);	(0, 1.4); (20, 2.1); (50, 5.2); (90, 13.2); (119, 23.8);	$y = 1123.6x^2 + 0.062x + 0.911 \cdot 10^{-6}$ ( $y = 1674x^2 - 0.0077x + 1.4 \cdot 10^{-6}$ )	$-471 \pm 31.7$	-375
IP	U-shape	180 μm	20 μm	(0, 1.75); (50, 6.2); (100, 17.7); (150, 35.6); (180, 44.7);	(0, 1.6); (50, 6.5); (100, 15.3); (150, 32.2); (180, 43);	$y = 989x^2 + 0.0606x + 1.75 \cdot 10^{-6}$ ( $y = 1162x^2 + 0.0208x + 1.6 \cdot 10^{-6}$ )	$-643 \pm 128$	-561
Bi	Beam	32 μm	10 μm	(5.6, 1.84); (10, 2.2); (16, 2.82); (24, 3.86); (32, 5.25);	(0, 1.2); (/, /); (15, 2.3); (/, /); (32, 4.8)	$y = 2186.6x^2 + 0.047x + 1.51 \cdot 10^{-6}$ ( $y = 2169x^2 + 0.0408x + 1.2 \cdot 10^{-6}$ )	$-248 \pm 109$	-242
Bi	Beam	44 μm	10 μm	(2.33, 1.57); (10, 2.23); (20, 3.2); (30, 4.82); (39, 6.68);	(0, 1.1); (/, /); (20, 3.4); (30, 4.5); (44, 7.9)	$y = 2500x^2 + 0.0339x + 1.51 \cdot 10^{-6}$ ( $y = 1650x^2 + 0.082x + 1.1 \cdot 10^{-6}$ )	$-217 \pm 57$	-327
Bi	Beam	55 μm	10 μm	(1.17, 1.59); (15, 3); (30, 5.34); (40, 8.23); (51, 10.8);	(0, 1.5); (15, 4); (30, 7); (40, 8.5); (55, 2, 10.8)	$y = 2607x^2 + 0.0488x + 1.53 \cdot 10^{-6}$ ( $y = -555x^2 + 0.2x + 1.5 \cdot 10^{-6}$ )	$-225 \pm 83$	927

Table 6.1: Device type, length, width and co-ordinates (x,y) of nine example cantilevers,  $x$  is the position of the measurement along the cantilever and  $y$  is the deflection. The parabolic equations describing the deflection of the cantilevers through the points (A; C; E) are reported for both the SEM and the interferometer data, the radii of curvature of each cantilever calculated from equation 6.3 with the parabola obtained from SEM and interferometry data are also given. The error analysis on the radius of curvature has been performed only on the SEM data because these are the data used to calculate the residual stress of the cantilevers. For two of the Bi devices due to the manual positioning involved with the interferometer measurements, it has not been possible to measure the deflection at five different distances from the anchor.

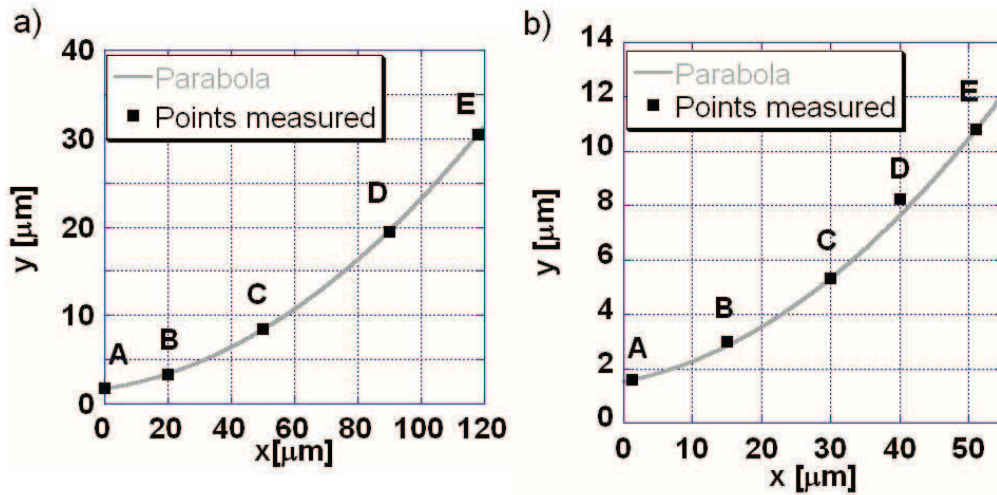


Figure 6.3: a) Parabola and deflection of the measured points for the 120  $\mu\text{m}$  long OP device. b) Parabola and deflections of the measured points for the 55  $\mu\text{m}$  long Bi device.

devices are reported in tab. 6.1. There is good agreement between the SEM and the interferometry deflection values. Because of the higher resolution associated with the SEM measurements the radii of curvature have been calculated from the SEM data.

The parabola describes the deflection of the cantilevers well, as can be seen from fig. 6.3 which shows the parabola and the measured points for the 120  $\mu\text{m}$  long OP device and for the 55  $\mu\text{m}$  long Bi cantilever. However it has to be emphasized that eq. 6.5 is an approximation [32]. A parabola might not be a good approximation generally, in which case an expression of the curve which better approximate the deflection of the beam has to be used for the calculation of the radius of curvature. For the analysed devices the deviations in the measured coordinates of *B* and *D* from the parabolic approximation are reported in table 6.2. These deviations are in the error

<i>Device</i>	<i>Cantilever type</i>	<i>Length [μm]</i>	<i>Width [μm]</i>	<i>Deviation on B for SEM par. [μm]</i>	<i>Deviation on D for SEM par. [μm]</i>	$e_a$ <i>SEM – INT</i>	$e_b$ <i>SEM – INT</i>
OP	U-shape	120 μm	20 μm	+ 0.1	+ 0.22	5.3%	8.11%
OP	U-shape	128 μm	20 μm	+ 0.23	+ 0.4	13.51%	51%
OP	U-shape	234 μm	20 μm	+ 0.59	+ 1.97	3.85%	24.87%
IP	U-shape	120 μm	20 μm	+ 1.22	- 0.28	20%	18.3%
IP	U-shape	122 μm	20 μm	- 0.1	- 0.21	49%	88%
IP	U-shape	180 μm	20 μm	+ 1.05	- 2.51	17%	66%
Bi	Beam	32 μm	10 μm	0	- 0.22	0.8%	13.19%
Bi	Beam	44 μm	10 μm	- 0.13	- 0.04	51.5%	142%
Bi	Beam	55 μm	10 μm	- 0.15	- 0.58	121%	310%

Table 6.2: Deviations on the points *B* and *D* consequence of the parabolic approximation used for the delection of the cantilever. Also reported are the percentage errors  $e_a$  and  $e_b$  of the parabola coefficients obtained for the interferometers measurements with respect to the SEM data.

range of the SEM coordinates.

As already reported, to validate the method, the deflections of the cantilevers have been measured by interferometer technique. Tab. 6.2 also shows the percentage difference between the values of the coefficients *a* and *b* obtained using the SEM technique ( $a_{SEM}$  and  $b_{SEM}$ ) and interferometry ( $a_{INT}$  and  $b_{INT}$ ) respectively. These differences were calculated using:

$$e_a = \left| \frac{a_{SEM} - a_{INT}}{a_{SEM}} \right| \cdot 100 \quad (6.7)$$

$$e_b = \left| \frac{b_{SEM} - b_{INT}}{b_{SEM}} \right| \cdot 100. \quad (6.8)$$

The coefficient *c* is not considered because according to eqs. 6.6 and 6.3 its value does not affect the radii of curvature of the cantilevers. For some devices

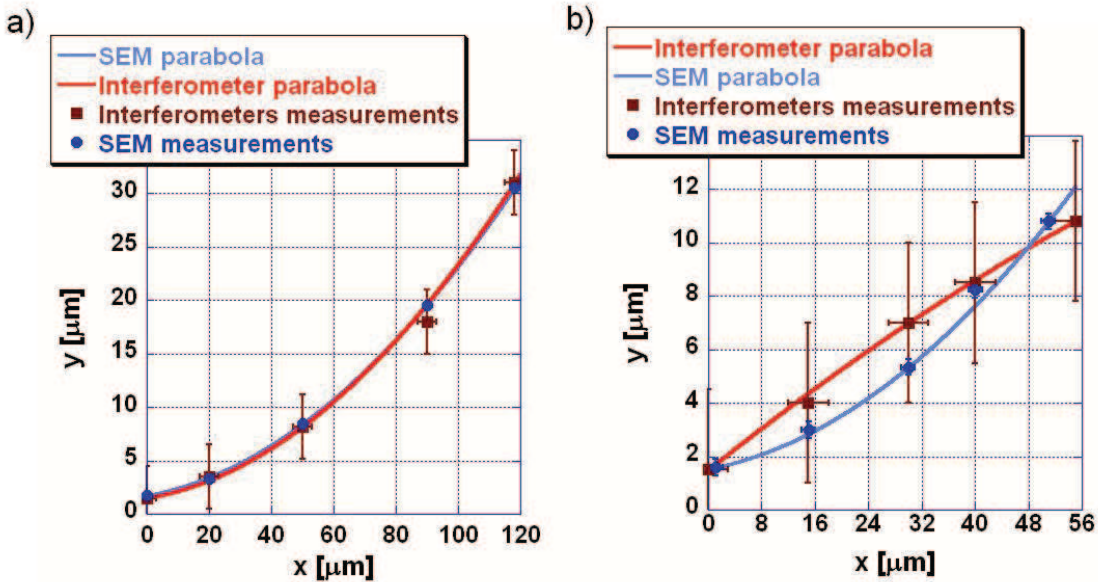


Figure 6.4: a) SEM and interferometers parabolas plus SEM and interferometers deflection measurements with the relative error bars for the 120  $\mu\text{m}$  long OP device. b) SEM and interferometers parabolas plus SEM and interferometers deflection measurements with the relative error bars for the 55  $\mu\text{m}$  long Bi device.

a significant difference between the parabola coefficients obtained with SEM and interferometer analysis is present. The Bi devices have lengths between 32  $\mu\text{m}$  and 55  $\mu\text{m}$  and experience a maximum deflection of the free end equal to 10  $\mu\text{m}$ . For these small deflections the resolution of the interferometry method, as consequence of the manual measurement involved, does not allow the application of the method on these data fig. 6.4b.

Fig. 6.4a shows the parabolas calculated from the SEM and from the interferometers data together with the deflections measured with both techniques for the 120  $\mu\text{m}$  long OP device. In this case there is a good agreement between the two methods, so the two parabolas overlap and they approximate

the data within the instrument error.

Fig. 6.4b is relative to the  $55 \mu\text{m}$  long Bi device, which is the device showing the maximum difference between the values of the coefficients  $a$  and  $b$  obtained from SEM and interferometer measurements. In this case the instrument resolution is equal to the 30% of the deflection of the free end, this large error does not allow to calculate a parabola which is in agreement with that one obtained from the SEM data. This explains why only the SEM measurements are considered for the evaluation of the residual stress.

The longitudinal stress at the free end cross section of each cantilever is evaluated by using eq. 6.1. The value of the Young's Modulus appropriate for a multilayer system is that of the material with maximum Young's modulus [32]. In fact in a cantilever system with heterogeneous cross section the width of each layer is normalized to the maximum Young Modulus according to transformed section theory fig. 2.2 (see sec. 2.1), [32].

To calculate the residual stress at the cantilever top surface, eq. 6.1, it is necessary to know the distance between the cantilever's top surface and the neutral axis, the position on the neutral axis in the proposed multi-layers is evaluated according eq. 2.9. The experimental values of the residual stress at the cantilever top surfaces for the analysed devices are reported in tab. 6.3.

There are three sources of uncertainty in this analysis. The first source is due to the measurement technique and it is linked to the resolution of the measurement instruments. The second source is linked to the curve chosen to approximate the deflection of the beam. The third source of error is due to the fabrication process, this kind of error arises from the undercut and

<i>Device</i>	<i>Cantilever type</i>	<i>Length [μm]</i>	<i>Width [μm]</i>	<i>Experimental stress [10<sup>9</sup> N/m<sup>2</sup>]</i>	<i>Theoretical thermal stress [10<sup>9</sup> N/m<sup>2</sup>]</i>	<i>Theoretical thermal + misfit stress [10<sup>9</sup> N/m<sup>2</sup>]</i>
OP	U-shape	120 μm	20 μm	-0.104 ± 0.002	-0.051	-0.0013
OP	U-shape	128 μm	20 μm	-0.093 ± 0.009	-0.051	-0.0013
OP	U-shape	234 μm	20 μm	-0.051 ± 0.026	-0.051	-0.0013
IP	U-shape	120 μm	20 μm	-0.153 ± 0.011	-0.145	-7.21
IP	U-shape	122 μm	20 μm	-0.131 ± 0.009	-0.145	-7.21
IP	U-shape	180 μm	20 μm	-0.112 ± 0.028	-0.145	-7.21
Bi	beam	32 μm	10 μm	-0.173 ± 0.136	-0.071	1.2
Bi	beam	44 μm	10 μm	-0.200 ± 0.069	-0.071	1.2
Bi	beam	55 μm	10 μm	-0.190 ± 0.112	-0.071	1.2

Table 6.3: Experimental stress, theoretical thermal stress and theoretical stress due to combined effect of thermal and misfit stress evaluated at the top surface of each cantilever. For each cantilever the device type corresponding to different layer sequence is indicated, also the cantilever shapes and the cantilever lengths and widths are reported.

from the resist resolution.

The uncertainties on the values of the residual stresses have been calculated developing an error analysis on the radius of curvature.

As already stated, to evaluate the radius of curvature, the parabola passing only through the points *A*, *C* and *E* has been considered, that is usually the parabola which better approximate the deflection of the beam.

From the measured points ten parabolas can be worked out, this means that ten values of the parameters *a*, *b* and *c* can be calculated for each cantilever. The standard deviations for such parameters can be then evaluated to provide an estimate of the uncertainty of the fit. The standard deviations  $\Delta_a$  and  $\Delta_b$  have been evaluated considering the parabolas which approximate

the deflection of the cantilever within the measurement error.

In some cases, one or two parabolas (usually those one passing through  $C, D, E$  and  $B, D, E$ ) did not approximate the deflection of the beam well, resulting in an error larger than the measurement error. Such parabolas were rejected and were not included in the error analysis. By choosing only parabolas which approximate the deflection of the cantilevers within the measurement error, we are choosing a series of curves which approximate the deflection of the beams within the error of the instrument.

The radius of curvature depends only on the parameters  $a$  and  $b$  in eq. 6.6, so the uncertainty in the radius of curvature is dependent on the uncertainties in  $a$  and  $b$  but not in  $c$ .

The radius of curvature of each cantilever has been calculated at the free end of the structure, so an error on the length of the cantilever also affects its final value. The principle error on the cantilever lengths is due to the undercut at the anchors points. Undercuts between  $9 \mu m$  and  $20 \mu m$  have been measured.

The uncertainty on the radius of curvature has been evaluated using the following formula:

$$(\Delta\rho)^2 = \left( \frac{\partial\rho}{\partial a} \Delta_a \right)^2 + \left( \frac{\partial\rho}{\partial b} \Delta_b \right)^2 + \left( \frac{\partial\rho}{\partial l} \Delta_l \right)^2 \quad (6.9)$$

where  $\Delta_a$  and  $\Delta_b$  are the standard deviations on the parabola factors  $a$  and  $b$ ,  $\Delta_l$  is the uncertainty on the length of the cantilever due to the undercut and the resolution of the photoresist.

With the error on the radius of curvature also the error on the residual

longitudinal stress can be calculated. The radius of curvature with its uncertainty and the evaluated residual stress with its uncertainty are reported in tabs. 6.1 and 6.3 respectively.

## 6.2 Theoretical values of the residual stress

Usually vacuum deposited films are in a state of stress. Causes of stress are the mismatch of thermal expansion coefficients between the different layers (thermal stress), the mismatch of lattice constants between the different materials (misfit stress) and the presence of defects in the layers [90]. In sec. 5.1 the critical thickness values for the films present in the analysed multi-layers have been discussed and evaluated. In our layer combinations all the critical thicknesses are less than  $10\text{ nm}$ , the film thicknesses in the three stacks are in the order of hundred of  $\text{nm}$ , this means that only the thermal stress will be considered in the following stress analysis, as the misfit is released by the generated dislocations. Similar considerations have been also reported in [73, 92].

The deposition of the cantilever films is performed at temperatures of  $740^\circ\text{C}$  and  $780^\circ\text{C}$ , then the film stack is cooled down to room temperature. The thermal stress will be the result of the differences in the film thermal expansion coefficients.

On a rigid substrate the in plane thermal stress in the layer  $n$  applied by the layer  $n - 1$  can be expressed as

$$\sigma_n = \frac{\tilde{E}_n}{1 - \nu_n} (\alpha_n - \alpha_{n-1})(T_s - T_a) \quad (6.10)$$

where  $\tilde{E}_n$  is the Young modulus,  $\nu_n$  is the Poisson's ratio,  $\alpha_n$  and  $\alpha_{n-1}$  are the thermal expansion coefficients of the layers  $n$  and  $n - 1$ ,  $T_s$  is the temperature during the deposition and  $T_a$  is the temperature during the measurement. Thin films can be considered as two dimensional systems. Equation 6.10 is the two dimensional extension of the relation reported in [93].

Eq. 6.10 reveals that the longitudinal strain in the film varies linearly with temperature. To verify the accuracy of the linear approximation it is important to understand how the lattice parameters of the different materials vary with temperature. The main problem may arise from the  $BaTiO_3$  layer, in fact this material experiences a change of its crystal structure at  $120^\circ C$  (see sec. 1.3), this change consist into an elongation of the  $c$  axis, also called the polar axis, below  $120^\circ C$ .

In the OP structures the polar axis is perpendicular to the surface of the film, the longitudinal stress in the plane of the film arise from a variation of the length of the other two axes, labeled as  $a$  and  $b$ . Choi et al. [22] reported that for  $BaTiO_3$  grown on  $SrRuO_3$ , the lengths of the  $a$  and  $b$  axes linearly varies with temperature in the temperature range  $0^\circ C - 800^\circ C$ , so the linear approximation of eq. 6.10 hold. The same discussion is valid when  $BaTiO_3$  is grown on  $SrTiO_3$  (Bi structures), in fact also in this case the polar axis is perpendicular to the surface of the film.

In the case of the IP devices the polar axis lies parallel to the plane of the film but it is randomly oriented in plane. This produces a polar axis with an average length shorter than that one of (001) oriented  $BaTiO_3$  (see sec. 5.1)

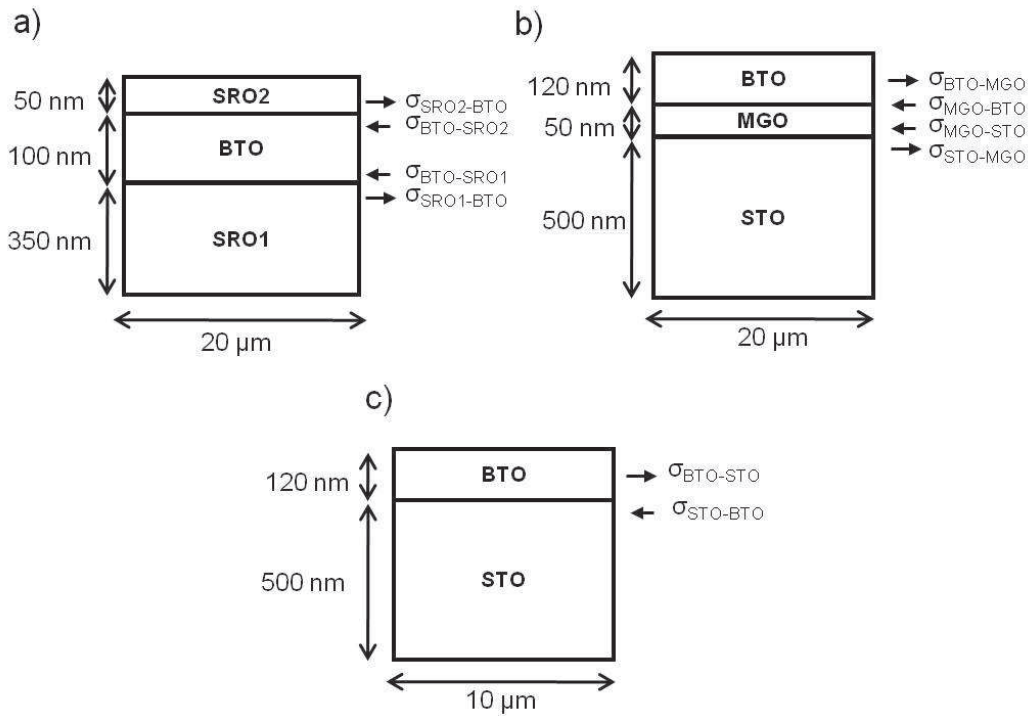


Figure 6.5: Longitudinal stress at the interface of each film present in the stack, in a)  $\sigma_{SRO1-BTO}$  indicates the stress on the  $SrRuO_3$  surface layer applied by the  $BaTiO_3$  film, similar nomenclature applies to the other layers. The arrows indicate if the stress in each layer is compressive (←) or tensile (→).

corresponding in this way to a reduction of the quantity:

$$c_{tetragonal} - c_{cubic} \quad (6.11)$$

due to this reason eq. 6.10 is also applied in the case of the *IP* devices. A better understanding of how the thermal expansion coefficients of the films vary with temperature is desirable, however these data do not seem to be available in literature.

When the  $YBa_2Cu_3O_7$  is undercut and the beam suspended, the constraint which keeps the multilayer anchored to the substrate is removed. The multilayered structure will bend because of the unbalanced thermal stress present at the film interfaces. Fig. 6.5 show the thermal stresses at the interfaces in the OP, IP and Bi stacks after the  $YBa_2Cu_3O_7$  undercutting. Where  $\sigma_{SRO1-BTO}$  indicates the stress on the  $SrRuO_3$  surface layer applied by the  $BaTiO_3$  film. Similar nomenclature applies to the other layers. The thermal expansion coefficients [85, 86, 87, 88, 89] the Poisson's ratio [25, 74, 75, 76, 77] and the measured Young Modulus are reported in tab. 5.2.

With these values it is possible to calculate the thermal stress at the interface of each film by using eq. 6.10. In the OP multilayer structure each film has to be heated to  $780^\circ C$  during the  $SrRuO_3$  deposition, so  $T_s$  is chosen equal to  $780^\circ C$ . The temperature during the measurement  $T_a$ , is  $20^\circ C$ . In this system the algebraic sum of the thermal stresses at each interface is:

$$\begin{aligned} \sigma_{SRO1-BTO} + \sigma_{BTO-SRO1} &= \\ &= \sigma_{BTO-SRO2} + \sigma_{SRO2-BTO} = \\ &= -0.0255 \cdot 10^9 \left[ \frac{N}{m^2} \right] \end{aligned} \quad (6.12)$$

the minus sign indicates a compressive stress.

For the IP multilayer system  $T_s$  is equal to  $740^\circ C$  and  $T_a$  is still  $20^\circ C$ . The algebraic sum of the thermal stresses at each interface is:

$$\sigma_{STO-MGO} + \sigma_{MGO-STO} =$$

$$= -0.111 \cdot 10^9 \left[ \frac{N}{m^2} \right] \quad (6.13)$$

for the  $SrTiO_3 - MgO$  interface and

$$\begin{aligned} \sigma_{MGO-BTO} + \sigma_{BTO-MGO} = \\ = -0.034 \cdot 10^9 \left[ \frac{N}{m^2} \right] \end{aligned} \quad (6.14)$$

for the  $MgO - BaTiO_3$  interface.

In the case of the Bi device,  $T_s$  is equal to  $740^\circ C$  while  $T_a$  is  $20^\circ C$ , the resulting stress at the  $BaTiO_3/SrTiO_3$  interface is:

$$\begin{aligned} \sigma_{STO-BTO} + \sigma_{BTO-STO} = \\ = -0.071 \cdot 10^9 \left[ \frac{N}{m^2} \right] \end{aligned} \quad (6.15)$$

as already discussed in sec. 5.2 the value of the  $BaTiO_3$  Young's modulus used for the calculations of the stress at the interface of the Bi structures is smaller than that one used for the OP and IP devices.

According to eq. 6.1, the longitudinal stress in each layer varies linearly with the film thickness.

The cantilevers under investigation have total thicknesses of  $500\text{ nm}$  and  $670\text{ nm}$ , widths between  $10\text{ }\mu\text{m}$  and  $20\text{ }\mu\text{m}$  and lengths between  $32\text{ }\mu\text{m}$  and  $230\text{ }\mu\text{m}$ . So at a first approximation it is possible to consider each layer in the stack as a two dimensional system, this means that the stress will occur only at the interfaces.

For the OP system shown in Fig. 5a it is possible to assume that the

stress at the top surface of the beam is equal to the sum of the stresses at the  $SRO_2/BTO$  and at the  $BTO/SRO_1$  interfaces, Eq. 6.16.

$$\sigma_a = -0.051 \cdot 10^9 \left[ \frac{N}{m^2} \right] \quad (6.16)$$

This is similar in magnitude to the values determined experimentally for the three OP stacks and in excellent agreement with the experimentally determined stress for one of them, table 6.3. For the IP stacks, the stress at the top surface of the beam will be equal to the sum of the stresses at the  $BTO/MGO$  and at the  $MGO/STO$  interfaces, Eq. 6.17.

$$\sigma_b = -0.145 \cdot 10^9 \left[ \frac{N}{m^2} \right] \quad (6.17)$$

In this case we have excellent agreement with all the experimentally determined values, table 6.3.

For the Bi device the stress at the top surface is assumed equal to the stress at the  $BTO/STO$  interface:

$$\sigma_c = -0.071 \cdot 10^9 \left[ \frac{N}{m^2} \right]. \quad (6.18)$$

There is a factor 3 between the experimental and the theoretical values, however a large uncertainty is present in the experimental stresses and for two devices the theoretical value falls inside the uncertainty range, table 6.3.

If the contributions coming from the lattice mismatches are considered the stresses at the interfaces of fig. 6.5 are given by the sum of the thermal stress and of the stress generated by the lattice mismatch. The stress due to

the lattice mismatch generated by the layer  $n - 1$  on the layer  $n$  is:

$$\sigma_{mis.n} = \frac{E_n}{1 - \nu_n} f \quad (6.19)$$

where  $f$  is the lattice misfit defined in eq. 5.1.

Considering the algebraic sum of the stresses at the interfaces of the OP stack, the theoretical longitudinal stress at the top surface is:

$$\hat{\sigma}_a = -0.0013 \cdot 10^9 \left[ \frac{N}{m^2} \right] \quad (6.20)$$

this is between five times and one order of magnitude smaller than the experimental values. For the IP devices the introduction of the lattice mismatch in the calculations results in the following top surface stress:

$$\hat{\sigma}_b = -7.21 \cdot 10^9 \left[ \frac{N}{m^2} \right] \quad (6.21)$$

in this case there are two order of magnitude between experiment and theory. Finally in the case of the Bi cantilevers the contribution of the misfit stress produces the following theoretical value:

$$\hat{\sigma}_c = 1.2 \cdot 10^9 \left[ \frac{N}{m^2} \right] \quad (6.22)$$

also in this case a difference of two orders of magnitude between the experimental and the residual stress is present. Furthermore the positive value of the residual stress at the beam top surface indicates a downward bending of the cantilever, in clear contrast with observations. The values of the resi-

dual stress calculated with the contributions of the thermal stress and lattice mismatch are reported in table 6.3.

When the contributions of the lattice mismatch are included in the calculation of the residual stress there is a clear disagreement between theoretical and experimental values, this is why the residual stress is mainly attributed to the differences in the thermal expansion coefficients between the materials of the different layers.

### 6.3 Discussion

There are two different techniques used to evaluate the residual stress in thin films. In the first method the curvature of a flat substrate is measured after the film deposition and the residual stress is evaluated using the Stoney formula [4, 90, 14, 94].

The assumptions in this method are: the properties of the film-substrate system are such that the film materials contribute negligibly to the overall elastic stiffness; the change in film stress due to substrate deformation is small; the thickness of the film is small compared to the thickness of the substrate and the curvature of the substrate midplane is spatially uniform [15]. Corrections to the original Stoney formula can be made in the case of films having a thickness which is not negligible with respect to the thickness of the substrate.

Thus the Stoney formula may not accurately describe the bending of our cantilever, for example the radius of curvature of the fabricated cantilevers is not uniform along the length of the beam and furthermore in multilayer

cantilevers all the films contribute to the overall elastic stiffness.

When this method is applied to a multilayer structure grown on a certain substrate it is assumed that the individual layers in the film are added sequentially and that the mismatch strain in each layer depends only on the substrate but not on the order in which the layers are formed [15]. To evaluate the stress in a multilayer the substrate curvature has to be measured before and after each layer deposition [4, 15].

All these assumptions can lead to systematic errors in the evaluation of the local residual stresses.

The second technique involves the measurement of the bending of the multilayer structure when all the constraints are removed [90]. This is the method usually used to evaluate the residual stress in released cantilevers. Under the assumption of small deflections, the deflection of the free end is measured [12, 13], and is used to calculate an approximate value for the radius of curvature (eq. 6.2). This is only valid for small deflections of the cantilever free end, and so to calculate a more precise value for the radius of curvature, the method proposed in this chapter can be followed. Measurement of the deflections at different distances from the anchor point is a straighfroward way to experimentally evaluate the residual stress in multilayers cantilevers.

For the OP devices, one of the experimentally determined residual stress values is in good agreement with the theoretical value and the other two are of a similar order of magnitude. All of the experimentally determined residual stress values for the IP devices agree well with the theoretical value. The level of agreement between experiment and theory may be somewhat fortuitous, since there is more than one value available in the literature for

key parameters such as the thermal expansion coefficients of the materials. In particular for  $MgO$  a different value from that one reported in the table is also found [26].

$$\alpha_{MgO}(300K) = 10.4 \cdot 10^{-6} \left[ \frac{1}{K} \right] \quad (6.23)$$

Assuming this value for the  $MgO$  thermal expansion coefficient, the value for the theoretical residual stress at the top surface of the IP device is:

$$\sigma_b = -0.072 \cdot 10^9 \left[ \frac{N}{m^2} \right]. \quad (6.24)$$

In the case of Bi devices the magnitude of the absolute error on the parabolic approximations (error on points  $B$  and  $D$ , table 6.2) is comparable to the absolute error of the IP and OP structures. The Bi devices experiences deflections which are between three and six times smaller than the deflections experienced by the IP and OP cantilevers, this produces a larger relative error on the parabolic approximation used for the Bi structures. This explains why a bigger error on the residual stress of these cantilevers is present. Furthermore in the Bi structures all the thin films are deposited *in situ* while for the IP and OP stacks this is not possible because our deposition system allows the deposition of only three layers *in situ*. In the IP and OP devices before the deposition of the  $BaTiO_3$  the thin film stacks are heated up in oxygen at the deposition temperature and annealed for about 30 minutes before the deposition. It is known that heating and cooling cycles can reduce stresses in ceramics like  $BaTiO_3$  [88], stresses in the Bi structures may be higher than those in the IP and OP because the IP and OP structures were grown with extra heating/cooling steps. Thirdly, the Bi structures are

smaller than the IP and OP devices so edges effects might contribute to the total longitudinal stress [15].

Nevertheless for two of the Bi structures the theoretical stress lies with the error range of the experimental value. Therefore we consider that the overall agreement with theory is good and that the mismatch between the thermal expansion coefficients is the main cause of the residual stress in these devices. If instead the lattice mismatches are used to calculate the longitudinal stresses at the top surfaces of the cantilevers, there is a difference of one or two orders of magnitude between theoretical and experimental values. This rules out the lattice mismatch as the cause of residual stress.

We believe that the variation in stress values can arise from variations in deposition parameters, associated with the alignment of the laser ablation plume with the centre of the substrate. For the sample containing the OP structures, two of the devices were much closer to each other than the third device. If the thickness of each layer deposited on the  $SrTiO_3$  substrate were not uniform all over the sample, this would give errors in the position of the neutral axis and according to eq. 6.1 an error on the value of the residual longitudinal stress.

Another potential source of variation is the value of the Young's modulus. Measurements show that an uncertainty up to 22% is present around the central value of the Young's modulus across the thickness of each film, fig. 5.3. Another source of error might be due to the not perfect undercut in fact it is possible that material from the top part of the sacrificial layer might remain attached to the bottom surface of the cantilever. Finally other sources of stress like microscopic voids, incorporation of impurities and recrystallization

[15, 72] could be present in the deposited films.

To validate the method, the measurements of the deflection of the cantilevers have been also performed with the interferometry technique. The measured values together with the corresponding parabola are reported in table 6.1. Table 6.2 reports the percentage differences on the parabola coefficients  $a$  and  $b$ ,  $e_a$  and  $e_b$  respectively, obtained from the interferometer measurements respect to the parabola coefficients relative to the SEM data. For the IP and OP devices errors on the coefficients between 5 % and 20 % validate the method applied on the SEM measurements. For the Bi devices errors on the coefficients over 50 % are reported, this is attributed to the smaller resolution associated with the interferometer measurements. The Bi devices have lengths between  $32 \mu m$  and  $55 \mu m$  and experience a maximum deflection of the free end equal to  $10 \mu m$ . For these small deflections, the resolution of the method as consequence of the manual measurement involved does not allow the application of the method on these data.

The SEM measurements present better resolution than the interferometers data, this is why the radius of curvature and the values of the residual stresses at the top surface of the cantilevers have been calculated from the SEM measurements.

## 6.4 A refinement of our analysis

To refine the residual stress analysis performed on the fabricated cantilevers, the parabolas approximating the deflection curve of the cantilevers have been calculated by means of a least square fitting routine. In this routine, to

<i>Device</i>	<i>Cantilever type</i>	<i>Length [μm]</i>	<i>Width [μm]</i>	<i>Radius of curvature [μm]</i>	<i>Residual stress [10<sup>9</sup> N/m<sup>2</sup>]</i>
OP	U-shape	120 μm	20 μm	414 ± 6.5	-0.101 ± 0.002
OP	U-shape	128 μm	20 μm	435 ± 13	-0.096 ± 0.003
OP	U-shape	234 μm	20 μm	931 ± 94	-0.045 ± 0.005
IP	U-shape	120 μm	20 μm	726 ± 20	-0.099 ± 0.003
IP	U-shape	122 μm	20 μm	494 ± 73	-0.146 ± 0.025
IP	U-shape	180 μm	20 μm	640 ± 86	-0.113 ± 0.017
Bi	beam	32 μm	10 μm	244 ± 50	-0.176 ± 0.045
Bi	beam	44 μm	10 μm	224 ± 21	-0.191 ± 0.02
Bi	beam	55 μm	10 μm	250 ± 46	-0.172 ± 0.038

Table 6.4: Radius of curvatures, and residual stress at the top surface of the fabricated cantilevers obtained from the parabola calculated with the least square fitting routine.

find the expression of the parabolas, all the five measured points have been considered.

The radius of curvatures and the top surface residual stresses calculated from these parabolas are comparable with the results obtained in sec. 6.2, such agreement confirms the correctness of the analysis performed. The radius of curvatures and the residual stresses at the top surface of the cantilevers obtained from these new parabolas are reported in tab. 6.4.

## 6.5 Summary

In this chapter a method to evaluate the residual stress in released cantilevers has been presented. The method makes use of the equations of the beam theory, it is not limited to small deflections of the free end and it does not

suffer of some limitations which apply to the Stoney formula.

In the presented method the deflection of a released micro-cantilever is measured at different distances from the anchor point, with these data, the mathematical expression of the deflection curve is calculated. This enables us to calculate the radius of curvature of the structure and so the residual stress at the cantilever top surface.

The analysis has been performed on cantilevers having layer sequences:

- $SrRuO_3/BaTiO_3/SrRuO_3$  (OP);
- $BaTiO_3/MgO/SrTiO_3$  (IP);
- $BaTiO_3/SrTiO_3$  (Bi).

U-shape and single beam micro-cantilevers with lengths between  $32\ \mu m$  and  $234\ \mu m$  have been analysed, the experimental residual stresses at the top surface vary between  $-0.051 \cdot 10^9\ N/m^2$  and  $-0.200 \cdot 10^9\ N/m^2$ .

The experimental results have been compared to two models in which the stresses are determined by lattice parameter mismatch or differences in thermal expansion coefficients. The experimentally determined residual stresses of the IP and OP devices were found to agree with the calculated thermal stresses, suggesting that the latter is the source of the curvature, rather than the lattice mismatch. For the Bi structures the experimental stresses are three times bigger than the theoretically calculated thermal stress, however in this case a large uncertainty (up to  $\pm 0.136 \cdot 10^9\ N/m^2$ ) is associated with the experimental values.

Comparing experimental and theoretical values the analysis reveals that the bending of the structures after their release is mainly due to the mis-

match of the thermal expansion coefficients between the different layers. This happens because the stress due to the lattice mismatch is released by the formation of dislocations when the film exceeds its critical thickness.

Finally other sources of stress like microscopic voids, incorporation of impurities and recrystallization can give rise to deviations from the theoretical values of the thermal stresses.

# Chapter 7

## Electrical characterization

In this chapter the resistivity measurements of  $SrRuO_3$  films plus the impedance and hysteresis loop measurements on the  $BaTiO_3$  based ferroelectric capacitors are discussed and analysed.

Section 7.1 reports the resistivity measurements performed on a  $SrRuO_3$  line grown by pulse laser deposition. Section 7.2.1 presents the lumped element model adopted for the fabricated  $BaTiO_3$  based capacitive structures. In section 7.2.2 the impedance measurements performed on the  $BaTiO_3$  capacitors grown directly on  $SrTiO_3$  substrate are reported and analysed. Instead in section 7.2.3 the impedance measured of  $BaTiO_3$  based capacitive structures grown on  $YBa_2Cu_3O_7$  and  $MgO$  sacrificial layers are discussed and compared to the measurements performed on the capacitors grown on  $SrTiO_3$  substrate. Section 7.2.4 shows how the  $BaTiO_3$  deposition parameters affect the properties of the fabricated capacitors. Finally section 7.3 reports the results of the hysteresis loop measurements performed on the  $BaTiO_3$  ferroelectric capacitors.

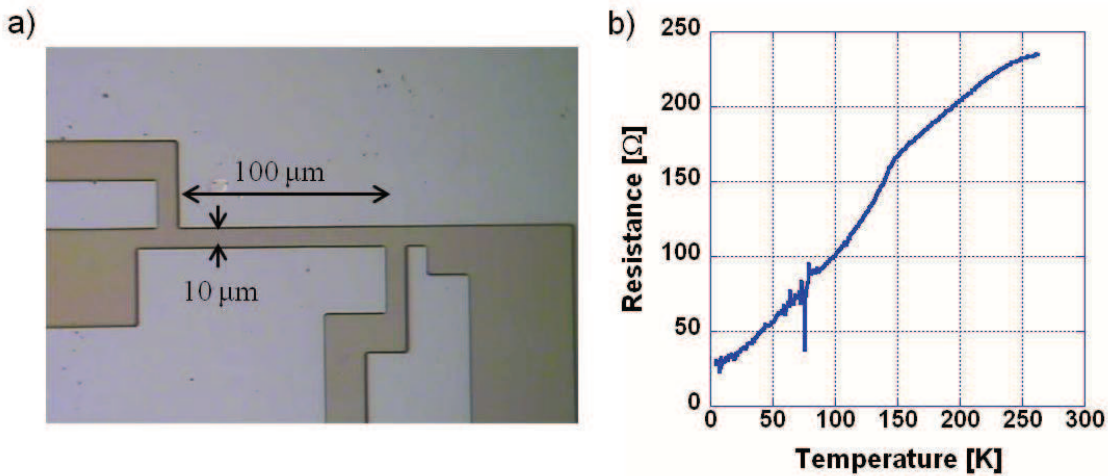


Figure 7.1: a) 100  $\mu m$  long, 10  $\mu m$  wide and 0.12  $\mu m$  high  $SrRuO_3$  line. b) Resistance versus temperature measurement of the  $SrRuO_3$  line, the measurement has been run with the 4-tip technique.

## 7.1 Resistivity of the $SrRuO_3$ layer

In this project the  $SrRuO_3$  has been used as an electrode layer. It has been reported that the resistivity of the  $SrRuO_3$  deposited by pulsed laser deposition technique varies as function of the deposition temperature and it approaches its minimum value for deposition temperatures over 780°C [25].

The ablation conditions for the  $SrRuO_3$  are reported in tab. 4.1,  $SrRuO_3$  films have been grown at a temperature of 780°C and in oxygen flow at a pressure of 40 Pa.

Resistivity measurements on the deposited  $SrRuO_3$  layers have been conducted to check that the deposited films have the expected conductive behaviour. In order to achieve this a 100  $\mu m$  long, 10  $\mu m$  wide and 0.12  $\mu m$  high  $SrRuO_3$  line has been prepared (fig. 7.1a). Resistance versus tempera-

ture measurements have been run with the 4-probe technique by using the method which will be described in sec. D.2.5.

Fig. 7.1b show the resistance of the  $SrRuO_3$  line as function of temperature, the value of the resistance decreases with temperature indicating a metallic behaviour of the line. The room temperature resistivity is  $284 \mu\Omega cm$ , at  $4 K$  the value of the resistivity is equal to  $31 \mu\Omega cm$  in agreement with [95]. Such values confirm that the grown  $SrRuO_3$  can be used as electrode layer.

## 7.2 Measured impedance of the $BaTiO_3$ based capacitors

### 7.2.1 Device modeling

Let us imagine measuring the impedance of a certain film sandwiched between two electrodes layers, and let us assume a certain value for the real part of the impedance and a certain value for its imaginary part. Alternatively it is possible to consider the representation of the impedance as modulus and phase. If the imaginary part of the impedance or alternatively the phase of the impedance is negative, the structure under investigation exhibits capacitive behaviour. The real part is associated with the losses present in the film. Two models are possible for such an impedance, they consist of a capacitor and a resistor connected in series or a capacitor and a resistor connected in parallel. In both cases the total impedance is given by a positive real part and a negative imaginary part or alternatively by a certain value of the modulus and a negative value of the phase. The diffe-

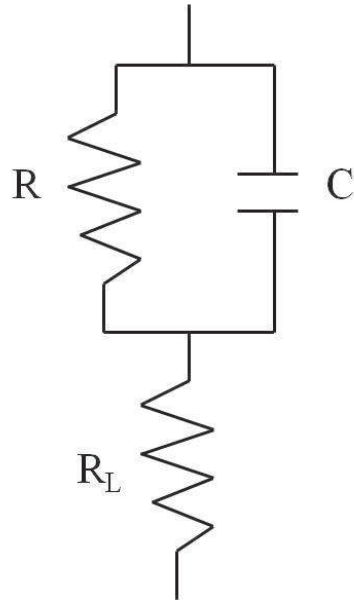


Figure 7.2: The equivalent model of the  $BaTiO_3$  based capacitive structures is constituted by a capacitor  $C$  and a resistor  $R$  connected in parallel, the resistor  $R_L$  models the resistive contribution of the  $SrRuO_3$  lines connecting the device to the contact pads.

rence between the two models consists in the different values (resistance and capacitance) of the lumped elements in the model.

In sec. 3.6 the method used to measure the hysteresis loop of our  $BaTiO_3$  based capacitive structures has been discussed, in that case the model consisting of a resistor and a capacitor connected in series has been introduced. However the model which is usually adopted to model capacitive structures based on ceramic materials is that one of a capacitor and a resistor connected in parallel fig. 7.2 [96]. This is not inconsistent with what has been reported in sec. 3.6. In that case the modeling of the structure is only necessary to establish the values of the external capacitance and of the external resistance ( $C_0$  and  $R_0$ , see sec. 3.6) to introduce in the Sawyer and Tower circuit in

order to compensate the phase factor introduced in the hysteresis loop by the finite conductivity of the structure under investigation [97].

Here the fabricated capacitive structures are modelled with a resistor  $R$  and a capacitor  $C$  connected in parallel as shown in fig. 7.2.  $R_L$  is the series resistance which models the resistive contribution of the  $SrRuO_3$  lines connecting the device to the contact pads. The capacitor  $C$  represents the capacitance of the device,  $R$  is a parallel resistor modeling the parasitic shunting conductance representing the losses present in the  $BaTiO_3$  film.

As already reported in sec. 1.4  $SrRuO_3/BaTiO_3/SrRuO_3$  parallel plate capacitors are integrated on the top of the cantilevers to produce energy harvesting devices working with the 31 piezoelectric mode, instead

$SrRuO_3/BaTiO_3/MgO$  capacitive structures are used for the 33 mode cantilevers. Both structures are grown on a  $YBa_2Cu_3O_7$  sacrificial layer, eventually a  $SrTiO_3$  buffer layer might be introduced between the  $YBa_2Cu_3O_7$  and the capacitive structure, see sec. 4.3. When the  $MgO$  is used as sacrificial layer the 31 mode layer sequence is:

$SrRuO_3/BaTiO_3/SrRuO_3/(SrTiO_3)/MgO$ ; while the 33 mode layer sequence is  $SrRuO_3/BaTiO_3/MgO$ .

Fig. 7.3 shows one 33 mode and one 31 mode capacitive structures fabricated during this Phd.

Let us consider the model of fig. 7.2, when a dc voltage is applied to the circuit, the capacitor behaves as an open circuit, so the total impedance is given by the sum of the parallel and of the series resistor. This means that dc current versus voltage measurements allow the value of the parallel resistor  $R$  to be estimated. Sec. 7.1 reports the room temperature resistivity

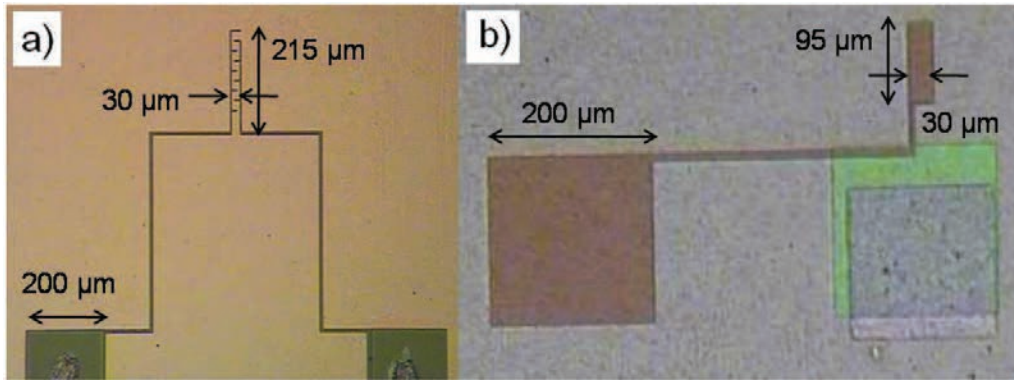


Figure 7.3: a)  $SrRuO_3/BaTiO_3/MgO$   $215\text{ }\mu\text{m} \times 30\text{ }\mu\text{m}$  interdigitated 33 mode capacitor grown on  $SrTiO_3$  substrate. In the picture the lines and the contact pads are shown. b)  $SrRuO_3/BaTiO_3/SrRuO_3/SrTiO_3/YBa_2Cu_3O_7$   $95\text{ }\mu\text{m} \times 30\text{ }\mu\text{m}$  31 mode parallel plate capacitor grown on  $SrTiO_3$  substrate. In the picture the lines and the contact pads are shown.

of the grown  $SrRuO_3$  films, this value can be used to estimate the series resistance  $R_L$  associated with the lines connecting the capacitor to the pads. The parallel resistor  $R$  is calculated by subtracting the series resistance from the measured dc resistance. The impedance of the circuit shown in fig. 7.2 has the following expression:

$$z(j\omega) = R_L + \frac{R}{1 + (\omega CR)^2} - j \frac{\omega CR^2}{1 + (\omega CR)^2}. \quad (7.1)$$

The value of the capacitance can be estimated by equating the measured imaginary part of the impedance to the imaginary part of eq. 7.1. This gives rise to a quadratic equation, the root that is inconsistent with the real part of the impedance, is rejected.

This can be repeated at different frequencies and finally the estimated

capacitance can be chosen equal to the average of the calculated values. Once that the parameters  $R$ ,  $R_L$  and  $C$  have been estimated, their value have been refined by minimizing the quantity:

$$[Re(z)_m - Re(z)_p]^2 + [Im(z)_m - Im(z)_p]^2 \quad (7.2)$$

with the help of a least square fitting routine of Excel, where  $Re(z)_m$  is the measured real part of the impedance and  $Re(z)_p$  is the real part of the impedance calculated by assuming the lumped element model of fig. 7.2, similar nomenclature has been used for the imaginary part of the impedance.

After the refinement the resistance and capacitance values changed by some percent ( $1\% - 10\%$ ).

Now the impedance of the lumped element model can be compared with the measured data.

### 7.2.2 Analysis of $BaTiO_3$ capacitive structures grown directly on $SrTiO_3$ substrate

At the beginning on this project 33 and 31 mode capacitive structures have been grown on  $SrTiO_3$  substrates. They showed resistive behaviour when the  $BaTiO_3$  has been grown in oxygen flow at a pressure of  $20\text{ Pa}$ , fig. 7.4, this can be seen by the low value of the phase of the impedance. When the growing pressure is reduced to  $8\text{ Pa}$  the capacitive behaviour is recovered.

The continuous lines of fig. 7.5a report the measured modulus and the measured phase of a 31 mode  $SrRuO_3/BaTiO_3/SrRuO_3$  parallel plate capacitor belonging to the sample  $GV33(P)$  while the continuous lines of fig.

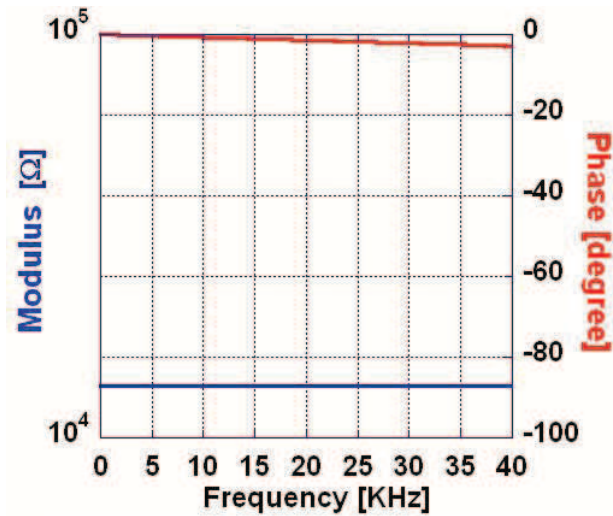


Figure 7.4: Impedance measurements on a  $215\mu m \times 30\mu m$   $SrRuO_3(100\text{nm})/BaTiO_3(300\text{nm})/MgO(60\text{nm})$  interdigitated capacitor grown on a (001) oriented  $SrTiO_3$  substrate. The  $BaTiO_3$  was grown at  $780^\circ C$  at a pressure of  $20\text{ Pa } O_2$ . Impedance measurements were performed with an input signal amplitude of  $1\text{ V}$ .

7.5b report the measured modulus and the measured phase of a 33 mode  $SrRuO_3/BaTiO_3/MgO$  interdigitated capacitor belonging to the sample  $GV36(P)$ , both devices have been grown on  $SrTiO_3$  substrate. The 31 mode capacitor presents an impedance phase between  $-85^\circ$  and  $-82^\circ$  in the frequency range  $40\text{ Hz} - 40\text{ KHz}$  while the 33 mode capacitor has an impedance phase around  $-89^\circ$  in the frequency range  $40\text{ Hz} - 50\text{ KHz}$ . With these values of the impedance phase both devices can be approximated as a pure capacitor, this means that the parallel resistor  $R$  in the model of fig. 7.2, is approximated as an open circuit and the model for both devices reduces to a capacitor connected in series with the resistor  $R_L$ . The moduli and the phases of the two models are represented in fig. 7.5 by the dotted lines.

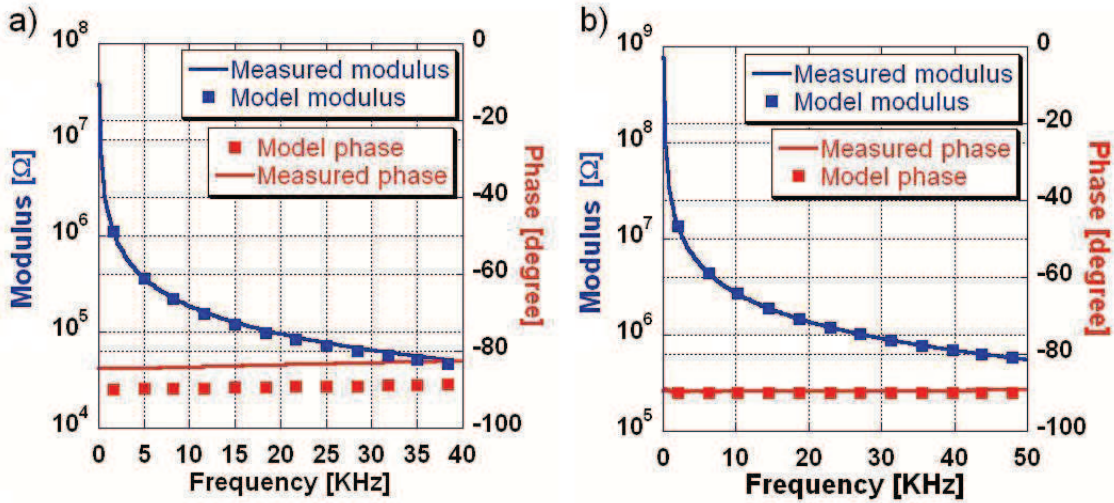


Figure 7.5: a) Impedance measurements on a  $105\text{ }\mu\text{m} \times 30\text{ }\mu\text{m}$   $\text{SrRuO}_3(100\text{ nm})/\text{BaTiO}_3(300\text{ nm})/\text{SrRuO}_3(150\text{ nm})$  parallel plate capacitor grown on a (001) oriented  $\text{SrTiO}_3$  substrate. The  $\text{BaTiO}_3$  was grown at  $780^\circ\text{C}$  at a pressure of  $8\text{ Pa O}_2$ . Impedance measurements were performed with an input signal amplitude of  $1\text{ V}$ ; b) Impedance measurement on a  $\text{SrRuO}_3(100\text{ nm})/\text{BaTiO}_3(300\text{ nm})/\text{MgO}(60\text{ nm})$  interdigitated capacitive structure, the spacing between the fingers is equal to  $30\text{ }\mu\text{m}$ .

With the reduction of the deposition pressure the capacitive behaviour of our devices has been recovered, an higher deposition pressure implies a larger number of collisions in the path between the material target and the substrate during the pulsed laser deposition of the film. The energy lost in the ablation path produces a lower mobility of the atomic species on the substrate which is further reduced by the relatively high deposition pressure. The growth of the film is accompanied by the formation of stacking faults and amorphous and void like grain boundaries and their density depends upon the surface mobility of the incoming atoms [92]. The higher kinetic energy of the impinging species at lower pressure [98], which produces the increase of

the mobility on the substrate, is believed to improve the structure of the films leading to the capacitive behaviour. An investigation of the crystal structure of the  $BaTiO_3$  grown at a deposition pressure lower than  $20\text{ Pa}$  is necessary to confirm this idea; however Wang et al. [67] reported the presence of sharp and intense peaks, indication of a good crystal structure, for  $BaTiO_3$  grown on  $MgO$  substrate at an oxygen pressure of  $5\text{ Pa}$ . Sato et al. [99] showed that X-ray diffraction does not show remarkable change for  $BaTiO_3$  films grown in the pressure range  $1.33 \cdot 10^{-2} - 1.33 \cdot 10^{-4}\text{ Pa}$  on  $MgO$  and  $SrTiO_3$  substrates.

On each sample 24 capacitive structures are integrated, not all the devices present the same behaviour as some structures present more resistive losses than others. The data relative to the impedance measurements of all the investigated devices are reported in appendix C.

On sample  $GV33(P)$  at the frequency of  $500\text{ Hz}$  five devices present an impedance phase between  $-80^\circ$  and  $-90^\circ$  (the device in fig. 7.5 is one of these capacitors), for nine devices the phase of the impedance lies between  $-70^\circ$  and  $-90^\circ$ . At  $5\text{ KHz}$  five structures present an impedance phase between  $-80^\circ$  and  $-90^\circ$  while sixteen devices show a value between  $-70^\circ$  and  $-90^\circ$ . For an ideal capacitor, the phase of the impedance is equal to  $-90^\circ$ , we consider good capacitive structures devices having an impedance phase in the range between  $-70^\circ$  and  $-90^\circ$  on all the measurement range. An increase of the impedance phase is an indication of an increased numbers of resistive paths in the film. On sample  $GV33(P)$  two fabricated structures behave as resistors all over the measured frequency range.

We believe that some areas of the grown films might not have a perfect

crystal structure and/or the right stoichiometry, leading to resistive losses in the layer. Abe et al. [100] hypothesize the presence of a *non-switching* layer at the  $BaTiO_3/SrRuO_3$  interface containing dislocations and other type of defects, such non-switching layer could also influence the growth and the density of defects of the  $BaTiO_3$  film. Nevertheless a further investigation is necessary to understand the origin of the resistive paths.

On sample  $GV36(P)$  eleven interdigitated structures behave as resistors in the frequency range  $40\text{ }HZ - 50\text{ }KHz$ , while at  $500\text{ }Hz$  nine devices present an impedance phase between  $-80^\circ$  and  $-90^\circ$  indicating good capacitive behaviour. Ten of the eleven structures showing resistive behaviour are near to each other indicating a problem in that region of the  $BaTiO_3$  film. Alternatively problems might arise from a not uniform milling of the top electrode all over the sample, for example because the thickness of the  $SrRuO_3$  is not the same everywhere, this might leave some resistive paths between the fingers of the interdigitated top electrode.

It is important to highlight that 31 and 33 mode capacitors having parallel plate or interdigitated area equal to  $95\text{ }\mu m \times 30\text{ }\mu m$ ,  $105\text{ }\mu m \times 30\text{ }\mu m$ ,  $205\text{ }\mu m \times 30\text{ }\mu m$  and  $215\text{ }\mu m \times 30\text{ }\mu m$  have been fabricated. For  $BaTiO_3$  thicknesses in the range  $200\text{ }nm - 400\text{ }nm$  capacitance value with orders of magnitude  $10^{-12}\text{ }F - 10^{-10}\text{ }F$  have been measured. Of course the probability of finding defects in the dielectric layer of the capacitor increases when the area of the device increases leading to resistive losses.

Sample  $GV36(P)$  contains a larger number of structures having resistive behaviour than sample  $GV33(P)$ , however for the devices of sample  $GV36(P)$  which behaves as capacitors, the impedance phase is around  $-89^\circ$  all over

the measured frequency range. In general the 33 mode structures can be approximated as ideal capacitors, the worst case is represented by the 31 mode devices. This might also be a consequence of the spacing between the two electrodes, in fact in a 31 mode capacitor such spacing is equal to  $300\text{ nm}$  while in a 33 structure the spacing between the fingers of the electrode is at least equal to  $10\text{ }\mu\text{m}$ .

In the following part of this chapter an optimization of the worst case represented by the 31 mode devices, is performed. By optimatizing the 31 mode capacitors the improvements are also reflected on the 33 mode devices.

### 7.2.3 Analysis of $\text{BaTiO}_3$ capacitive structures grown on the sacrificial layer

Different multilayer structures have been investigated:

- $\text{SrRuO}_3/\text{BaTiO}_3/\text{SrRuO}_3/\text{SrTiO}_3/\text{YBa}_2\text{Cu}_3\text{O}_7$  labeled as *SBSSY*;
- $\text{SrRuO}_3/\text{BaTiO}_3/\text{SrRuO}_3/\text{SrTiO}_3/\text{MgO}$  labeled as *SBSSM*;
- $\text{SrRuO}_3/\text{BaTiO}_3/\text{SrRuO}_3/\text{MgO}$  labeled as *SBSM*.

In this investigation parameters like the RA (Resistance-Area) product and the C/A (Capacitance/Area) ratio are introduced because they do not depend on the area of the devices and allow to compare structures with different faced area.

The  $\text{BaTiO}_3$  deposition pressures and temperatures, the RA products and the C/A ratios of the investigated structures are reported in tab. 7.1.

Device (fig.) (Sample)	Top-down layer sequence	$BaTiO_3$ dep. temperature [°C]	$BaTiO_3$ dep. pressure [Pa]	RA [Ωμm <sup>2</sup> ]	C/A [F/μm <sup>2</sup> ]
SBSSY (fig. 7.6a) (GV38(P))	$SrRuO_3(100nm)/BaTiO_3(300nm)/$ $SrRuO_3(150nm)/SrTiO_3(250nm)/$ $YBa_2Cu_3O_7(500nm)$	780	8	$44.1 \cdot 10^5$	$6.28 \cdot 10^{-13}$
SBSSY (fig. 7.6b) (GV42(P))	$SrRuO_3(100nm)/BaTiO_3(300nm)/$ $SrRuO_3(150nm)/SrTiO_3(1000nm)/$ $YBa_2Cu_3O_7(500nm)$	780	8	$19.54 \cdot 10^7$	$7.8 \cdot 10^{-14}$
SBSSM (fig. 7.6c) (GV41(P))	$SrRuO_3(100nm)/BaTiO_3(300nm)/$ $SrRuO_3(150nm)/SrTiO_3(250nm)/$ $MgO(400nm)$	780	8	$61.93 \cdot 10^8$	$3.04 \cdot 10^{-14}$
SBSM (fig. 7.6e) (GV45(P))	$SrRuO_3(100nm)/BaTiO_3(300nm)/$ $SrRuO_3(150nm)/MgO(800nm)/$	830	8/ 0.027	$\approx \infty$	$3.9 \cdot 10^{-14}$
SBSM (fig. 7.6d) (GV43(P))	$SrRuO_3(100nm)/BaTiO_3(300nm)/$ $SrRuO_3(150nm)/MgO(400nm)/$	780	0.013	$\approx \infty$	$1.76 \cdot 10^{-14}$

Table 7.1: Top down layer sequences,  $BaTiO_3$  deposition pressure and temperature, RA product and C/A ratio of the structures under investigation.

With the introduction of an oxide sacrificial layer under the multi-layer capacitive structures the electrical properties of the  $BaTiO_3$  change. When the  $YBa_2Cu_3O_7$  is used as sacrificial layer, *SBSSY* stacks have been investigated (sample *GV38(P)*), here the  $BaTiO_3$  film has been grown at an oxygen pressures of 8 Pa. In contrast with the structure directly grown on the  $SrTiO_3$  substrate, these devices presented poor capacitive behavior. Fig. 7.6a shows the impedance measurement on a *SBSSY* 31 mode device of sample *GV38(P)*. In this case the impedance is mainly resistive, around 20 KHz some capacitive effects start to be visible, at 50 KHz the impedance phase is around  $-23^\circ$ .

Our impedance analyzer allows a minimum measurement frequency of 40 Hz, at this frequency the phase of the impedance is equal to  $-0.1^\circ$  so

the impedance can be considered as pure resistive and the parallel and the series resistances can be calculated. The parallel resistance is estimated equal to  $1.4 K\Omega$  resulting in a resistance area (RA) product of  $44.1 \cdot 10^5 \Omega \mu m^2$ . The calculated series resistance has a value of  $1.086 K\Omega$  and the estimated capacitance is equal to  $1.98 nF$  resulting in a capacitance over area (C/A) ratio of  $6.28 \cdot 10^{-13} F/\mu m^2$ .

Fig. 7.6a also shows a fit of the data obtained using the lumped element model (dotted lines), there is a good agreement between the model and the measured data. This device shows poor capacitive behavior to the extent that the low value of the parallel resistance dominates the parallel capacitor.

Studies on the pulsed laser deposition of  $YBa_2Cu_3O_7$  films reported the presence of different types of particulates on their surface [98]. It is likely that such particulates degrade the quality of the layers deposited on their surface, by creating resistive paths through the capacitive structures which might be responsible for the low value of the RA product. In order to investigate this, an Atomic Force Microscope was used to examine the surface of the deposited  $YBa_2Cu_3O_7$  films. Fig. 7.7a shows an AFM scan (for more details on AFM measurements see sec. D.2.4) on the surface of a  $150 nm$   $YBa_2Cu_3O_7$  layer, on whose surface it is possible to see an outgrowth with a height comparable to the film thickness. Some outgrowths might be present even after the optimization of the  $YBa_2Cu_3O_7$  ablation parameters performed for the superconductivity project during the first part of this phd and described in sec. D.3.2.

Such outgrowths are also present after the deposition of a  $100 nm$   $SrTiO_3$  layer as shown in, fig. 7.7b. Their effect on the upper films can be reduced

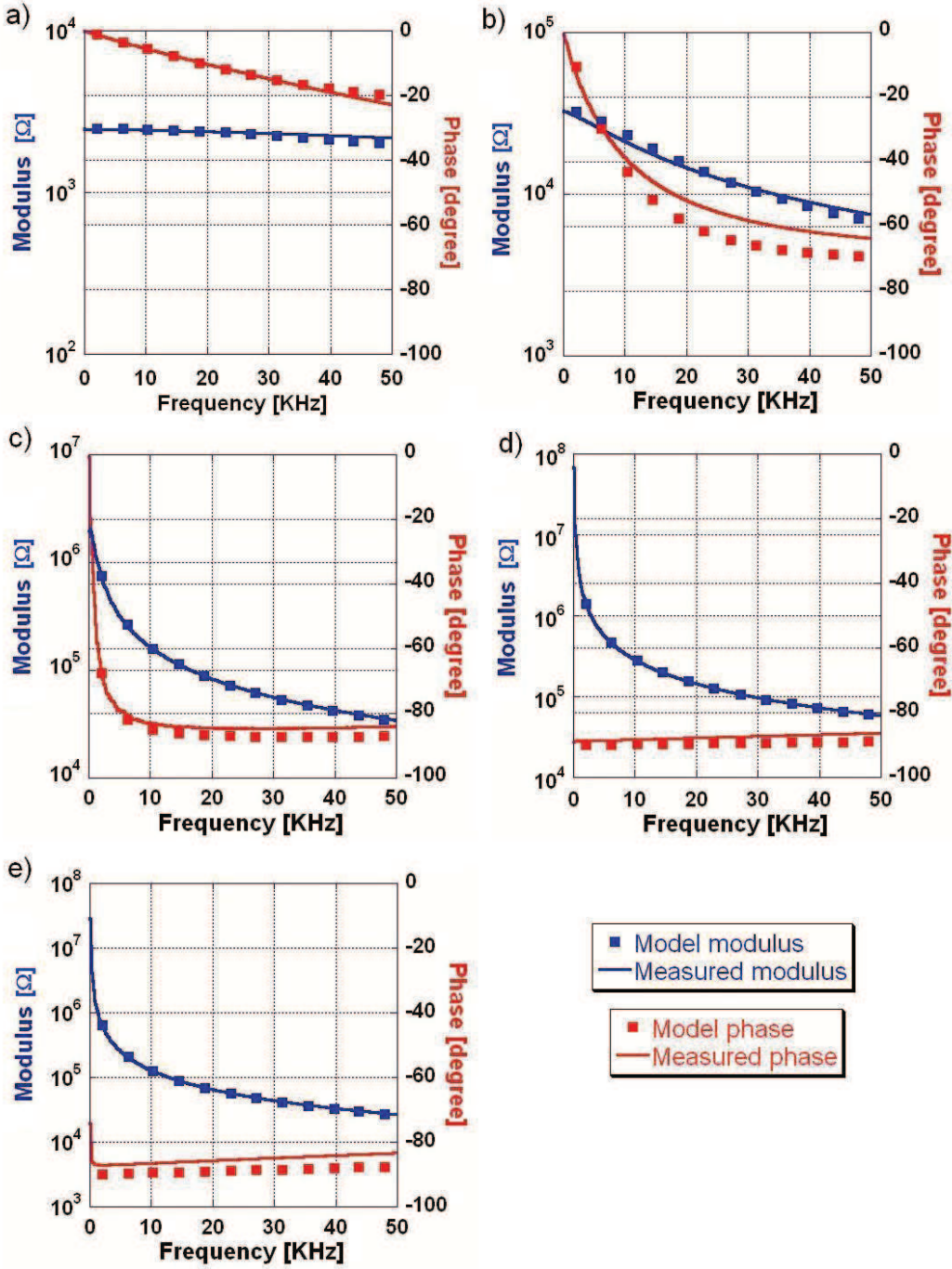


Figure 7.6: Impedance measurement of a: a) 105  $\mu\text{m} \times 30 \mu\text{m}$  SBSSY parallel plate capacitor. The BaTiO<sub>3</sub> has been grown at 780°C at a pressure of 8 Pa O<sub>2</sub>; b) 205  $\mu\text{m} \times 30 \mu\text{m}$  SBSSY parallel plate capacitor with 1  $\mu\text{m}$  thick SrTiO<sub>3</sub> buffer layer. The BaTiO<sub>3</sub> was grown at 780°C at a pressure of 8 Pa O<sub>2</sub>; c) 105  $\mu\text{m} \times 30 \mu\text{m}$  SBSSM parallel plate capacitor. The BaTiO<sub>3</sub> was grown at 780°C at a pressure of 8 Pa O<sub>2</sub>; d) 105  $\mu\text{m} \times 30 \mu\text{m}$  SBSM parallel plate capacitor. The BaTiO<sub>3</sub> was grown at 780°C at a pressure of 0.013 Pa O<sub>2</sub>; e) 105  $\mu\text{m} \times 30 \mu\text{m}$  SBSM parallel plate capacitor. The BaTiO<sub>3</sub> was grown at 830°C at a pressure of 0.027 Pa and 8 Pa O<sub>2</sub>.

The continuous lines represent the measured modulus and phase, the dotted lines are the modulus and phase of the assumed lumped elements model. The thicknesses of the layers in the stacks are reported in tab. 7.1

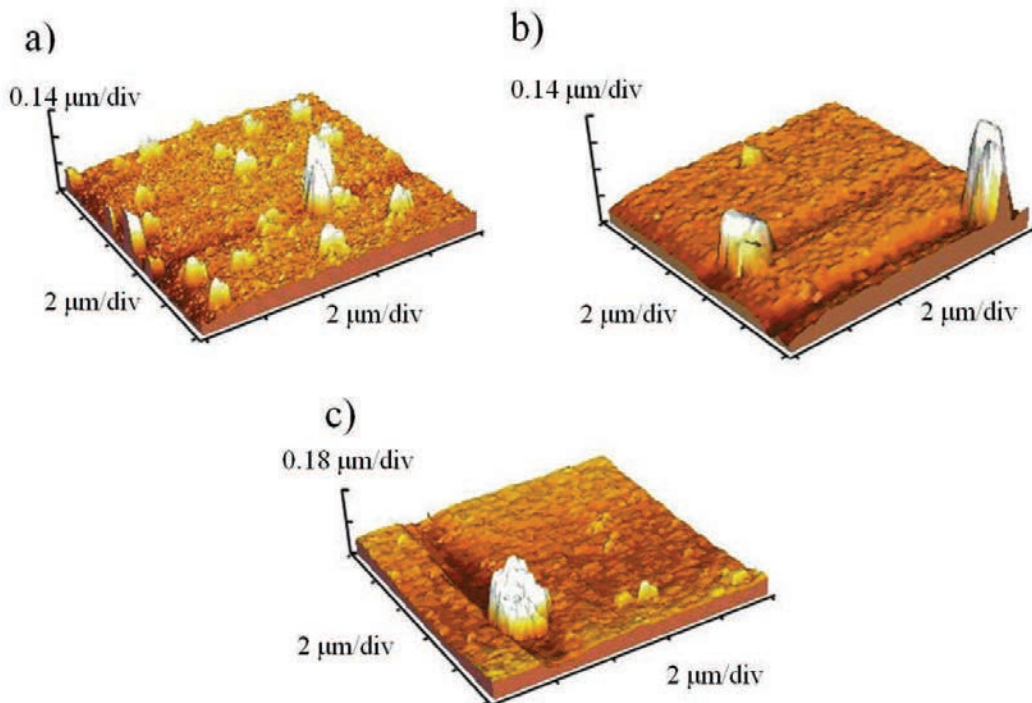


Figure 7.7: AFM scan of a  $10\text{ }\mu\text{m} \times 10\text{ }\mu\text{m}$  area of: a)  $150\text{ nm}$   $\text{YBa}_2\text{Cu}_3\text{O}_7$  film, b)  $\text{SrTiO}_3(100\text{ nm})/\text{YBa}_2\text{Cu}_3\text{O}_7(150\text{ nm})$  bi-layer, c)  $\text{SrTiO}_3(500\text{ nm})/\text{YBa}_2\text{Cu}_3\text{O}_7(400\text{ nm})$  bi-layer.

using a thicker  $\text{SrTiO}_3$  layer. Fig. 7.7c shows an AFM scan on a  $\text{SrTiO}_3(500\text{ nm})/\text{YBa}_2\text{Cu}_3\text{O}_7(400\text{ nm})$  bi-layer which confirms that the particulates present on the surface of the film are fewer in number and generally smaller.

Fig. 7.6b reports the impedance measurements (continuous lines) of a *SBSSY* device with a  $1\text{ }\mu\text{m}$  thick  $\text{SrTiO}_3$  film on the  $\text{YBa}_2\text{Cu}_3\text{O}_7$  sacrificial layer (sample *GV42(P)*), the  $\text{BaTiO}_3$  deposition pressure used was equal to  $8\text{ Pa}$ . Also in this case the impedance is not fully capacitive, at  $40\text{ Hz}$  the impedance phase is equal to  $-0.5^\circ$ . The series resistance is equal to

$1.086\text{ }K\Omega$ , the parallel resistance has a value of  $31.78\text{ }K\Omega$  resulting in a RA product of  $19.54 \cdot 10^7\text{ }\Omega\mu\text{m}^2$  and the capacitance is equal to  $480\text{ }pF$  giving a C/A ratio of  $7.8 \cdot 10^{-14}\text{ }F/\mu\text{m}^2$ . The dotted lines in figs. 7.6b represent the modulus and the phase of the lumped element model. The impedance modulus of the lumped element model agrees quite well with the measured data while an error of 8% is present in the value of the impedance phase over  $20\text{ }KHz$ .

The introduction of a thicker  $SrTiO_3$  buffer layer reduces the parasitic shunting conductance and so the losses which are present in the  $BaTiO_3$  film due to the outgrowths on the surface of the  $YBa_2Cu_3O_7$  sacrificial layer. This is illustrated by the higher value of the RA product, however the quality of this device is still not satisfactory especially at low frequencies where the resistive part of the impedance dominates.

In the case of capacitors grown directly on the substrate it has been demonstrated that the reduction of the  $BaTiO_3$  deposition pressure reduces the parasitic shunting conductance and so the losses present in the film. When a  $YBa_2Cu_3O_7$  sacrificial layer is used a further reduction of the  $BaTiO_3$  deposition pressure is not possible as it would cause the dissociation of the sacrificial layer at the  $BaTiO_3$  deposition temperature [101].

Another solution is to use an  $MgO$  sacrificial layer, see sec. 4.4. Fig. 7.6c shows the impedance measurement on a SBSSM device (sample GV41(P)). In this case the  $BaTiO_3$  has been grown at  $780^\circ C$  at a pressure of  $8\text{ }Pa$ .

Assuming for this device the model of fig. 7.2, the resistance of the lines  $R_L$  is  $1.17\text{ }K\Omega$ , the parallel resistor  $R$  is equal to  $1.966\text{ }M\Omega$  resulting in a RA product of  $61.93 \cdot 10^8\text{ }\Omega\mu\text{m}^2$ , the capacitance is equal to  $95.66\text{ }pF$  and gives a

C/A ratio of  $3.04 \cdot 10^{-14} F/\mu m^2$ . The modulus and the phase of the model are represented by the dotted lines of fig. 7.6c. The plots show good agreement between the model and the measured data.

There is a difference of one order of magnitude between the RA product of this device and that one of the device using a  $1 \mu m$  thick  $SrTiO_3$  buffer layer on a  $YBa_2Cu_3O_7$  sacrificial layer. Compared to that case, this high value of the RA product makes the capacitive part of the impedance dominate at much lower frequencies. At  $5.5 KHz$  the phase of the total impedance is equal to  $-80^\circ$ , the capacitive part of the impedance is roughly 7 times smaller than the parallel resistance and 250 times bigger than the series resistance, so over  $5.5 KHz$  the device can be approximated as a pure capacitor.

If the  $BaTiO_3$  deposition pressure is further reduced to  $0.013 Pa$  the losses are eliminated also at low frequency (sample  $GV43(P)$ ), this is shown in fig. 7.6d, and an impedance phase of  $-88^\circ$  is already present at  $50 Hz$ . Due to the high value of the impedance phase at low frequencies, the parallel resistor can be approximated as an open circuit and the equivalent model of the device is given by the resistor  $R_L$  in series with the capacitor  $C$ . For this device the series resistance was estimated equal to  $1.086 K\Omega$  while the capacitance is equal to  $55.57 pF$  resulting in a C/A ratio of  $1.76 \cdot 10^{-14} F/\mu m^2$ . By using these values in the lumped element model good agreement is obtained with the measured data.

This demonstrates that a reduction of the  $BaTiO_3$  deposition pressure reduces the parasitic shunting conductance and so the resistive losses present in the film, furthermore in this case the approximation of the parallel resistor with an open circuit works quite well and the behavior of the device can be

approximated as pure capacitive.

Besides the reduction of the  $BaTiO_3$  deposition pressure, the mobilities of the ablated species on the substrate can be increased by increasing the  $BaTiO_3$  deposition temperature. Fig. 7.6e reports the impedance measurement of a *SBSM* device with a  $BaTiO_3$  deposited at a temperature of  $830^\circ C$  and at two different pressures. Initially a  $50\text{ nm}$   $BaTiO_3$  seed layer has been grown in oxygen flow at a pressure of  $0.027\text{ Pa}$  then  $250\text{ nm}$   $BaTiO_3$  have been grown at a pressure of  $8\text{ Pa}$ . The low deposition pressure used for the seed layer is supposed to provide a layer with few losses acting as a seed for the  $BaTiO_3$  grown at the pressure of  $8\text{ Pa}$  which presents good hysteresis properties (see sec. 7.3).

The device of fig. 7.6e presents an impedance phase of  $-86^\circ$  at  $300\text{ Hz}$  indication of good capacitive properties. Also in this case as consequence of the high value of the impedance phase all over the measured frequency range, the parallel resistor is approximated with an open circuit. The series resistor  $R_L$  is estimated equal to  $1.086\text{ K}\Omega$  while the capacitance of the device is approximately  $123\text{ pF}$  resulting in a C/A ratio equal to  $3.9 \cdot 10^{-14}\text{ F}/\mu\text{m}^2$ . Also in this case there is a good agreement between the measurements and the lumped element model, fig. 7.6e.

#### 7.2.4 Discussion on the impedance measurements

Except for the presence of the seed layer the  $BaTiO_3$  layer of the devices of fig. 7.6c and e have been grown at the same oxygen pressure. The higher deposition temperature used for the device of fig. 7.6e produced an higher

RA product which has been approximated with an open circuit. The higher deposition temperature has the same effects of a pressure reduction: both of them increase the mobility of the atomic species on the substrate which contribute to a reduction of the losses in the piezoelectric layer. This is confirmed by the fact that in both cases the parallel resistor is approximated with an open circuit.

Another parameter which can be used to increase the mobility on the substrate of the incoming atoms, is the laser energy, however the employed deposition energy is very near to the maximum achievable with our apparatus.

It is important to highlight that some problems arose for the stack containing the  $BaTiO_3$  grown at a temperature of  $830^{\circ}C$ , on some areas of the sample in fact the deposited layers peeled off leading to the damaging of eleven of the fabricated devices. This has been attributed to the thermal stress generated by the mismatch of the thermal expansion coefficients generated when the multi-layer is cooled down.

The reduction of the  $BaTiO_3$  deposition pressure not only produces an increase of the RA product, but it also produce a reduction of the C/A ratio which corresponds to a reduction of the parallel capacitance. Figs. 7.6c and d report the impedance measurements of two devices with the same faced area and the same  $BaTiO_3$  thickness, however for a  $BaTiO_3$  deposition pressure of  $8\text{ Pa}$  a C/A ratio of  $3.04 \cdot 10^{-14}\text{F}/\mu\text{m}^2$  was measured while for a  $BaTiO_3$  deposition pressure of  $0.013\text{ Pa}$  the C/A ratio is reduced to  $1.76 \cdot 10^{-14}\text{F}/\mu\text{m}^2$ . It was reported that in  $SrTiO_3/BaTiO_3$  systems grown by pulsed laser deposition the dielectric constant increases when the oxygen

deposition pressure increases [79]. If the oxygen pressure during the growth of the thin films is low it is more favorable to form oxygen vacancies in the oxide films during the process which results in a decrease of the dielectric constant [79].

It is important to report that the thickness of the sacrificial layer for the *SBSM* device of fig. 7.6e is equal to  $800\text{ nm}$ . During this project it has been verified that an increase in the thickness of the sacrificial layer usually corresponds to a more lossy capacitive structure. For example a *SBSSM* stack with a  $800\text{ nm}$  thick  $MgO$  sacrificial layer has been grown using a  $BaTiO_3$  deposition pressure of  $8\text{ Pa}$  and a deposition temperature of  $780^\circ$  (sample *GV46(P)*). These devices except for the thickness of the sacrificial layer are equal to the device of fig. 7.6c, however only resistive structures are present on this sample.

We believe that a thicker laser ablated layer contains more imperfections than a thinner one so it might not constitute an ideal seed layer for the epitaxial growth, that is why a stackable approach for the fabrication of the 31 and 33 mode cantilever already discussed in secs. 4.2 and 4.3 looks extremely challenging.

The devices of each samples do not present exactly the same properties, in fact some devices are more lossy than others, this can be seen by the value of the impedance phase of each device. A detailed description of the phase value of the impedance for all the devices of each of the analysed samples is reported in appendix C.

### 7.3 Hysteresis loop measurements

The method used to perform the hysteresis loop measurements has been already reported in sec. 3.6. Fig. 7.8 reports the hysteresis loop measurements of three  $SrRuO_3/BaTiO_3/SrRuO_3$  parallel plate capacitors.

In fig. 7.8a the hysteresis loop of a 31 mode device belonging to the sample  $GV33(P)$  is reported, for this sample a  $BaTiO_3$  layer with a thickness equal to  $400\text{ nm}$ , deposited at a pressure of  $8\text{ Pa}$  and grown at a temperature of  $780^\circ C$  has been used. The measured residual polarization is equal to  $5.3\text{ }\mu\text{C/cm}^2$ .

The hysteresis loop reported in fig. 7.8b belongs to the sample  $GV41(P)$  (see tab. 7.1), here the residual polarization is equal to  $2.5\text{ }\mu\text{C/cm}^2$ . Finally fig. 7.8c shows the hysteresis loop of a device belonging to the sample  $GV43(P)$  (see tab. 7.1), in this case the hysteresis behavior is not clear and the loop seems to be degraded into a double loop.

Yang et al. [65] reported the values of the residual polarization for  $BaTiO_3$  grown on different substrates and films. When the  $BaTiO_3$  is grown on  $SrTiO_3$  substrate a residual polarization equal to  $26\text{ }\mu\text{C/cm}^2$  is reported, this value is reduced to  $7\text{ }\mu\text{C/cm}^2$  for  $BaTiO_3$  grown on a  $Pt$  film on  $Si$  substrate and to  $5\text{ }\mu\text{C/cm}^2$  for  $BaTiO_3$  on a  $Ni$  foil substrate.

When our  $BaTiO_3$  films have been grown on a  $SrRuO_3$  layer the value of the residual polarization agrees with that one of the  $BaTiO_3/Pt$  system, indication that the residual polarization is reduced when the  $BaTiO_3$  is not directly grown on a single crystal substrate. A single crystal substrate constitutes a better seed layer than a thin film where a different number of

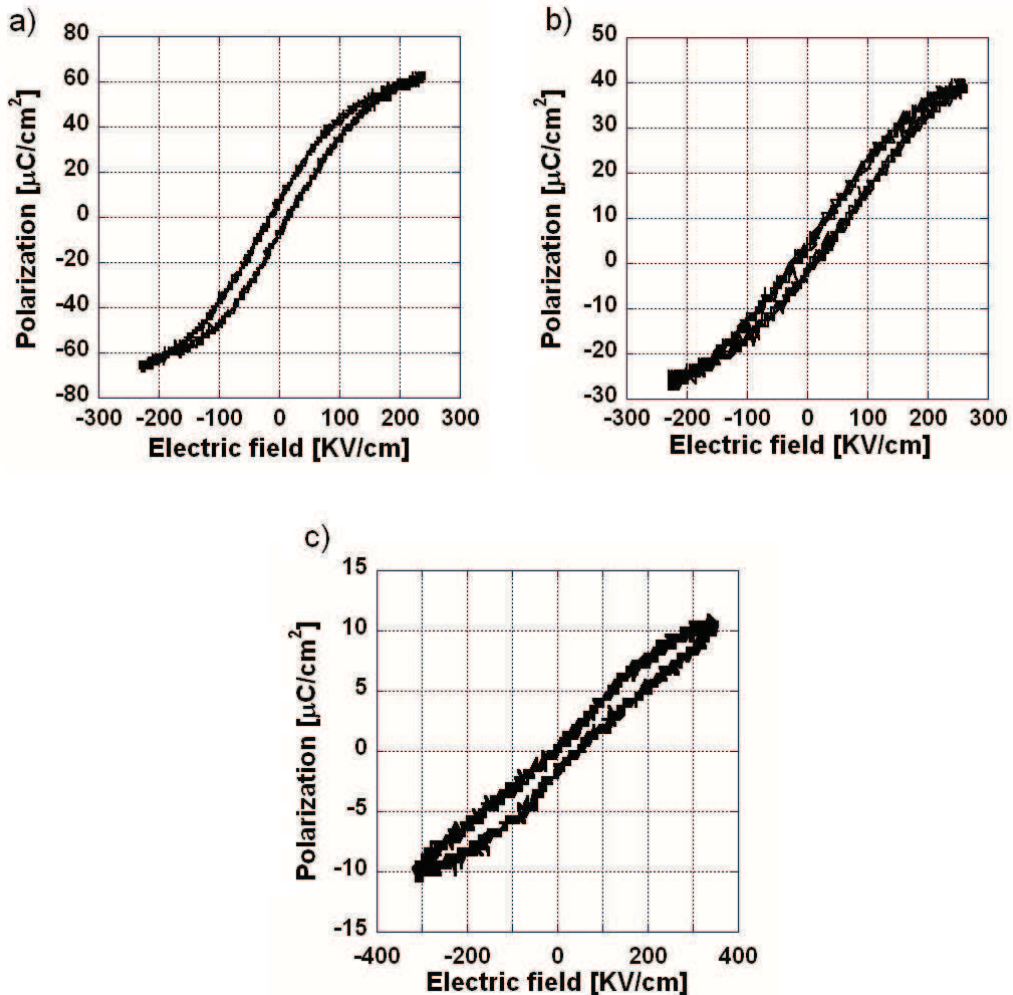


Figure 7.8: a) Hysteresis loop measurements on a  $SrRuO_3(100\text{ nm})/BaTiO_3(400\text{ nm})/SrRuO_3(150\text{ nm})$  parallel plate capacitor directly deposited on the  $SrTiO_3$  substrate, the  $BaTiO_3$  film has been grown at a pressure of  $8\text{ Pa}$ . b) Hysteresis loop measurements on a  $SrRuO_3(100\text{ nm})/BaTiO_3(300\text{ nm})/SrRuO_3(150\text{ nm})$  parallel plate capacitor deposited on a  $SrTiO_3(250\text{ nm})/MgO(400\text{ nm})$  bi-layer, the  $BaTiO_3$  film has been grown at a pressure of  $8\text{ Pa}$ . c) Hysteresis loop measurements on a  $SrRuO_3(100\text{ nm})/BaTiO_3(300\text{ nm})/SrRuO_3(150\text{ nm})$  parallel plate capacitor deposited on a  $400\text{ nm}$  thick  $MgO$  layer, the  $BaTiO_3$  film has been grown at a pressure of  $0.013\text{ Pa}$ .

defects can form during the crystal growth. This idea is confirmed by the fact that the residual polarization is further reduced with the introduction of a sacrificial layer under the capacitive structure.

Choi et al. [22] reported a residual polarization of  $50 \mu C/cm^2$  for a  $200\text{ nm}$   $BaTiO_3$  film sandwiched between two  $SrRuO_3$  electrode layers. They attributed this high residual polarization to the in plane biaxial stress experienced by the  $BaTiO_3$  when it is grown on  $SrRuO_3$  as consequence of the epitaxy. In this project  $300\text{ nm}$  thick  $BaTiO_3$  layers have been used for our 31 mode capacitors and though the measured  $BaTiO_3$  lattice parameters agreed with those reported by Choi, smaller values of the residual polarization have been measured. This implies that a relaxation of the misfit strain takes place in our stacks, this is in agreement with the assumption of a misfit stress relaxation after a critical thickness of less than  $10\text{ nm}$  discussed in chap. 6. Finally it has to be remarked that Choi et al. have grown their capacitive structures on  $GdScO_3$  and  $DyScO_3$  substrates rather than  $SrTiO_3$  and a detailed description of their fabrication process is not reported in [22].

Our hysteresis loops have been measured in the frequency range  $10\text{ KHz} - 20\text{ KHz}$ , Yang et al. [65] measured their hysteresis loop at  $100\text{ KHz}$  while Choi et al. does not report at which frequency the hysteresis loops have been measured. The frequency used to measure the hysteresis loops might have an influence on the switching of the dipoles in the piezoelectric layer. Ideally measurements performed at the same frequency should be compared, however no works reporting hysteresis loops measurements in the frequency range  $10\text{ KHz} - 20\text{ KHz}$  have been found.

The  $BaTiO_3$  of sample  $GV43(P)$  has been grown at a pressure signifi-

cantly lower than that one used for the other two samples. A reduction of the deposition pressure reduces the losses in the  $BaTiO_3$  film, however as shown by fig. 7.8c it also downgrades the quality of the hysteresis loop. Kim et al. [79] reported that in  $BaTiO_3/SrTiO_3$  systems a reduction of the deposition pressure promotes the formation of oxygen vacancies into the  $BaTiO_3$  layer. Such vacancies at the  $BaTiO_3/SrRuO_3$  interface [17, 100] can contribute to the degradation of the hysteresis loop. Lines reports that the presence of defects in the  $BaTiO_3$  film can produce a distorted loop as that one reported in fig. 7.8c [19].

## 7.4 Summary

In this chapter the electrical properties of the fabricated multi-layers have been discussed.

It has been shown that the grown  $SrRuO_3$  can be used as electrode layer, in fact its room temperature resistivity is  $284 \mu\Omega cm$ , in agreement with [95].

The performances of  $BaTiO_3$  based ferroelectrics capacitors grown on  $SrTiO_3$  substrate and on  $MgO$  and  $YBa_2Cu_3O_7$  sacrificial layers have been assessed.

For the fabricated capacitors a lumped element model consisting of a capacitor in parallel with a resistor well describes the  $BaTiO_3$  film. The lines contribution is taken into account by a resistor connected in series with the impedance of the  $BaTiO_3$  layer.

Our investigations show that a reduction of the  $BaTiO_3$  deposition pressure reduces the losses present in the fabricated capacitors. This happens

either in the case of capacitors grown on the substrate or on the sacrificial layers.

The phase of the impedance of  $SrRuO_3/BaTiO_3/SrRuO_3$  structures directly grown on  $SrTiO_3$  substrate varies between  $-85^\circ$  and  $-90^\circ$  in the frequency range  $40\text{ Hz} - 50\text{ KHz}$ . Growing pressures equal or lower than  $8\text{ Pa}$  and ablation temperatures of  $780^\circ C$  have been used for  $BaTiO_3$ . For higher  $BaTiO_3$  deposition pressures resistive losses are introduced in the dielectric layer.

The phase of the impedance of  $SrRuO_3/BaTiO_3/SrRuO_3$  structures grown on  $MgO$  sacrificial layers varies between  $-80^\circ$  and  $-90^\circ$  in the frequency range  $6\text{ KHz} - 50\text{ KHz}$  at a  $BaTiO_3$  deposition pressure of  $8\text{ Pa}$ . The ablation temperatures is still  $780^\circ C$ . Below  $6\text{ KHz}$  resistive losses produce a decrease of the impedance phase (up to  $-20^\circ$  at  $200\text{ Hz}$ ). The full capacitive behaviour is recovered in the frequency range  $40\text{ Hz} - 50\text{ KHz}$  for  $BaTiO_3$  deposition pressures equal or lower than  $0.013\text{ Pa}$ .

Higher deposition pressures imply a larger number of collisions in the path between the material target and the substrate. The energy lost in the ablation path produces a lower mobility of the atomic species on the substrate which is further reduced by the relatively high deposition pressure. The lower energy of the adatoms on the substrate affect the crystal structure of the  $BaTiO_3$  film.

The  $YBa_2Cu_3O_7$  is easy to etch in weak acids like  $0.1\% HNO_3$  however the capacitive structures grown on its top do not behave as pure capacitors but present losses.  $SrRuO_3/BaTiO_3/SrRuO_3$  capacitors on  $YBa_2Cu_3O_7$  sacrificial layer present impedance phases around  $-20^\circ$  at the frequency of

50  $KHz$  and at a  $BaTiO_3$  growing pressures equal to 8  $Pa$ .

The introduction of a 1  $\mu m$   $SrTiO_3$  buffer layer between the  $YBa_2Cu_3O_7$  and the  $SrRuO_3/BaTiO_3/SrRuO_3$  capacitors reduces the losses in the piezoelectric film. This is testified by an increase of the RA product (from  $44.1 \cdot 10^5 \Omega \mu m^2$  to  $19.54 \cdot 10^7 \Omega \mu m^2$ ) of the structures containing the buffer layer.

On the surface of the  $YBa_2Cu_3O_7$  sacrificial layer some not stoichiometric outgrowths and particulates are present. They reduce the quality of the layers grown on their top by introducing losses in the  $SrRuO_3/BaTiO_3/SrRuO_3$  capacitors. The impedance phase of capacitors grown on a 1  $\mu m$  thick  $SrTiO_3$  buffer layer is equal to  $-64^\circ$  at 50  $KHz$ . A further reduction of the film losses which correspond to an increase of the RA product and to a decrease of the parasitic shunting conductance is desirable. However in this case a decrease of the  $BaTiO_3$  deposition pressure below 8  $Pa$  produces the dissociation of the  $YBa_2Cu_3O_7$  sacrificial layer [101].

The use of  $MgO$  as sacrificial layer produces an RA product which is at least one order of magnitude bigger than that of the devices grown on  $YBa_2Cu_3O_7$  sacrificial layer. The minimum value of the RA product measured for  $SrRuO_3/BaTiO_3/SrRuO_3$  structures grown on  $MgO$  sacrificial layer is equal to  $61.93 \cdot 10^8 \Omega \mu m^2$ . In this case a  $BaTiO_3$  deposition pressure of 8  $Pa$  and a growing temperature of  $780^\circ C$  have been used.

The problem with the use of  $MgO$  as sacrificial layer is represented by its long etching time see sec. 4.4. As the RA product increases with the reduction of the  $BaTiO_3$  deposition pressure, structures approaching the behavior of a pure capacitor can be obtained on  $MgO$ . However with the

reduction of the deposition pressure the value of the  $C/A$  ratio decreases from  $3.04 \cdot 10^{-14} F/\mu m^2$  at a  $BaTiO_3$  deposition pressure of  $8 Pa$  to  $1.76 \cdot 10^{-14} F/\mu m^2$  at a  $BaTiO_3$  deposition pressure of  $0.013 Pa$ . Furthermore with the reduction of the  $BaTiO_3$  deposition pressure the quality of the hysteresis loop degrades. This may be due to the oxygen vacancies present in  $BaTiO_3$  grown at low pressures.

For a  $BaTiO_3$  deposition pressures of  $8 Pa$  and an ablation temperature of  $780^\circ C$ ,  $SrRuO_3/BaTiO_3/SrRuO_3$  structures behave as pure capacitor over  $6 KHz$  and present a  $BaTiO_3$  residual polarization equal to  $2.5 \mu C/cm^2$ . A further optimization of the ablation conditions used for the multi-layers, is necessary to reach a good compromise between the reduction of the resistive losses in the piezoelectric film and a good hysteresis behaviour for working frequencies below  $6 KHz$ .

# Chapter 8

## Conclusions and future developments

In this thesis the properties of different multi-layers based on lead-free materials and containing  $BaTiO_3$  have been analysed and discussed. The goal of this work is to find multi-layer structures which can be used to produce energy harvesting micro-cantilevers.

The major results of this thesis are:

- $YBa_2Cu_3O_7$  can be used as sacrificial layer to suspend micro-cantilevers containing  $BaTiO_3$  and  $SrRuO_3$  based capacitive structures, the use of all oxide materials allows to maintain the epitaxy through the stack;
- when the  $BaTiO_3$  is grown on  $SrRuO_3$ , the  $BaTiO_3$  polar axis is perpendicular to the surface of the film, this configuration can be used to fabricate energy harvesting devices using the 31 piezoelectric mode;
- when the  $BaTiO_3$  is grown on  $MgO$ , the  $BaTiO_3$  polar axis is parallel

to the surface of the film this configuration can be used to fabricate energy harvesting devices using the 33 piezoelectric mode;

- the properties of  $SrRuO_3/BaTiO_3/SrRuO_3$  piezoelectric capacitors grown on  $YBa_2Cu_3O_7$  sacrificial layers are degraded by the particulates present on the surface of the sacrificial layer itself;
- a reduction of the deposition pressure (below  $8\text{ Pa}$ ) during the growth of  $BaTiO_3$  thin films reduces the resistive losses in  $BaTiO_3$  based capacitors, however also the value of the  $BaTiO_3$  residual polarization is reduced below  $2.5\text{ }\mu C/cm^2$ ;
- $SrRuO_3/BaTiO_3/SrRuO_3$  capacitive structures fabricated on  $MgO$  sacrificial layer at a  $BaTiO_3$  deposition pressure equal to  $8\text{ Pa}$  and at a growing temperature of  $780^\circ C$  present an impedance phase between  $-80^\circ C$  and  $-90^\circ$  over  $6\text{ KHz}$  and a  $BaTiO_3$  residual polarization of  $2.5\text{ }\mu C/cm^2$ . These structures can be used as energy harvesting devices at working frequencies bigger than  $6\text{ KHz}$ .

Now the results presented in each chapter together with the findings previously listed are going to be discussed and compared to the current state of the data.

In chap. 1 a discussion on the basic properties of ferroelectric and piezoelectric material has been reported. The materials used for the fabrication of the multi-layers are:

- $BaTiO_3$ ;
- $SrRuO_3$ ;

- $SrTiO_3$ ;
- $MgO$ ;
- $YBa_2Cu_3O_7$ ;
- $Au$ ;

with the exception of gold, only oxide materials have been used for the fabrication of our cantilevers. In previous works [1, 2, 3, 4, 5], materials like  $Pb(Zr, Ti)O_3$ ,  $SiO_2$ ,  $SiN_x$  and  $Pt$  were used. Our materials do not contain lead in agreement with the Directive 2002/95/EC of the European Parliament [9] which restricts the use of hazardous substances like lead in the manufacture of various types of electronic and electrical equipment.

In the first chapter the two cantilever structures fitting the 31 and the 33 piezoelectric mode [4] have been presented, fig. 1.7. Both devices contain a capacitive structure on their top. The  $BaTiO_3$  is the capacitor dielectric layer, the  $SrRuO_3$  (or  $Au$ ) works as electrode, the  $YBa_2Cu_3O_7$  is the sacrificial layer, the  $MgO$  changes the growing orientation of the  $BaTiO_3$  and the  $SrTiO_3$  is used as buffer layer between the  $YBa_2Cu_3O_7$  and the capacitive structure. Eventually the  $MgO$  can be used as sacrificial layer.

The 31 mode devices have separate top and bottom electrode while the 33 mode devices eliminate the need for a bottom electrode by employing an interdigitated conductive layer. Equations 1.11 and 1.12 reports the expressions of the open circuit voltages generated with the 33 and the 31 mode devices respectively. The 33 design presents the advantage to produce an higher open circuit voltage than the 31 design in fact the spacing  $L$  between

the fingers of the electrode of a 33 device is usually bigger than the spacing  $t$  between the top and the bottom electrode of a 31 device [1, 4], eq. 1.16. Furthermore in  $BaTiO_3$  the  $g_{33}$  piezoelectric constant is bigger than the  $g_{31}$  piezoelectric constant:

$$g_{33} = 57.5 \cdot 10^{-3} \text{ Vm/N}$$

and

$$g_{31} = -23.0 \cdot 10^{-3} \text{ Vm/N.}$$

When the micro-cantilever is vibrating an ac current is generated across the load connected to the device. A rectifying circuit and a storage capacitor are required to harvest energy from each micro-cantilever [1, 4]. It is important that the amplitude of the generated output voltage is big enough to overcome the threshold voltage of the rectifying diodes (Schottky diodes present a threshold voltage of 0.2 V [4]).

Chap. 2 presents the mathematical model and the design rules used for the design of simple beam and u-shape micro-cantilevers having a seismic mass on their free end. The u-shape cantilever contains a much bigger area where it is possible to integrate the seismic mass. A bigger seismic mass implies a lower resonance frequency, this is useful because the vibrations present in the environment have frequencies in the range few  $Hz$  - few  $KHz$  so a reduction of the resonance frequency might be useful for the device tuning.

To reduce the resonance frequency of a single beam cantilever the thickness of the seismic mass layer can be increased. It has to be kept in mind that the deposition of a  $1\mu m$  thick perovskite film (with our deposition pa-

rameters) takes something like 8 hours. To reduce the deposition time, in the case of big seismic masses, the u-shape structure can be used.

Another advantage of the u-shape design is that two capacitive structures are integrated on each arm. According to eq. 2.58 the energy stored in these structures is twice the energy stored in a simple beam cantilever having the dimensions equal to those of a single arm of the u-shape cantilever.

Simple beam and u-shape micro-cantilevers having the top-down layer sequence  $Au/BaTiO_3/MgO/SrTiO_3$ , lengths comprised between  $130\ \mu m$  and  $500\ \mu m$  and widths of  $30\ \mu m$  and  $50\ \mu m$  have been designed. Their theoretical resonance frequencies varies between  $80\ Hz$  and  $20\ KHz$ , tabs. 2.3 and 2.5, covering in this way the frequency range of the environment vibrations. Their theoretical output voltage has been calculated assuming a deflection of the free end equal to  $5\ \mu m$ . The amplitude of the generated voltage varies between  $2.3\ V$  and  $21\ V$ , tabs. 2.3 and 2.5. This is enough to overcome the threshold voltage of the rectifying diodes. Such voltage levels are not surprising because for cantilevers with similar size employing  $PZT$ ,  $100\ V$  are required in order to have a deflection of the free end equal to  $30\mu m$  [23].

The output voltage of the designed micro-cantilevers has been analysed. However these structures should be used as energy scavenging devices, so it is important to understand the amount of power which they can supply. As previously stated, to take advantage of the separation of charges which takes place in the piezoelectric layer when an input stress is applied, capacitors are integrated on the top of the micro-cantilevers. Eqs. 2.58 and 2.59 are the expressions for the energy stored in the capacitors and the power which can be extracted respectively. According to these equations a design aimed

to maximaze the output voltage, also maximises the energy stored in the capacitor.

Considering the resonance frequencies and the output voltages reported in tables 2.3 and 2.5 and the fact that the capacitance values measured in chap. 7 have magnitude between  $10^{-12} F$  and  $10^{-10} F$ , the theoretical power which can be extracted from the designed structure is in the range:

$$10^2 \mu W - 10^{-1} nW. \quad (8.1)$$

The power extracted from PZT devices is in the range  $\mu W - mW$  [5]. This is due to the superior piezoelectric coefficients of PZT. The maximum value of the  $d_{33}$  and  $g_{33}$  piezoelectric coefficients in PZT are  $520 \text{ pC/N}$  and  $71 \cdot 10^{-3} \text{ Vm/N}$  respectively [8]. For  $BaTiO_3$  the values of the  $d_{33}$  and  $g_{33}$  piezoelectric coefficients are  $85.6 \text{ pC/N}$  and  $57.5 \cdot 10^{-3} \text{ Vm/N}$  [6]. The smaller values of the  $BaTiO_3$  piezoelectric coefficients lead to a reduction of the performances achievable with the devices employing  $BaTiO_3$  as piezoelectric layer. However the power extracted from the  $BaTiO_3$  capacitors can be increased by using capacitors with a bigger coupled area.

In chap. 3 the experimental methods used for the fabrication and the characterization of the multi-layer structures have been presented. Here the Pulsed Laser Deposition system, the photolithography techniques, the critical point drying and the wirebonding system used for the fabrication of the mico-cantilever devices have been described. In this chapter also the X-ray diffraction techniques together with the methods used for the electrical characterization of the capacitors are reported. Finally the nano-indentation

method employed to measure the Young's modulus of each film in the multi-layer stacks has been discussed.

Chap. 4 reports the fabrication process of the 33 and 31 mode micro-cantilevers. Here the reasons which lead to the introduction of each step in the fabrication process have been explained. This chapter showed that it is possible to use  $YBa_2Cu_3O_7$  or  $MgO$  as sacrificial layers, they both allow the epitaxial growth of the layers employed in our stacks on their top (see chap. 5).

The  $YBa_2Cu_3O_7$  is easy to etch in weak acid solutions like 0.1%  $HNO_3$ , in this case, the etching time necessary to suspend a cantilever of area  $200\ \mu m \times 30\ \mu m$  varies between 6 and 8 minutes. When the  $MgO$  is used as sacrificial layer stronger acid solutions like 20%  $HNO_3$  are necessary. In this case to suspend a beam with an area of  $200\ \mu m \times 30\ \mu m$  8 hours are required. Furthermore to obtain a well defined geometry the sacrificial layer is removed by a combination of argon ion beam milling and wet etching, if only wet etching is used a much less well defined cantilever is produced, fig. 4.5.

Chapter 5 presents the results of the X-ray diffraction analysis performed on different multi-layer sequences containing  $BaTiO_3$ ,  $SrRuO_3$ ,  $MgO$ ,  $SrTiO_3$  and  $YBa_2Cu_3O_7$  thin films. This analysis showed that epitaxy is maintained through stacks containing a combination of the previous layers.

The analysed works on energy harvesting micro-cantilevers [1, 4, 5] do not report which is the orientation of the polar axis in the piezoelectric film respect to the position of the electrodes of the capacitive structure. This aspect is quite important as the charge collected between the electrodes of

Sample label	Material [Top-down layer sequence]	In plane a axis measured [ $\text{\AA}$ ] (bulk [ $\text{\AA}$ ])	In plane b axis measured [ $\text{\AA}$ ] (bulk [ $\text{\AA}$ ])	Out of plane c axis measured [ $\text{\AA}$ ] (bulk [ $\text{\AA}$ ])
$GV03(P)$	$\text{BaTiO}_3$ [ $\text{BaTiO}_3$ (126 nm)/ $\text{SrTiO}_3$ (500 nm)/ $\text{YBa}_2\text{Cu}_3\text{O}_7$ (400 nm)]	<b>3.996 ± 0.006</b> (3.992)	<b>3.996 ± 0.006</b> (3.992)	<b>4.015 ± 0.003</b> (4.036)
$GV16(P)$	$\text{BaTiO}_3$ [ $\text{BaTiO}_3$ (100 nm)/ $\text{MgO}$ (60 nm)/ $\text{YBa}_2\text{Cu}_3\text{O}_7$ (400 nm)]	<b>4.002 ± 0.003</b> (3.992)	<b>4.002 ± 0.003</b> (3.992)	<b>3.997 ± 0.002</b> (4.036)
$GV10(P)$	$\text{BaTiO}_3$ [ $\text{BaTiO}_3$ (100 nm)/ $\text{MgO}$ (60 nm)/ $\text{SrTiO}_3$ (500 nm)/ $\text{YBa}_2\text{Cu}_3\text{O}_7$ (400 nm)]	<b>4.028 ± 0.008</b> (3.992)	<b>4.028 ± 0.008</b> (3.992)	<b>3.985 ± 0.010</b> (4.036)
$GV21(P)$	$\text{BaTiO}_3$ [ $\text{SrRuO}_3$ (50 nm)/ $\text{BaTiO}_3$ (100 nm)/ $\text{SrRuO}_3$ (350 nm)/ $\text{YBa}_2\text{Cu}_3\text{O}_7$ (400 nm)]	<b>3.951 ± 0.002</b> (3.992)	<b>3.951 ± 0.002</b> (3.992)	<b>4.069 ± 0.002</b> (4.036)

Table 8.1: Lattice parameters of the  $\text{BaTiO}_3$  in different multi-layer sequences.

the piezoelectric capacitor depends on the orientation of the polar axis in the piezoelectric film. The surface charge density  $\sigma_p$  on the surface of the electrode layer is [102]:

$$\sigma_p = \vec{P} \cdot \hat{u}_n = |\vec{P}| \cdot \cos(\vartheta) \quad (8.2)$$

where  $\hat{u}_n$  is the unit vector perpendicular to the surface of the electrode layer and  $\vartheta$  is the angle between the polarization vector  $\vec{P}$  and the unit vector  $\hat{u}_n$  perpendicular to the surface of the electrode. From eq. 8.2 it is clear that the maximum charge density on the electrode layer is obtained when the polarization vector  $\vec{P}$  is perpendicular to the electrode area.

Table 8.1 contains the lattice parameters of  $\text{BaTiO}_3$  grown in different multi-layer sequences. The  $\text{BaTiO}_3$  grows (001) oriented which means with the polar axis perpendicular to the surface of the film on  $\text{SrTiO}_3$  and on  $\text{SrRuO}_3$ , table 8.1 and fig. 5.2a-b, while it grows with the polar axis parallel to the surface of the film on  $\text{MgO}$ , table 8.1 and fig. 5.2c-d. The (002)

reflection of sample  $GV03(P)$  corresponds to a  $BaTiO_3$   $c$  axis having a length of  $4.015\text{ \AA}$  while the  $(002)$  reflection of sample  $GV21(P)$  corresponds to a  $c$  axis with a length of  $4.069\text{ \AA}$ , so in this case the  $c$  axis is associated with the polar axis. The  $(002)$  reflections of samples  $GV16(P)$  and  $GV10(P)$  correspond to a  $c$  axis with a length of  $3.997\text{ \AA}$  and  $3.985\text{ \AA}$  respectively, here the  $c$  axis does not correspond to the  $BaTiO_3$  polar axis.

When the polar axis is perpendicular to the plane of the film, the polarization can be easily accessed by a parallel plate capacitor fig. 1.7b, so  $BaTiO_3$  grown on  $SrRuO_3$  can be used to produce 31 mode cantilevers. When the polar axis is parallel to the surface of the film, the polarization can be accessed by using an interdigitated capacitor fig. 1.7a, so an  $MgO$  film is introduced as seed layer to orientate the  $BaTiO_3$  in a way that fits the 33 piezoelectric mode.

As previously stated when the  $BaTiO_3$  is grown on  $SrTiO_3$  the polar axis is equal to  $4.015\text{ \AA}$ , this is smaller than the value reported in bulk materials. Kim et al. [79] reported that in  $SrTiO_3/BaTiO_3$  superlattices the  $c$  axis lattice parameter decreases from  $4.12\text{ \AA}$  to  $4.06\text{ \AA}$  when the oxygen pressure during the deposition is increased from  $1.33 \cdot 10^{-3}\text{ Pa}$  to  $0.133\text{ Pa}$ . The  $BaTiO_3$  of the investigated sample has been grown at an oxygen pressure of  $20\text{ Pa}$  so this can explain the shorter value measured.

$BaTiO_3$  grown on  $SrRuO_3$  also has a polar axis perpendicular to the surface of the film, here an elongation of the polar axis equal to 0.83% respect to bulk materials is observed. This is highlighted by a shift of  $-0.5^\circ$  for the diffraction peak of the  $BaTiO_3$  relative to the  $(002)$  plane respect to the same peak on  $SrTiO_3$ , fig. 5.2b. The measured polar axis is equal to  $4.069\text{ \AA}$ ,

table 8.1, this value is in excellent agreement with that one reported by Choi et. al [22]. The elongation of the polar axis is attributed to the in plane biaxial stress experienced by the  $BaTiO_3$  layer. Calculations of the critical thickness for the  $BaTiO_3/SrRuO_3$  system gives a value equal to  $9\text{ nm}$  this suggests that the first layers of the  $BaTiO_3$  grow elastically strained and the in plane biaxial stress produces an elongation of the polar axis, this is in agreement with observations. The in plane lattice constants as consequence of the biaxial stress have a value equal to  $3.951\text{ \AA}$ , table 8.1.

Thin film stacks where the  $BaTiO_3$  has been grown on an  $MgO$  layer are present in the samples  $GV10(P)$  and  $GV16(P)$ , in both cases the polar axis lies parallel to the plane of the film, table 8.1. This is confirmed by the  $\vartheta - 2\vartheta$  scans relative to the (002) plane of  $BaTiO_3$  films fig. 5.2c-d. The smaller lattice mismatch between the  $c$  axis of  $BaTiO_3$  and the  $MgO$  lattice parameter is the reason for such orientation [66, 67].

According to eq. 5.2 the critical thickness of  $BaTiO_3$  on  $MgO$  is negligible so unstrained lattice parameters should be measured in the plane of the film. Despite that the measured polar lattice parameter appears smaller than the bulk value, this happens because the measurements provide an average value, in fact there are two possible orthogonal orientations when the polar axis is in the plane of the substrate and a non polar axis must also lie in plane.

With these considerations, the layer sequences fitting the 31 and the 33 piezoelectric mode are:

- $SrRuO_3/BaTiO_3/SrRuO_3/YBa_2Cu_3O_7$  (31 piezoelectric mode);
- $SrRuO_3/BaTiO_3/MgO/SrTiO_3/YBa_2Cu_3O_7$  (33 piezoelectric mode);

when  $YBa_2Cu_3O_7$  is used as sacrificial layer, and

- $SrRuO_3/BaTiO_3/SrRuO_3/MgO$  (31 piezoelectric mode);
- $SrRuO_3/BaTiO_3/MgO$  (33 piezoelectric mode);

when  $MgO$  is used as sacrificial layer.

In the 33 mode stack where  $YBa_2Cu_3O_7$  is used as sacrificial layer, the  $SrTiO_3$  film functions as buffer layer, it has been introduced to improve the interface quality between the  $YBa_2Cu_3O_7$  and the  $MgO$  film. Fig. 4.6 shows secondary ion mass spectroscopy (SIMS) data during the milling of two samples, one with the  $SrTiO_3$  buffer layer and one without. The  $SrTiO_3/YBa_2Cu_3O_7$  interface, fig. 4.6b, is better defined than the  $MgO/YBa_2Cu_3O_7$  interface, fig. 4.6a, with a sharp transition between layers evidenced by the SIMS signal. Wu et al. [69] studied the atomic configurations of  $YBa_2Cu_3O_7/MgO$  interfaces, they reported that diffusion induced interstitial or substitutional  $Mg$  atoms in the first  $YBa_2Cu_3O_7$  layers. Without a well defined interface, it was difficult to undercut the  $YBa_2Cu_3O_7$  and suspend the structure. Tab. 4.2 reports the number of suspended devices for the 33 and 31 mode layer sequences, the stacks containing the  $SrTiO_3$  buffer layer show an higher number of suspended devices.

Chap. 5 also reports the nanoindentation measurements run on the grown multilayers. The measured values of the Young's modulus are reported in tab. 8.2.

Indentations measurements on  $BaTiO_3$  grown on a  $SrTiO_3$  layer have been run on the sample labeled as  $GV03(P)$ , such sample has top down layer sequence:  $BaTiO_3/SrTiO_3/YBa_2Cu_3O_7$ ; this three-layer has been grown in

<i>Material</i>	<i>Young's modulus [GPa]</i>
$YBa_2Cu_3O_7$	129
$SrRuO_3$	190
$BaTiO_3$ (on $MgO$ or $SrRuO_3$ )	175
$BaTiO_3$ (on $SrTiO_3$ )	79
$MgO$	233
$SrTiO_3$	130

Table 8.2: Young's Modulus of the deposited films. The Young's Modulus has been measured by nanoindentation technique.

situ. In this sample the measured value of the Young's modulus is smaller than the value measured in the case of  $BaTiO_3$  films grown on  $SrRuO_3$  or on  $MgO$  layers. The smaller value of the Young's modulus equal to  $79\text{ GPa}$  is in agreement with that one reported in [81]. It is known that  $MgO$  and  $SrRuO_3$  are stiffer than  $SrTiO_3$ , so an influence of the underlying layer on the Young's modulus of the  $BaTiO_3$  can not be excluded. Furthermore it has to be highlighted that in sample  $GV03(P)$  all the thin films are deposited in situ, while for the 33 and 31 mode stacks, used to evaluate the Young's modulus of  $BaTiO_3$  on  $MgO$  and on  $SrRuO_3$ , this is not possible because our deposition system allows the deposition of only three layers in situ.

The measured Young's modulus for the  $SrRuO_3$  and the  $MgO$  well agreed with the value reported in literature [82, 83] while the measured value for the  $SrTiO_3$  film is smaller than  $265\text{ GPa}$  reported in [84]. The Young's modulus measured on the  $SrTiO_3$  substrate is equal to  $191\text{ GPa}$  which is still smaller than the value reported in literature, however the  $SrTiO_3$  substrate supplier

[58] does not report the Young's modulus of the substrate in the datasheet.

The Young's modulus of the materials used here are significantly higher than the Young's modulus of  $PZT$  ( $63\text{ GPa}$ ) and  $SiO_2$  ( $69\text{ GPa}$ ), these materials have been used for the fabrication of energy harvesting cantilevers by Jeon et al. [4]. They introduced a  $SiN_x$  buffer layer in their film stack to reduce the curling of the beam after its release. The Young's modulus measured for the thin films employed in our stack are high enough to not require the use of an additional buffer layer.

In chap. 6 an experimental method useful to determine the residual stresses at the top surface of thin film multi-layer cantilevers has been discussed. The method consists into the measuring of the cantilever deflection at different distances from the anchor point, in this way the mathematical expression of the curve approximating the deflection of the cantilever is calculated. Using eq. 6.3 the value of the radius of curvature can be worked out and so also the residual stress at the cantilever top surface can be evaluated with the help of eq. 6.1.

In previous works the residual stress in microcantilevers was caculated by measuring the deflection of the free end in the case of small deflections [12, 13], or by using the Stoney formula [4, 14]. In our multilayer cantilevers the Stoney formula does not apply because some of the hypothesis necessary for the application of this method are not fulfilled [15]. Furthermore deflections of the free end equal to  $40\mu m$  for cantilevers with lengths of  $180\mu m$  have been measured, so also the hypothesis of small deflections of the free end does not apply.

The proposed method is applicable either in the case of large deflections

of the free end or when the Stoney formula does not apply, the deflections of the cantilevers are measured by using SEM and interferometry techniques.

The proposed analysis has been performed on  $SrRuO_3/BaTiO_3/SrRuO_3$  and  $BaTiO_3/MgO/SrTiO_3$  u-shape cantilevers and on  $BaTiO_3/SrTiO_3$  simple beam cantilevers. The lenght of the analysed devices varies between  $32\ \mu m$  and  $234\ \mu m$ .

The main causes of stress in released cantilevers are the mismatch of thermal expansion coefficients between the different layers (thermal stress), the mismatch of lattice constants between the different materials (misfit stress) and the presence of defects in the layers [90].

Residual stresses at the cantilever top surface between  $-51\ MPa$  and  $-200\ MPa$  have been measured. These values suggest that the mismatch between the thermal expansion coefficients is the main cause of residual stress in these devices. If instead the lattice mismatches are used to calculate the longitudinal stresses at the top surfaces of the cantilevers, there is a difference of one or two orders of magnitude between theoretical and experimental values. This rules out the lattice mismatch as the cause of residual stress.

In our layer combinations the critical thicknesses of the deposited films are less than  $10\ nm$  (see chap 5), the film thicknesses in the analysed stacks are in the order of hundred of  $nm$ . When the critical thickness is exceeded the misfit stress is released with the generation of dislocations in the layer [73, 92], that is why the residual stress is mainly due to the mismatch of thermal expansion coefficients.

In chap. 7 the impedance and hysteresis loop measurements have been mainly run on the 31 mode devices. In the 31 mode devices the spacing

between the top and the bottom electrode is equal to  $300\text{ nm}$ . In 33 mode structures the spacing between the fingers of the electrode is at least equal to  $10\text{ }\mu\text{m}$ , the higher spacing reduces the probability of shorts as confirmed by measurements, see sec. 7.2.2. The worst case is so represented by the devices employing the 31 piezoelectric mode, by optimatizing the 31 mode capacitors the improvements are also reflected on the 33 mode devices.

Chap. 7 showed that  $\text{SrRuO}_3/\text{BaTiO}_3/\text{SrRuO}_3$  tri-layers behaving as high quality (i.e. with an impedance phase between  $-80^\circ$  and  $-90^\circ$ ) capacitive structures, in the frequency range  $6\text{ KHz} - 50\text{ KHz}$ , have been fabricated on  $400\text{ nm}$  thick  $\text{MgO}$  sacrificial layer by using the fabrication process reported in chap. 4. These structures showed a  $\text{BaTiO}_3$  residual polarization equal to  $2.5\text{ }\mu\text{C/cm}^2$ .

Jeon et. al. [4] reported the successful fabrication of a  $\text{Pb}(\text{Zr}, \text{Ti})\text{O}_3$  micro-cantilever having a resonance frequency of  $13.9\text{ KHz}$ .

Limitations to the maximum working frequency come from the vibration sources present in the environment. Suitable vibrations can be found in applications like household goods (fridges, washing machines, microwave ovens etc.), industrial plant equipment, moving structures such as automobiles, aeroplanes, buildings and bridges [5]. All these applications suggest working frequencies ranging from few hertz to few kilo-hertz.

The fabricated capacitive structures allow the design of micro-cantilevers with a minimum resonance frequency of  $6\text{ KHz}$ , the advantage respect to the device proposed in [4] is that the energy of vibrations with frequency in the range  $6\text{ KHz} - 13.9\text{ KHz}$  can be used.

It is desirable to have devices which are able to harvest energy at fre-

quencies below  $6\text{ KHz}$ . Capacitive structures containing a  $\text{BaTiO}_3$  film deposited in oxygen environment at a pressure of  $0.013\text{ Pa}$  and at a temperature of  $780^\circ\text{C}$  showed an impedance phase between  $-80^\circ$  and  $-90^\circ$  over the frequency range  $40\text{ Hz} - 50\text{ KHz}$ . However at such  $\text{BaTiO}_3$  deposition temperature a degradation of the  $\text{BaTiO}_3$  hysteresis loop takes place, this means that also the piezoelectric properties of the device are degraded. Kim et al. [79] reported that in  $\text{BaTiO}_3/\text{SrTiO}_3$  systems a reduction of the deposition pressure promotes the formation of oxygen vacancies into the  $\text{BaTiO}_3$  layer. Such vacancies can contribute to the degradation of the hysteresis loop.

An optimization of the  $\text{BaTiO}_3$  deposition is necessary to produce devices with working frequency below  $6\text{ KHz}$ , however it has to be kept in mind that the power extracted from a micro-cantilever with a piezoelectric capacitive structure on its top is directly proportional to the working frequency eq. 2.59.

The reduction of the  $\text{BaTiO}_3$  deposition pressure reduces the losses in the  $\text{BaTiO}_3$  layers of  $\text{SrRuO}_3/\text{BaTiO}_3/\text{SrRuO}_3$  capacitors. This is testified by an increase of the  $RA$  product of these devices when the  $\text{BaTiO}_3$  deposition pressure is reduced, table 8.3.

Higher deposition pressures imply a larger number of collisions in the path between the material target and the substrate during the pulsed laser deposition of the film. The energy lost in the ablation path produces a lower mobility of the atomic species on the substrate which is further reduced by the relatively high deposition pressure.

In pulse laser deposition, the growth of the film is accompanied by the

Device (fig.) (Sample)	Top-down layer sequence	$BaTiO_3$ dep. temperature [°C]	$BaTiO_3$ dep. pressure [Pa]	RA [Ωμm <sup>2</sup> ]	C/A [F/μm <sup>2</sup> ]
SBSSY (fig. 7.6a) (GV38(P))	$SrRuO_3(100nm)/BaTiO_3(300nm)/$ $SrRuO_3(150nm)/SrTiO_3(250nm)/$ $YBa_2Cu_3O_7(500nm)$	780	8	$44.1 \cdot 10^5$	$6.28 \cdot 10^{-13}$
SBSSY (fig. 7.6b) (GV42(P))	$SrRuO_3(100nm)/BaTiO_3(300nm)/$ $SrRuO_3(150nm)/SrTiO_3(1000nm)/$ $YBa_2Cu_3O_7(500nm)$	780	8	$19.54 \cdot 10^7$	$7.8 \cdot 10^{-14}$
SBSSM (fig. 7.6c) (GV41(P))	$SrRuO_3(100nm)/BaTiO_3(300nm)/$ $SrRuO_3(150nm)/SrTiO_3(250nm)/$ $MgO(400nm)$	780	8	$61.93 \cdot 10^8$	$3.04 \cdot 10^{-14}$
SBSM (fig. 7.6e) (GV45(P))	$SrRuO_3(100nm)/BaTiO_3(300nm)/$ $SrRuO_3(150nm)/MgO(800nm)/$	830	8/0.027	$\approx \infty$	$3.9 \cdot 10^{-14}$
SBSM (fig. 7.6d) (GV43(P))	$SrRuO_3(100nm)/BaTiO_3(300nm)/$ $SrRuO_3(150nm)/MgO(400nm)/$	780	0.013	$\approx \infty$	$1.76 \cdot 10^{-14}$

Table 8.3: Top down layer sequences,  $BaTiO_3$  deposition pressure and temperature, RA product and C/A ratio of the structures under investigation.

formation of stacking faults and amorphous and void like grain boundaries and their density depends upon the surface mobility of the incoming atoms [92]. The higher kinetic energy of the impinging species at lower pressure [98], produces the increase of the mobility of the atomic species on the substrate, this is believed to improve the structure of the films leading to the capacitive behaviour.

The reduction of the  $BaTiO_3$  deposition pressure not only produces an increase of the RA product, but it also produce a reduction of the C/A ratio which corresponds to a reduction of the parallel capacitance, tab. 8.3. It was reported that in  $SrTiO_3/BaTiO_3$  systems grown by pulsed laser deposition the dielectric constant increases when the oxygen deposition pressure increases [79]. If the oxygen pressure during the growth of the thin films is

low it is more favorable to form oxygen vacancies in the oxide films during the growth, this results in a decrease of the dielectric constant [79].

When  $YBa_2Cu_3O_7$  has been used as sacrificial layer the capacitive structures grown on its top do not behave as pure capacitors but present losses.  $SrRuO_3/BaTiO_3/SrRuO_3$  capacitors on  $YBa_2Cu_3O_7$  sacrificial layer present impedance phases around  $-20^\circ$  at the frequency of  $50\text{ KHz}$  and at a  $BaTiO_3$  growing pressures equal to  $8\text{ Pa}$ .

Studies on the pulsed laser deposition of  $YBa_2Cu_3O_7$  films reported the presence of different types of particulates on their surface [98]. It is likely that such particulates degrade the quality of the layers deposited on their surface, by creating resistive paths through the capacitive structures which might be responsible for the low value of the RA product. In order to investigate this, an Atomic Force Microscope was used to examine the surface of the deposited  $YBa_2Cu_3O_7$  films. Fig. 7.7a shows an AFM scan on the surface of a  $150\text{ nm}$   $YBa_2Cu_3O_7$  layer, on whose surface it is possible to see an outgrowth with a height comparable to the film thickness. Some outgrowths might be present even after the optimization of the  $YBa_2Cu_3O_7$  ablation parameters performed for the superconductivity project during the first part of this phd and described in sec. D.3.2.

Such outgrowths are also present after the deposition of a  $100\text{ nm}$   $SrTiO_3$  layer as shown in, fig. 7.7b. Their effect on the upper films can be reduced using a thicker  $SrTiO_3$  layer. Fig. 7.7c shows an AFM scan on a  $SrTiO_3(500\text{ nm})/YBa_2Cu_3O_7(400\text{ nm})$  bi-layer which confirms that the particulates present on the surface of the film are fewer in number and generally smaller.

The impedance phase of capacitors grown on a  $1\ \mu m$  thick  $SrTiO_3$  buffer layer is equal to  $-64^\circ$  at  $50\ KHz$ . A further reduction of the film losses which correspond to an increase of the RA product and to a decrease of the parasitic shunting conductance is desirable. However in this case a decrease of the  $BaTiO_3$  deposition pressure below  $8\ Pa$  produces the dissociation of the  $YBa_2Cu_3O_7$  sacrificial layer [101]. This is why capacitive structures have been grown on  $MgO$  sacrificial layer.

The use of  $MgO$  as sacrificial layer produces an RA product which is at least one order of magnitude bigger than that of the devices grown on  $YBa_2Cu_3O_7$  sacrificial layer, tab. 8.3. The problem with the use of  $MgO$  as sacrificial layer is represented by its long etching time (8 hours in 20%  $HNO_3$ ).

In conclusion this work showed that  $SrRuO_3/BaTiO_3$  capacitive structures grown on  $MgO$  sacrificial layers can be used to produce energy harvesting micro-cantilevers at working frequencies over  $6\ KHz$ . With PZT, micro-cantilevers with a minimum resonance frequency of  $13.9\ KHz$  have been produced [4]. The advantage of the  $BaTiO_3$  based capacitive structures is that micro-cantilevers which extract energy from vibrations with frequency  $6\ KHz - 13.9\ KHz$  can be designed. However it has to be kept in mind that the power extracted from PZT devices is in the range  $\mu W - mW$  [5] while the theoretical power which can be extracted from the  $BaTiO_3$  based devices is in the range  $0.1\ nW - 100\ \mu W$ . This is due to the superior piezoelectric coefficients of PZT.

An optimization of the  $BaTiO_3$  deposition parameters is necessary to improve the quality of the  $SrRuO_3/BaTiO_3$  capacitors in the frequency range

$40\text{ }Hz - 6\text{ }KHz$ . There are three deposition parameters which affect the properties of the deposited films, they are: laser fluence, deposition temperature and deposition pressure. A reduction of the deposition pressure and an increase of the deposition temperature reduced the losses in the  $BaTiO_3$  layer. The next step could be the deposition of  $BaTiO_3$  films at fluences bigger than  $2.4\text{ }J/cm^2$ . The higher fluence produce an increase of the energy of the atomic species on the substrate and this is beneficial for the crystal growth (see chap. 7).

Alternatively an optimization of the stack using the  $YBa_2Cu_3O_7$  sacrificial layer can be attempted, in fact it has been demonstrated that the introduction of a thick  $SrTiO_3$  buffer layer between the sacrificial layer and the capacitive structure reduces the losses in the piezoelectric film. In this case to reduce the number of particulates on the  $YBa_2Cu_3O_7$  the target to substrate distance can be varied, furthermore the introduction of a thick ( $1\text{ }\mu m$ )  $SrTiO_3$  buffer layer can improve the planarization of the multi-layer (see chap. 7).

I point out that problems with the equipments arose during the development of this project. Problems with the X-ray source of the diffractometer did not allow the investigation of stacks containing  $BaTiO_3$  films grown at pressures lower than  $20\text{ }Pa$ . Instead problems with the pulsed laser deposition systems did not allow the successfull fabrication of an energy harvester prototype. In particular during the last 6 months of this Phd the pulsed laser deposition system has not been available, this resulted in the impossibility of the fabrication of samples.

In spite of these problems, I believed that the investigations performed

during this Phd show that the proposed multilayers can find applications in the field of energy harvesting devices and as sensors and actuators.

# Part I

# Appendices

# Appendix A

## Mechanics:

### general concepts and cantilever properties

#### A.1 Basic concepts

[32]

A body is formed by molecules linked to each other. When an external force is applied to the body, the forces linking the molecules resist the change in the shape of the body. Under the action of external forces the molecules of the body are displaced until the equilibrium between the external and the intermolecular forces is reached. The body is then in a state of **strain**.

When a body recovers its original shape after the release of the external forces, it is said to be **perfectly elastic**. If the deformation does not com-

pletely disappear after the release of the external forces the body is **partially elastic**

For a perfectly elastic body the work done by the external forces is completely transformed into potential energy of strain. For a partially elastic body part of the work done by the external forces is dissipated as heat during the non-elastic deformation.

Usually materials are considered perfectly elastic within certain limits.

In 1678, by direct experiment with the extension of prismatic bars, Robert Hooke established that within certain limits, for many materials, the elongation of the bar is proportional to the tensile force applied perpendicularly to the section of the bar, eq. A.1.

$$\vec{\Delta l} = \frac{\vec{P}l}{A\tilde{E}} \quad (\text{A.1})$$

where  $\vec{P}$  represents the tensile force,  $l$  is the length of the bar,  $A$  represents the bar cross-sectional area,  $\vec{\Delta l}$  is the total bar elongation and  $\tilde{E}$  is the elastic modulus of the material. The **normal stress** is defined as:

$$\vec{\sigma} = \frac{\vec{P}}{A} \quad (\text{A.2})$$

the elongation of the bar per unit length is called **normal strain** and it is defined as follow:

$$\vec{\epsilon} = \frac{\vec{\Delta l}}{l} \quad (\text{A.3})$$

using eq. A.2 and A.3 the Hooke law can be written in its classical form.

$$\vec{\sigma} = \tilde{E} \vec{\epsilon} \quad (\text{A.4})$$

When a force is applied on a surface of a body and the force is not perpendicular to the surface, the stress is usually separated into a normal component and into a tangential component. These two components are the **normal stress** ( $\sigma$ ) and the **shearing stress** ( $\tau$ ) respectively.

The **shearing strain** may be visualized in the following way: let us apply a tangential (shear) stress to the side  $\overline{ab}$  of the parallelogram  $abcd$ , fig. A.1, the result will be the sliding of the side  $\overline{ab}$  and the parallelogram  $a_1b_1cd$  is obtained. The shearing strain is represented by the magnitude of the small angle  $\gamma$  and it may be taken equal to the following ratio:

$$\vec{\gamma} = \frac{\overline{aa}_1}{\overline{ad}} \hat{u}_i \quad (\text{A.5})$$

which means equal to the horizontal sliding  $\overline{aa}_1$  of the side  $\overline{ab}$  with respect to the side  $\overline{dc}$  divided by the distance between these two sides,  $\hat{u}_i$  is the unit vector in the direction of the shear.

If the material obeys Hooke's law the classical relationship between shear stress and shear strain is obtained, eq. A.6,

$$\vec{\gamma} = \frac{\vec{\tau}}{G} \quad (\text{A.6})$$

$G$  is called the **Shear Modulus**.

In isotropic materials the relationship between the Young's Modulus and

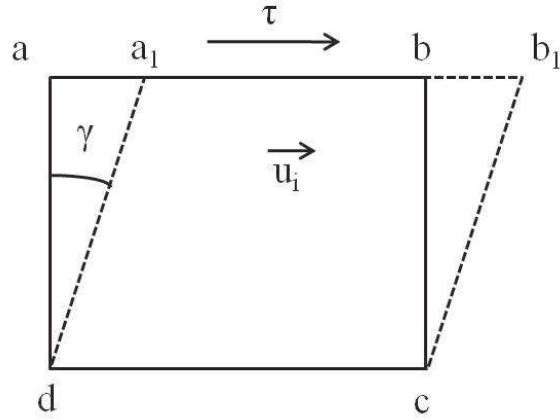


Figure A.1: Deformation induced by the shear stress  $\tau$ .

the Shear Modulus is expressed as follow:

$$G = \frac{\tilde{E}}{2(1 + \nu)} \quad (\text{A.7})$$

the quantity  $\nu$  is the **Poisson's ratio** and it is a characteristic of the material.

When a tensile normal stress is applied to the cross-section of a bar, experiments show that the axial elongation is always accompanied by lateral contraction of the bar, within the elastic limit the ratio:

$$\nu = \frac{\text{unit lateral contraction}}{\text{unit axial elongation}} \quad (\text{A.8})$$

is constant for a given material and it is known as Poisson's ratio.

Now if a two dimensional body at mechanical equilibrium is considered and a small square element is extracted from the body, fig. A.2a, on each side of the square the stress can be decomposed into a normal ( $\sigma$ ) and into a

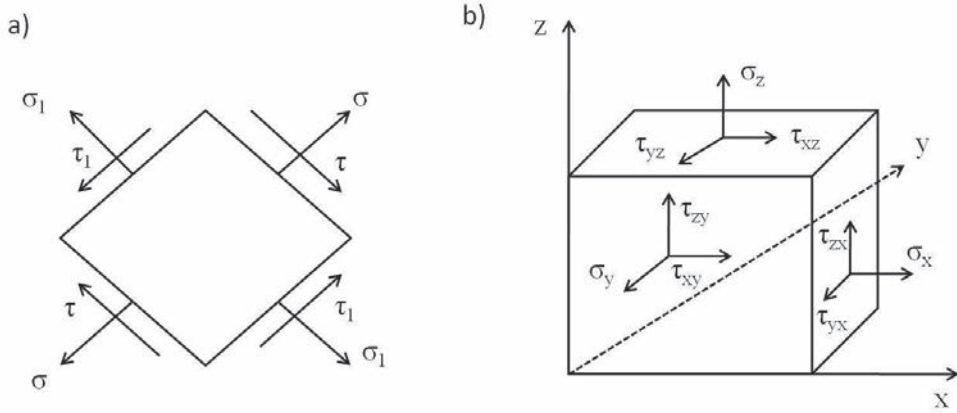


Figure A.2: a) Stress components on the sides of a two dimensional body. On each side the stress can be decomposed into a normal component  $\sigma$  and into a tangential component  $\tau$ . b) Stress components on the surfaces of a three dimensional body. On each surface the stress can be decomposed into a normal component  $\sigma_j$  and into two tangential components  $\tau_{ij}$  and  $\tau_{kj}$ .

tangential ( $\tau$ ) component. The shear stresses  $\tau$  acting on two parallel sides produce a couple in the clockwise direction, the shear stresses  $\tau_1$  acting on the others two parallel sides produce a couple in the anticlockwise direction, if the body is at equilibrium the following relation is valid.

$$\vec{\tau} = -\vec{\tau}_1 \quad (\text{A.9})$$

In the case of a three dimensional body, when a cubic element is extracted from the body, on each surface of the cube the stress can be decomposed into a normal component and two tangential components in the two perpendicular directions, fig. A.2, [30]. For an isotropic and homogeneous three dimensional

body the following conditions hold:

$$\left\{ \begin{array}{l} \vec{\tau}_{xy} = \vec{\tau}_{yx} \\ \vec{\tau}_{yz} = \vec{\tau}_{zy} \\ \vec{\tau}_{zx} = \vec{\tau}_{xz} \end{array} \right. \quad (\text{A.10})$$

with these conditions only six variables are free, in the case of a cubic volume the Hooke's law can be written in the following way.

$$\left\{ \begin{array}{l} \vec{\epsilon}_x = \left(1/\tilde{E}\right) (\vec{\sigma}_x - \nu (\vec{\sigma}_y + \vec{\sigma}_z)) \\ \vec{\epsilon}_y = \left(1/\tilde{E}\right) (\vec{\sigma}_y - \nu (\vec{\sigma}_x + \vec{\sigma}_z)) \\ \vec{\epsilon}_z = \left(1/\tilde{E}\right) (\vec{\sigma}_z - \nu (\vec{\sigma}_x + \vec{\sigma}_y)) \\ \vec{\gamma}_{xy} = \vec{\tau}_{xy}/G \\ \vec{\gamma}_{yz} = \vec{\tau}_{yz}/G \\ \vec{\gamma}_{zx} = \vec{\tau}_{zx}/G \end{array} \right. \quad (\text{A.11})$$

## A.2 Mechanical behaviour of cantilevers

[32]

The cantilevers which have been fabricated during the developing of the piezoelectric project can be thought as cantilevers with an end built into the wall fig. A.3. This means that the end *A* can not move in the three spatial directions and can not rotate during the bending of the beam, on the other side the end *B* is entirely free. This represents a statically determinate problem since the reactions at the support produced by a given load ( $\vec{P}$ ) can be

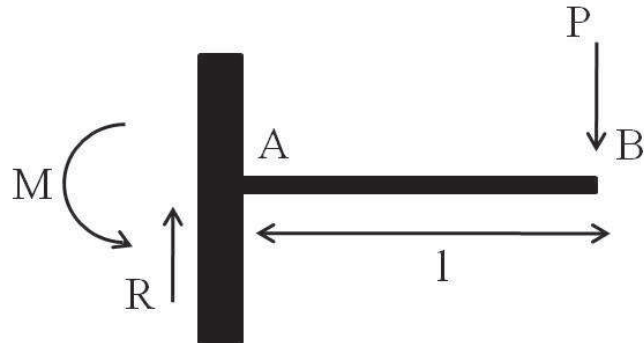


Figure A.3: Cantilever with a built in end  $A$ , the end  $B$  is free. The cantilever is loaded with the force  $\vec{P}$ , this produces a reaction at the built in end  $A$  which consists in a reactive force  $\vec{R}$  and in a reactive moment  $\vec{M}$ ,  $l$  is the length of the cantilever.

determined from the equations of statics which are:

$$\sum_i \vec{F}_i = 0 \quad (\text{A.12})$$

$$\sum_i \vec{M}_i = 0 \quad (\text{A.13})$$

where  $\vec{F}_i$  and  $\vec{M}_i$  represent the forces and the moments acting on the beam.

Suppose that a concentrated load  $\vec{P}$  is applied to the free end of the cantilever, the load is balanced by the reactive forces acting on the built-in end. From the equations of statics results that the reactive force  $\vec{R}$  is:

$$\vec{R} = -\vec{P} \quad (\text{A.14})$$

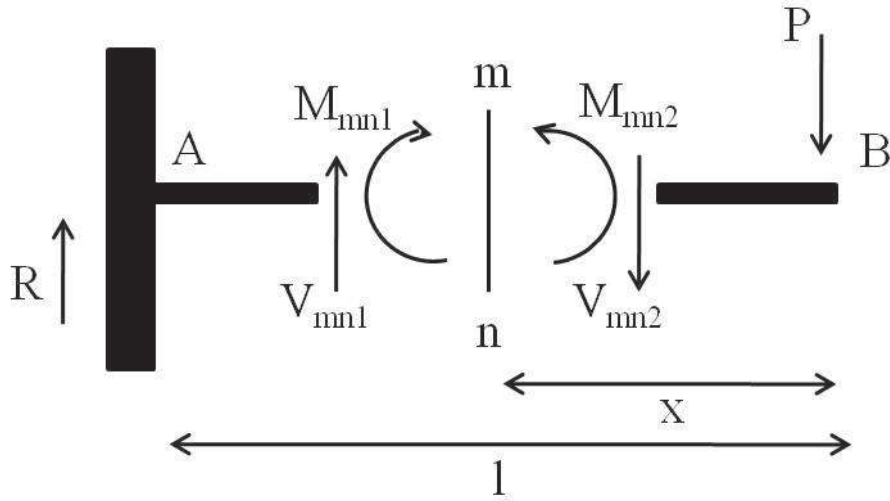


Figure A.4: To investigate the stress along the beam, the cantilever is cut in two parts by a cross section  $mn$ . The shear forces  $\vec{V}_{mn1}$  and  $\vec{V}_{mn2}$  with the moments  $\vec{M}_{mn1}$  and  $\vec{M}_{mn2}$  replace the system of external forces,  $x$  is the distance between the cross section and the point in which the load is applied and  $l$  is the length of the cantilever.

and the moment of the reactive force is:

$$|\vec{M}| = |\vec{P}| l \quad (\text{A.15})$$

and it acts in the counter-clockwise direction fig. A.3,  $l$  represents the length of the cantilever.

To investigate the stress produced in a beam during its bending, the beam is cut into two parts by a cross section  $mn$  taken at any distance from the left built in end  $A$ , fig. A.4, then the right portion is removed. In discussing the equilibrium of the left part of the beam, besides the reaction  $\vec{R}$  also the internal forces which are distributed over the cross section  $mn$  must be

considered. These forces represent the action of the right portion on the left portion of the beam. The internal forces equilibrate the external forces  $\vec{P}$  and  $\vec{R}$ .

The system of external forces to the left of the cross section  $mn$  can be replaced by the static equivalent system consisting of the shearing force  $\vec{V}_{mn1}$  and the couple  $\vec{M}_{mn1}$ , where:

$$\begin{cases} \vec{V}_{mn1} = \vec{R} \\ \vec{M}_{mn1} = \vec{R}(l - x) \end{cases} \quad (\text{A.16})$$

where  $x$  is the distance between the cross section and the point in which the force  $\vec{P}$  is applied. The force  $\vec{V}_{mn2}$  and the couple  $\vec{M}_{mn2}$  on the right side of the cross section  $mn$  which represent the action of the right portion of the beam on the left portion, balance the bending moment  $\vec{M}_{mn1}$  and the shearing force  $\vec{V}_{mn1}$ . For them the following relationships hold:

$$\begin{cases} \vec{V}_{mn2} = \vec{P} \\ \vec{M}_{mn2} = -\vec{P}x. \end{cases} \quad (\text{A.17})$$

$\vec{V}_{mn1}$ ,  $\vec{M}_{mn1}$ ,  $\vec{V}_{mn2}$  and  $\vec{M}_{mn2}$  are considered positive when their directions are as indicated in fig. A.4.

Equalizing  $\vec{V}_{mn1}$  with  $\vec{V}_{mn2}$  it is easy to find that the shear stress along each cross section of the cantilever is equal to the load  $\vec{P}$  and this is true for each cross section along the length of the beam. The equation of moment of system A.17 shows that the moment varies linearly along the length of the cantilever and assumes its maximum value (eq. A.15) at the built in end of

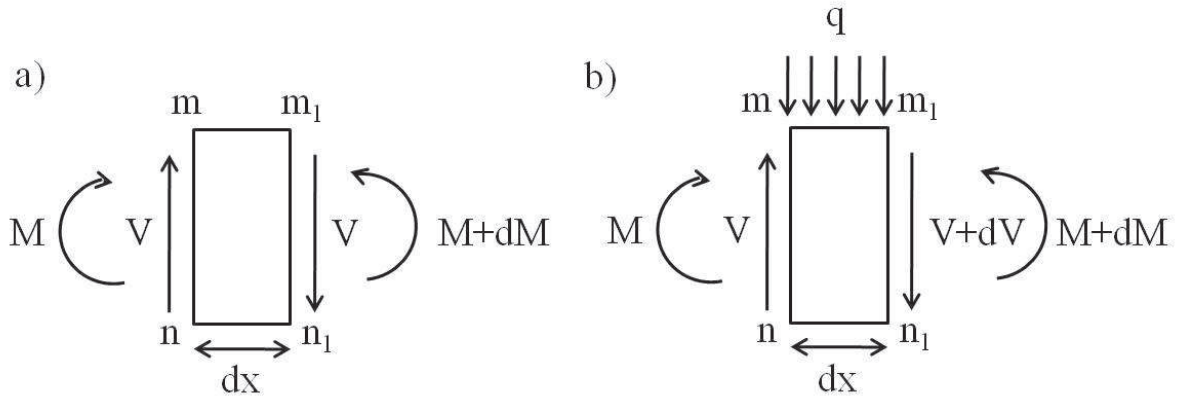


Figure A.5: a) Element of a cantilever with a built in end loaded with a concentrated load  $\vec{P}$ . The shearing forces at the cross sections  $mn$  and  $m_1n_1$  are equal, the bending moment increases of a quantity equal to  $d\vec{M}$  at the cross section  $m_1n_1$ . b) Element of a cantilever with a built in end loaded with a distributed load  $\vec{q}$ . At the cross section  $m_1n_1$  both shearing force and bending moment increase of a quantity equal to  $d\vec{V}$  and  $d\vec{M}$  respectively.

the beam.

To find the relation between the bending moment and the shearing force for the cantilever loaded with a concentrated load, fig. A.3, an element of the beam cut by two adjacent cross sections  $mn$  and  $m_1n_1$  which are a distance  $dx$  apart can be considered, fig. A.5a. Let us assume positive directions for the shearing forces and the moments at both cross sections. If no forces act on the beam between the cross sections  $mn$  and  $m_1n_1$  the two shearing forces at  $mn$  and  $m_1n_1$  are equal. From the equilibrium of the element the bending moments are not equal at the two cross sections; in fact at the cross section  $m_1n_1$  the bending moment increases of a quantity:

$$d\vec{M} = \vec{V} \cdot d\vec{x} \quad (\text{A.18})$$

and

$$\frac{d\vec{M}}{dx} = \vec{V} \quad (\text{A.19})$$

this means that on all the portions of the beam the shearing force represents the rate of change of the bending moment with respect to  $x$ .

To calculate how the bending moment and the shearing force are linked in the case of a distributed load, a distributed load  $\vec{q}$  acting between the two cross sections  $mn$  and  $m_1n_1$  can be considered, fig. A.5b, the total load acting on the element is  $\vec{q} \cdot d\vec{x}$ . If  $\vec{q}$  is considered positive when it acts downward, it may be concluded from the equilibrium of the element, that the shearing force at the cross section  $m_1n_1$  is different from that at  $mn$  by an amount equal to:

$$d\vec{V} = -\vec{q} \cdot d\vec{x} \quad (\text{A.20})$$

from which it follows that:

$$\frac{d\vec{V}}{dx} = -\vec{q} \quad (\text{A.21})$$

thus the rate of change of the shearing force is equal to the intensity of the distributed load with negative sign.

Taking the moment of all forces acting on the element:

$$d\vec{M} = \vec{V} \cdot d\vec{x} - \vec{q} \cdot d\vec{x} \cdot \frac{d\vec{x}}{2} \quad (\text{A.22})$$

neglecting the second term on the right end side as a small quantity of the second order, eq. A.19 is obtained. So also in the case of a distributed load the rate of change of the bending moment is equal to the shearing force.

It is now clear that the magnitude of the stresses at any cross section

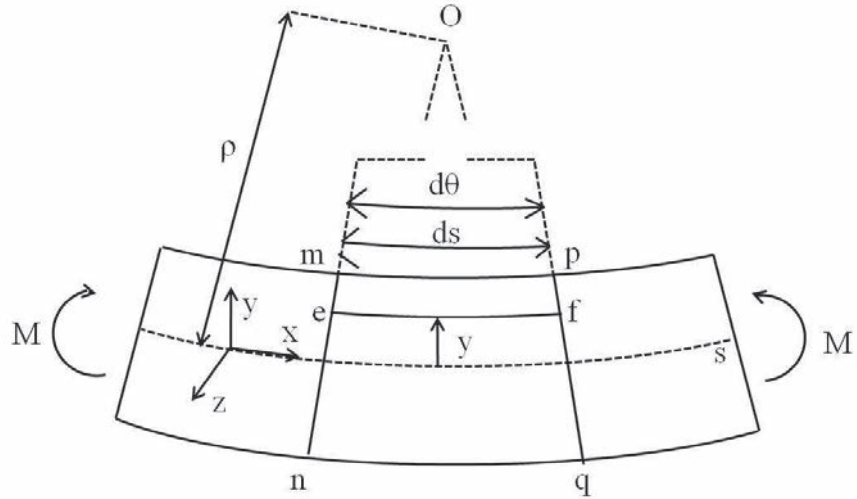


Figure A.6: Element  $mnpq$  of a cantilever under pure bending. The longitudinal fibers on the convex side experience extension, those on the concave side experience compression,  $s$  represents the neutral surface,  $\rho$  is the radius of curvature,  $y$  is the distance of the generic fiber  $ef$  from the neutral axis,  $ds$  is the length of a generic fiber and  $d\theta$  is the angle formed by the two radius of curvatures passing through  $mn$  and  $pq$ .

of the cantilever consist of two contributions: shearing force and bending moment.

Now we want to study what happens to the different fibers of a cantilever during its bending. To do that we consider an element of a cantilever in which the shearing forces are zero and only the bending moment is present, fig. A.6. This approximation is called **pure bending**, and is based on the assumption that the lines  $mn$  and  $pq$  remain straight after bending and the entire transverse section on the beam (in the  $yz$  plane), originally plane, remains plane and normal to the longitudinal fibers of the beam after bending fig. A.6. The effect of the shear stresses like  $\tau_{yx}$  and  $\tau_{zx}$  produce a curvature

of the lines  $mn$  and  $pq$  in the  $x$  and  $z$  directions. In this treatment this effect will be neglected.

During the bending the cross sections  $mn$  and  $pq$  rotate respect to each other, the longitudinal fibers on the convex side experience an extension and those on the concave side experience compression fig. A.6.

The line  $s$  do not experience strain during the bending, this surface is called the **neutral surface** and its intersection with any cross section is called the **neutral axis**.

Denoting by  $\rho$  the radius of curvature, defined as:

$$k = \frac{1}{\rho} = \left| \frac{d\theta}{ds} \right| \quad (\text{A.23})$$

where  $k$  is the curvature of the beam. For small  $ds$  it is possible to use the approximation:

$$ds \approx dx \quad (\text{A.24})$$

and eq. A.23 can be approximated as follow.

$$\frac{1}{\rho} \approx \left| \frac{d\theta}{dx} \right| \quad (\text{A.25})$$

The fiber  $ef$ , of fig. A.6, during the bending experiences compression, using the approximation A.24 its length  $L_{ef}$  can be expressed as follow.

$$L_{ef} = (\rho - y) \theta = dx - \frac{y}{\rho} dx \quad (\text{A.26})$$

So after compression the length of the fiber  $ef$  is equal to the initial length

minus a coefficient which multiplies the initial length, such coefficient represents the strain in the  $x$  direction eq. A.27.

$$\epsilon_x = \frac{y}{\rho} \quad (\text{A.27})$$

The strain of the longitudinal fibers are proportional to the distance from the neutral surface and inversely proportional to the radius of curvature. With the expression of the strain  $\epsilon_x$  the expression of the longitudinal stress  $\sigma_x$  can be written.

$$\sigma_x = \frac{\tilde{E}y}{\rho} \quad (\text{A.28})$$

Fig. A.7 shows the distribution of the longitudinal stresses  $\sigma_x$  on the cantilever cross section, the longitudinal stress increases when the distance from the neutral axis increases and it changes its sign when it passes over or under the neutral axis.

Due to the fact that all the forces distributed over the cross section  $A$  represent a system equivalent to a couple, from the laws of statics, it follows that the resultant of these forces in the  $x$  direction must be equal to zero.

$$\int_A \sigma_x da = \frac{\tilde{E}}{\rho} \int_A y dA = 0 \quad (\text{A.29})$$

This means that the neutral axis passes through the centroid of the section.

The moment of the force acting on the area element  $dA$  with respect to the neutral axis is:

$$dM = \sigma_x y dA \quad (\text{A.30})$$

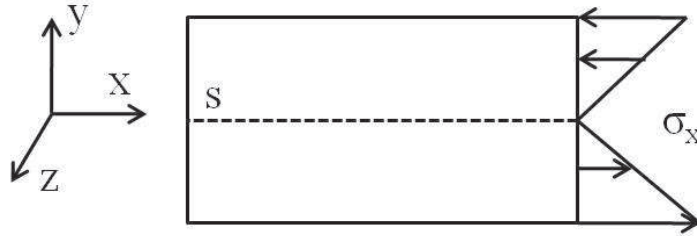


Figure A.7: Distribution on the stresses  $\sigma_x$  on the cantilever cross section,  $s$  indicates the position of the neutral axis and  $t$  is the thickness of the cantilever.

adding all the infinitesimal moments  $dM$  over the cross section the total moment is obtained eq.A.31

$$M = \int_A \sigma_x y dA = \frac{\tilde{E}}{\rho} \int_A y^2 dA. \quad (\text{A.31})$$

Defining:

$$\hat{I} = \int y^2 dA \quad (\text{A.32})$$

as the **moment of inertia of the cross section** with respect to the neutral axis, and considering eq. A.28 the following expression for the modulus of the longitudinal stress is obtained eq. A.33.

$$\sigma_x = \frac{My}{\hat{I}} \quad (\text{A.33})$$

The sign in eq. A.33 depends upon the direction of the coordinate axes.

The moment of inertia of the cross section  $I_z$  quantifies the resistance of a surface to the deformations according to its shape. For a rectangular cross

section with a width equal to  $b$  and a depth equal to  $h$  the moment of inertia of the cross section is:

$$\hat{I} = \int_{-\frac{b}{2}}^{\frac{b}{2}} \int_{-\frac{h}{2}}^{\frac{h}{2}} y^2 dy dx = \int_{-\frac{b}{2}}^{\frac{b}{2}} \frac{h^3}{12} dx = \frac{bh^3}{12}. \quad (\text{A.34})$$

The maximum tensile and compressive stresses occur at the two cantilever outermost fibers and for a rectangular cross section with the centroid at the middle of the depth  $h$  the following expression hold.

$$\sigma_{comp, max} = \sigma_{tens, max} = \frac{Mh}{\hat{I}2} \quad (\text{A.35})$$

Fig. A.6 shows the element of a cantilever under pure bending. Let us now consider the shape of the axis of the beam after bending fig. A.8, this curve is called the **deflection curve**. combining eq. A.28 with eq. A.33 the relation between bending moment and radius of curvature is derived, eq. A.36.

$$\frac{1}{\rho} = \frac{M}{\tilde{E}\hat{I}} \quad (\text{A.36})$$

To derive an expression for the relation between the curvature and the shape of the curve, two adjacent points on the deflection curve,  $m$  and  $n$ , separated by a distance  $ds$  can be considered. If the angle which the tangent at  $m$  makes with the  $x$  axis is denoted with  $\theta$ , the angle between the normals to the curve at  $m$  and  $n$  is  $d\theta$ . The intersection point  $O$  of these normals gives the centre of curvature and defines the radius of curvature  $\rho$ , eq. A.23. Regarding the sign of the radius of curvature, if the bending moment is taken positive when an upward concavity is produced, the curvature is positive when the centre

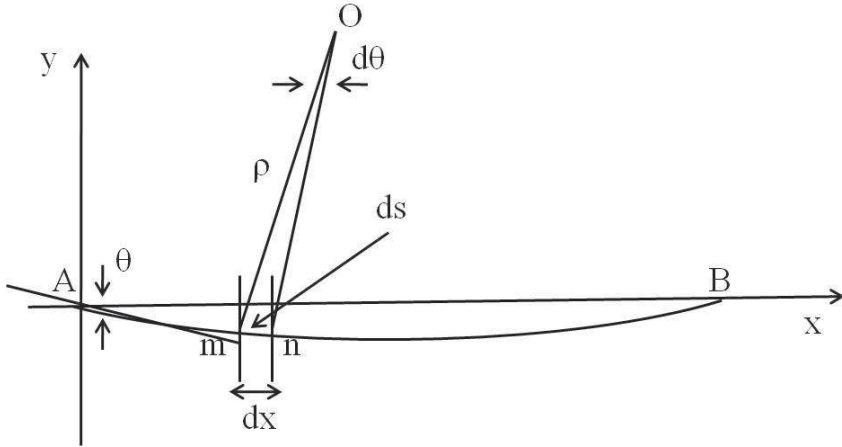


Figure A.8: Deflection curve  $AB$  of a beam after bending, it is the shape of the axis of the beam after bending,  $m$  and  $n$  are two points taken on the curve separated by a distance  $ds$ ,  $\theta$  is the angle which the tangent at  $m$  makes with the  $x$  axis,  $d\theta$  is the angle between the normals to the curve at  $m$  and  $n$  and  $\rho$  is the radius of curvature.

of curvature is above the curve. For such curvature the angle  $\theta$  decreases as the point  $m$  moves from  $A$  to  $B$ , this means that to a positive increment  $ds$  corresponds a negative  $d\theta$ , so to have the proper sign eq. A.23 must be written as follow.

$$\frac{1}{\rho} = -\frac{d\theta}{ds} \quad (\text{A.37})$$

For small deflections, approximation A.24 holds, in such case also another approximation can be used:

$$\theta \approx \tan(\theta) = -\frac{dy}{dx} \quad (\text{A.38})$$

with these approximations the expression of the radius of curvature becomes:

$$\frac{1}{\rho} \approx -\frac{d^2y}{dx^2} \quad (\text{A.39})$$

integrating both sides of eq. A.39 over the length of the cantilever  $l$ , equation A.40 is obtained:

$$y = \frac{l^2}{2\rho} \quad (\text{A.40})$$

$y$  represents the deflection of the free end and  $l$  is the length of the cantilever.

Substituting eq. A.39 in eq. A.36 the differential equation of the deflection curve is obtained eq. A.41.

$$\tilde{E}\hat{I}\frac{d^2y}{dx^2} = M \quad (\text{A.41})$$

The sign of eq. A.41 depends on the choice of the reference system. If the  $y$  axis is taken positive downwards, it is necessary to put:

$$\theta \approx \frac{dy}{dx} \quad (\text{A.42})$$

and a minus sign will be present on the right side of eq. A.41.

When the bar experience a large deflection, approximation A.38 can not be used, in this case the exact expression has to be considered:

$$\theta = \arctan\left(\frac{dy}{dx}\right) \quad (\text{A.43})$$

then the radius of curvature is:

$$\begin{aligned} \frac{1}{\rho} &= -\frac{d\theta}{ds} = -\frac{d \arctan \left( \frac{dy}{dx} \right)}{dx} \frac{dx}{ds} = \\ &= -\frac{\frac{dy}{dx^2}}{\left[ 1 + \left( \frac{dy}{dx} \right)^2 \right]^{\frac{3}{2}}}. \end{aligned} \quad (\text{A.44})$$

Differentiating eq. A.41 with respect to  $x$  and using eq. A.18 the relation between the deflection curve  $y(x)$  and the shearing force is obtained:

$$\tilde{E}\hat{I} \frac{d^3}{dx^3} = V \quad (\text{A.45})$$

differentiating eq. A.45 again and using eq. A.21 it is possible to write:

$$\tilde{E}\hat{I} \frac{d^4}{dx^4} = -q \quad (\text{A.46})$$

the last equation is used in considering the deflection of a beam under a distributed load.

Equations A.18, A.45 and A.46, constitute the system of equations which has to be solved to find the expression of the deflection curve for a cantilever under the action of the external forces.

Let us consider the cantilever of fig. A.9, where a load  $P$  and a moment  $M_0$  act on the free end  $B$ . The system of equations to solve, in order to find

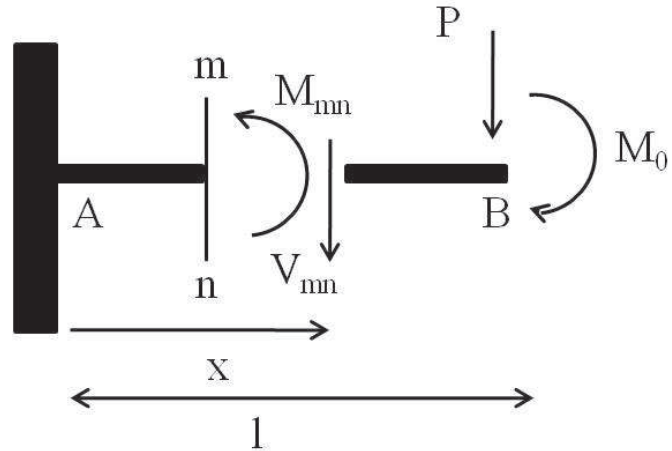


Figure A.9: Cantilever loaded with a load  $P$  and a moment  $M_0$ .

the analytical expression of the deflection curve is:

$$\left\{ \begin{array}{l} -q = \tilde{E}\hat{I}\frac{d^4y}{dx^4} \\ V = \tilde{E}\hat{I}\frac{d^3y}{dx^3} \\ M = \tilde{E}\hat{I}\frac{d^2y}{dx^2} \end{array} \right. \quad (\text{A.47})$$

in the case of fig. A.9 the following boundary conditions hold:

$$\left\{ \begin{array}{l} y(0) = 0 \\ \frac{dy}{dx}(0) = 0 \end{array} \right. \quad (\text{A.48})$$

$x = 0$  correspond to the point  $A$  in fig. A.9, these conditions imply that the built in end  $A$  can not move and can not rotate. The integration of the

system A.47 produces:

$$\left\{ \begin{array}{l} \tilde{E}\hat{I}\frac{d^4y}{dx^4} = 0 \\ \tilde{E}\hat{I}\frac{d^3y}{dx^3} = C_1 = P \\ \tilde{E}\hat{I}\frac{d^2y}{dx^2} = C_1x + C_2 = -P(l-x) - M_0 \\ \tilde{E}\hat{I}\frac{dy}{dx} = C_1\frac{x^2}{2} + C_2x + C_3 \\ \tilde{E}\hat{I}y = C_1\frac{x^3}{6} + C_2\frac{x^2}{2} + C_3x + C_4 \end{array} \right. \quad (\text{A.49})$$

considering the boundary conditions it is possible to calculate the values of the integration constants, system A.50.

$$\left\{ \begin{array}{l} C_1 = P \\ C_2 = -Pl - M_0 \\ C_3 = C_4 = 0 \end{array} \right. \quad (\text{A.50})$$

The deflection at the cantilever free end  $B$ , is then:

$$\delta_B = |y(l)| = \frac{Pl^3}{3\tilde{E}\hat{I}} + \frac{M_0l^2}{2\tilde{E}\hat{I}} \quad (\text{A.51})$$

this expression shows the contribution of the load and of the bending moment to the total deflection.

# Appendix B

## Design of cantilevers with unusual geometries

### B.1 Design of beams with different width connected in series

A way to decrease the resonance frequency of a suspended cantilever is to connect two cantilevers with different widths in series. When the cross sectional moment of inertia of the cantilever connected to the anchor is smaller than the cross sectional moment of inertia of the other part, the elastic constant of the composite structure is smaller than the elastic constant of the cantilever having the same length and the width of the wider beam.

Fig. B.1 shows a 33 mode cantilever constituted of two cantilever with different width connected in series.

Let us consider two cantilevers having widths  $b_1$  and  $b_2$  with  $b_1 > b_2$ ,

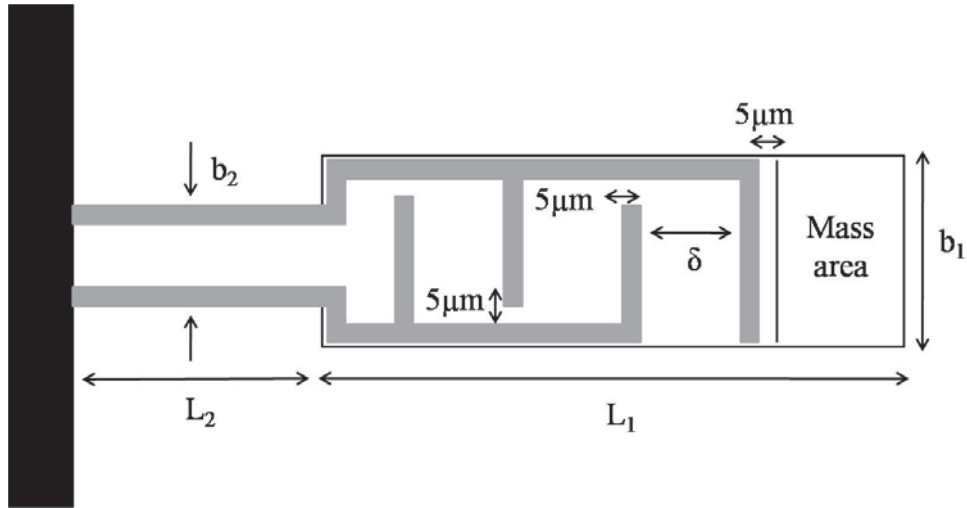


Figure B.1: Cantilever using the 33 mode constituted by two beams with different width connected in series. The area near the free end, labeled as *Mass area*, represents the part of the beam where the seismic mass will be housed,  $\delta$  is the spacing between the fingers of the electrode,  $L_1$  is the length of the wider cantilever,  $L_2$  is the length of the other part of the cantilever,  $b_1$  is the width of the wider part of the cantilever and  $b_2$  is the width of the other part of the cantilever. The lines of the interdigitated electrode (in gray) are  $5\mu m$  wide.

lengths  $L_1$  and  $L_2$ , made of the same material and connected in series. To find the expression of the elastic constant  $K_{1-z}$  eq. 2.3 can be considered, in this case, considering the convention of fig. 2.1, such equation becomes:

$$\frac{1}{K_{1-z}} = \frac{1}{E} \int_0^L \frac{x^2}{I_y(x)} dx = \frac{1}{E} \left[ \frac{1}{I_{1y}} \int_0^{L_1} x^2 dx + \frac{1}{I_{2y}} \int_{L_1}^{L_2} x^2 dx \right] \quad (\text{B.1})$$

where  $I_{1y}$  is the cross sectional moment of inertia of the part of beam having width  $b_1$  and  $I_{2y}$  is the cross sectional moment of inertia of the part of the beam having width  $b_2$ . If the integrals are solved it is possible to write the

Device	$L_1$ [ $\mu m$ ]	$L_2$ [ $\mu m$ ]	$b_1$ [ $\mu m$ ]	$b_2$ [ $\mu m$ ]	$\delta$ [ $\mu m$ ]	Mass area [ $\mu m \times \mu m$ ]	Seismic mass [Kg]	Gold thickness [ $\mu m$ ]	$M_{eq}$ [Kg]
dev.1	115	70	30	15	20	/	/	0.07	$8.953 \cdot 10^{-12}$
dev.2	115	70	30	15	20	$30 \times 45$	$5.211 \cdot 10^{-12}$	0.2	$14.643 \cdot 10^{-12}$
dev.3	190	70	30	15	20	/	/	0.07	$11.485 \cdot 10^{-12}$
dev.4	195	70	30	15	20	$30 \times 50$	$14.475 \cdot 10^{-12}$	0.5	$27.309 \cdot 10^{-12}$
dev.2	170	90	30	15	20	$30 \times 50$	$14.475 \cdot 10^{-12}$	0.5	$26.23 \cdot 10^{-12}$

Table B.1: Lengths  $L_1$  and  $L_2$ , widths  $b_1$  and  $b_2$ , electrode spacing  $\delta$ , mass area, seismic mass and equivalent mass  $M_{eq}$  of the designed 33 mode cantilevers, constituted by two beams with different width connected in series.

expression of the elastic constant in the following way:

$$K_{1-z} = \frac{3EI_{1y}}{L_1^3 + [(L_1 + L_2)^3 - L_1^3] (I_{1y}/I_{2y})} \quad (\text{B.2})$$

comparing this expression of the elastic constant, with the expression of the elastic constant of a beam having total length  $L_1 + L_2$  and width  $b_1$ , the elastic constant of the composite structure is smaller when:

$$\frac{I_{1y}}{I_{2y}} > 1 \quad (\text{B.3})$$

such conditions is always true for the structure of fig. B.1. Considering eqs. 2.21 and 2.24 a lower elastic constant implies a lower natural frequency and a lower resonance frequency.

Tabs. B.1 and B.2 report the dimensions and the parameters of the designed 33 mode cantilevers constituted by two beam with different width connected in series. Also in this case the calculations have been done assum-

<i>Device</i>	$K_{1-z}$ [N/m]	$f_n$ [KHz]	$\xi$	$f_r$ [KHz]	$V_{out}$ [V]
dev.1	0.0089	5.02	0.3	4.55	15.7
dev.2	0.009	3.95	0.23	3.73	15.7
dev.3	0.0035	2.78	0.62	1.34	5.75
dev.4	0.0036	1.83	0.4	1.51	5.75
dev.5	0.0033	1.79	0.41	1.46	5.75

Table B.2: Elastic constant  $K_{1-z}$ , natural frequency  $f_n$ , damping factor  $\xi$ , resonance frequency  $f_r$  and generated output voltage  $V_{out}$  of the designed 33 mode cantilevers constituted by two beams with different width connected in series. The output voltage has been calculated assuming a deflection of the free end equal to  $5\mu m$ .

ing the use of a gold seismic mass, and a deflection of the free end equal to  $5\mu m$  necessary to estimate the generated output voltage.

## B.2 Design of tuning fork cantilevers

The tuning fork design has been chosen because the tuning fork can vibrate in many different ways, the tines move either in the plane or perpendicular to the plane of the fork. This is beneficial in energy harvesting applications because there is the possibility to harvest energy from each of these motions.

To a first approximation, the fork can be considered to be made of two beam cantilevers joined together at the base. The modes of vibration of a tuning fork can be classified in four groups [43]:

- symmetrical modes in the plane of the fork;
- antisymmetrical mode in the plane of the fork;

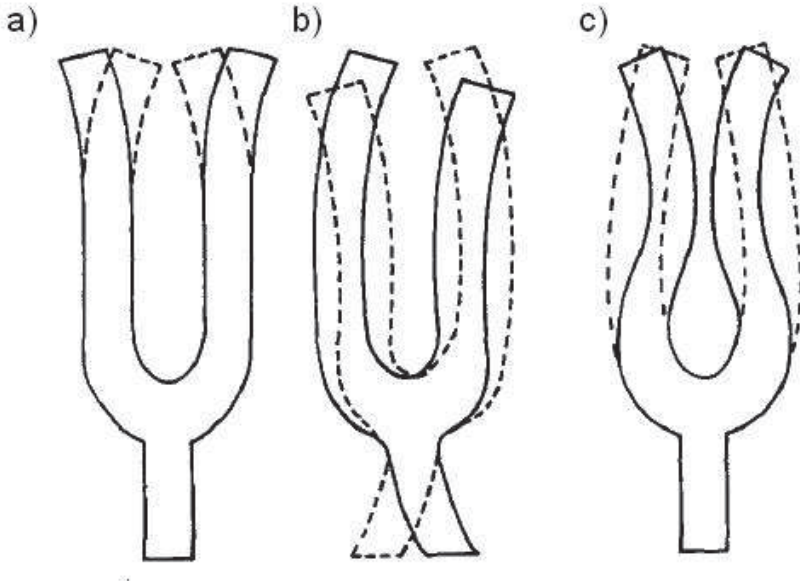


Figure B.2: First three in-plane vibrational modes of a tuning fork.  
a) Principal symmetrical in plane mode, b) principal antisymmetrical in plane mode, c) second symmetrical in plane mode [43].

- symmetrical modes out of the plane of the fork;
- antisymmetrical modes out of the plane of the fork.

Fig. B.2 shows the first three in plane modes, figs. B.2a and c show the principal and the second symmetrical in plane modes while fig. B.2 shows the first antisymmetrical in plane mode. In the symmetrical in plane modes the motion of each tine resembles that of a cantilever beam whose modal frequencies  $f_{ip.s.n}$  are given by [43]:

$$f_{ip.s.n} = \frac{\pi \tilde{K}_z}{8L^2} \sqrt{\frac{\tilde{E}}{\rho}} [1.194^2, 2.988^2, 5^2, 7^2, \dots, (2n+1)^2] \quad (\text{B.4})$$

where  $\tilde{E}$  is the elastic Young's modulus,  $\rho$  is the density of the material used to made the tuning fork and  $\tilde{K}_i$  is the radius of gyration of the beam cross section defined as:

$$\tilde{K}_i = \sqrt{\frac{I_i}{A}} \quad i = x, y, z \quad (\text{B.5})$$

$I_i$  is the moment of inertia of the cross section respect to the axis of interest and  $A$  is the area of the cross section.

In the antisymmetrical in plane modes the entire fork bends in the manner of a beam with free ends whose modal frequencies  $f_n$  are given by [43]:

$$f_{ip.a.n} = \frac{\pi \tilde{K}_z}{8L^2} \sqrt{\frac{\tilde{E}}{\rho}} [3.011^2, 5^2, 7^2, \dots, (2n+1)^2]. \quad (\text{B.6})$$

Also in the case of the symmetrical and antisymmetrical out of plane modes, the motion can be approximated as that one of a beam with a built in end and as that one of a free beam respectively [43]. For the out of plane motion only the symmetrical out of plane motion will be considered, because its modal frequencies are lower than the antisymmetrical out of plane motion frequencies [43], and we are interested in low frequency ( $Hz - KHz$ ) applications. For the out of plane motion the model of two cantilever with different widths connected in serie will be adopted, the cantilever connected to the anchor is the stem of the tuning fork, while the other part of the cantilever is constituted by a cantilever having as width the sum of the widths of each tine.

Fig. B.3 reports a tuning fork cantilever, in order to catch energy from

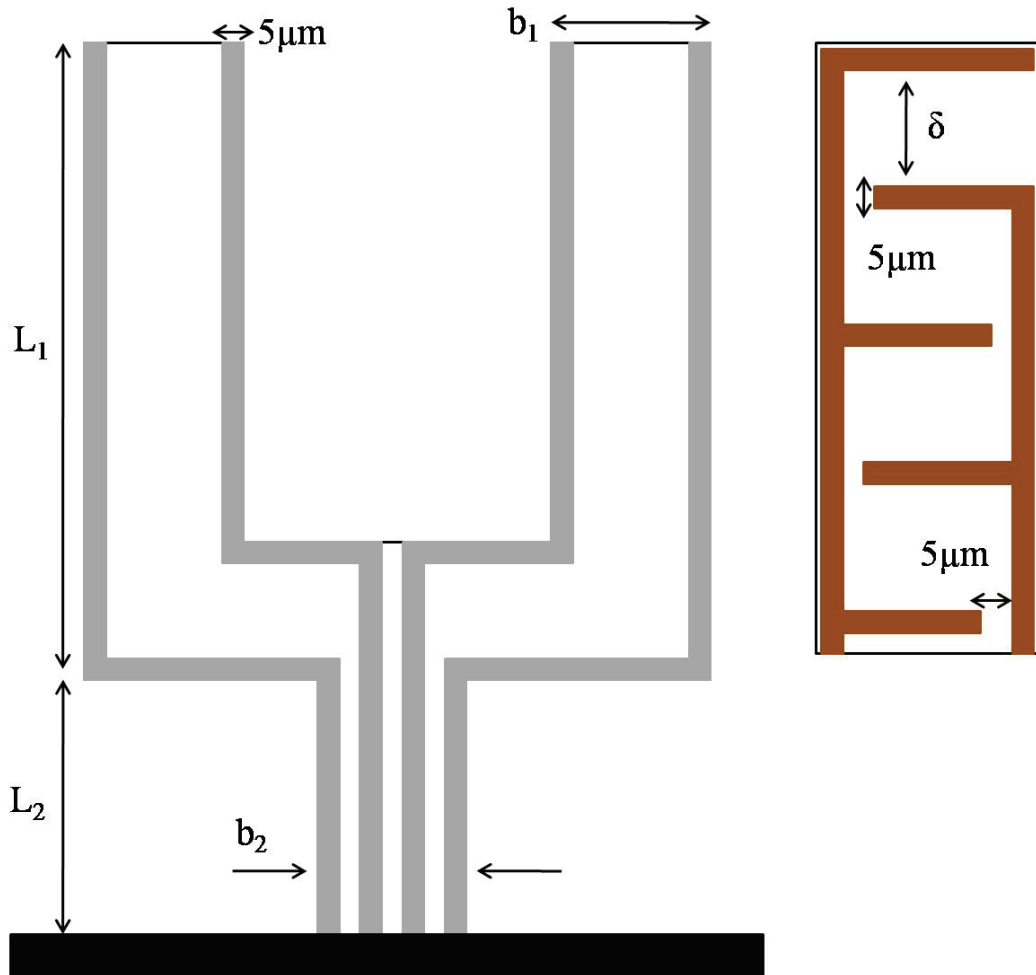


Figure B.3: Top view of the tuning fork cantilever, the parallel line electrode (in gray) allows to catch the energy coming from the in plane vibrations, the interdigitated electrode (in brown) allows to catch the energy coming from the out of plane vibration;  $L_1$  is the length of the tines,  $L_2$  is the length of the stem,  $b_1$  is the width of the tines,  $b_2$  is the width of the stem and  $\delta$  is the spacing between the fingers of the interdigitated electrode.

the in plane vibrations an electrode constituted by two parallel lines has been designed, instead to catch the energy coming from the out of plane vibrations an interdigitated electrode can be used. Eventually two piezoelectric layers

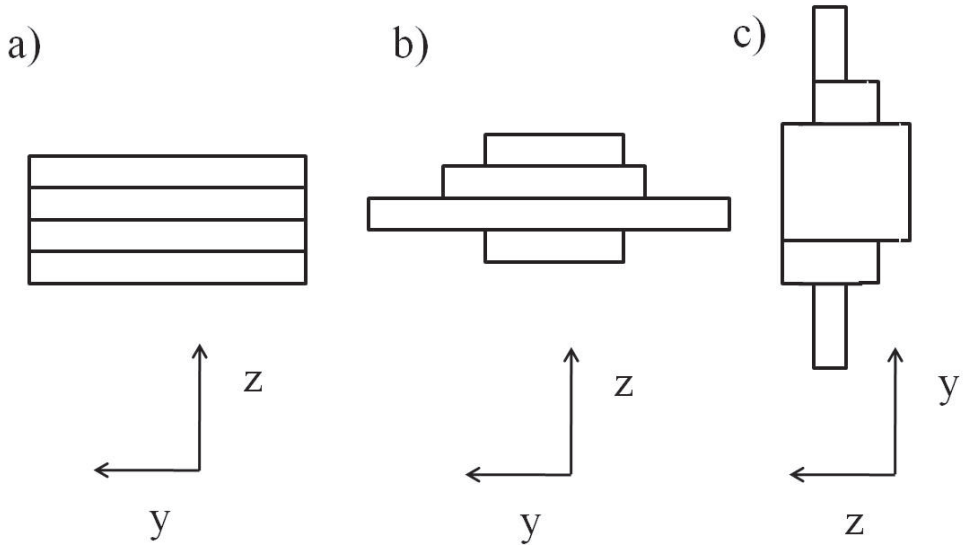


Figure B.4: a) Multilayer cross section. b) Equivalent cross section which has to be considered to calculate the cross sectional moment of inertia respect to the  $y$  axis  $I_y$ . c) Equivalent cross section which has to be considered to calculate the cross sectional moment of inertia respect to the  $z$  axis  $I_z$ .

and two electrodes can be stacked on the same cantilever this would allow to catch energy from both the in plane and the out of plane vibration modes, however as previously stated the deposition of a further piezoelectric layer on top of the first electrode might results in a film which does not present good electrical properties (look sec. 7.2).

In the case of the out of plane motion the design is equal to that one performed for the two cantilevers with different widths connected in series.

In the case of the in plane motion the cross section moment of inertia respect to the  $z$  axis has to be calculated. The way to calculate the moment of inertia respect to the  $y$  axis has been discussed in sec. 2.1, to calculate the

<i>Device</i>	$L_1$ [ $\mu m$ ]	$L_2$ [ $\mu m$ ]	$b_1$ [ $\mu m$ ]	$b_2$ [ $\mu m$ ]	$\delta$ [ $\mu m$ ]	$f_{ip.s.n}$ [KHz]	$f_{ip.a.n}$ [KHz]	$f_{o.p.s.n}$ [KHz]
dev.1	210	80	30	35	30	280	1536	2.26
dev.2	210	80	20	35	30	150.32	829	2.56
dev.3	270	80	30	35	30	136.3	955	1.42
dev.4	270	80	20	35	30	129.52	520	1.79
dev.5	390	100	30	35	50	49.46	412	0.828
dev.6	390	100	20	35	50	26.47	223.6	0.923

Table B.3: Lengths  $L_1$  and  $L_2$ , widths  $b_1$  and  $b_2$ , electrode spacing  $\delta$ , first in plane symmetrical modal frequency  $f_{ip.s.n}$ , first in plane antisymmetrical modal frequencies  $f_{ip.a.n}$  and first out of plane symmetrical modal frequency  $f_{o.p.s.n}$  of a tuning fork cantilever.

moment of inertia  $I_z$  of a multilayer cross section, fig. B.4a, the equivalent section is calculated fig. B.4b, to do that the same procedure showed in sec. 2.1 is used. Then the cross section is rotated by  $90^\circ$  and the different rectangular areas showed in fig. B.4c, are considerd then eqs. 2.10 and 2.11 can be used.

Tab. B.3 reports the dimensions and the first modal symmetrical in plane  $f_{ip.s.n}$ , antisymmetrical in plane  $f_{ip.a.n}$  and symmetrical out of plane  $f_{o.p.s.n}$  frequencies for the designed tuning fork cantilevers. The in plane modal frequencies are quite high to find applications in the field of energy harvesting, instead suitable values have been found for the out of plane symmetrical modal frequencies. It has to be remarked that no seismic masses on the tip of the tines have been considered, hence a future developement for this kind of devices consist in the analysis of the modal frequencies when a mass is added on each tine.

# Appendix C

## Impedance measurement data

In chap. 7 the impedance measurements of the fabricated capacitive structures have been discussed. It has been reported that the capacitive behaviour of a device can be evaluated by looking at the phase of the measured impedance. For an ideal capacitor the impedance phase is equal to  $-90^\circ$  but we consider good capacitive structures the devices having an impedance phase between  $-70^\circ$  and  $-90^\circ$ .

In chap. 7 the following samples have been discussed:  $GV33(P)$ ,  $GV36(P)$ ,  $GV38(P)$ ,  $GV41(P)$ ,  $GV42(P)$ ,  $GV43(P)$  and  $GV45(P)$ .

Each sample contains 24 capacitive structures and not all the devices present an equal value of the impedance phase at a certain frequency.

In this appendix, the number of devices having a certain value of the impedance phase at a certain frequency are reported. Samples  $GV38(P)$  and  $GV42(P)$  present lossy capacitive structures, for them the measurements of the impedance phase at  $10\text{ KHz}$  and  $50\text{ KHz}$  are reported. This because according to the model of fig. 7.2 the capacitive contribution becomes more

Sample	Top-down layer sequence	$BaTiO_3$ dep. temperature [°C]	$BaTiO_3$ dep. pressure [Pa]
$GV33(P)$	$SrRuO_3(100nm)/BaTiO_3(300nm)/SrRuO_3(150nm)/$	780	8
$GV36(P)$	$SrRuO_3(100nm)/BaTiO_3(300nm)/MgO(60nm)/$	780	8
$GV38(P)$	$SrRuO_3(100nm)/BaTiO_3(300nm)/SrRuO_3(150nm)/$ $SrTiO_3(250nm)/YBa_2Cu_3O_7(500nm)$	780	8
$GV41(P)$	$SrRuO_3(100nm)/BaTiO_3(300nm)/SrRuO_3(150nm)/$ $SrTiO_3(250nm)/MgO(400nm)$	780	8
$GV42(P)$	$SrRuO_3(100nm)/BaTiO_3(300nm)/SrRuO_3(150nm)/$ $SrTiO_3(1000nm)/YBa_2Cu_3O_7(500nm)$	780	8
$GV43(P)$	$SrRuO_3(100nm)/BaTiO_3(300nm)/$ $SrRuO_3(150nm)/MgO(400nm)/$	780	0.013
$GV45(P)$	$SrRuO_3(100nm)/BaTiO_3(300nm)/$ $SrRuO_3(150nm)/MgO(800nm)/$	830	8/0.027

Table C.1: Top down layer sequences and  $BaTiO_3$  deposition pressure and temperature of the investigated samples.

important when the frequency is increased.

The devices of the samples  $GV33(P)$ ,  $GV36(P)$ ,  $GV43(P)$  and  $GV45(P)$  present quite good capacitive behaviour, for them the phase of the impedance at  $500\text{ Hz}$  and  $5\text{ KHz}$  is reported.

Finally sample  $GV41(P)$  presents devices with losses but also some good structures, for this sample the impedance phases at  $1\text{ KHz}$ ,  $10\text{ KHz}$  and  $50\text{ KHz}$  are shown.

The histograms relative to the different samples and table C.1 with the top-down layer sequence of each sample and the  $BaTiO_3$  deposition conditions are reported.

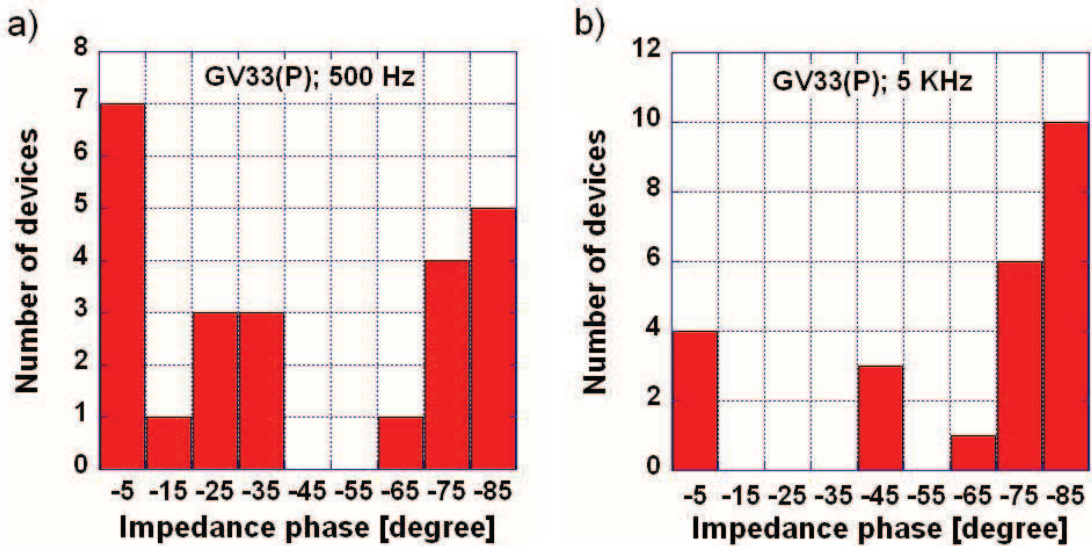


Figure C.1: Number of devices as function of the impedance phase in the sample  $GV33(P)$  at: a)  $500\text{ Hz}$ ; b)  $5\text{ KHz}$ .

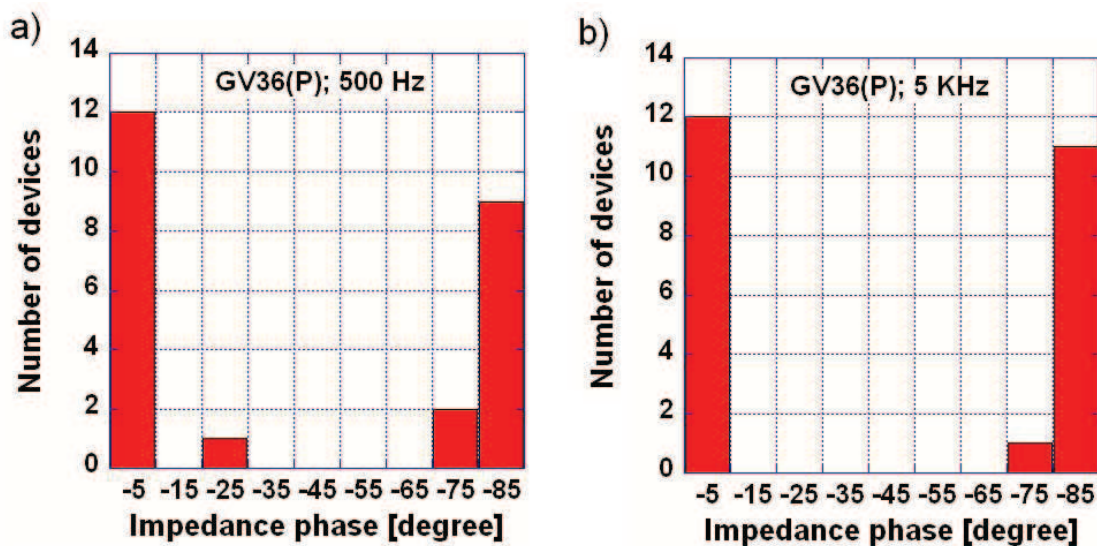


Figure C.2: Number of devices as function of the impedance phase in the sample  $GV36(P)$  at: a)  $500\text{ Hz}$ ; b)  $5\text{ KHz}$ .

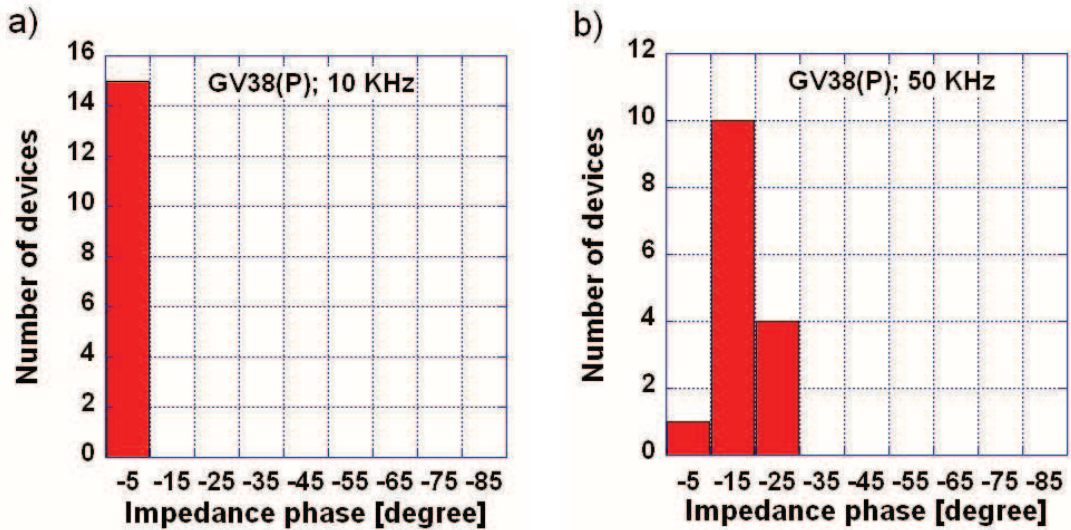


Figure C.3: Number of devices as function of the impedance phase in the sample  $GV38(P)$  at: a)  $10\text{ KHz}$ ; b)  $50\text{ KHz}$ . On this sample only 15 devices have been measured.

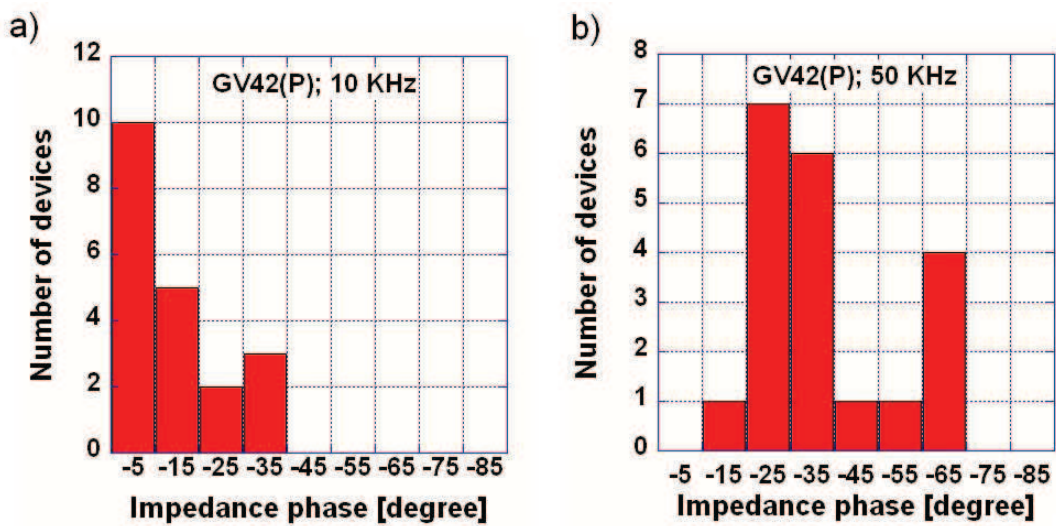


Figure C.4: Number of devices as function of the impedance phase in the sample  $GV42(P)$  at: a)  $10\text{ KHz}$ ; b)  $50\text{ KHz}$ . On this sample only 20 devices have been measured.

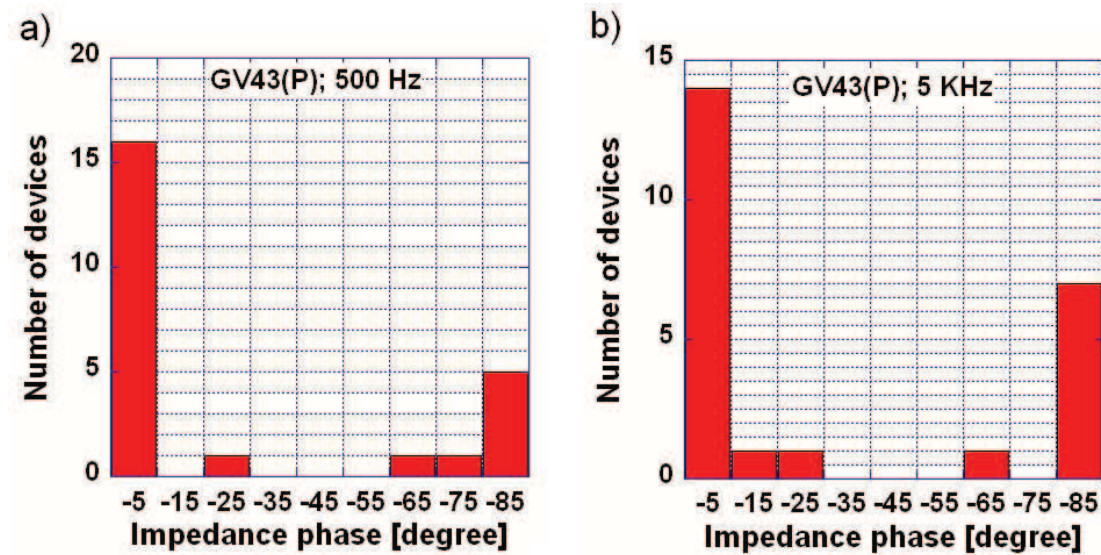


Figure C.5: Number of devices as function of the impedance phase in the sample  $GV43(P)$  at: a)  $500\text{ Hz}$ ; b)  $5\text{ KHz}$ .

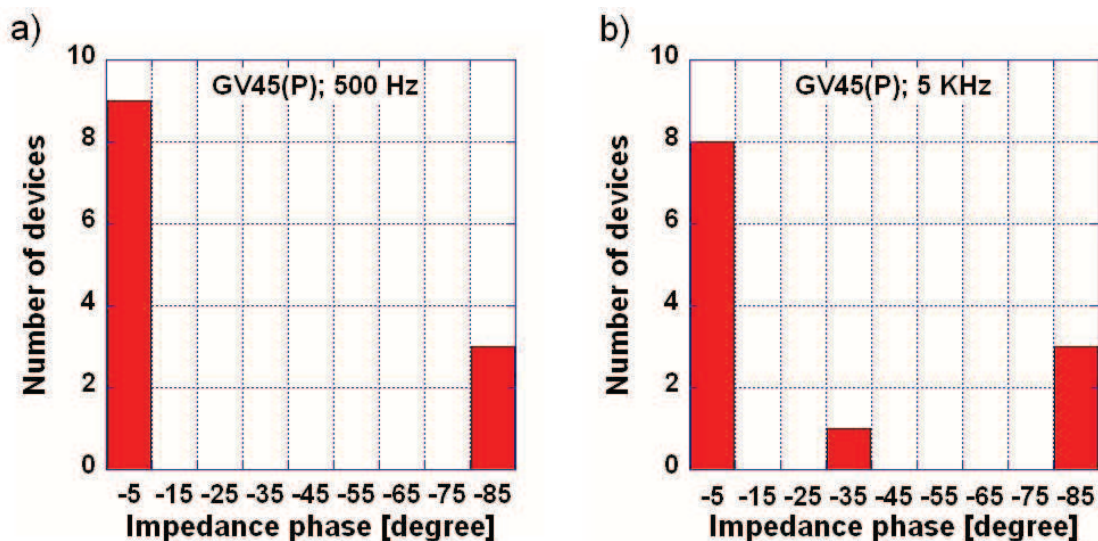


Figure C.6: Number of devices as function of the impedance phase in the sample  $GV45(P)$  at: a)  $500\text{ Hz}$ ; b)  $5\text{ KHz}$ . Only 12 devices have been measured as the others are damaged.

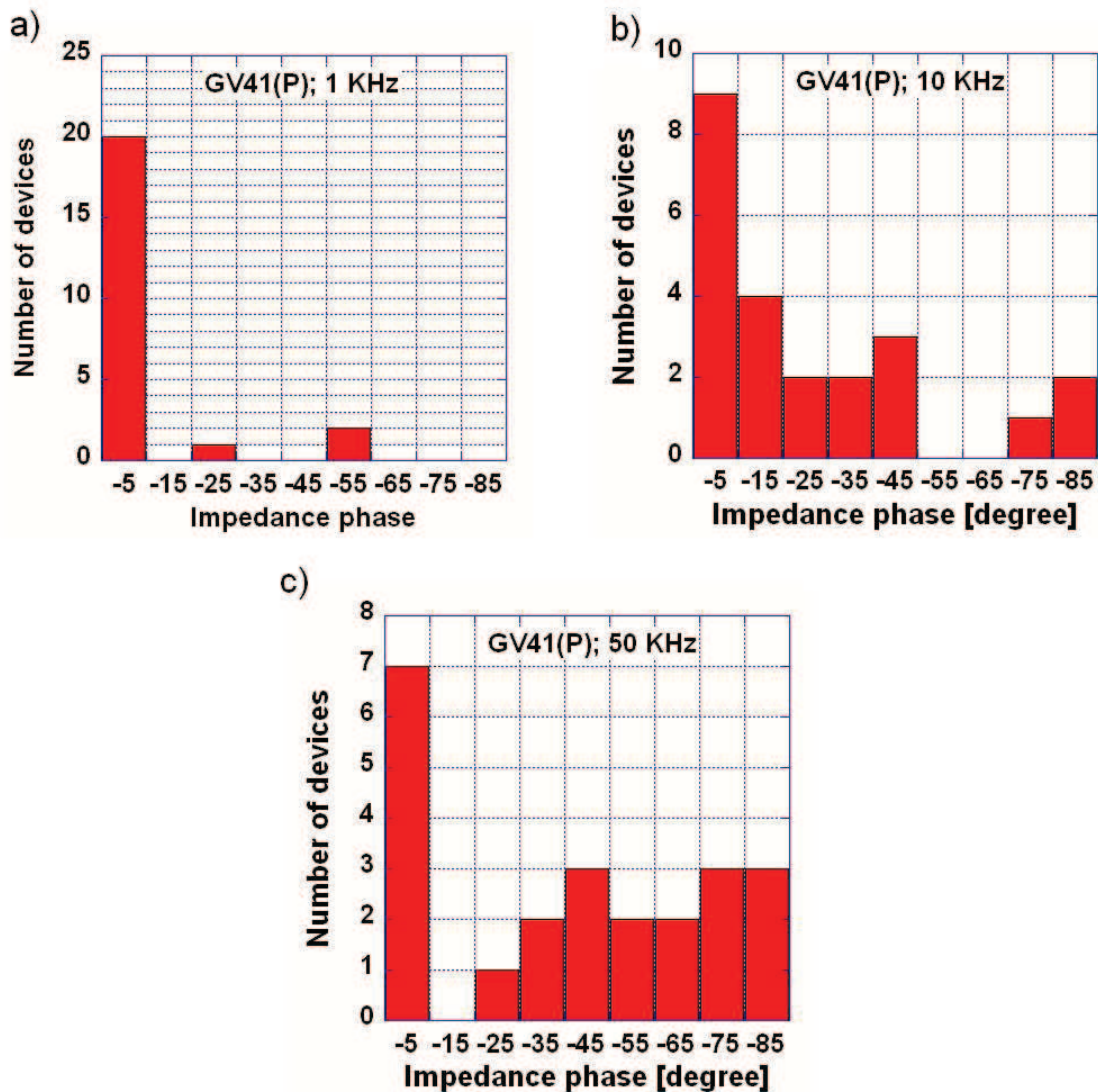


Figure C.7: Number of devices as function of the impedance phase in the sample  $GV41(P)$  at: a)  $1\text{ KHz}$ ; b)  $10\text{ KHz}$ ; c)  $50\text{ KHz}$ .

# Appendix D

## Superconductive devices

### D.1 Superconductivity and Josephson Junctions

This section present an introduction to the basic concepts of superconductivity and to the Josephson junctions devices. The idea and the applications of  $Nb/Au/YBa_2Cu_3O_7$  ramp type junctions which leads to the investigation of the  $Au/YBa_2Cu_3O_7$  ramp type contacts developed during the first part of this Phd are also introduced.

#### D.1.1 Fundamentals about superconductivity

Superconductivity is a particular state of matter achieved when a material is cooled down under a certain temperature called the **critical temperature** or the **transition temperature** and indicated with  $T_c$ . The characteristic of this state is the vanishing of the electrical resistance when the material

undergoes the superconductive transition. Superconductivity occurs in many metals and in copper based oxides known with the name of *high temperature superconductors*.

Interesting properties of superconductive materials are the **Meissner effect** and the **flux quantization in a superconducting ring**.

Let us consider an ideal conductor which turns into an ideal superconductor below its critical temperature. If a magnetic field is applied in the normal state, currents are generated by induction, they screen the magnetic field from the interior of the sample. As soon as the magnetic field reaches its final value and it does not change anymore, the permanent currents decay and finally the magnetic field within and outside the material becomes the same. When the sample is cooled down below  $T_c$  in the presence of a small magnetic field, the field is expelled from the interior of the superconductor except for a very thin layer at the sample surface. This state represents an ideal diamagnetic state and occurs independently of the sequence in which the magnetic field was applied and the sample was cooled down.

In the previous discussion it has been assumed that the applied magnetic field was small and that the sample was cooled down below the critical temperature. The property of ideal diamagnetism depends on the applied field and on the temperature, in fact such behaviour only exist within a finite range of magnetic fields and temperatures.

There exist two types of superconductors, for **type-I superconductors**, when the sample is cooled below the critical temperature, and an external magnetic field  $\vec{B}$  is applied it is only expelled if  $|\vec{B}| < |\vec{B}_c|$ ,  $\vec{B}_c$  is known as **critical field**. When the critical field is exceeded superconductivity breaks

down and the sample assumes the normal conducting state. The critical field depends on the temperature and reaches zero at the transition temperature.

For **type-II superconductors** the property of ideal diamagnetism exists below the transition temperature up to a **lower critical magnetic field**  $B_{c1}$ . Superconductivity disappears for magnetic fields larger than the **upper critical magnetic field**  $B_{c2}$ , which is usually larger than  $B_{c1}$ . Both critical fields reach zero at the transition temperature, such behaviour is found in many alloys and in the high temperature superconductors.

For values of the applied magnetic field between  $B_{c1}$  and  $B_{c2}$  the material consists of normal regions, penetrated by the applied field, next to superconductive regions where the external field does not penetrate. The flux of the magnetic field penetrating the normal regions can not vary continuously but is a multiple of a quantity called the **flux quantum** [103].

As previously stated the other interesting phenomenon in supeconductive is the flux quantization in a superconductive ring. Let us consider a ring made of a superconductive material and let us apply an external magnetic field before the ring undergoes the superconducting transition. When the ring becomes superconducting a current flows on the outer surface to expel the applied magnetic field from the bulk material as required by the property of perfect diamagnetism. In addition another current flows in the opposite direction on the inner surface of the ring to maintain the applied field in the free space region as required by Ampere law. When the external field is removed, due to the zero resistance in the superconducting state, the currents are supported without any dissipation and the flux trapped into the ring can not assume an arbitrary value but is always a discrete number of flux quanta

$\Phi_0$ :

$$\int_S \vec{B} \cdot \hat{n} dS = n\Phi_0; \quad n \in N \quad (\text{D.1})$$

where the contour of the surface  $S$  is taken between the two walls of the ring where no currents are flowing [104].

The BCS theory demonstrates that in a material which undergoes the superconductive transition two electrons with opposite momentum of equal magnitude and with opposite spins are linked together into a pair, such pairs are called **Cooper pairs** [103]. All the Cooper pairs occupy the same state which is called the *ground state*, such state is described by one wave function  $\psi(\vec{r}, t)$  which describes the entire ensemble of Cooper pairs [104]. Below  $T_c$  exists an energy gap  $\Delta$  between the electrons bounded into Cooper pairs and the normal ones, this gap represents the energy necessary to break a Cooper pair and form two excitations.

The flux quantization in a superconductive ring is a consequence of the wavefunction associated with the Cooper pairs [103].

To have an idea on how two electrons can link together, a lattice made of ions can be considered, when the material is cooled down the electrons are inserted. These electrons polarize the medium by attracting the positive ions which in turn attract the second electron, giving an effective attractive interaction between the electrons. If this attraction is strong enough to override the repulsive screened coulomb interaction, it gives rise to a net attractive force which results in superconductivity.

We must keep in mind that this discussion is meaningful only in a heuristic sense and do not allow quantitative conclusions, for a quantitative approach,

a quantum mechanical treatment is necessary.

### D.1.2 Josephson junctions

The Josephson junction system is constituted by two superconductive electrodes separated by a thin non superconductive barrier layer fig. D.1, for instance an electrical insulator or a normal metal. Let us indicate with  $\psi_1(\vec{r}, t)$  the wave function associated with the Cooper pairs of the first electrode and with  $\psi_2(\vec{r}, t)$  the wave function associated with the Cooper pairs of the second electrode. When the two electrodes are separated each wave function satisfy a Schrodinger equation:

$$\frac{\partial\psi_1}{\partial t} = -\frac{i}{\hbar}E_1\psi_1; \quad \frac{\partial\psi_2}{\partial t} = -\frac{i}{\hbar}E_2\psi_2 \quad (\text{D.2})$$

and the two wave functions assume the following forms:

$$\psi_1 = |\psi_1| e^{i\phi_1}; \quad \psi_2 = |\psi_2| e^{i\phi_2} \quad (\text{D.3})$$

where

$$|\psi_i|^2 = n_{si} \quad (\text{D.4})$$

represents the density of the Cooper pairs and  $\phi_i$  is the phase of the wave function.

When the two superconductive electrodes are brought together and separated by a thin barrier layer (few nanometers) the Cooper pairs can tunnel from the first to the second electrode, this correspond to the fact that a small part of the wavefunction of each electrode penetrates the barrier fig. D.1, this

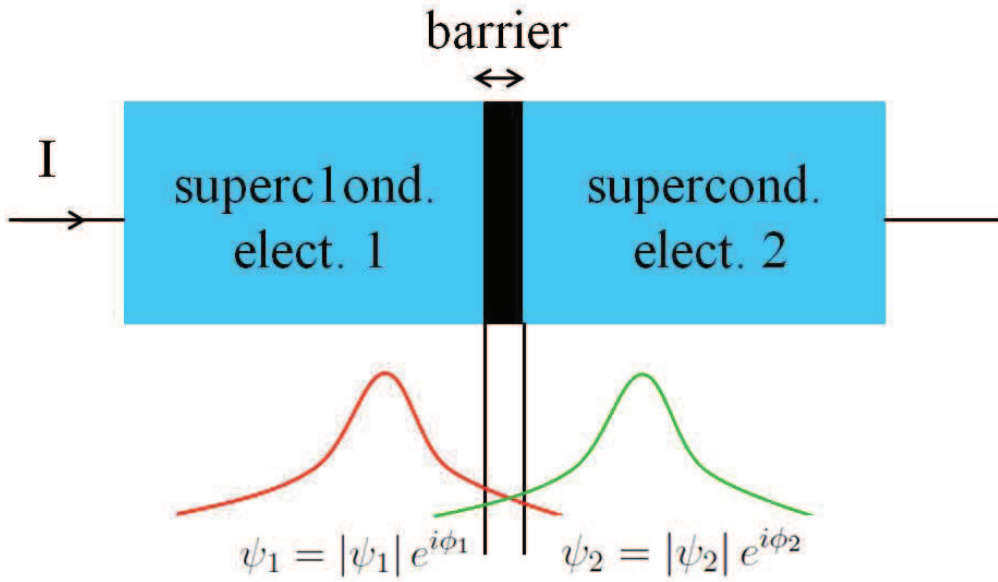


Figure D.1: Josephson junction consisting of two superconducting electrodes separated by a thin, non superconducting barrier layer, in the picture also a representation of the macroscopic wave function across the barrier is reported.

phenomenon is modeled with the help of the tunneling coefficient  $K$ . By using this formalism the Schrodinger equation in each of the two electrodes can be written as follow:

$$\frac{\partial \psi_1}{\partial t} = -\frac{i}{\hbar} (E_1 \psi_1 + K \psi_2) \quad (\text{D.5})$$

$$\frac{\partial \psi_2}{\partial t} = -\frac{i}{\hbar} (E_2 \psi_2 + K \psi_1). \quad (\text{D.6})$$

By solving the Schrodinger equations the current through the junction can be calculated:

$$I_s = I_c \sin(\phi_2 - \phi_1) \quad (\text{D.7})$$

this is known as **first Josephson equation** and  $I_c$  is called the **critical**

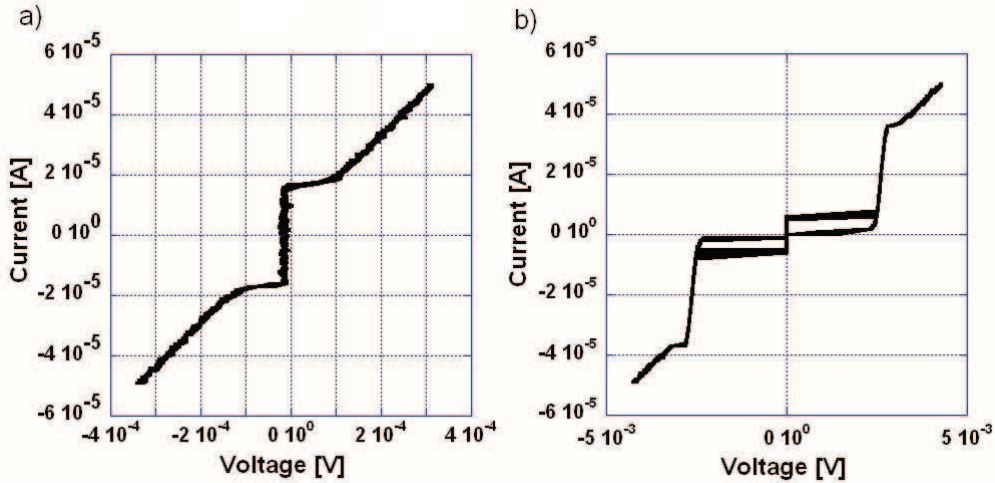


Figure D.2: a) I-V at 4.2KK for an IPHT  $Nb/Al_2O_3/Nb$  shunted junction. b) I-V at 4.2 K for an IPHT  $Nb/Al_2O_3/Nb$  unshunted junction. Measurements performed at the University of Birmingham.

**current.** Eq. D.7 reveals that the current through the junction is function of the phase difference between the two wavefunctions associated with the superconductive electrodes [103].

The key point about the Josephson junctions is that as long as the bias current supplied to the junction, does not exceed the critical value  $I_c$  no voltage drop across the junction is present. When the bias current is bigger than the critical value also the normal electrons contribute to the total current across the junction, this results in the developing of a resistance across the device and a voltage is generated between the two electrodes.

The second characteristic of a Josephson junction is that when a constant voltage  $V$  is applied between the electrodes an alternating current appears,

the frequency  $f_j$  of this current is given by:

$$f_j = \frac{V}{\Phi_0} = V \frac{2e}{h}. \quad (\text{D.8})$$

The last equation is consequence of the **second Josephson equation** [103, 104].

Fig. D.2b shows the  $I - V$  curve for a Josephson junction, when the current is increased above zero, the current flows as a Josephson current at zero voltage and it remains at zero voltage until the critical value is exceeded. At this point the voltage switches to the nonzero value of  $2\Delta/e$  which is the energy necessary to break a Cooper pair. As the current is further increased beyond its critical value, a voltage develops and increases as the current increases until a linear regime is approached fig. D.2a. As the current is then decreased from the linear regime, the voltage retraces the previous curve until it reaches  $2\Delta/e$ . As the current is further reduced the characteristic follows a new curve, which drops sharply to zero. When the current reaches zero the voltage switches to zero, as it was initially when there was no driving current.

### D.1.3 SQUIDS: superconductive quantum interference devices

In sec. D.1.1 it has been reported that if a superconducting ring is placed into a magnetic field, the magnetic flux through the ring is always a multiple of the flux quanta  $\Phi_0$ . When an arbitrary magnetic field, generating an arbitrary flux, is applied to the ring, circulating currents will start flowing on the outer

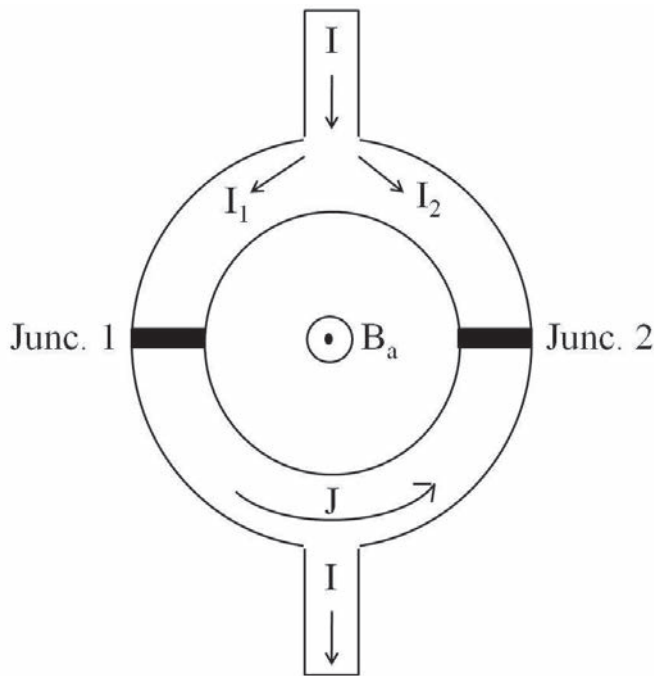


Figure D.3: SQUID: Superconducting Quantum Interference Device,  $B_a$  is the applied magnetic field,  $I$  is the bias current,  $I_1$  and  $I_2$  represent the currents through the first and through the second Josephson junctions and  $J$  is the circulating current.

surfaces of the ring. The flux generated by the circulating current balances the flux of the applied magnetic field in such a way that the flux threading the ring is a multiple of the flux quantum.

If two Josephson junctions are integrated in a superconductive ring, a device called SQUID (Superconducting Quantum Interference Device) is obtained fig. D.3. Now let us suppose that the ring is located in a region where a magnetic field  $\vec{B}_a$  perpendicular to the area of the ring exists and a bias current  $I$  is applied to the SQUID. This current separates into two currents  $I_1$  and  $I_2$  flowing along the two halves of the ring. Because of the current

conservation the following holds:

$$I = I_1 + I_2 \quad (\text{D.9})$$

in terms of the circulating current  $J$  flowing in the ring the currents  $I_1$  and  $I_2$  can be written as:

$$I_1 = \frac{I}{2} + J; \quad I_2 = \frac{I}{2} - J \quad (\text{D.10})$$

$I_1$  is the current flowing through the first Josephson junction while  $I_2$  is the current flowing through the second junction, their expression are:

$$I_1 = I_c \sin(\Delta\phi_1); \quad I_2 = I_c \sin(\Delta\phi_2). \quad (\text{D.11})$$

For simplicity it has been assumed that the critical currents  $I_c$  of the two Josephson junctions are identical. If the expressions D.11 are substituted in eqs. D.10 and then subtracted the expression of the circulating current of the ring as function of the phase difference across the two junctions is obtained [103]:

$$J = \frac{I_c}{2} [\sin(\Delta\phi_1) - \sin(\Delta\phi_2)]. \quad (\text{D.12})$$

As in the case of a simple superconducting ring, also in this case the phase of the macroscopic wave function around the ring changes by an integer multiple of  $2\pi$  [103]. This happens though two phase jumps are present across the two junctions. Such condition implies that the magnetic flux threading the ring is a multiple of the flux quantum. The circulating current of the

SQUID depends on the phase differences across the two junctions, so the currents flowing through the two junctions interferes either constructively or destructively in order to respect the condition on the flux threading the ring. From eq. D.12 it is clear that the maximum circulating current is equal to  $I_c$  this happens every time that the applied magnetic flux reaches the value  $(n + 1/2)\Phi_0$ , when the applied flux correspond to an integer multiple of flux quantum the circulating current is zero and two equal currents flow across the two Josephson junctions [103].

#### D.1.4 Conventional and unconventional superconductivity

In conventional superconductivity the macroscopic wave function associated with the Cooper pairs is isotropic, this means that it does not depend on the wave vector  $\vec{k}$  of the electrons.

It is convenient to illustrate this situation in the  $k$ -space, let us consider the  $(k_x, k_y)$  space, the amplitude  $\psi_0$  of the pair wave function is symbolized for a fixed value of  $\vec{k}$  by the vector describing the distance of the curve from the origin. If  $\psi_0$  does not depend on  $\vec{k}$  the distance vector has the same value for all the vectors  $\vec{k}$ , so in two dimensions it represents the radius of a circle fig. D.4a, in three dimensions it represents the radius of a sphere. If  $\psi_0$  depends on the vector  $\vec{k}$  the circle is deformed.

In unconventional superconductivity the amplitude of the macroscopic wave function depends on the wave vector  $\vec{k}$ . Fig. D.4b represents the macroscopic wave function of the  $YBa_2Cu_3O_7$  which is an high temperature and

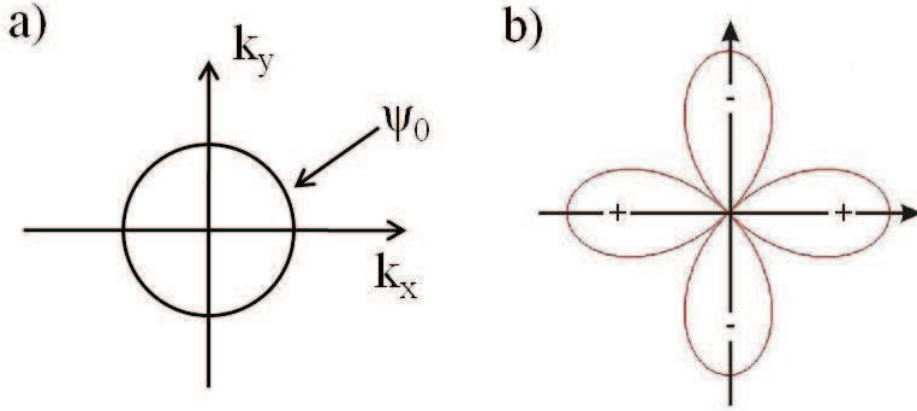


Figure D.4: a) Amplitude of the wave function in the  $k$ -space for a conventional superconductor. b) Amplitude of the wave function in the  $k$ -space for the  $YBa_2Cu_3O_7$  unconventional superconductor.

unconventional superconductor;  $YBa_2Cu_3O_7$  is employed in the Josephson junctions project for the fabrication of  $Au/YBa_2Cu_3O_7$  ramp type contacts. The modulus square of the wave function  $\psi_0$  represents the density of the Cooper pairs, by looking at fig. D.4b the amplitude of the wave function is zero along certain crystal directions, this means that the Cooper pairs can not move along those directions. **The wave function of fig. D.4b experiences a change of sign between certain crystal directions [103].**

Let us now consider a SQUID device where one of the electrodes of the junction is an unconventional superconductor and the other is a conventional superconductor fig. D.5. The wave function associated with the conventional superconductor is always positive. The device can be constructed in a way that a sign change in the macroscopic wave function only appears at one of the two Josephson junctions integrated into the ring fig. D.5. The expression

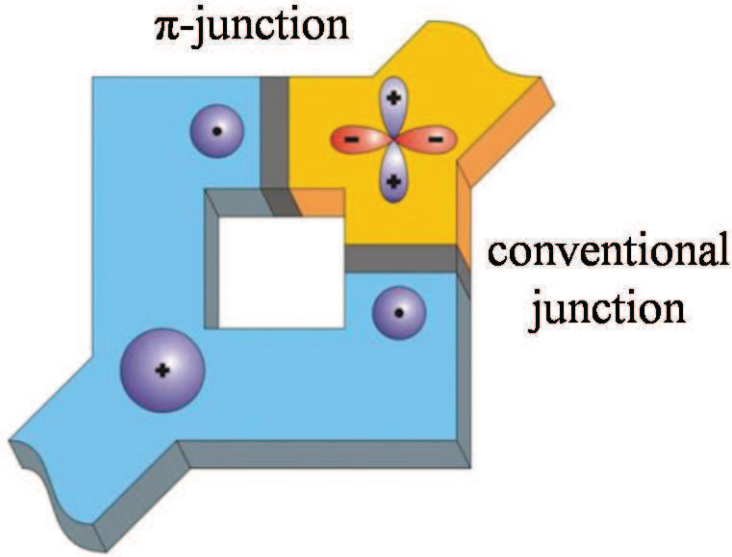


Figure D.5: SQUID device containing a standard Josephson junction and a  $\pi$ -junction. Such device is constructed by using a conventional and an unconventional superconductor [105].

of the current though the Josephson junction experiencing the sign change is:

$$I_s = I_c \sin(\Delta\phi + \pi) = -I_c \sin(\Delta\phi) \quad (\text{D.13})$$

it is clear that the phase difference across the juction is increased by  $\pi$  that is why this kind of Josephson junctions are known with the name of  **$\pi$ -junctions**. A  $\pi$ -juntion behaves like a standard junction but with a negative critical current [105]. The ramp type juctions investigated by C. Schuppler [11], for which the  $Au/YBa_2Cu_3O_7$  ramp type contacts (investigated during the first part of this Phd) constitute a method of making the device, are an example of  $\pi$ -junctions.

For a macroscopic wave function the total phase change encountered along

the closed path of the SQUID must be a multiple of  $2\pi$ , which implies that somewhere in the structure an additional  $\pi$ -phase shift has to compensate that across the  $\pi$ -junction. This additional phase shift can take the form of a spontaneously generated magnetic **half flux quantum**  $\Phi_0/2$  also known as **semifluxon**. The magnitude of the spontaneously generated magnetic flux depends on the product of the critical current of the Josephson junction present and the inductance  $L$  of the structure. In the case of large  $LI_c$  limit, the  $\pi$ -junction can reach its lowest energy state  $\Delta\phi = \pi$ , with the spontaneous generation of a half integer flux quantum  $\Phi_0/2$  by the ring. In the small  $LI_c$  case, the ring does not generate enough magnetic flux and the  $\pi$ -junction is forced to stay in the energetically less favorable  $\Delta\phi = 0$  state [105].

### D.1.5 Superconductive devices and qubit applications

SQUID structures can find application in digital electronic, superconducting rings are suitable for the storage of binary information, in which the information can be carried by neighboring quantized flux states, such states are known as **flux qubits** [103].

Let us consider a SQUID containing two conventional Josephson junctions, a qubit is a two-level quantum system based on the superposition of two distinct quantum states [106]. In the case of a flux qubit, the quantum states are represented by the two directions of the persistent supercurrent of Cooper pairs of the two Josephson junctions [107]. Depending on the direction of the persistent current, a magnetic moment is generated facing either

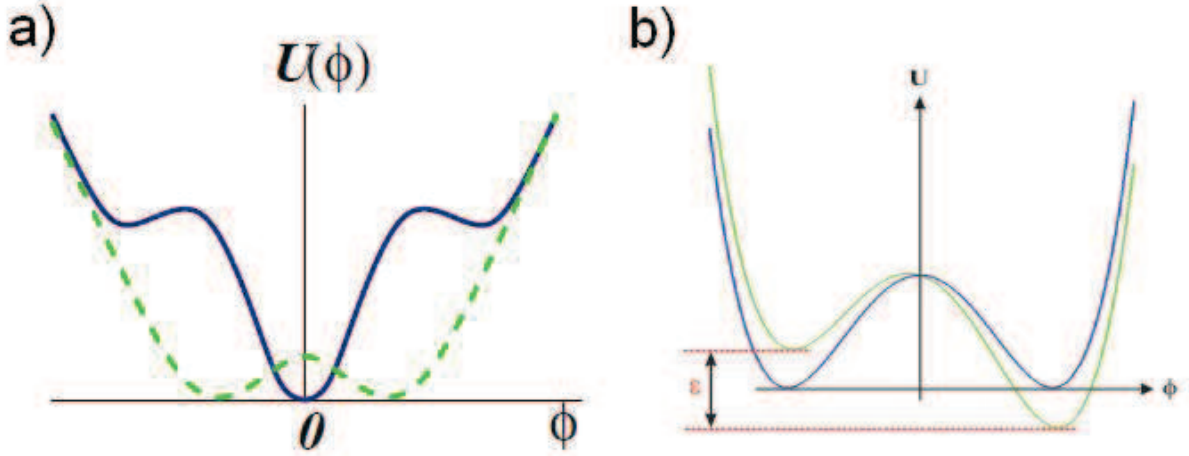


Figure D.6: a) SQUID potential, the full dark curve corresponds to integer bias flux (in unit of flux quanta), while the dashed curve corresponds to half integer bias flux [108]. b) By changing the applied magnetic field in a way that the flux threading the ring is not equal to half integer flux quanta the height of the barrier can be reduced, this is equivalent to the tilting of the qubit potential [109].

up or down, hence flux qubit [11].

Fig. D.6a represents the potential energy of a SQUID, containing two conventional Josephson junctions, as function of the total phase difference across the SQUID  $\phi = \Delta\phi_1 - \Delta\phi_2$ , this phase difference depends on the flux of the applied magnetic field which threads the ring. When the applied bias flux is equal to an integer number of flux quanta, the potential energy of the SQUID has one absolute minimum, this is represented by the dark line of fig. D.6a. For half integer flux quanta the potential energy has two degenerate minima (dashed green line of fig. D.6a), which correspond to the two persistent current states circulating in the SQUID loop in the opposite directions [108]. By changing the applied magnetic field in a way that the

flux threading the ring is not equal to a half integer flux quanta, the height of the barrier can be reduced, this is equivalent to the tilting of the qubit potential fig.D.6b, the consequence is that one can prepare the qubit in a known initial state [109].

The consequence of the previous discussion is that in the case of a SQUID containing two conventional Josephson juctions, an external field generating a flux equal to a half integer flux quanta, has to be applied in order to create two logical states. In the case of a SQUID containing a  $\pi$ -junction (for example a  $Nb/Au/YBa_2Cu_3O_7$  ramp type junction) and in the case of large  $LI_c$  products, the double well potential of fig. D.6a is reached without the need to apply a fine tuned external field. This happens because of the spontaneous generated half flux quanta in a SQUID containing a  $\pi$ -junction. Furthermore if such ring is used as a memory element the difference between the 0 (semifluxon down) and 1 (semifluxon up) states equals exactly a full flux quantum [105]. For a SQUID containing a  $\pi$ -junction, beside the advantage of the qubit not to need fine tuned magnetic fields applied in order to generate the double well potential, it has been demonstrated that such qubit is much less sensitive to external electromagnetic interference [110].

### D.1.6 $Nb/Au/YBa_2Cu_3O_7$ ramp type Josephson junctions

Ramp type  $Nb/Au/YBa_2Cu_3O_7$  Josephson junctions have been investigated by C. Schuppler [11] at *The University of Birmingham*, and by Smilde [10, 111] at the University of Twente. The crucial point in the fabrication of a

ramp type junction is the realization of a good  $Au/YBa_2Cu_3O_7$  ramp type contact. The purpose of the first part of this Phd project was aimed to improve the quality of such contact.

Fig. D.7 shows the side and the top views of a ramp type  $Nb/Au/YBa_2Cu_3O_7$  Josephson junction connecting the unconventional superconductor  $YBa_2Cu_3O_7$  and the conventional superconductor  $Nb$ . As the name suggests this type of Josephson junction is fabricated by means of a ramp and the adopted scheme is in the form  $S_1/N/S_2$  (superconductor/normal metal/superconductor), where niobium is the superconductive top electrode  $S_1$ , gold is the normal metal barrier  $N$  and  $YBa_2Cu_3O_7$  is the base superconductive electrode  $S_2$ . A thin  $YBa_2Cu_3O_7$  interlayer is introduced between the  $Au/YBa_2Cu_3O_7$  interface to reduce the resistance of the ramp contact [10, 111]. The top and the base electrode are separated by an insulating  $SrTiO_3$  layer along the  $c$  axis direction, ensuring current flow only through the ramp.

Fig. D.7b reports the top view of two ramp type junctions, depending on the orientation of the  $Nb$  top electrode respect to the  $YBa_2Cu_3O_7$  base electrode a  $\pi$ -junction or a conventional junction can be formed.

Fig. D.8a reports the unit cell of the  $YBa_2Cu_3O_7$ , as already reported in sec. 1.4 the unit cell presents an orthorhombic structure, the bidimensional cooper pair wave function shown in figs. D.4b and D.7b is associated with the  $CuO_2$  planes of the unit cell, that is where superconductivity takes place. Oxygen deficiencies which may take place during the fabrication process can lead to the crystallization of the  $YBa_2Cu_3O_6$  tetragonal structure which is not superconductive [101].

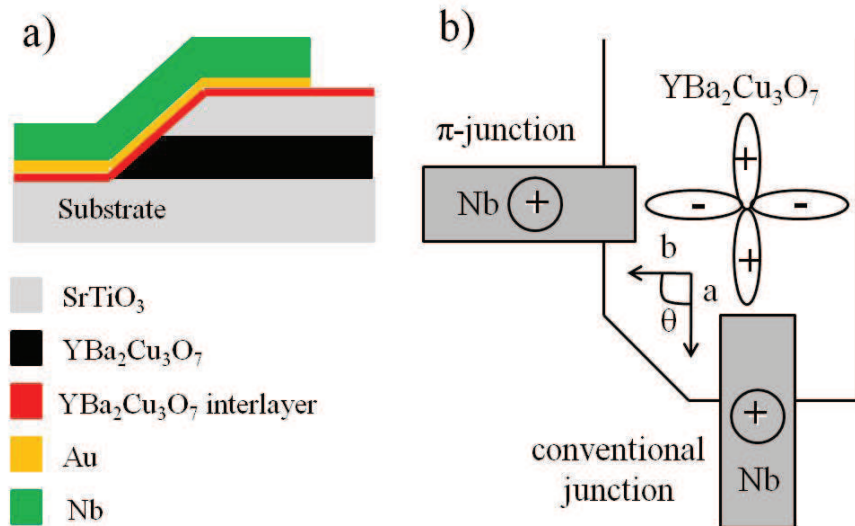


Figure D.7: a) Side view of a  $Nb/Au/YBa_2Cu_3O_7$  ramp type junction,  $Nb$  is the superconductive top electrode,  $Au$  is the metal barrier and  $YBa_2Cu_3O_7$  is the superconductive bottom electrode. A thin  $YBa_2Cu_3O_7$  is introduced between the  $Au/YBa_2Cu_3O_7$  interface to reduce the resistance of the ramp contact, the  $SrTiO_3$  insulating layer between the top and the base superconductive electrodes ensures a current flow only through the ramp. b) Top view of  $\pi$  and of a conventional ramp type junction. When the  $Nb$  top electrode overlaps the  $YBa_2Cu_3O_7$  base electrode along the  $a$  axis ( $\theta = 0$ ) a conventional junction is formed, if the  $Nb$  overlaps the  $YBa_2Cu_3O_7$  along the  $b$  axis a  $\pi$ -junction is created.

To produce a  $\pi$ -type Josephson junction, the  $Au/YBa_2Cu_3O_7$  contact has to be established along the  $ab$  plane fig. D.7b, this is the reason which brings to the ramp type geometry. When the  $Nb$  top electrode overlaps the  $YBa_2Cu_3O_7$  base electrode along the  $a$  axis ( $\theta = 0$ ) a conventional junction is formed, if the  $Nb$  overlaps the  $YBa_2Cu_3O_7$  along the  $b$  axis a  $\pi$ -junction is created ( $\theta = 90^\circ$ ). Between these two extreme cases there is a series of intermediate situations which happen when  $\theta$  is comprised between  $0^\circ$  and

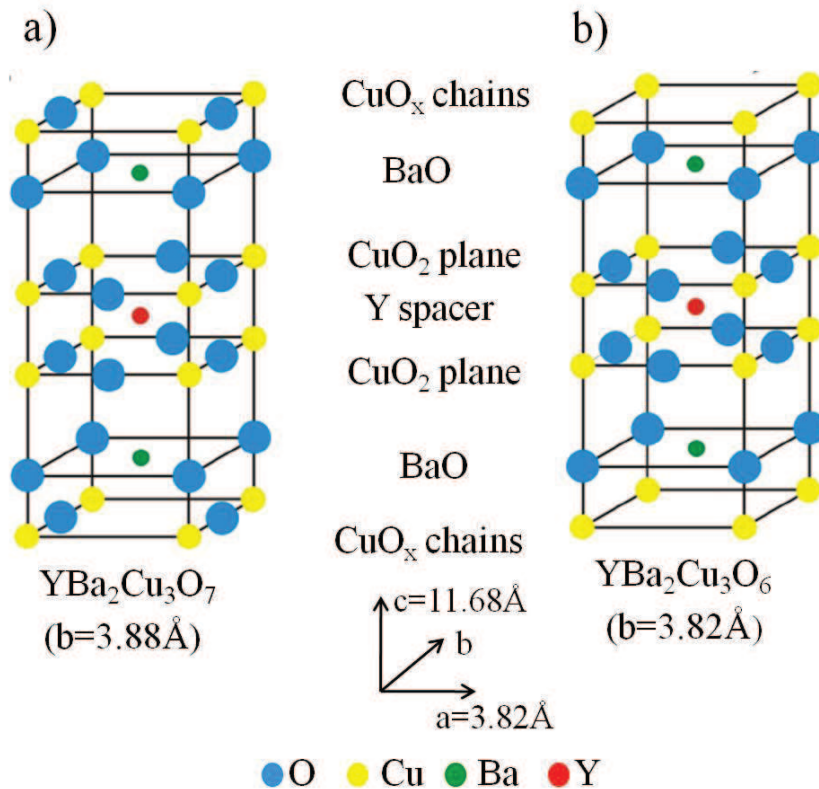


Figure D.8: a) Unit cell for  $\text{YBa}_2\text{Cu}_3\text{O}_7$ . b) Unit cell for  $\text{YBa}_2\text{Cu}_3\text{O}_6$ .

90°.

The coupling between the superconductive electrodes can be controlled by varying the thickness of the gold barrier, the critical current density across the junction decreases when the barrier thickness is increased [111].

The disadvantage of the ramp type geometry is represented by the technological challenge in the fabrication process. In order to have transmission of the Cooper pairs through the  $\text{Au}$  barrier, a good  $\text{Au}/\text{YBa}_2\text{Cu}_3\text{O}_7$  ramp type contact has to be established. A method of assessing the quality of a contact

is to consider its resistance area (RA) product at  $4\text{ K}$ , which is a measure of the resistivity of the contact interface independent on its area [112]. Values of the  $4\text{ K}$  RA product in the range of  $10^{-7} - 10^{-8}\Omega\text{cm}^2$  have been reported for successfully fabricated  $\text{Nb}/\text{Au}/\text{YBa}_2\text{Cu}_3\text{O}_7$  ramp type junctions [10, 111].

There are different factors which contribute to the degradation of the  $4\text{ K}$  RA product in  $\text{Au}/\text{YBa}_2\text{Cu}_3\text{O}_7$  contacts along the  $ab$  plane. The first problem consists in the formation of an intrinsic tunnel barrier at the noble-metal/ $\text{YBa}_2\text{Cu}_3\text{O}_7$  interface due to oxygen depletion and disorder at the  $\text{YBa}_2\text{Cu}_3\text{O}_7$  surface resulting in an approximately  $1\text{ nm}$  thick barrier layer [113]. The second issue is due to the reactivity of  $\text{YBa}_2\text{Cu}_3\text{O}_7$  with water vapor contained in the atmosphere or as impurity in the residual gas of a vacuum system [114, 115], degraded  $\text{YBa}_2\text{Cu}_3\text{O}_7$  layers are the results of this chemical reaction which forms a tunnel barrier up to  $2\text{ nm}$  in thickness [116]. With our equipment, a fabrication process where the surface of the  $\text{YBa}_2\text{Cu}_3\text{O}_7$  ramp does not come in contact with the atmosphere is not possible, in fact to define the ramp geometry a photolithography and a milling step are necessary. This introduce to the third factor which contributes to the degradation of the  $4\text{ K}$  RA product, the milling damages the surface of the  $\text{YBa}_2\text{Cu}_3\text{O}_7$  producing an amorphous layer and redeposited material [117]. All these factor contribute to the increase of the value of the  $4\text{ K}$  RA product into the range  $10^{-3} - 10^{-4}\Omega\text{cm}^2$ . This high RA products prevent transmission of the Cooper pairs through the gold barrier [111].

Smilde reported that the crystal structure on the top of the ramp surface can be recovered with the introduction of an annealing step after the ion beam milling followed by a low energy milling and the deposition of  $\text{YBa}_2\text{Cu}_3\text{O}_7$

interlayer [10, 111].

A requirement for a low  $4\text{ K}$  RA product is that the surface of the ramp is perfectly flat, the ramp surface should provide a good seed layer for the epitaxial growth of the barrier, this is achieved when no amorphous layers are present on the surface of the ramp. Furthermore roughnesses will prevent the homogeneous coverage of the ramp resulting in pinholes which can lead to short circuits [115, 118].

C. Schuppler, during his Phd at the University of Birmingham, reported the successfull fabrication of Josephson junctions [11] by following the fabrication method described by Smilde [10, 111]. However the minimum  $4\text{ K}$  RA product which he achieved was of  $10^{-7}\ \Omega\text{cm}^2$  while the lowest  $4\text{ K}$  RA product reported by Smilde is of  $10^{-8}\ \Omega\text{cm}^2$ . Furthermore the fabrication process at The University of Birmingham does not look reproducible in fact sample prepared with the same fabrication process sometimes result in a low  $4\text{ K}$  RA product sometimes do not [11]. This inconsistency has been attributed to the material redeposition during the low energy milling necessary for the recovery of the ramp surface.

The purpose of the first part of this Phd was to investigate the ramp surface recoverage process necessary for the production of a  $\text{Au}/\text{YBa}_2\text{Cu}_3\text{O}_7$  ramp type contact with a low  $4\text{ K}$  RA product.

## D.2 Equipment and experimental methods

This section provides a description of the equipment and of the experimental methods which have been used for the fabrication and the characterization of the  $Au/YBa_2Cu_3O_7$  ramp type contacts. The fabrication techniques are similar to those described in chap. 4 so a detailed discussion of such equipment is not repeated here. More attention is dedicated to the experimental methods used to characterize the superconductive films and the  $Au/YBa_2Cu_3O_7$  ramp type contacts.

### D.2.1 Pulsed Laser Deposition system

The pulsed laser deposition system which has been used for the fabrication of the ramp type contacts is identical to that one described in sec. 3.1. The only difference is that at the beginning of this Phd a different heater was used, this has been also used by C. Schuppler during his Phd project [11]. The old heater, like the new one, was mounted on an adjustable  $x - y - z$  stage, however there was no mechanism which allowed its rotation. With reference to fig. 3.1, it was not possible to move the heater in front of the Kaufman argon ion gun, this implied that the soft milling necessary to clean the ramp after the definition of the ramp geometry sec. D.3.4, could only be done with a beam incident the sample at an angle of  $45^\circ$ . With this heater only few samples have been produced. As will be explained in sec. D.3.4 the need for soft milling with a beam perpendicular to the surface of the sample required the introduction of the new heater and of the rotational mechanism.

### D.2.2 Photholithography and Milling

Also in this project photolithography techniques and argon ion beam milling have been used to define the geometry of the  $Au/YBa_2Cu_3O_7$  ramp type contact. The equipment the photoresist and the developer used have already been described in sec. 3.3.

### D.2.3 Susceptibility measurements

Susceptibility measurements were used to measure the critical temperature  $T_c$  of the deposited  $YBa_2Cu_3O_7$  films. These measurements make use of the property of diamagnetism which occurs in the superconductive state. The measurement equipment comprises a computer data acquisition system controlled by a Labview program, developed at the School of Electrical Electronic and Computer Engineering of The University of Birmingham before the beginning of this Phd, a lock in amplifier, a temperature controller, a cryostat containing a susceptometer and a vacuum pump.

Our susceptometer consists of a primary coil and a secondary which is made with four coils connected in series, with the primary surrounding the secondary. The secondary coils can be divided into two pairs: the sample pair and the reference pair, with the sample pair wound opposite to the reference pair.

The film under investigation is inserted into the sample pair of the secondary, and an ac voltage is applied to the primary coil generating in this way a magnetic field threading the secondary. The ac voltage across the secondary

is due to Faraday induction:

$$V = -\frac{d\Phi(\vec{B})}{dt}. \quad (\text{D.14})$$

Where  $\Phi$  is the net flux through the entire secondary and includes contributions from both the applied field and the sample magnetization.

When no sample is placed inside the secondary, as the two pairs are wound in opposite directions and connected in series, the net secondary flux due to the applied magnetic field is small, it is not zero because of the small mismatches which are always present between the four coils. Let us apply the reference voltage  $V_R$  generated by the lock-in amplifier to the primary of the susceptometer, where:

$$V_R(t) = V_{ref} \sin(\omega_{ref}t). \quad (\text{D.15})$$

If the film under investigation is placed inside the sample coil it experiences the magnetic induction:

$$\vec{B} = \mu_0 \vec{H}_0 \cos(\omega_{ref}t). \quad (\text{D.16})$$

The general form for the magnetization induced into the sample is given by a Fourier series, however as first approximation only the first term of the series can be considered, so the induced magnetization  $\vec{M}$  can be written as follows [120]:

$$\vec{M} = \vec{H} \left[ \chi' \cos(\omega_{ref}t) + \chi'' \sin(\omega_{ref}t) \right] \quad (\text{D.17})$$

where  $\chi'$  is the real part of the susceptibility and  $\chi''$  is the imaginary part of the susceptibility. When  $\chi'' = 0$  and  $\chi' > 0$  the magnetization is in phase with the applied field and the material is paramagnetic, if  $\chi'' = 0$  and  $\chi' < 0$  the magnetization is  $180^\circ$  out of phase respect to the applied field and the material is diamagnetic, finally for  $\chi'' \neq 0$  the magnetization will be neither perfect in phase or out of phase with the applied field. At the transition temperature, superconductive materials assume diamagnetic behaviour, so for a superconductor which is not diamagnetic in the normal state, there is a jump in the real part of the susceptibility at such temperature fig. D.9. In this thesis the transition temperature is defined as the middle point of the transition, to assess the quality of the transition the temperature range over which the transition takes place is considered, a good transition presents a narrow temperature range. The temperature range is taken between the 90% and the 10% of the height of the jump. For the case of fig. D.9 the transition temperature is equal to  $83\text{ K}$  and the range of the transition is  $82.88 - 82.29\text{ K}$ .

The flux through the secondary is [120]:

$$\Phi(t) = \mu_0 \pi a^2 N \left[ (\vec{M} + \vec{H}) - \vec{H} \right] = \mu_0 \pi a^2 N \vec{M} \quad (\text{D.18})$$

where  $\pi a^2$  is the section of the secondary and  $N$  its number of turns. Therefore considering eq. D.14 the measured voltage results:

$$V_{meas}(t) = V_0 \left[ \chi' \sin(\omega_{ref} t) - \chi'' \cos(\omega_{ref} t) \right] \quad (\text{D.19})$$

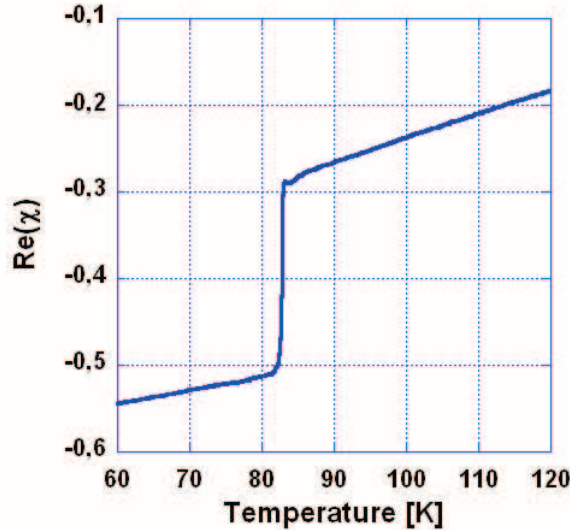


Figure D.9: Susceptibility measurements on a 150 nm thick  $YBa_2Cu_3O_7$  film, at the transition temperature  $T_c$ , which in this case is around 83 K, a jump in the real part of the susceptibility takes place. The sample is a  $SrTiO_3/YBa_2Cu_3O_7$  bi-layer grown on a  $SrTiO_3$  substrate, the  $SrTiO_3$  is 100 nm thick.

where:

$$V_0 = \mu_0 \pi a^2 \omega N \left| \vec{H} \right|. \quad (\text{D.20})$$

The measured voltage has two components: one is in phase and the other is out of phase with the applied reference voltage  $V_R(t)$ . The voltage  $V_R(t)$  is the reference signal of the lock-in amplifier while  $V_{\text{meas}}(t)$  is passed as input signal to the lock-in. The lock-in amplifier produces the voltage  $V_L$  which is sensitive to the phase difference  $\Delta\phi$  between its input and its reference signal [121, 122]:

$$V_L = \frac{1}{2} V_R V_0 \left[ \chi' \cos(\Delta\phi) - \chi'' \sin(\Delta\phi) \right]. \quad (\text{D.21})$$

By adjusting the phase adjust  $\Theta$  feature of the lock-in,  $\Delta\phi$  can be determined using:

$$V_L = \frac{1}{2} V_R V_0 \left[ \chi' \cos(\Delta\phi - \Theta) - \chi'' \sin(\Delta\phi - \Theta) \right]. \quad (\text{D.22})$$

The lock-in output is maximum when  $\Delta\phi = \Theta$ , to separate the real and imaginary component of  $\chi$ ,  $\Theta$  must be determinated, the lock-in signal measured at  $\Theta$  will be proportional to  $\chi'$ , the signal measured at  $\Theta + 90^\circ$  is proportional to  $\chi''$  [120]. The real and imaginary parts of the susceptibility are then extracted from the output signal supplied by the lock-in amplifier with the help of the labview program. Such program controls the lock-in amplifier and the temperature inside the cryostat.

#### D.2.4 AFM investigation

Atomic Force Microscope (AFM) investigations have been used to measure the roughness of the deposited films. Particular emphasis has been dedicated to the investigation of the roughnesses on the surfaces of the  $YBa_2Cu_3O_7$  films and of the ramp structures.

The measurements system consists of a Veeco autoprobe CB based unit *AP0100* controlled by a data acquisition software supplied by Veeco.

The measurements have been run in contact mode, in this mode the AFM laser beam is focused on the tip of the AFM cantilever. The cantilever scans the surface of the sample under investigation, this is achieved by keeping the cantilever in a fixed position and by moving the sample with the help of a piezoelectric scanner.

The laser beam focused on the tip of the cantilever is reflected on the

surface of a photodiode. During the scan, the deflection of the cantilever, reproduces the profile of the surface under investigation, in this way the laser beam hits different points of the photo-sensitive surface of the photodiode. An electrical signal proportional to the roughness of the film is generated, such signal is then processed by the AFM software and the surface profile of the film can be reconstructed [119].

### D.2.5 Current-Voltage (I-V) and Resistance versus Temperature (R-T) measurements

To perform resistance versus temperature and  $4\text{ K}$  current-voltage measurements on the  $\text{Au}/\text{YBa}_2\text{Cu}_3\text{O}_7$  ramp type contacts, the sample as discussed in sec. 3.5, is first glued on the chip carrier and then wirebonded fig. 3.9. Both measurements requires the use of a continuous flow cryostat connected to a dewar containing liquid helium fig. D.10a. The liquid helium is pumped inside the cryostat with the help of a diaphragm, a recovery line allows to recover the helium from the bottom of the cryostat to be recovered inside the dewar. With such setup a decrease in temperature of the inner part of the cryostat up to  $4\text{ K}$  is possible.

A probe with a 20 pin socket on one end, is used to insert the fabricated sample inside the cryostat, the chip carrier is plug into the socket electrically connected to the head of the probe. The probe top remains outside the cryostat during the low temperature measurements, it allows to access the pins of the chip carrier while the space inside the cryostat is cooled down.

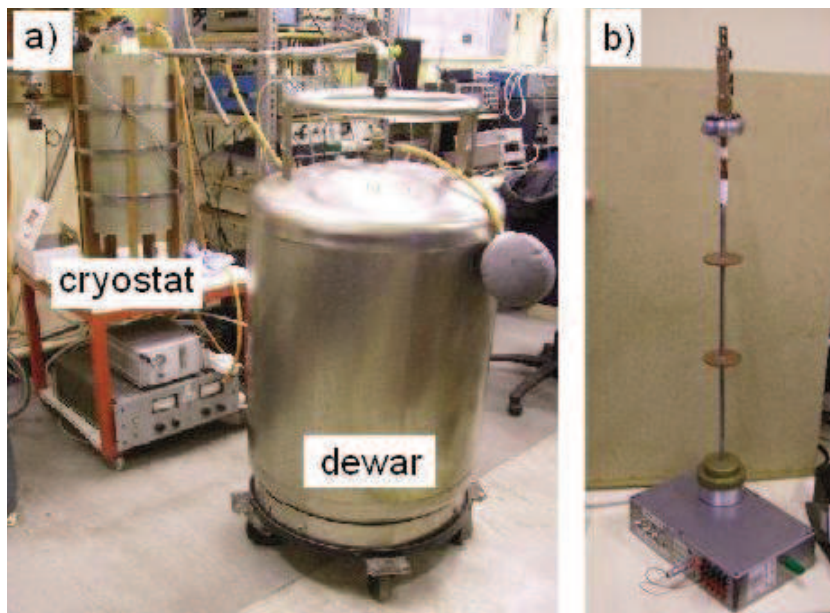


Figure D.10: a) Continuous flow cryostat connected to a dewar containing liquid helium. b) Cryostat probe.

For the  $I - V$  measurements a Labview program called *Superpippoo* has been developed, before describing how the program works the setup used to record the  $I - V$  characteristics will be discussed.

Fig. D.11 reports a schematic of the equipment used to perform the  $I - V$  measurements on the  $Au/YBa_2Cu_3O_7$  ramp type contacts. The equipment comprises a personal computer with a data acquisition card, a temperature controller, a current source, a voltage amplifier and the cryostat system, the current source and the voltage amplifier are connected to the head of the probe. The current voltage measurements have been run by using the four terminal technique. In this technique both the gold top layer and the  $YBa_2Cu_3O_7$  base electrode are connected to two pads for a total of two different lines connected to the device under investigation. One line is used

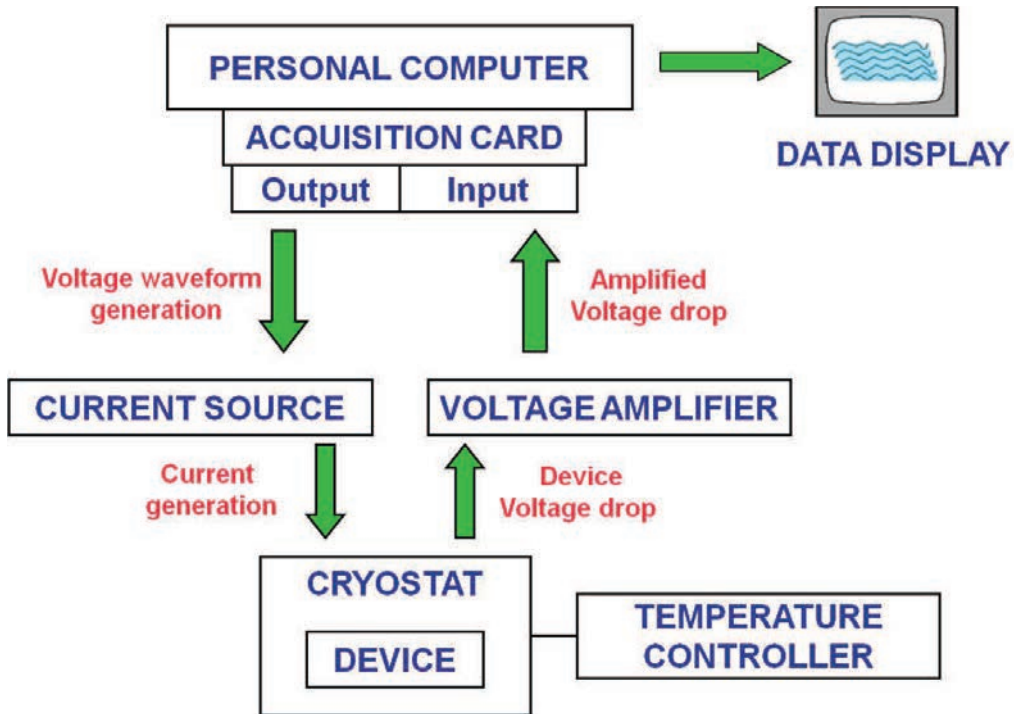


Figure D.11: Schematic of the measurement equipment used to record the  $I - V$  characteristics of the  $Au/YBa_2Cu_3O_7$  ramp type contacts.

to supply the current through the ramp contact while the other is used to measure the voltage drop across the device, fig. D.12. In this method only the voltage drop across the ramp device is measured while the voltage drops coming from the pads and the contacts lines are not present in the measured values.

The measurement system works in the following way:

- the labview program generates a voltage waveform, such waveform is passed to the current source through the output channel of the data acquisition card;

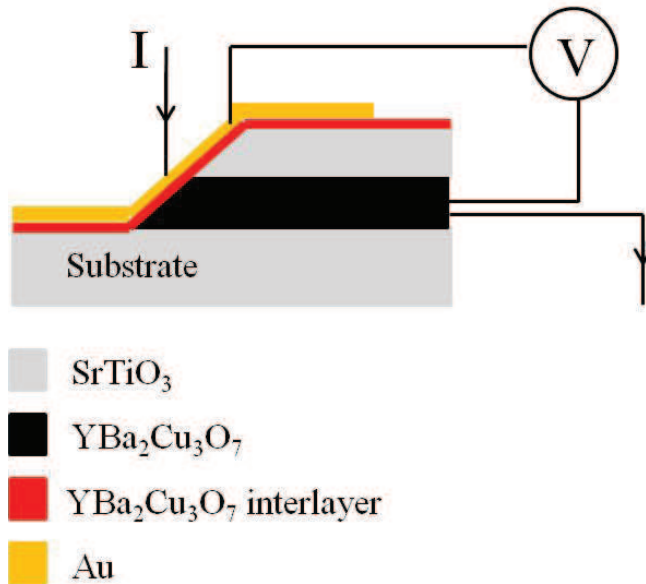


Figure D.12: Side view of a  $\text{Au}/\text{YBa}_2\text{Cu}_3\text{O}_7$  ramp type contact. The gold top layer and the  $\text{YBa}_2\text{Cu}_3\text{O}_7$  base electrode are connected to two different lines one is used to force a current through the ramp while the other is used to measure the voltage drop across the device.

- the current source circuit produces a current proportional to the applied voltage, its current ranges are:  $10 \mu\text{A/V}$ ,  $100 \mu\text{A/V}$ ,  $1 \text{mA/V}$  and  $10 \text{mA/V}$ ;
- the output channel of the current source is connected to the head of the cryostat probe, in this way a current is forced through the  $\text{Au}/\text{YBa}_2\text{Cu}_3\text{O}_7$  ramp type contact while the sample under investigation is kept inside the continuous flow cryostat at a temperature of  $4.2 \text{ K}$ ;
- the voltage drop across the device is supplied to a voltage amplifier having the gains: 100, 1000 and 10000, they allow the amplification of

the small voltage drop across the device. The amplified voltage drop is then passed to the input channel of the data acquisition card;

- finally the current and voltage waveforms and so also the  $I - V$  curves are plotted on the computer screen.

Fig.D.13 reports the main panel of the labview program which has been developed to acquire the  $I - V$  characteristic, such program has been called *Superpippo*.

The right hand side of the main panel shows the generation section, it contains two wave-function generators. The first function generator is used to supply voltage to the current source circuit. The reason for the introduction of a second function generator is to supply voltage to a second current source connected to a coil surrounding the sample under measurements inside the cryostat. This allows to investigate the effect of an external magnetic field on the  $I - V$  characteristic of a Josephson junction. The second wave-function generator has not been used during the measurements on the ramp type contacts, its introduction into the program results useful for the future developments of the project.

Each generator is able to produce sine wave, square wave, triangle wave and sawtooth waveforms, furthermore for each function, parameters like frequency, amplitude, duty cycle, phase and number of samples per cycle can be set. It is also possible to select the channel of the data acquisition card which will be used as output channel.

The left side of the main panel contains the acquisition section, here the supplied currents and the measured voltages can be acquired and displayed.

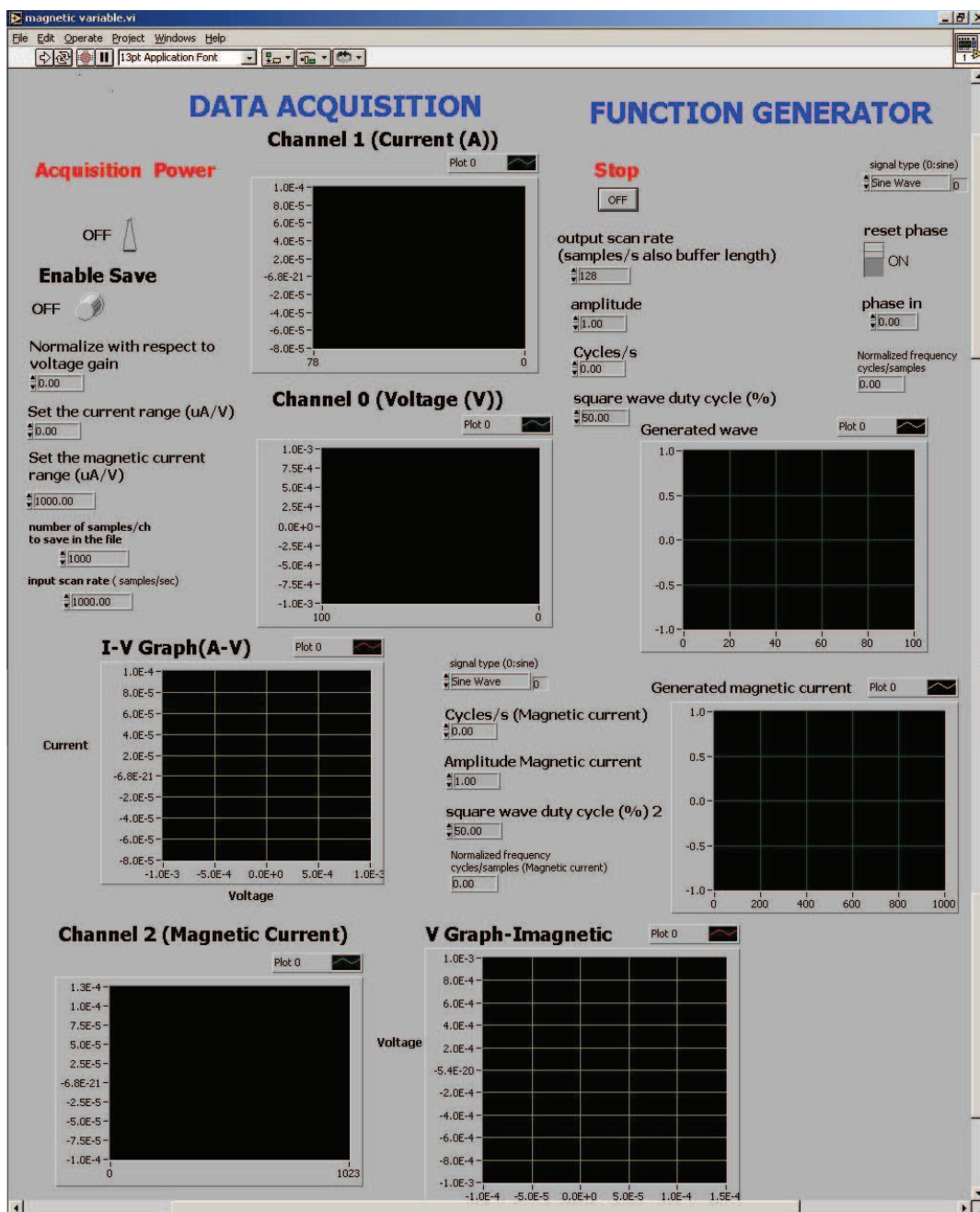


Figure D.13: Main panel view of the software developed to perform the  $I - V$  measurements.

The program also acquires and displays the current supplied to the coil, in this way measurements of the critical magnetic field and of the  $I - V$  curve for different magnetic fields are possible.

The sample rate used to acquire the data can be set into the data acquisition section, the program enables the normalization of the data respect to the amplifier gain and to the current range, in this way the  $I - V$  curves are plotted according to the units of the international system.

The input signal of the current source is generated through the data acquisition card, this is a digital signal. The sampling frequency used to acquire the voltage drop across the device, must be less or equal than the sampling frequency of the voltage applied to the current source. If this condition is satisfied over-sampling problems are avoided, of course the Nyquist criterion has to be fulfilled to not incur in under-sampling issues.

If the acquired signal has a small amplitude, it is not possible to take advantage of all the quantization levels present in the input channel of the acquisition card fig. D.14. In this case if:

$$f_s \gg f \quad (\text{D.23})$$

where  $f_s$  is the sampling frequency and  $f$  is the signal frequency, it is possible to encounter oversampling problems resulting in a step-like  $I - V$  curve. The solution to this problem is to lower the sampling frequency and the up and down limits for the acquisition card channels [123].

During the  $I - V$  measurements on the  $\text{Au}/\text{YBa}_2\text{Cu}_3\text{O}_7$  devices when a  $10 \text{ Hz } 100 \mu\text{A}$  current is applied, a sample rate of  $1000 \text{ sample/s}$  has been

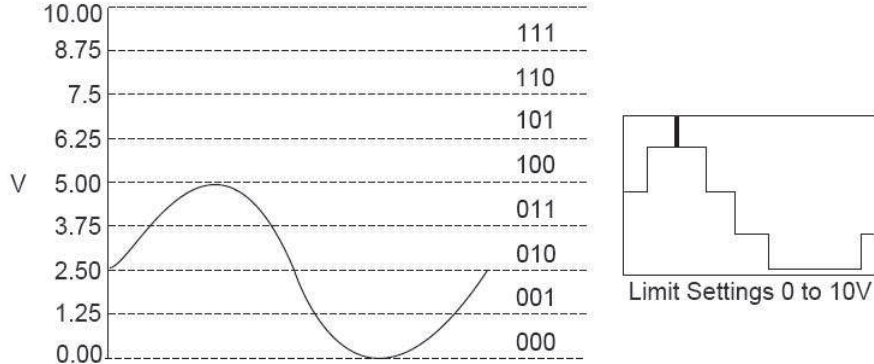


Figure D.14: Digital levels used to quantify an analogue signal at the I/O acquisition card channel [123].

used. Instead when a  $10\text{Hz}$  and  $10\mu\text{A}$  amplitude current is forced through the ramp a scan rate of  $350 \text{ sample/sec}$  is necessary to avoid over-sampling problems.

Fig. D.15 reports a schematic of the equipment used to perform the resistance versus temperature measurements, also in this case the data are acquired by using a labview program. Such program was developed at the School of Physics of the University of Birmingham before the beginning of this Phd.

In this kind of measurements a dc voltage  $V_B$  is generated by using the data acquisition card and a reference voltage  $V_R$  is supplied by the lock in amplifier where:

$$V_R = V_{ref} \sin(\omega_{ref} t + \vartheta_{ref}) \quad (\text{D.24})$$

the dc and the ac voltages are then added together and supplied to the current source. In this way a current consisting of a bias current  $I_B$  with superimposed a sinusoidal component is forced through the device under

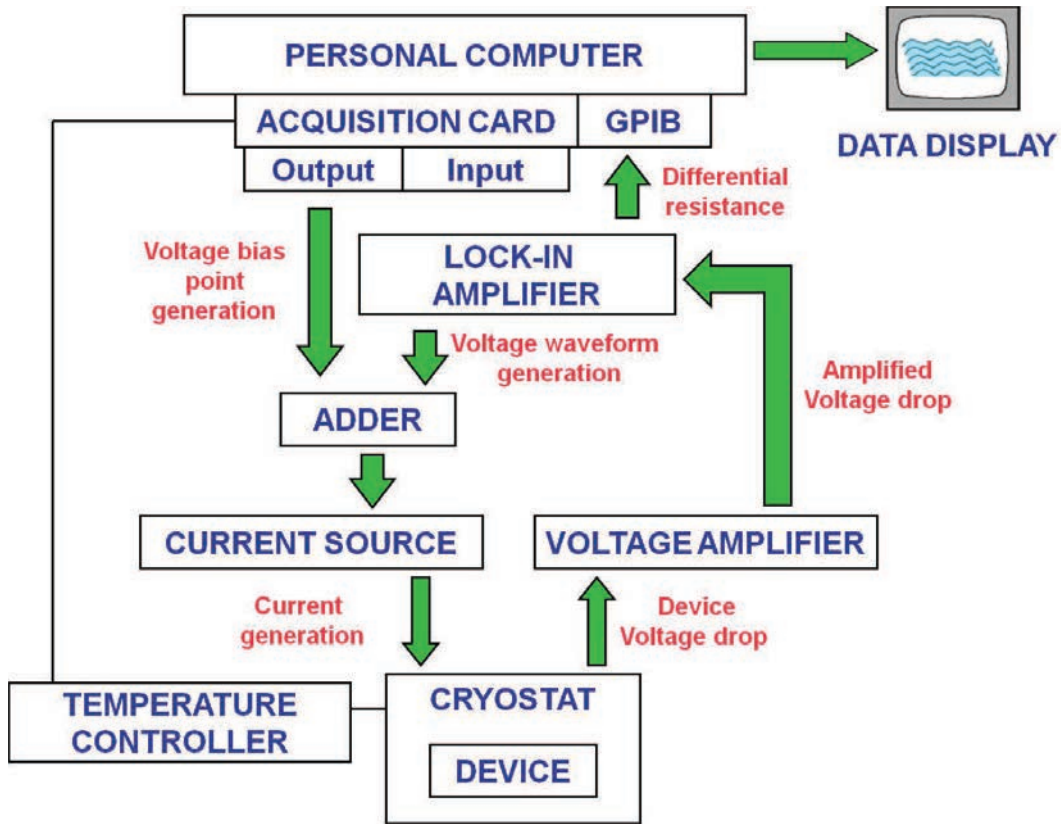


Figure D.15: Schematic of the measurement equipment used to record the  $R - T$  measurements on the  $Au/YBa_2Cu_3O_7$  ramp type contacts.

measurement inside the cryostat:

$$I_F = I_B + I_{ac} \sin(\omega_{ref}t + \vartheta_{ac}). \quad (\text{D.25})$$

A voltage is then developed across the device, it is amplified and given back to the input channel of the lock-in amplifier. As  $I_B \gg I_{ac}$  a Taylor expansion

of the voltage drop around  $I_B$  is valid:

$$V(I_F) = KV(I_B) + K \frac{dV(I_B)}{dI} (I_F - I_B) + K \frac{1}{2!} \frac{d^2V(I_B)}{dI^2} (I_F - I_B)^2 + \dots \quad (\text{D.26})$$

where  $K$  is the amplifier gain. Only the first two terms of the series are considered, the higher order terms do contribute to the measured voltage, but as long as  $I_B \gg I_{ac}$  second order terms and higher can be neglected [11, 124]. With these considerations the voltage drop across the device under measurement can be approximated as:

$$V(I_F) = K \left[ V(I_B) + \frac{dV(I_B)}{dI} I_{ac} \sin(\omega_{ref}t + \vartheta_{ac}) \right]. \quad (\text{D.27})$$

The lock-in amplifier measures the voltage in a narrow bandwidth measurement around  $\omega_{ref}$ , so only the ac term of eq. D.27 is selected, this term is then multiplied with the reference signal and the voltage  $V_{out}$  is produced at the output channel of the lock-in amplifier:

$$V_{out} = \frac{1}{2} KV_{ref} \frac{dV(I_B)}{dI} I_{ac} \cos(\vartheta_{ac} - \vartheta_{ref}) \quad (\text{D.28})$$

such voltage is proportional to the differential resistance:

$$R_{dif} = \frac{dV(I_B)}{dI_F}. \quad (\text{D.29})$$

The output voltage of the lock-in amplifier is passed to the labview program through the *GPIB* interface and the differential resistance is extracted from the measured voltage. If these measurements are repeated a certain number

of times while the sample is cooled down the resistance versus temperature curve is obtained.

### D.3 Device Fabrication

This section describes the fabrication process used to produce  $Au/YBa_2Cu_3O_7$  ramp type contacts. The reasons for each step adopted in the fabrication process are discussed.

Fig. D.12 reports the side view of a  $Au/YBa_2Cu_3O_7$  ramp type contact, the gold and the  $YBa_2Cu_3O_7$  are the top and the base electrode of the device. As already discussed in sec. D.1.6 a thin  $YBa_2Cu_3O_7$  interlayer is introduced between the  $Au$  and the  $YBa_2Cu_3O_7$  contact to reduce the resistance of the  $YBa_2Cu_3O_7$  interface. The top and the base electrode are separated by an insulating  $SrTiO_3$  layer along the  $c$  axis direction, ensuring a current flow only through the ramp.

At the beginning of this project, to deposit the thin films using PLD a heater fabricated at the School of Physics of The University of Birmingham, fig. D.16a, was used, such a heater contains a metal disc to which the sample is glued. In the heater, a resistor supported by a ceramic spacer is used to warm the sample up, the problem with the ceramic spacer is the outgassing of such material during the film deposition [124].

Christian Schuppler during his Phd at The University of Birmingham adapted the fabrication process of the ramp type Josephson junctions developed at the University of Twente [10, 111, 125]. With the old heater the parameters of the fabrication process defined by C. Schuppler have been adopted. The introduction of a new heater necessary to avoid problems with outgassing and to improve the ramp cleaning process, sec. D.3.4, led to a recalibration of the deposition parameters for the  $YBa_2Cu_3O_7$  films.

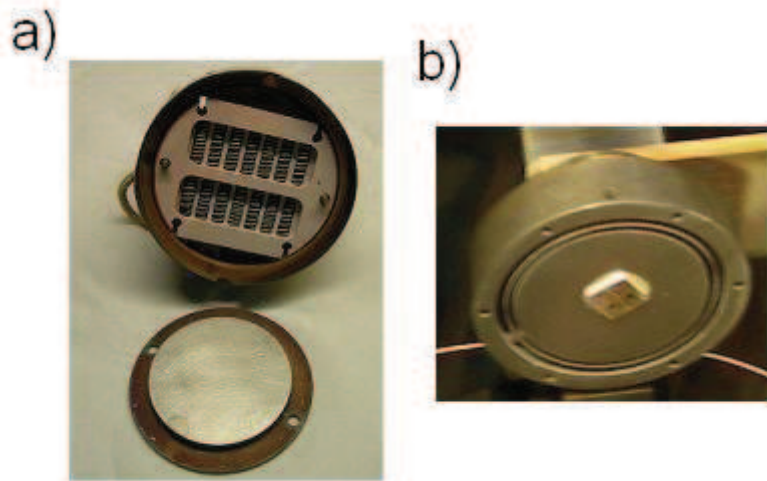


Figure D.16: a) Old heater built at the School of Physics of The University of Birmingham and used during the first part of the ramp type contact project. This heater contains a metal disc where the sample is glued, a resistor supported by a ceramic spacer is used to warm the sample up. b) Thermocoax heater supplied by Twente Solid State Technology [126] used during the second part of the ramp type contact project.

### D.3.1 Introduction to the fabrication process

The main steps for the fabrication of the  $Au/YBa_2Cu_3O_7$  ramp type contacts are represented in fig. D.17, they are:

- growth of a  $SrTiO_3/YBa_2Cu_3O_7$  bilayer on a (001) oriented  $SrTiO_3$  substrate;
- definition of the pad geometry by contact photolithography and argon ion beam milling;
- patterning of the ramp structure by contact photolithography and ar-

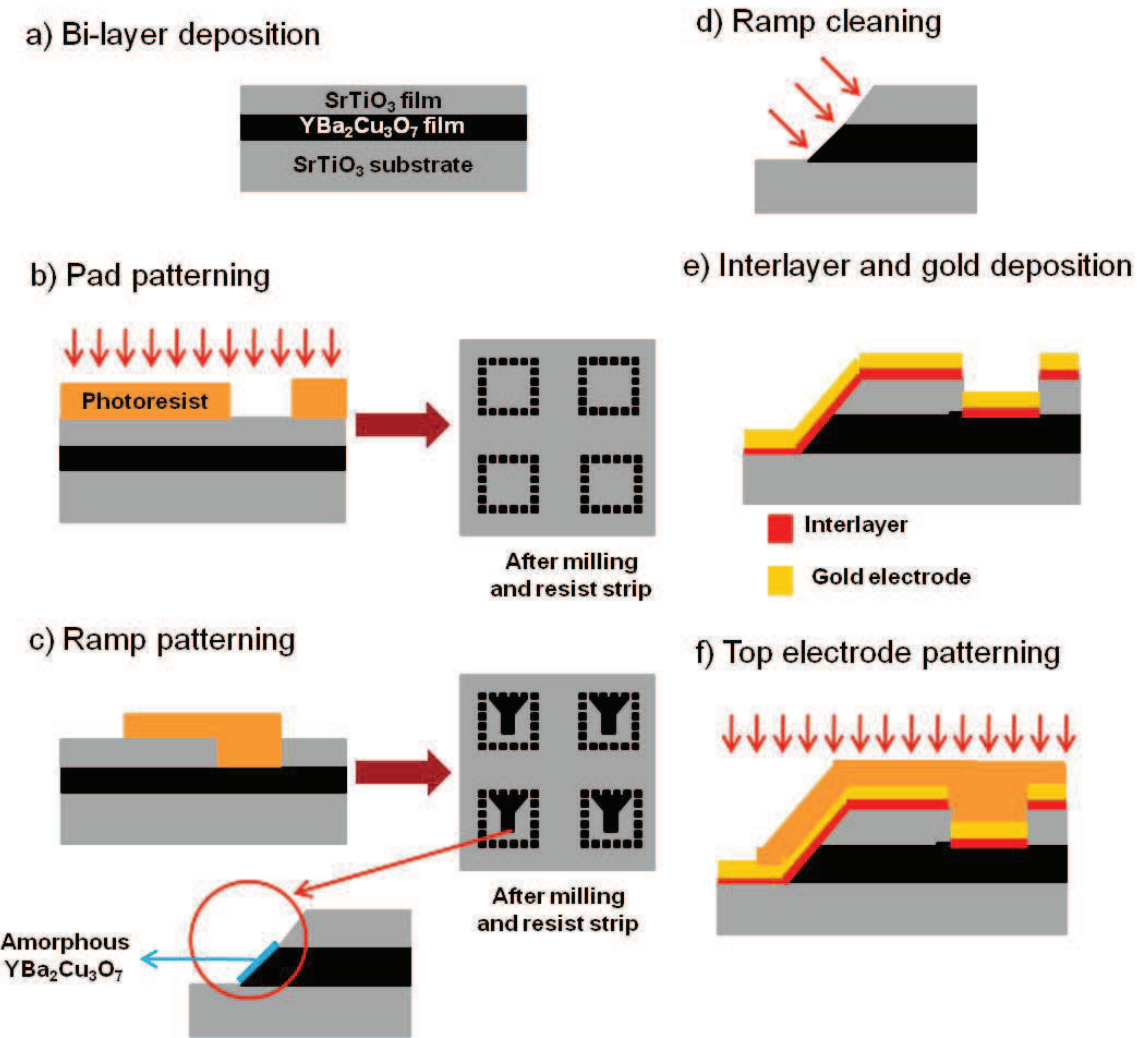


Figure D.17: Fabrication process for the  $Au/YBa_2Cu_3O_7$  ramp type contact.

gon ion beam milling;

- partial recovery of the crystal structure on the surface of the  $YBa_2Cu_3O_7$  ramp, this is done with the use of an etching step followed by an an-

nealing step;

- deposition of a  $6\text{ nm}$   $YBa_2Cu_3O_7$  interlayer to complete the recovery of the  $YBa_2Cu_3O_7$  crystal structure on the ramp surface;
- deposition of the gold layer
- patterning of the gold top electron by argon ion beam milling and contact photolithography.

Each of these steps will be further developed in the next sections.

### D.3.2 $SrTiO_3/YBa_2Cu_3O_7$ bilayer deposition

The first step in the fabrication process of the  $Au/YBa_2Cu_3O_7$  ramp type contacts is the deposition of the  $SrTiO_3(100\text{ nm})/YBa_2Cu_3O_7(150\text{ nm})$  bilayer on a (001) oriented  $SrTiO_3$  substrate. The  $SrTiO_3$  substrates used in this project, are the same employed during the project on the piezoelectric devices.

First the bilayer deposition performed with the old heater is going to be described.

A single crystal (001) oriented  $SrTiO_3$  substrate is glued with silver paint onto the metal disc of the heater fig.D.16a. The silver paint is dried for 10 minutes at  $100^\circ C$  before to mount the metal disc on the heater inside the deposition chamber.

The ablation preparation and the cleaning of the targets are performed as described in chap. 4 and so they are not repeated here.

When the pressure inside the deposition chamber is about  $10^{-5} \text{ Pa}$ , the substrate is heated to  $780^\circ\text{C}$  at  $35^\circ\text{C}/\text{min}$ , at this temperature a bilayer of about  $150 \text{ nm}$  thick (001)-oriented  $\text{YBa}_2\text{Cu}_3\text{O}_7$  and  $100 \text{ nm}$  thick (001)-oriented  $\text{SrTiO}_3$  is grown by pulsed laser deposition fig. D.17a. Both materials are ablated in an oxygen flow environment at a pressure  $P$  of  $20 \text{ Pa}$  for the  $\text{YBa}_2\text{Cu}_3\text{O}_7$  and of  $28 \text{ Pa}$  for the  $\text{SrTiO}_3$ . A pulse repetition rate  $f$  of  $4 \text{ Hz}$  is used, the fluence  $U$  on target for both material is equal to  $3.6 \text{ J/cm}^2$  while the distance between the target and the sample  $d_{TS}$  is set to  $5.3 \text{ cm}$ , the deposition parameters which have been used are reported in tab. D.1.

Next the vacuum system is filled with  $90 \cdot 10^3 \text{ Pa}$  oxygen, the  $\text{SrTiO}_3/\text{YBa}_2\text{Cu}_3\text{O}_7$  bilayer is cooled down via two dwells, one at  $600^\circ\text{C}$  for 15 minutes and one at  $450^\circ\text{C}$  for 30 minutes to fully oxygenate the  $\text{YBa}_2\text{Cu}_3\text{O}_7$  film and avoid oxygen deficiencies which can lead to a transition between the superconducting  $\text{YBa}_2\text{Cu}_3\text{O}_7$  orthorhombic phase and the non superconducting  $\text{YBa}_2\text{Cu}_3\text{O}_6$  teragonal phase [101]. At room temperature the chamber is vented and the film is taken off the metal disc of the heater, finally the silver paint on the back side of the substrate is carefully removed with sandpaper.

The success of the oxygenation process can be verified with susceptibility or with the resistance versus temperature measurements, such techniques allow to measure the transition temperature  $T_c$  of the  $\text{YBa}_2\text{Cu}_3\text{O}_7$  film, a transition in a narrow temperature range around  $90 \text{ K}$ , as that one reported in fig. D.9, is an indication of a successful oxygenation.

In sec. D.1.6 it has been stated that a requirement necessary to have a ramp type contact with a low  $4 \text{ K RA}$  product is a flat ramp surface. The first

<i>Material (heater)</i>	<i>P</i> [Pa]	<i>T</i> [°C]	<i>d<sub>TS</sub></i> [cm]	<i>U</i> [J/cm <sup>2</sup> ]	<i>Spotsize</i> [mm <sup>2</sup> ]	<i>f</i> [Hz]	<i>dep. rate</i> Å/pulse
<i>YBa<sub>2</sub>Cu<sub>3</sub>O<sub>7</sub></i> (old heater)	20	780	5.3	3.6 – 3.9	2.5	4	0.25
<i>SrTiO<sub>3</sub></i> (old heater)	28	780	5.3	3.6 – 3.9	2.5	4	0.35
<i>Au</i> (old heater)	16.5	<i>RT</i>	5.7	4.3	2.1	4	0.092
<i>YBa<sub>2</sub>Cu<sub>3</sub>O<sub>7</sub></i> (new heater)	20	740	5.7	3.4 – 3.6	2.3	4	0.15
<i>SrTiO<sub>3</sub></i> (new heater)	28	740	5.7	3.4 – 3.6	2.3	4	0.16
<i>Au</i> (new heater)	16.5	<i>RT</i>	5.7	4	2	4	0.087

Table D.1: Laser ablation condition for the *YBa<sub>2</sub>Cu<sub>3</sub>O<sub>7</sub>*, *SrTiO<sub>3</sub>* and *Au* films, *YBa<sub>2</sub>Cu<sub>3</sub>O<sub>7</sub>* and *SrTiO<sub>3</sub>* have been grown in an oxygen flow environment, instead *Au* has been grown in an argon environment at room temperature (*RT*). Also shown are: the deposition pressure *P*, the deposition temperature *T*, the target-sample distance *d<sub>TS</sub>*, the fluence on target *U*, the spotsize on target, the pulse frequency *f* and the deposition rate.

step to achieve that is the deposition of a *SrTiO<sub>3</sub>/YBa<sub>2</sub>Cu<sub>3</sub>O<sub>7</sub>* which does not present an excessive number of particulates and outgrowths on its top. C. Schuppler during his Phd at The University of Birmingham produced ramp structures presenting a smooth profile [11] by using the described fabrication process whose has been successfully reproduced during the first part of this Phd. With the introduction of the new thermocoax heater into the deposition chamber, a recalibration of the deposition parameters was necessary, in fact the existing fabrication process did not produced the same results.

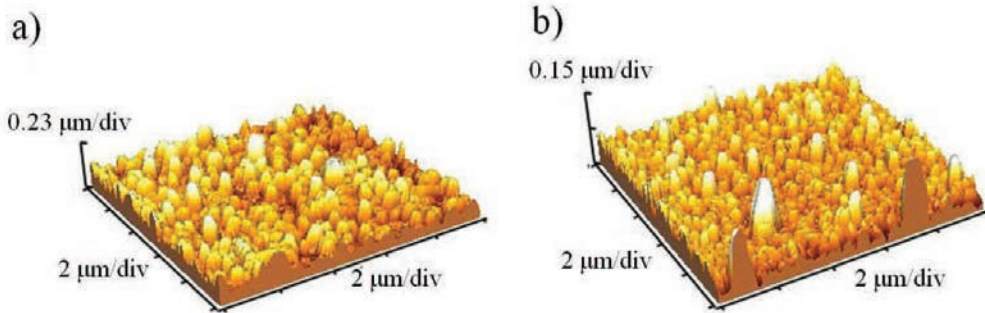


Figure D.18: a) AFM scan on the sample labelled as *GV15* after the deposition of the  $SrTiO_3/YBa_2Cu_3O_7$  bilayer, the  $SrTiO_3$  is 100 nm thick, the  $YBa_2Cu_3O_7$  is 150 nm thick, the scan area is  $100 \mu m^2$ . b) AFM scan on the sample labeled as *GV16* after the deposition of a 100 nm thick  $YBa_2Cu_3O_7$  film, the scan area is  $100 \mu m^2$ .

Fig. D.18a reports the AFM scan on the surface of a  $SrTiO_3/YBa_2Cu_3O_7$  bilayer (sample labeled as *GV15*), while fig. D.18b shows the AFM scan on the surface of a  $YBa_2Cu_3O_7$  film (sample labeled as *GV16*). Both samples have been prepared using the deposition parameter previously reported. The  $SrTiO_3/YBa_2Cu_3O_7$  present an average roughness of 30.41 nm, the  $YBa_2Cu_3O_7$  instead has an average roughness of 23.14 nm. These films show the presence of particulates on their surface, it is believed that such particulates increase the roughness of the ramp structure and the 4 K RA product of the ramp type contact, the reason is that their chemical composition often differs from that one of the surrounding film [98].

A series of studies on the growth of  $YBa_2Cu_3O_7$  by pulsed laser deposition reported the influence of temperature,  $O_2$  pressure, laser energy, fluence and spotsize on the occurrence of particulates on the surface of such films fig. D.19 [98], these investigations have been used to improve the quality of our

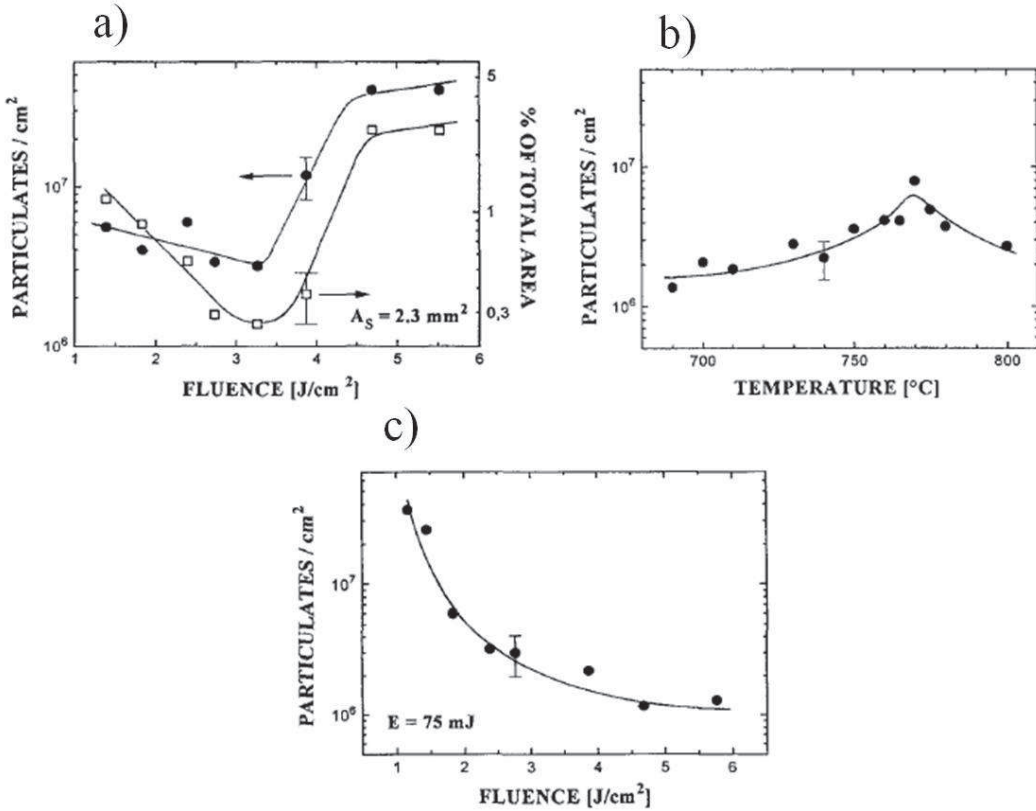


Figure D.19: Particulates on the surface of the  $YBa_2Cu_3O_7$  films grown by pulsed laser deposition as function of different deposition parameters [98]. a) Dependence of particulate number density and fraction of total area covered by particulates on the laser fluence for a constant spotsize of  $2.3 \text{ mm}^2$ , deposition pressure of  $71 \text{ Pa}$ , deposition temperature of  $750^\circ\text{C}$  and number of pulses equal to 6000. b) Dependence of particulate number density on deposition temperature for a deposition pressure of  $71 \text{ Pa}$ , spotsize equal to  $2.3 \text{ mm}^2$ , laser energy of  $75 \text{ mJ}$  (fluence equal to  $3.25 \text{ J/cm}^2$ ), and number of pulses equal to 6000. c) Dependence of particulate number density on laser fluence for a constant laser energy equal to  $75 \text{ mJ}$ , deposition pressure equal to  $71 \text{ Pa}$ , deposition temperature equal to  $750^\circ\text{C}$  and number of pulses equal to 6000.

$YBa_2Cu_3O_7$  layers.

Fig. D.19a reports how the number of particulates/ $\text{cm}^2$  depends on the

Sample	$T$ [°C]	$E$ [mJ]	Spotsize [mm $^2$ ]	$U$ [J/cm $^2$ ]	$d_{TS}$ [cm]	avg. roughness [nm]
GV16	780	91	2.3	3.93	5.3	23.14
GV17	780	81.4	2.1	3.88	5.3	17.15
GV18	740	79	2.1	3.8	5.3	11.16
GV19	740	90.8	2	4.54	5.7	11.25
GV20	740	81.2	2.3	3.5	5.7	10.29
GV39	740	40	2.3	1.7	5.7	33.06
GV40	740	80.8	2.8	2.9	5.7	33.06

Table D.2: Average surface roughness for different 150 nm thick  $YBa_2Cu_3O_7$  films grown by pulsed laser deposition for different deposition parameters.  $T$  denotes the substrate temperature during the deposition,  $E$  is the laser energy,  $U$  is the laser fluence on target and  $d_{TS}$  is the target to substrate distance.

laser fluence when the spotsize on target is kept constant. This corresponds to the number of particulates as function of the laser energy, the minimum number of particulates is obtained at a fluence of 3.3 J/cm $^2$ . In order to reduce the particulates on the  $YBa_2Cu_3O_7$  film, the first thing which has been tried was a decrease of the laser energy. A laser energy of 91 mJ with a fluence of 3.93 J/cm $^2$  were used for the sample *GV16*, tab. D.2, the deposition energy has been reduced to 81.4 mJ for the sample *GV17* developing in this way a slightly low fluence equal to 3.88 J/cm $^2$ . This decrease in the laser fluence with constant spotsize on target, resulted in an improved surface in fact the average roughness from 23.14 nm in the case of sample *GV16*, has been reduced to 17.15 nm for the sample *GV17*, in agreement with [98].

For each sample the average roughness has been measured by averaging the roughnesses measured on areas of 10  $\mu\text{m} \times 10 \mu\text{m}$  taken on different parts of the samples.

As shown in fig. D.19b a further reduction of the particulates is possible with a decrease of the deposition temperature, however the superconductive properties of the  $YBa_2Cu_3O_7$  need to be maintained. Proyer et al. [98] reported that optimum superconductive properties for the  $YBa_2Cu_3O_7$  were obtained at a deposition temperature around  $740^\circ C$ . A reduction of the deposition temperature from  $780^\circ C$  to  $740^\circ C$  at a laser fluence of  $3.8 J/cm^2$  (sample *GV18*) decreased the surface roughness to  $11.16 nm$ , tab. D.2.

To reduce the number of particulates produced during the  $YBa_2Cu_3O_7$  deposition also the distance between the target and the  $SrTiO_3$  substrate  $d_{TS}$  has been varied. When the target to substrate distance is smaller than the length of the plume there is no difference in particulate size and density all over the sample [61]. As the target to substrate distance increases the proportion of the smaller particulates decreases and few larger particulates appear [61]. This behaviour has been verified with the preparation of sample *GV19*, in this case, as in the case of the sample *GV16*, the deposition parameters adopted by C. Schuppler have been used. The only difference between the two samples is in the ablation distance which has been increased to  $5.7 cm$  for the sample *GV 19*. In this case the reduction in the number of particulates produced a decrease of the average roughness on the surface of the  $YBa_2Cu_3O_7$  film.

Sample *GV20*, has been prepared using a deposition temperature of  $740^\circ C$  and a fluence of  $3.5 J/cm^2$  such parameters, as verified with the sample *GV18*, produce a reduction of the average roughness. In the case of *GV20* the target to substrate distance has been increased to  $5.7 cm$ , compared to *GV18* a small decrease of the average roughness of the  $YBa_2Cu_3O_7$  has been

reached tab. D.2.

It has to be remarked that the presence of few large particulates for the samples *GV19* and *GV20* are mainly concentrated at the centre of the  $SrTiO_3$  substrate, this area is where the tip of the laser plume is focused. The masks used for the fabrication of the ramp type contacts do not contain any structure in the center of the sample, for this reason it has been chosen to increase the substrate to target distance to  $5.7\text{ cm}$ .

Two other samples *GV39* and *GV40* have been prepared, for *GV39* a smaller laser energy has been set, while for *GV40* a bigger spotsize has been used, in both cases no improvements on the average value of the  $YBa_2Cu_3O_7$  roughness have been obtained this is in agreement with what is reported in [98].

All the results on the roughness of the  $YBa_2Cu_3O_7$  films prepared with different deposition parameters are reported in tab. D.2 and summarized in fig. D.20.

This investigation revealed that a minimum in the surface roughness of the  $YBa_2Cu_3O_7$  film is reached employing the following parameters:

- laser energy:  $81\text{ mJ}$ ;
- laser spotsize:  $2.3\text{ mm}^2$ ;
- fluence:  $3.5\text{ J/cm}^2$ ;
- deposition temperature:  $740^\circ C$ ;
- target to substrate distance:  $5.7\text{ cm}$ .

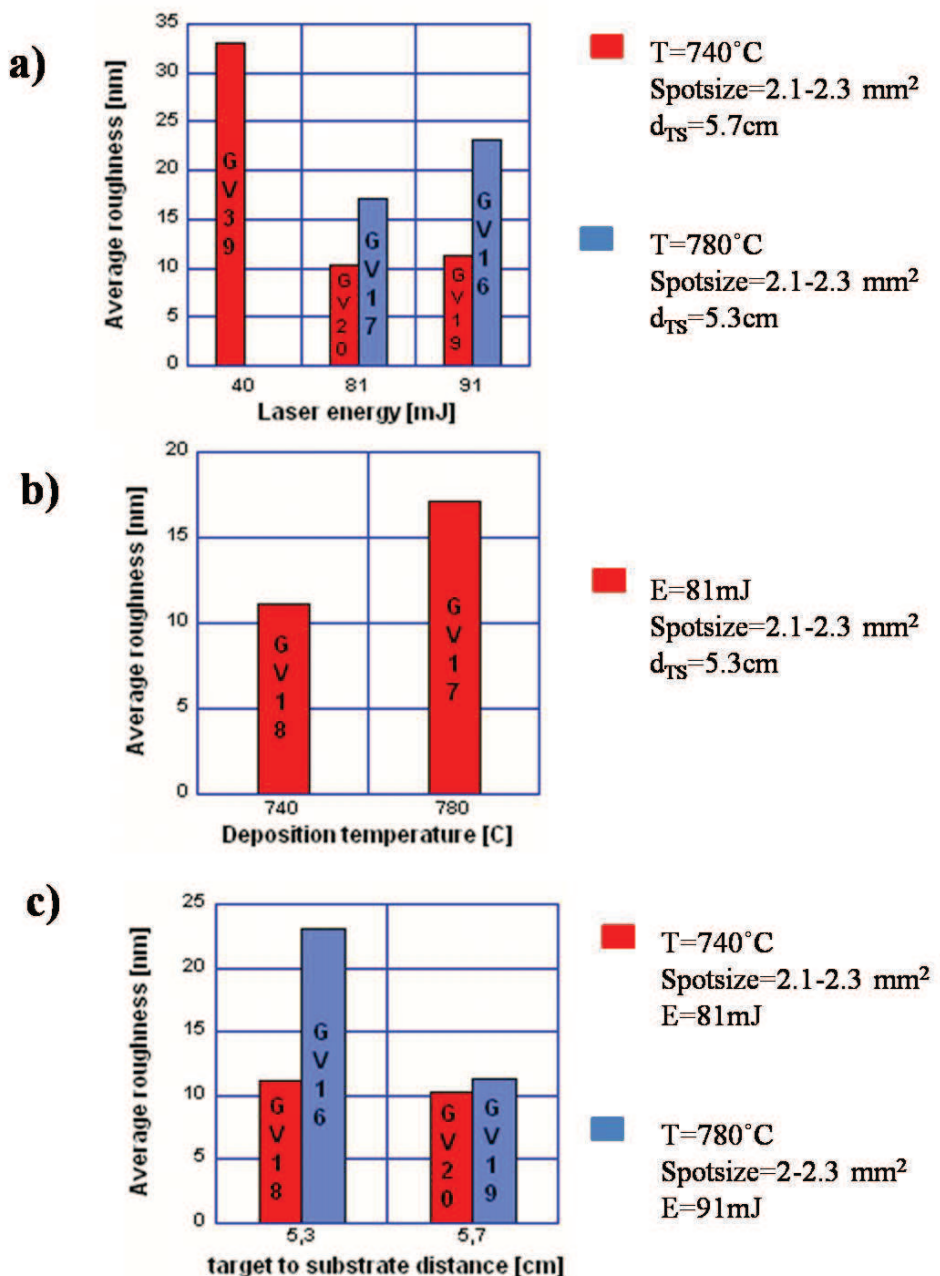


Figure D.20: Average surface roughness of 150 nm thick  $YBa_2Cu_3O_7$  films as function of: a) laser energy, b) deposition temperature, c) target to substrate distance.

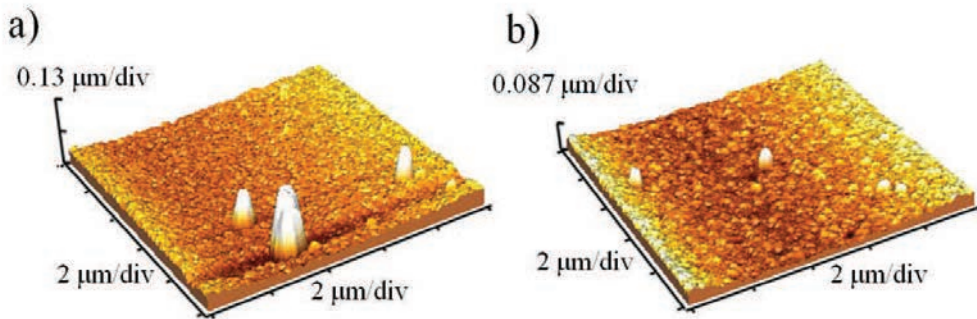


Figure D.21: a) AFM scan on the sample labelled as *GV20* after the deposition of a  $150\text{ nm}$  thick  $YBa_2Cu_3O_7$  film with the deposition parameter set for the new heater the scan area is  $100\text{ }\mu\text{m}^2$ . b) AFM scan on the sample labelled as *GV22* after the deposition of the  $SrTiO_3/YBa_2Cu_3O_7$  bilayer, the  $SrTiO_3$  is  $100\text{ nm}$  thick, the  $YBa_2Cu_3O_7$  is  $150\text{ nm}$  thick, the deposition parameter set for the new heater have been used, the scan area is  $100\text{ }\mu\text{m}^2$ .

Fig. D.21a reports the AFM scan of a  $10\mu\text{m} \times 10\mu\text{m}$  area on the surface of a  $YBa_2Cu_3O_7$  film (sample *GV20*) which has been grown using the new deposition parameters, in this case as previously reported the average roughness of the surface is equal to  $10.29\text{ nm}$ . Fig. D.21b reports a similar scan run on the surface of a  $SrTiO_3/YBa_2Cu_3O_7$  bilayer (sample *GV22*) grown using the listed ablation parameters, the average roughness on the surface of this sample is equal to  $7.94\text{ nm}$ .

### D.3.3 Pads and ramp patterning

After the  $SrTiO_3/YBa_2Cu_3O_7$  bilayer deposition the sample is processed in the clean room where the contact pads of the bottom electrode and the ramp structure are patterned.

The sample is processed as described in sec. 4.2, then it is exposed to the

UV light through the edge mask. The pads structure can now be patterned using the same photolithography process. The sample is than baked at  $100^{\circ}C$  for 4 minutes, such baking step is necessary to repair the damages on the photoresist layer due to the photolithography contact mode.

It follows an etching step which defines the pads geometry on the sample fig. D.17b, performed in an Oxford Applied Research (OAR) *IM150* argon ion milling system with a beam energy of  $500\text{ eV}$ . The milling process is performed under sample rotation with a sample stage angle of  $45^{\circ}$  to the film surface, the film milling is controlled by a Hiden mass spectrometer which enables to detect the end point of the etching. The sample holder of the OAR miller is covered with carbon before the starting of the milling, in this way due to the low milling rate of the carbon ( $110\text{ \AA/min}$ ), the redeposited material coming from the sample holder is reduced.

The bottom electrode and the ramp structure are now defined, however in this case the sample is exposed to the UV light through the ramp mask for 11 seconds and developed for 12 seconds.

As already reported the baking of the resist after the exposure is useful to repair possible damage to the resist profile as a consequence of the contact photolithography step [62] and irregularities in the ramp geometry due to the roughness of the grown bilayer [11]. These are important issues for the ramp type contacts, in fact holes on the ramp structure may cause irregularities on the ramp geometry due to errors in the resist profile and may change the area of the contact leading to a wrong estimation of the contact resistance.

The milling is again performed under rotation and at an angle of  $45^{\circ}$  respect to the film surface. A ramp structure forming an angle of about  $20^{\circ}$

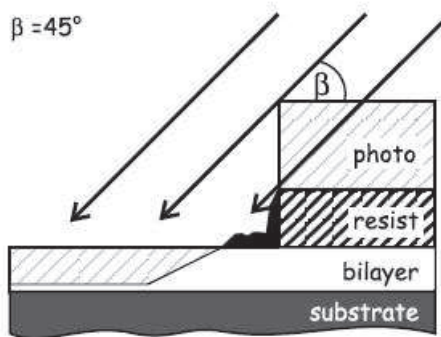


Figure D.22: Formation of the ramp structure through argon ion beam milling. In the shade of the resist stencil redeposited material is accumulated [118].

with the substrate is obtained.

There is a big debate in the literature whether the milling step necessary to produce ramp type Josephson junctions should be performed under rotation or not. Different publications [127, 128, 129] state that the milling into the ramp should be avoided in fact during the milling not only atoms are removed from the surface of the film but also the crystal structure of the ramp surface may be affected and a thin amorphous layer may be formed. This leads to a milling without rotation with an ion beam ideally parallel to the surface of the ramp.

However there is another issue which can deteriorate the resistance of the ramp contact, such issue is related to the redeposited material. Schopp et al. [118] reported the possibility of re-deposited material in the shade of a step-like resist stencil when the milling is performed without rotation fig. D.22.

The etched off-stoichiometric material can cover the ramp structure and

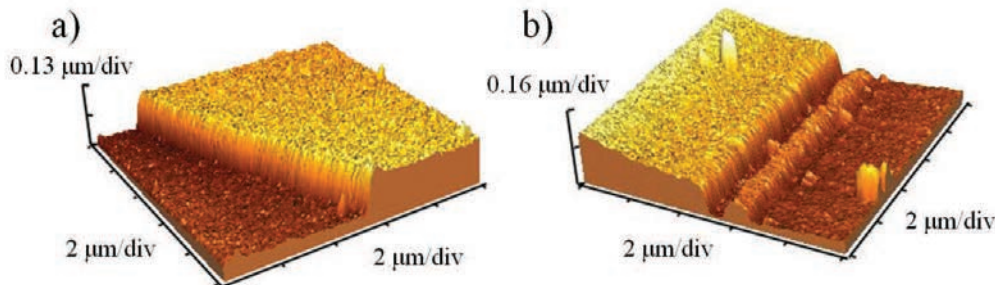


Figure D.23: AFM pictures of two ramp structures belonging to the same sample after the argon ion beam milling. The milling has been performed at  $45^\circ$  under rotation however some redeposited material is present in b).

re-crystallize during the ramp heat treatment process already introduced in sec. D.3.1. By diffusion the redeposited material can cover a significant part of the ramp forming in this way an unwanted layer on the contact area and contributing to an increase of the contact resistance.

The redeposited material is not an issue when the milling is performed under rotation because every ramp surface is always exposed to the ion bombardment.

C. Schuppler [11] observed redeposited material in ramp structures fabricated without sample rotation. Several works reported the fabrication of ramp type Josephson junctions using ion beam milling at an angle of  $45^\circ$  and under rotation [125, 130, 131]. Milling under rotation is preferred in this work too.

Fig. D.23 reports the AFM scans of two ramp structures belonging to the same sample after the argon ion beam milling. The milling has been performed at  $45^\circ$  under rotation. Usually redeposited material is not observed

for milling under rotation, fig. D.23a, sometimes redeposited materials is present at the bottom of the ramp even if the sample has been milled under rotation fig. D.23b. This indicates that an accurate control during the fabrication process is not always possible.

### D.3.4 Ramp cleaning, interlayer deposition, and gold top electrode definition

After the ramp fabrication the film is ultrasonically cleaned in acetone and isopropanol and placed inside the laser deposition chamber to undergo the ramp cleaning process, the annealing step, the deposition of the  $YBa_2Cu_3O_7$  interlayer and the gold top electrode deposition.

The sample is glued with silver paint on the heater and placed inside the vacuum chamber which is pumped down over night, on the next morning a pressure of  $10^{-5} \text{ Pa}$  is reached.

Now the process performed with the old heater is going to be described. The sample is heated to  $200^\circ\text{C}$ , at this temperature an argon ion clean of the ramp is performed, fig. D.24, such cleaning consists of 4 pulses at an argon ion beam voltage of  $500 \text{ V}$  and a beam current of  $10 \text{ mA}$ , this is called *hard etch*, then the sample is exposed to 10 pulses at an argon ion beam voltage of  $50 \text{ V}$  and a beam current of  $5 \text{ mA}$ , this is called *soft etch*. Pulse means shutter in front of the sample open for 8 seconds and closed for 12 seconds, this sequence should prevent sample heating [125]. The hard and the soft etches are performed with a beam parallel to the surface of the ramp to reduce the argon ion bombardment on the ramp itself, however, as already

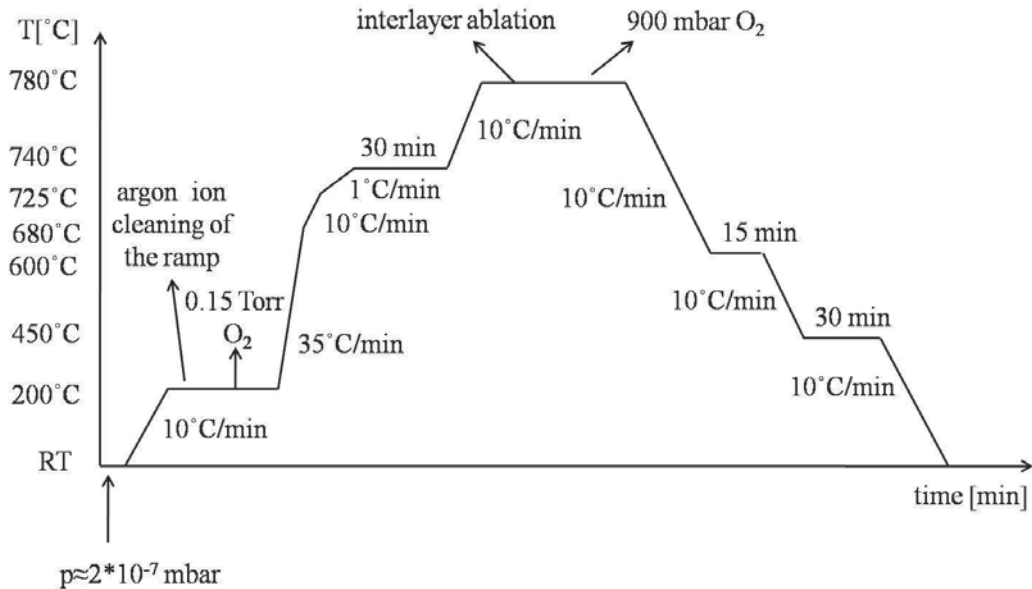


Figure D.24: Temperature versus time graph illustrating the ramp cleaning process, the heat treatment and the interlayer deposition.

discussed, an issue related to the redeposited material might be present in this case. The hard etch is designed to remove the amorphous layer formed on the  $YBa_2Cu_3O_7$  ramp as consequence of the milling process and of the exposure of the ramp to the atmosphere [116] however the hard etch can also damage the surface of the ramp. The subsequent soft etch will still remove material but due to the considerable decreased beam energy will also reduce the damage. The hard and the soft etches are performed at a temperature of  $200^\circ C$  to reduce the redeposited material on the surface of the ramp, this is due to a reduced sticking coefficient relative to room temperature [118].

Then follows an in-situ cleaning step of the ablation targets in oxygen flow at the pressure which will be used during the film deposition. The sample is then heated up in oxygen flow at a pressure of  $20 Pa$  to avoid

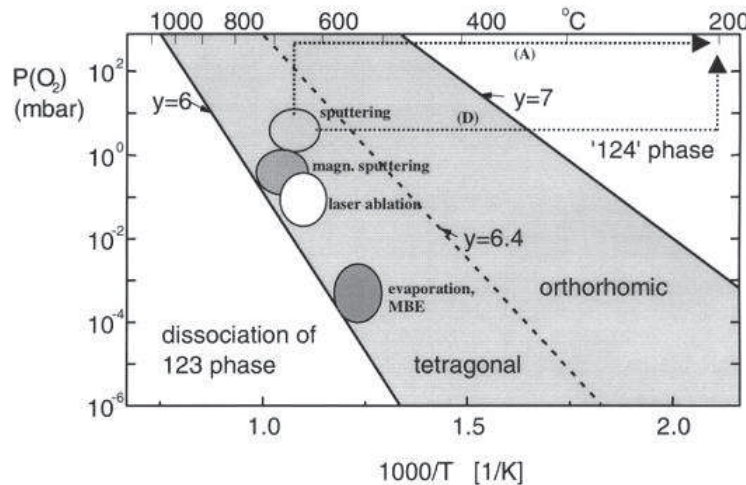


Figure D.25: Pressure ( $P$ ) versus temperature ( $T$ ) phase diagram of  $YBa_2Cu_3O_y$ . The YBCO 123-phase is stable in the regime indicated by the dashed area which is divided into the non-superconducting tetragonal and superconducting orthorhombic phases [101].

the dissociation of the  $YBa_2Cu_3O_7$ . Fig. D.25 shows the pressure versus temperature diagram of  $YBa_2Cu_3O_7$ , from the picture it is clear that if the sample were heated in vacuum dissociation of the  $YBa_2Cu_3O_7$  would start at about  $500^\circ C$  for a pressure of  $2 \cdot 10^{-4} Pa$ .

The sample containing the ramp structures is heated to  $740^\circ C$  as shown in fig. D.24 and kept there for 30 minutes, this is important to avoid outgrowths on the ramp structure which may occur at a temperature of  $780^\circ C$ . At  $780^\circ C$  the species on the ramp surface are mobile over long distances, at  $740^\circ C$ , however, species can still move to contribute to the ramp reconstruction but only over a short distance, in this case the reduced mobility does not allow the formation of outgrowths. During the recrystallization process which takes place at  $740^\circ C$  the species are thermally stabilized, and the ramp surface does

not show any visible change when it is heated to  $780^{\circ}C$  after the annealing step [62].

The argon ion beam cleaning and the heat treatment are not enough to recover the crystal structure on the surface of the  $YBa_2Cu_3O_7$  ramp, this is confirmed by a contact resistance of  $10^{-4} \Omega cm^2$  for a  $Au/YBa_2Cu_3O_7$  ramp type contacts fabricated without interlayer deposition [111]. This poor interface is attributed to the fact that an etching plus an annealing procedure are not enough to restore the correct stoichiometry on the ramp. Thus at  $780^{\circ}C$  a  $6\text{ nm}$  thick  $YBa_2Cu_3O_7$  interlayer is deposited. The deposition of this interlayer at the standard ablation conditions, table D.1, stabilizes the off-stoichiometric etched surface of the ramp leading to a contact resistance of  $3 \cdot 10^{-8} \Omega cm^2$  [111]. The interlayer becomes superconductive only if deposited on the  $YBa_2Cu_3O_7$  ramp area, on the  $SrTiO_3$  substrate and on the  $SrTiO_3$  insulation layer it is not superconductive due to lattice mismatch and to roughnesses,  $7\text{ nm}$  of  $YBa_2Cu_3O_7$  are necessary to obtain the superconductive orthorhombic phase [111].

After the interlayer deposition, the chamber is filled with oxygen up to a pressure of  $90 \cdot 10^3 Pa$ , the sample is then cooled down to room temperature at a rate of  $10^{\circ}C/min$  via a 15 minutes dwell at  $600^{\circ}C$  and a 30 minutes dwell at  $450^{\circ}C$  to fully oxygenate the  $YBa_2Cu_3O_7$  fig. D.24.

At room temperature the system is pumped down to a pressure of about  $2 Pa$  where an argon flow of  $5 sccm$  around the argon pressure of  $16.5 Pa$  is established, finally a  $40\text{ nm}$  thick gold layer is ablated on the sample.

When the gold is ablated, the gold particles in the laser plume can reach energies up to several hundred  $eV$  [11], at such energies they can damage the

ramp surface which has been repaired with the growth of the  $YBa_2Cu_3O_7$  interlayer. The energy of the impinging gold particles can be reduced to about 1 eV if the gold ablation is performed in a 20 Pa argon pressure with a laser fluence of 4  $J/cm^2$  and a target to substrate distance of about 5 cm [132]. Due to this reason the gold ablation is performed in argon environment.

The sample is then taken back to the clean room facilities for the patterning of the top electrode. It follows the process already described in sec. D.3.3, again the hump at the edge of the sample is removed by exposure to the UV light through the edge mask, then the top electrode geometry is patterned on the photoresist by exposing the sample to the UV light through the electrode mask for 11 seconds and developing the resist for 12 seconds. After the stripping of the resist the sample is inserted in the argon ion milling system and milled at an angle of 45° under rotation.

Fig. D.26a and b report the mask layout used for the fabrication of the  $Au/YBa_2Cu_3O_7$  ramp type contacts, in fig. D.26a the width  $w$  of each contact is reported, while in fig. D.26b the width  $w$  of each contact is equal to 10  $\mu m$ . The  $YBa_2Cu_3O_7$  film is 150 nm thick and the ramp forms an angle  $\vartheta$  of about 20° with the  $SrTiO_3$  substrate, this results in a contact area  $A_{cont}$  of:

$$A_{cont} = \frac{150 \text{ nm}}{\sin \vartheta} \cdot w. \quad (\text{D.30})$$

In fig. D.26a and b the blue areas represent the  $YBa_2Cu_3O_7$  base electrode which is connected to four contact pads, the gold top electrodes overlapping the ramp area (green parts of fig. D.26a and b) are instead connected to two contacts pads. The four contact pads of the bottom electrode allow

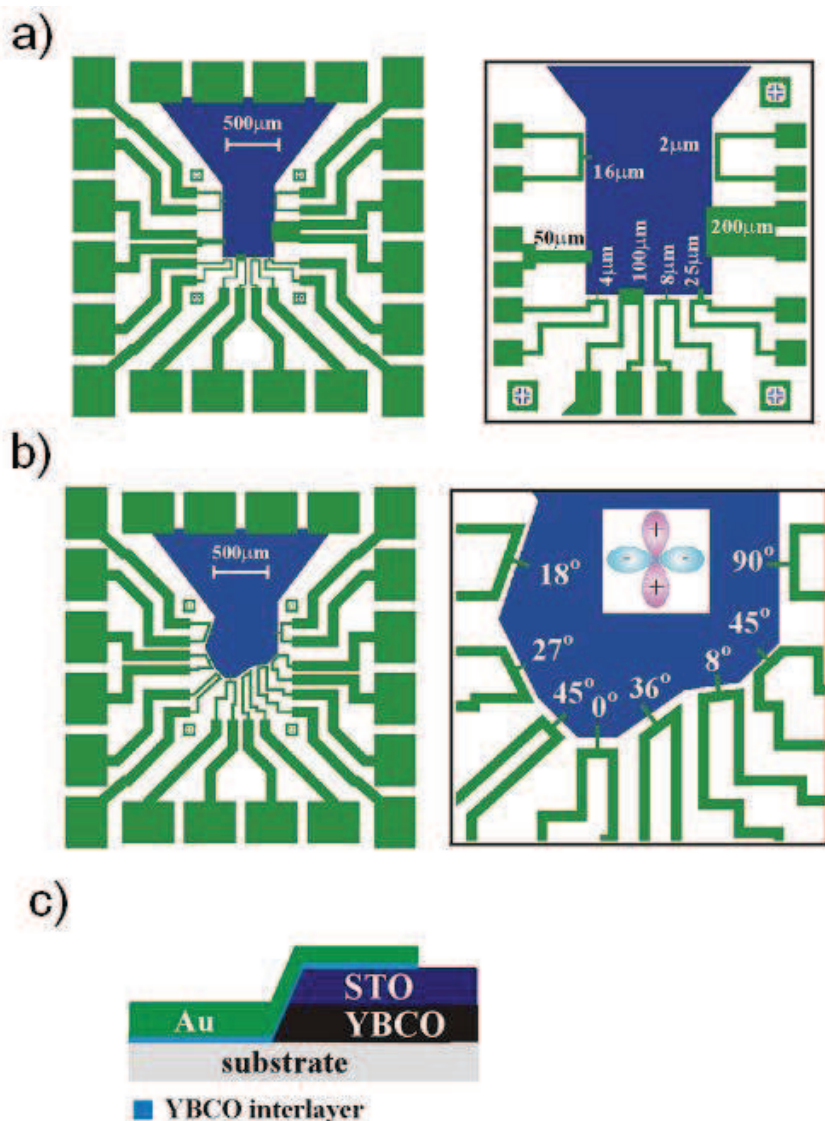


Figure D.26: a) Layout of the bottom left quarter (BL) of the mask used to pattern the  $Au/YBa_2Cu_3O_7$  ramp type contact, in the picture the width of each contact is reported. b) Layout of the bottom right quarter of the mask used to pattern the the  $Au/YBa_2Cu_3O_7$  ramp type contact, in this case the width of each device is  $10 \mu m$ . c) Side view of the  $Au/YBa_2Cu_3O_7$  ramp type contact. [11]

to run resistance versus temperature measurements of the  $YBa_2Cu_3O_7$  base electrode by employing the four terminal technique, sec. D.2.5. When two pads of the bottom electrode and two pads of the top electrode of a certain device are connected, current versus voltage and resistance versus temperature measurements with the four terminal technique can be performed sec. D.2.5.

The layout of fig. D.26b has been designed to probe the  $YBa_2Cu_3O_7$  base electrode from different angular directions when a superconducting top electrode is grown on the top of the sample. As already discussed in sec. D.1.6 at an angle of  $0^\circ$  a normal junction is obtained while at an angle of  $90^\circ$  a  $\pi$ -junction is formed, all the other angles allow an investigation of the Cooper pair wave function of the  $YBa_2Cu_3O_7$  base electrode.

The aim of the first part of this Phd is that one to improve the interface of the  $Au/YBa_2Cu_3O_7$  ramp type contact, so also the layout of fig. D.26b has been used for such purpose and no samples with  $Nb$  top electrode have been produced.

C. Schuppler [11] observed the presence of redeposited material at the bottom of the ramp after the soft and hard etch steps followed by the heat treatment, he reported that such redeposited material was not present after the ramp fabrication. The redeposited material reduces the useful contact at the  $Au/YBa_2Cu_3O_7$  interface, furthermore redeposited material may have homogeneously spread across the ramp surface which is not detectable by AFM scans [11]. During the ramp recrystallization process species originating from it may diffuse over the ramp area and add an additional unwanted layer to the previously cleaned ramp surface [118].

C. Schuppler in his Phd thesis reported that private communication with A. Andreski [133] revealed that in Twente (where the  $Nb/Au/YBa_2Cu_3O_7$  ramp type junctions have been successfully fabricated [10, 111, 125]) the soft and the hard etches are performed along the film normal in order to minimize the redeposited material. This led to the introduction of the in-situ tiltable heater in the deposition system, hence milling under different angles relative to the argon ion beam is possible.

With the introduction of the new heater the deposition parameters of the interlayer have been set equal to those ones used for the  $YBa_2Cu_3O_7$  base electrode deposition performed with the same heater, table D.1, the table also reports the deposition parameter for the gold ablation performed with the new heater.

Fig. D.27a shows the AFM 3D picture and the line scan profile of the  $SrTiO_3/YBa_2Cu_3O_7$  ramp structure after the ramp fabrication by argon ion beam milling, the ramp surface is smooth however an amorphous layer as a consequence of the ion bombardment and of the exposure to the atmosphere is present on its surface. Figs. D.27b and c show the ramp profile after the soft and the hard etch steps, the heat treatment and the interlayer deposition, all these steps have been performed with the new heater, this means that the soft and the hard etches have been run with the argon ion beam beam perpendicular to the surface of the sample. From the examination of fig. D.27b and c it is evident that in some part of the sample the ramp profile is smooth while in other areas the ramp profile looks rough.

As already reported the redeposited material is thought to be responsible for the rough profile, even with a cleaning step performed with an argon ion

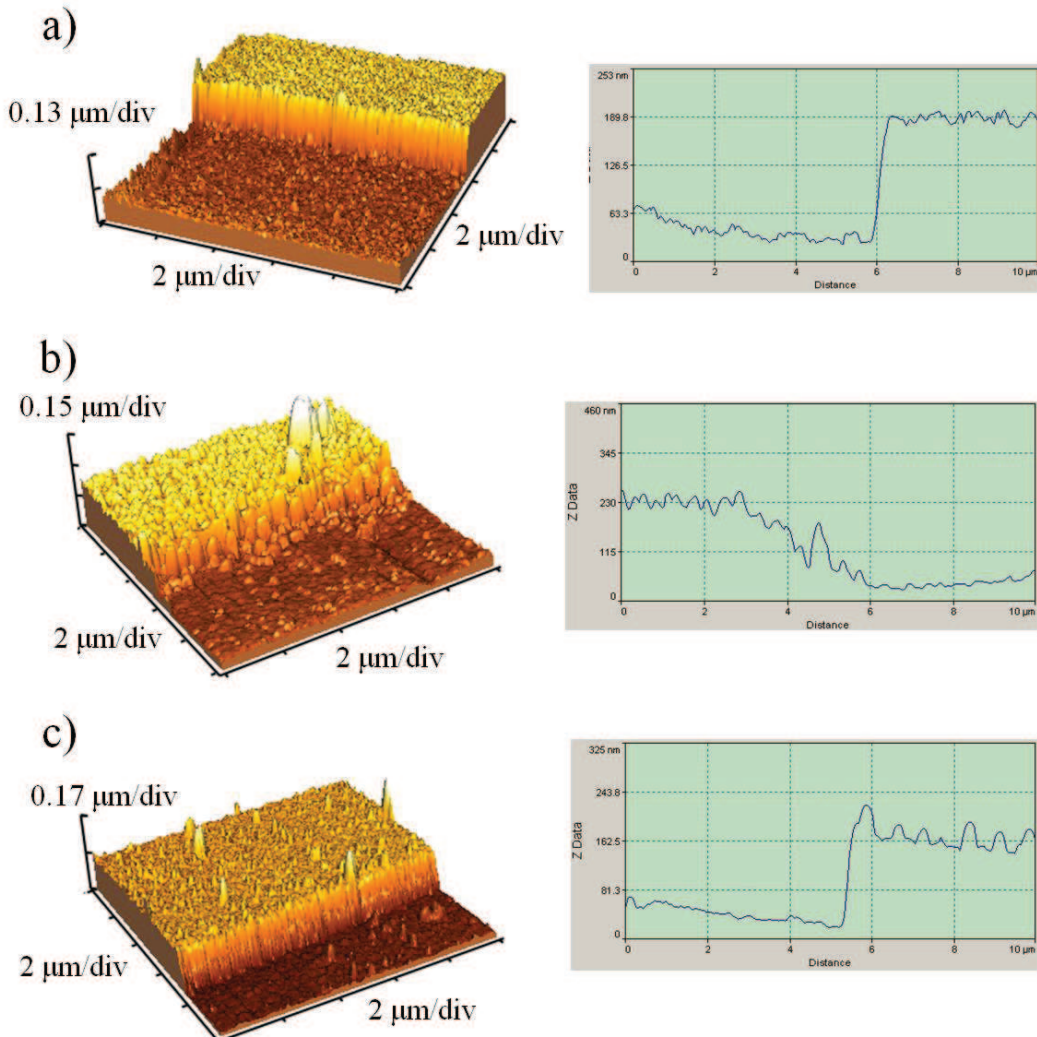


Figure D.27: AFM investigations on the sample labelled *GV22*. a) AFM 3D picture and line profile of the  $SrTiO_3/YBa_2Cu_3O_7$  ramp structure after the ramp fabrication by argon ion beam milling. b) AFM 3D picture and line profile of the  $SrTiO_3/YBa_2Cu_3O_7$  ramp structure after the soft and hard etch, the heat treatment and the interlayer deposition. c) AFM 3D picture and line profile of the  $SrTiO_3/YBa_2Cu_3O_7$  ramp structure after the soft and hard etch, the heat treatment and the interlayer deposition.

beam incident along the normal to the film. These steps of the fabrication process do not look easy to control, this is testified by the completely different profiles on different areas of the same sample.

Huang at al. [130] reported the fabrication of  $YBa_2Cu_3O_7$  ramp type Josephson junctions with a manganite barrier, they performed a ramp cleaning with an argon ion beam of  $100\text{ eV}$  and beam currents of  $0.1\text{ mA/cm}^2$  for 30 minutes followed by a cleaning in low energy  $Ar/O_2$  plasma. Schoop at al. reported a 5 minutes argon ion beam cleaning of the ramp at  $150\text{ eV}$  followed by a oxygen ion clean at  $100\text{ eV}$ . Our Kaufman ion gun can not be operated with oxygen ions [11], however cleaning processes of 5, 10, 20 and 30 minutes for beam energies ranging between  $50\text{ eV}$  and  $150\text{ eV}$  have been tried, the result is similar to what is shown in fig. D.27b and c, on some parts of the sample the ramp profile is smooth, on other areas the ramp profile is rough.

To better understand what is happening during the ramp process, AFM scans have been taken on the ramp structure after the hard etch, the soft etch and the heat treatment.

Fig D.28a shows an AFM 3D picture and a line scan profile of the  $SrTiO_3/YBa_2Cu_3O_7$  ramp structure taken after the hard etch step , the ramp profile is smooth and it shows no sensible change after the soft etch cleaning which follows the hard etch fig. D.28b. Both the hard and the soft etches have been run with the argon ion beam normal to the surface of the film. Fig. D.28c and d show two ramp profiles belonging to the same sample, after the soft etch, the hard etch and the heat treatment. As already observed on other fabricated ramps, same areas present a smooth profile while other areas have a rough profile. After the hard and soft etches the ramp

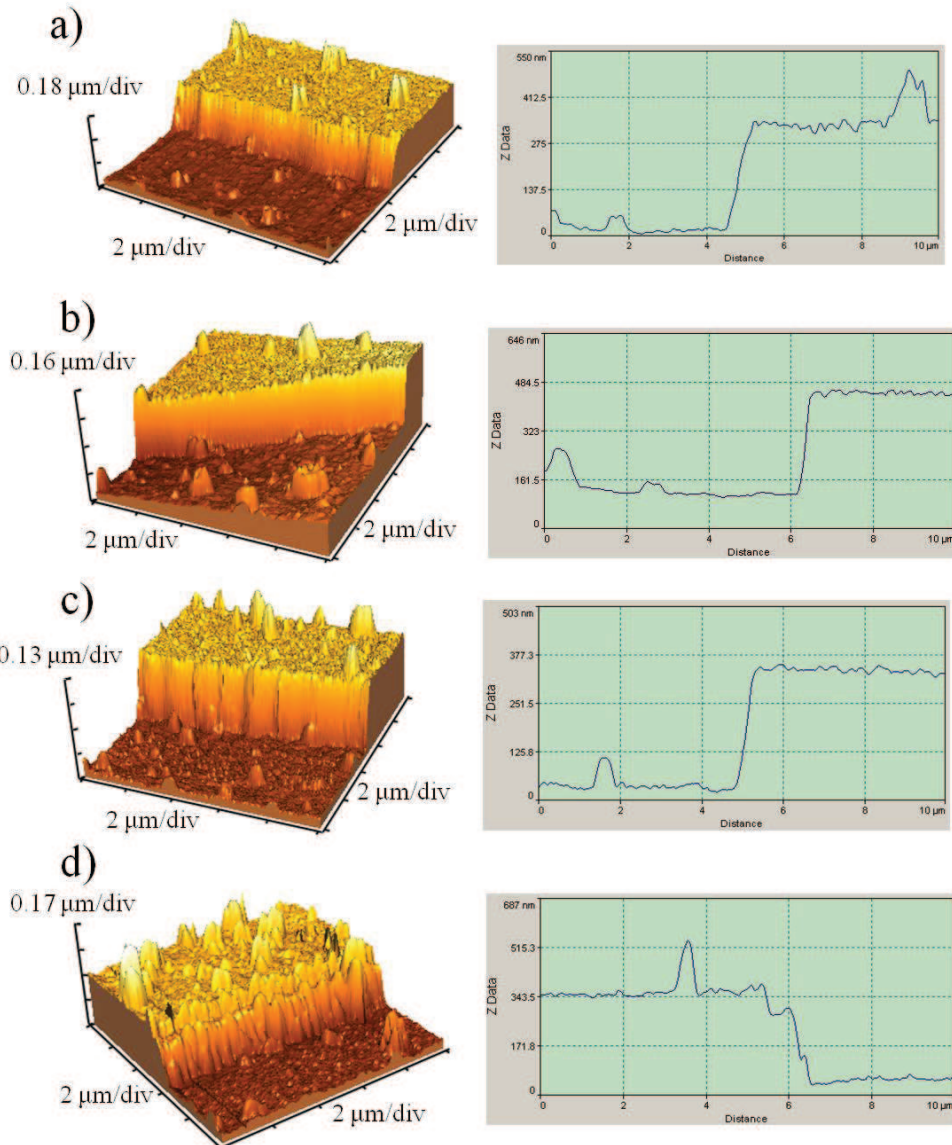


Figure D.28: AFM investigations on the sample labelled *GV36*. a) AFM 3D picture and line profile of the  $SrTiO_3/YBa_2Cu_3O_7$  ramp structure after the hard etch treatment. b) AFM 3D picture and line profile of the  $SrTiO_3/YBa_2Cu_3O_7$  ramp structure after the hard and soft etch treatment. c)-d) AFM 3D picture and line profile of the  $SrTiO_3/YBa_2Cu_3O_7$  ramp structure after the soft and hard etch and the heat treatment.

surface is smooth almost everywhere across the sample however we believe that on some areas the redeposited materials is homogeneously spread and so it is not detectable by AFM scans. When the sample undergoes the heat treatment the redeposited material diffuse on the ramp creating the profiles reported in figs. D.27b and D.28d.

A heat treatment where the sample was heated at a rate of  $5^{\circ}\text{C}/\text{min}$  with two dwells of 30 minutes at  $450^{\circ}$  and  $600^{\circ}$  did not show any significant difference respect to the structures previously fabricated.

### D.3.5 Summary

In this chapter the reasons which bring to a certain fabrication process have been discussed. A new tiltable heater has been introduced in the deposition chamber to perform the hard and soft etch cleaning steps with the argon ion beam normal to the surface of the film to reduce in this way the effects of the redeposited material on the ramp surface.

In order to reduce the roughness of the  $\text{SrTiO}_3/\text{YBa}_2\text{Cu}_3\text{O}_7$  bilayer which contribute to a degradation of the ramp profile and so also of the  $4\text{ K RA}$  product a recalibration of the  $\text{SrTiO}_3$  and  $\text{YBa}_2\text{Cu}_3\text{O}_7$  ablation parameters has been necessary when the new heater has been mounted inside the deposition chamber.

After the ramp fabrication by argon ion beam milling the soft and the hard etch plus the heat treatment and the interlayer deposition are necessary to recover the crystal structure along the ramp surface. The main issue in this process is represented by the redeposited material which may form an

unwanted off-stoichiometric layer on the ramp area and increases the value of the  $4K$  RA product of the contact. This redeposited material is very difficult to control in fact after the the ramp processing some areas of the ramp present a smooth profile while other areas present a rough profile. With our setup it is not possible to control the direction of the redeposited material, if a junction is fabricated on the smooth part of the ramp a low  $4K$  RA product is obtained otherwise the  $4K$  RA product increases by different orders of magnitude.

## D.4 Measurements and Results

In this section the results of the susceptibility, current versus voltage and resistance versus temperature measurements performed on the  $Au/YBa_2Cu_3O_7$  ramp type contacts are discussed and analyzed.

### D.4.1 Electrical measurements on the $Au/YBa_2Cu_3O_7$ ramp type contacts

Tab. D.3 reports the  $4K$  RA products together with some key parameters adopted for the the fabrication process of the  $Au/YBa_2Cu_3O_3$  ramp type contact.

In the following the results of the electrical measurements for the devices fabricated with the new and the old heater and the relations between the fabrication steps and the  $4K$  RA product are reported.

#### Devices fabricated with the old heater

C. Schuppler, during his Phd at the University of Birmingham, produced a sample (labeled as *CS82*) containing some  $Au/YBa_2Cu_3O_7$  ramp type contacts with a  $4K$  RA product in the range of  $10^{-7} \Omega cm^2$  [11]. The fabrication process adopted for this sample is similar to that one performed with the old heater and reported in chap. D.3. The differences between the discussed fabrication procedure and that one of the sample *CS82* are:

- in the case of sample *CS82* the soft and the hard etches are perfomed at room temperatures and not at  $200^\circ C$  as reported in sec. D.3.4;

<i>Device</i>	<i>Heater</i>	<i>Cooling rate after interlayer [°C/min]</i>	<i>Soft etching direction</i>	<i>Soft etching time</i>	<i>Soft etching temperature [°C]</i>	<i>Interlayer dep. frequency [Hz]</i>	<i>RA(4K) Ω · cm²</i>
GV03	old	35	parallel to the ramp	10 pulses of 8 s	RT	4	$10^{-3} - 10^{-5}$
GV04	old	35	parallel to the ramp	10 pulses of 8 s	RT	4	$10^{-3} - 10^{-4}$
GV05	old	35	parallel to the ramp	10 pulses of 8 s	RT	4	$10^{-3} - 10^{-5}$
GV06	old	10	parallel to the ramp	10 pulses of 8 s	200	4	$10^{-6} - 10^{-8}$
GV08	old	10	parallel to the ramp	10 min	200	4	$10^{-3} - 10^{-7}$
GV11	old	10	parallel to the ramp	10 min	200	4	$10^{-3} - 10^{-5}$
GV41	new	10	perpendicular to the ramp	10 pulses of 8 s	200	4	$10^{-4} - 10^{-6}$
GV42	new	10	perpendicular to the ramp	10 pulses of 8 s	200	1	$10^{-5} - 10^{-6}$

Table D.3: Key parameters for the fabrication of the  $Au/YBa_2Cu_3O_7$  ramp type contacts and RA product at 4 K, RT means room temperature.

- sample *CS82* after the interlayer deposition is cooled down to room temperature at a rate of  $35^{\circ}C/min$  and not at a rate of  $10^{\circ}C/min$  as reported in sec. D.3.4
- for sample *CS82* the cooling subsequent the interlayer deposition is performed without the two dwells at  $600^{\circ}C$  and  $450^{\circ}C$  reported in sec. D.3.4.

C. Schuppler repeated the fabrication process used for the sample *CS82* and a sample labeled as *CS84* was produced, *CS84* showed 4 K RA products in the range  $10^{-4} - 10^{-5} \Omega cm^2$ . The same fabrication process has been repeated during the first part of this Phd, two samples labeled as *GV03* and

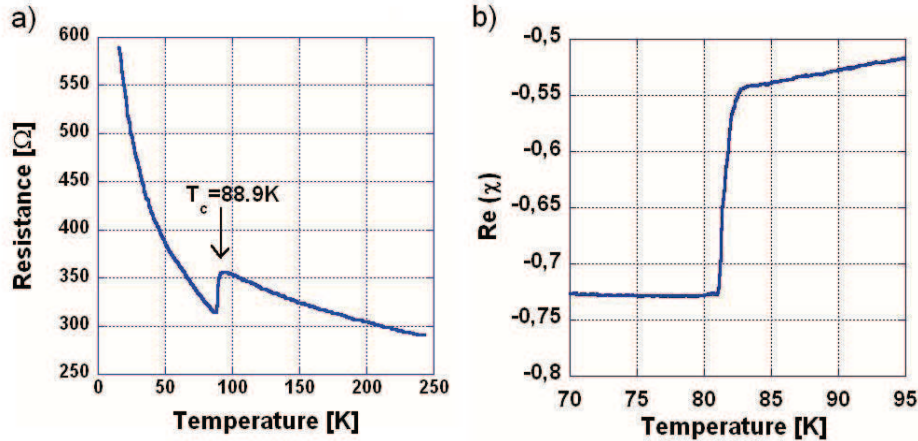


Figure D.29: a) Resistance versus temperature measurements on a ramp type contact having an area of  $42 \mu\text{m}^2$  and belonging to the BL quarter of sample *GV04*. b) Susceptibility measurements on the  $\text{SrTiO}_3/\text{YBa}_2\text{Cu}_3\text{O}_7$  bilayer of the sample labeled *GV11*.

*GV05* have been fabricated, in both cases current voltage measurements reveal  $4K$  RA products in the range of  $10^{-3} - 10^{-5} \Omega\text{cm}^2$ . A sample labeled as *GV04* has been produced using a process similar to that one employed for *CS82*, however in this case the fabrication of the ramp has been performed by milling without rotation. As already reported in sec. D.3.3 this is justified by the fact that during the milling not only the atoms are removed from the surface of the film but also from the ramp surface, damaging in this way its crystal structure. [127, 128, 129]. A ramp milling performed with a beam parallel to the surface of the ramp without rotation reduces the bombardment on the ramp area. Nonetheless  $4K$  RA products in the range  $10^{-3} - 10^{-4} \Omega\text{cm}^2$  have been measured.

Resistance versus temperature measurements for the  $\text{Au}/\text{YBa}_2\text{Cu}_3\text{O}_7$  contacts of the samples *GV03*, *GV04* and *GV05* have a similar trend. Fig.

D.29a reports the resistance versus temperature measurements of a  $Au/YBa_2Cu_3O_7$  ramp type contact having an area of  $42 \mu m^2$  and belonging to the BL quarter of the sample *GV04*. A drop in the  $R - T$  curve at  $88.9 K$  indicates the transition of the  $YBa_2Cu_3O_7$  bottom electrode in the superconducting state, this is confirmed by susceptibility measurements on a  $SrTiO_3/YBa_2Cu_3O_7$  bilayer grown with the same ablation parameters used for the fabrication of the sample *GV04*.

The trend shown in fig. D.29a is known as semiconducting behaviour and it is an indication of an unsuccessful recovery of the crystal structure on the ramp surface. Huang et al. [130] reported a similar behaviour for some of their  $YBa_2Cu_3O_7/La_{0.67}Sr_{0.33}MnO_3/YBa_2Cu_3O_7$  ramp type junctions. They attributed the semiconducting behaviour to oxygen depletion at the  $La_{0.67}Sr_{0.33}MnO_3/YBa_2Cu_3O_7$  interface, similar arguments have been also reported in [113], oxygen deficiency creates an insulating layer on the  $YBa_2Cu_3O_7$  ramp surface increasing in this way the  $4K RA$  product.

In a quantum-mechanical frame the semiconducting behaviour can be understood as follow: at the normal metal/superconductor interface is present a barrier having width  $w$  and an height  $E_0$ , the transmission coefficient  $T$  for an electron with energy  $E$  ( $E_F < E < E_0$ ) impinging on the barrier is:

$$T \propto e^{-2w\frac{2m\sqrt{\Delta E}}{\hbar}} \quad (\text{D.31})$$

where  $m$  is the electron mass and  $\Delta = E_0 - E$ . The probability of finding high energy electrons decreases with decreasing temperature, so  $\Delta E$  increases with decreasing temperature. This corresponds to a reduction of the number

of charge carriers and to an increase of the contact resistance.

Oxygen depletion at the ramp surface is the result of the ramp fabrication by argon ion beam milling, however this is not the only stoichiometry issue caused by the milling, Wen et al. [134] reported an high yttrium and low copper content on a  $YBa_2Cu_3O_7/YBa_2Cu_3O_7$  ramp type junction with a  $La_{0.3}Sr_{0.7}Al_{0.65}Ta_{0.35}O_y$  insulation layer along the  $c$  axis. In this case the ramp has not been exposed to the atmosphere as the milling of the bottom electrode plus the deposition of the  $YBa_2Cu_3O_7$  top electrode are performed in situ, in such devices the barrier is constituted by the off-stoichiometric layer at the interface between the two electrodes. In the barrier layer the presence of cubic yttrium-barium-copper-oxide is reported [134], cubic yttrium-barium-copper-oxide has semiconducting or insulating behaviour [127].

The stoichiometry is not the only problem which contributes to the degradation of the  $4\text{ K}$  RA product, the redeposition of unwanted material on the ramp surface, which takes place during the ramp fabrication and the ramp cleaning process, may reduce the contact area at the  $Au/YBa_2Cu_3O_7$  interface or it can create an uniform unwanted layer on the ramp which increases the  $4\text{ K}$  RA product. Hunt et al. [135] reported that during the ramp cleaning, material from the top insulator layer, in our case  $SrTiO_3$ , can be accumulated at the bottom of the ramp. They state that such material is irregularly distributed.

The resistance of a  $Au/YBa_2Cu_3O_7$  contact is inversely proportional to the area of the contact, fig. D.30 reports the  $4\text{ K}$  resistance of the devices belonging to the BL quarter of the samples  $GV05$  and  $GV04$  as function of the inverse of their width. Due to the scaling behaviour these values are expected

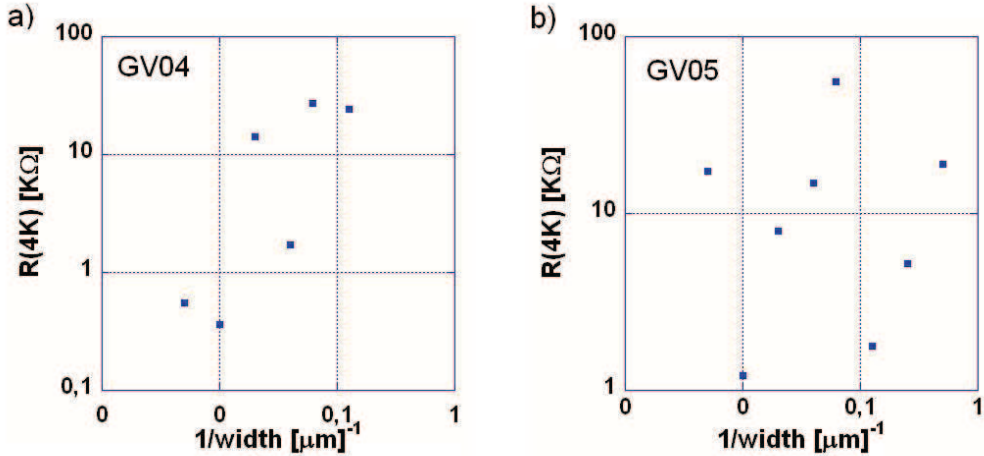


Figure D.30: Resistance of the  $Au/YBa_2cu_3O_7$  ramp type contacts belonging to the BL quarter as function of the inverse of the width for the samples a)  $GV04$  and b)  $GV05$ . The resistance has been measured at a temperature of  $4\text{ K}$ .

to stay on a straight line, this does not happen in the case of the samples  $GV04$  and  $GV05$ . Such behaviour is attributed to the insulating material irregularly distributed at the bottom of the ramp, in fact an homogeneous redeposition can cause the increase of the contact resistance but should not alter the scaling of the data [11].

The high  $4\text{ K}$  RA products of the samples  $GV03$ ,  $GV04$  and  $GV05$  is believed to be caused by a combination of the described issues in fact the semiconducting behaviour shown in fig. D.29 is an indication of the presence of an off-stoichiometric layer at the  $Au/YBa_2cu_3O_7$  interface while the absence of a scaling behaviour shown in fig. D.30 is an indication of the presence of redeposited material irregularly distributed on the ramp surface.

Two other samples have been prepared with the old heater, they are sample *GV06* and sample *GV08*. Sample *GV06* has been fabricated using the process described in chap. D.3. Also sample *GV08* has been fabricated using the fabrication process described in chap. D.3 except for the soft etching, here a continuous etch of 10 minutes at 50 V at a temperature of 200°C has been performed.

Table D.4 reports the 4 K RA products for the devices of the BL quarter of the samples *GV06* and *GV08*, the majority of the RA products are in the range of  $10^{-6} \Omega cm^2$ , these values are smaller than those ones measured in the BL quarter of samples *GV03*, *GV04* and *GV05* but they are one order of magnitude bigger than the RA product reported in [10] and two order of magnitude larger than the RA products reported in [111].

However in the BL quarter of sample *GV06*, the device having width equal to  $2 \mu m$  presents a 4 K RA product equal to  $2.9 \cdot 10^{-7} \Omega cm^2$ , in the BL quarter of sample *GV08* the device with a width of  $100 \mu m$  has a 4 K RA product equal to  $8.4 \cdot 10^{-7} \Omega cm^2$ , these values are similar to the RA products of sample *CS82* and to the RA products reported in [10].

For these samples the hard and the soft etches are performed at a temperature of 200°C, as already reported in sec. D.3.4, at such a temperature the sticking coefficient of the redeposited material is smaller than that one at room temperature [118] so the redeposited material on the ramp area should be reduced.

This is confirmed by the plots of the 4 K resistance as function of the inverse of the width, fig. D.31, in particular in the case of sample *GV06* the resistances of six devices approach a straight line fig. D.31a. The devices

<i>Sample</i>	<i>device</i>	width [ $\mu m$ ]	200	100	50	25	16	8	4	2
	Area [ $\mu m^2$ ]		84	42	21	10.5	6.72	3.36	1.68	0.84
GV06	$R(RT)$ [ $\Omega$ ]		49	63	76.7	80.5	65.7	89.8	153.7	84
BL	$R(4 K)$ [ $\Omega$ ]		3.5	15.4	15.7	24	29.7	68.3	207	34.7
	$RA(4K)$ [ $\Omega cm^2$ ]		$2.94 \cdot 10^{-6}$	$6.5 \cdot 10^{-6}$	$3.3 \cdot 10^{-6}$	$2.52 \cdot 10^{-6}$	$2 \cdot 10^{-6}$	$2.3 \cdot 10^{-6}$	$3.47 \cdot 10^{-6}$	$2.9 \cdot 10^{-7}$
GV08	$R(RT)$ [ $\Omega$ ]		65	77.6	93	108	107	214	300	<i>o. c.</i>
BL	$R(4 K)$ [ $\Omega$ ]		2.3	2	9.3	10.38	16	88	349	<i>o. c.</i>
	$RA(4K)$ [ $\Omega cm^2$ ]		$1.68 \cdot 10^{-6}$	$8.4 \cdot 10^{-7}$	$1.9 \cdot 10^{-6}$	$1.1 \cdot 10^{-6}$	$1.1 \cdot 10^{-6}$	$2.96 \cdot 10^{-6}$	$5.86 \cdot 10^{-6}$	<i>o. c.</i>

Table D.4: Room temperature (RT) resistance,  $4 K$  resistance and  $4 K$  RA product for the devices belonging to the BL quarter of the samples *GV06* and *GV08*, *o. c.* stands for open circuit.

<i>Sample</i>	<i>device</i>	1	2	3	4	5	6	7	8
GV06	$R(RT)$ [ $\Omega$ ]	75	100	31.3	94	95	92	94	91
BR	$R(4 K)$ [ $\Omega$ ]	27.8	102	2	63.6	38	40	66.7	98
	$RA(4K)$ [ $\Omega cm^2$ ]	$1.17 \cdot 10^{-6}$	$4.28 \cdot 10^{-6}$	$8.4 \cdot 10^{-8}$	$2.7 \cdot 10^{-6}$	$1.6 \cdot 10^{-6}$	$1.7 \cdot 10^{-6}$	$2.8 \cdot 10^{-6}$	$4.11 \cdot 10^{-6}$
GV08	$R(RT)$ [ $\Omega$ ]	2070	2060	1300	828	394	381	298	1100
BR	$R(4 K)$ [ $\Omega$ ]	44000	42400	39400	17200	570	590	400	29000
	$RA(4K)$ [ $\Omega cm^2$ ]	$3.7 \cdot 10^{-5}$	$3.56 \cdot 10^{-2}$	$4.13 \cdot 10^{-3}$	$5.8 \cdot 10^{-4}$	$2.4 \cdot 10^{-4}$	$9.91 \cdot 10^{-6}$	$8.4 \cdot 10^{-5}$	$1.95 \cdot 10^{-3}$

Table D.5: Room temperature (RT) resistance,  $4 K$  resistance and  $4 K$  RA product for the devices belonging to the BR quarter of the samples *GV06* and *GV08*, all the devices of the BR quarter have a width of  $10\mu m$  and an area of  $4.2\mu m^2$ .

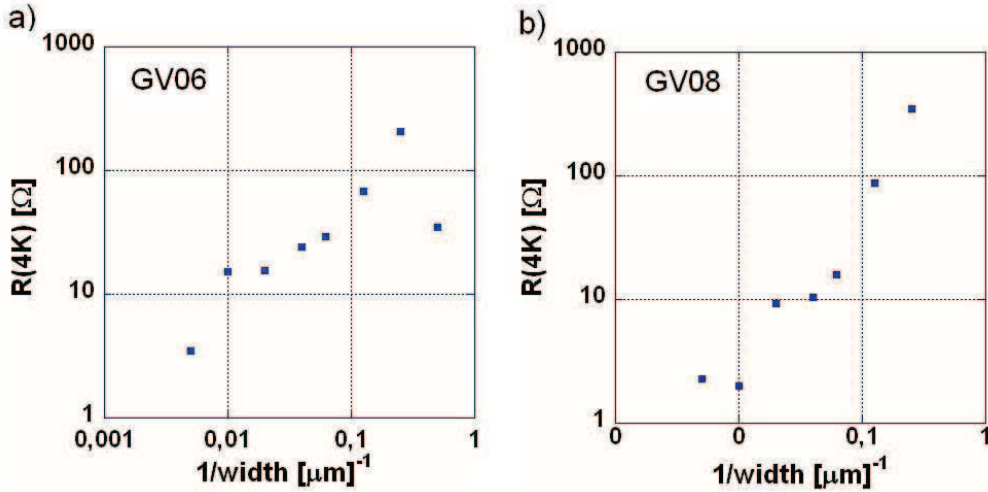


Figure D.31: Resistance of the  $Au/YBa_2Cu_3O_7$  ramp type contacts belonging to the BL quarter as function of the inverse of the width for the samples a) *GV06* and b) *GV08*. The resistance has been measured at a temperature of  $4\text{ K}$ .

having a width of  $100\text{ }\mu\text{m}$  and  $4\text{ }\mu\text{m}$  do not show scaling behaviour, this might again be attributed to an unevenly distributed redeposited material. Also for the BL quarter of sample *GV08* the  $4\text{ K}$  resistances as function of the inverse of the width of the contact seem to approach a straight line this despite the longer soft etch performed on this sample.

Resistance versus temperature investigations reveal that most of the devices on the BL and BR quarters of sample *GV06* present a resistance drop in correspondence of the  $YBa_2Cu_3O_7$  transition temperature, however when the temperature is further decreased the resistance of the contact increases showing in this way semiconducting behaviour fig. D.32a. The difference with fig. D.29a is that in this case the resistance of the contact decreases up to the transition temperature, then the semiconductive behaviour takes

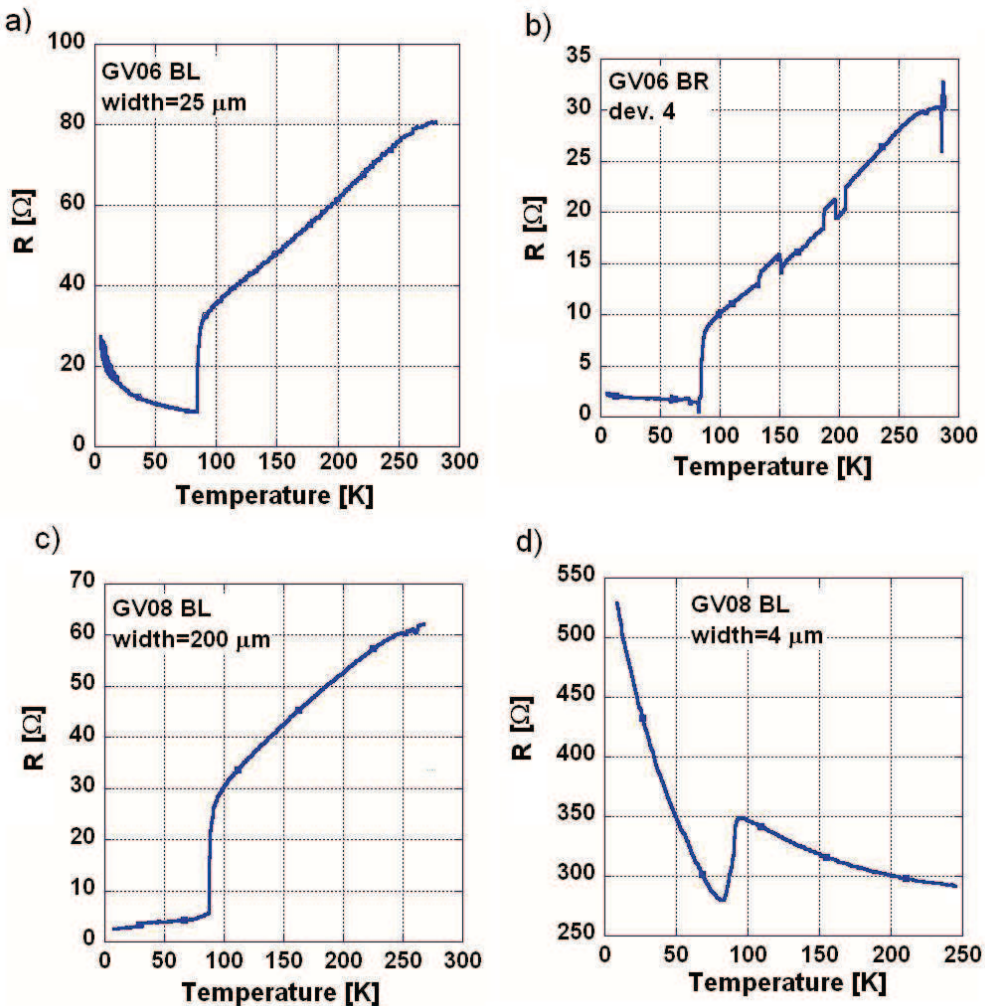


Figure D.32: Resistance versus temperature measurements for: a)  $Au/YBa_2Cu_3O_7$  ramp type contact belonging to the BL quarter of sample  $GV06$ , having a width equal to  $25 \mu\text{m}$  and a contact area of  $10.5 \mu\text{m}^2$ ; b)  $Au/YBa_2Cu_3O_7$  ramp type contact belonging to the BR quarter of sample  $GV06$ , having a width equal to  $10 \mu\text{m}$  and a contact area of  $4.2 \mu\text{m}^2$ ; c)  $Au/YBa_2Cu_3O_7$  ramp type contact belonging to the BL quarter of sample  $GV08$ , having a width equal to  $200 \mu\text{m}$  and a contact area of  $84 \mu\text{m}^2$ ; d)  $Au/YBa_2Cu_3O_7$  ramp type contact belonging to the BL quarter of sample  $GV08$ , having a width equal to  $4 \mu\text{m}$  and a contact area of  $1.68 \mu\text{m}^2$ .

place. Such low temperature behaviour might be due to a not perfect cleaning process, in fact after the ramp treatment some non uniform conduction channels might be opened through the device contact area improving in this way the  $4K$  RA product of these devices but the contact area is reduced in an unknown fashion. Not all the devices of the sample show scaling behaviour so unevenly redeposited material can contribute to the reduction of the contact area, furthermore the eventual presence of evenly distributed redeposited material might reduce the transparency of the contact.

It is important to highlight that the BR quarter of the sample *GV06* contains a device, labeled as device 4, which presents the lowest  $4K$  RA product between all the  $Au/YBa_2Cu_3O_7$  ramp type contacts fabricated at the University of Birmingham, such RA product is equal to  $8.4 \cdot 10^{-8} \Omega cm^2$ . This happens because the resistance of the contact does not increase with decreasing temperature after the  $YBa_2Cu_3O_7$  superconductive transition, fig. D.32b. The RA product of this device is in the same order of magnitude with the  $4K$  RA products reported in [111], it is also two orders of magnitude lower than the RA products of the devices belonging to the same quarter. The reason of such mismatch is unclear however the most likely hypothesis is the presence of less redeposited material on that area of the ramp, along with a successful cleaning process.

The idea of non uniform conduction channels on the ramp surfaces of the sample *GV06* led to the 10 minutes soft etching performed during the ramp treatment of sample *GV08*.

Current voltage measurements performed at the temperature of  $4K$  on the devices belonging to the BL quarter of sample *GV08* show a lower  $4K$

RA product than the equivalent devices of sample *GV06* tab. D.4.

Resistance versus temperature measurements on the devices of sample *GV08* show that for six of the eight devices belonging to the BL quarter the contact resistance does not increase with decreasing temperature after the  $YBa_2Cu_3O_7$  superconducting transition fig. D.32c, this explains why a lower  $4\text{ K}$  RA product has been measured.

The soft etch has been employed to remove damages caused by the argon ion beam milling during the fabrication of the ramp and during the hard etch. The measurements on the BL quarter of sample *GV08* seem to reveal that a continuous and longer soft etch is a more effective cleaning process than the pulsed soft etch procedure reported in sec. D.3.4, a long soft etch has been also employed in [118] and [130]. However one device of the BL quarter, fig. D.32d, and all the devices of the BR quarter of sample *GV08* show semiconducting behaviour, the  $4\text{ K}$  RA products of the devices belonging to the BR quarter of sample *GV08* are reported in tab. D.5, they are significantly higher than the  $4\text{ K}$  RA products of the same devices of sample *GV06*.

From the devices of the BL quarter of sample *GV08* it might be argued that a longer soft etch improves the  $4\text{ K}$  RA product, however from the devices of the BR quarter of sample *GV08* it might be stated that a longer soft etch increases the  $4\text{ K}$  RA products of the ramp type contacts.

The fabrication process of sample *GV08* has been repeated and sample *GV11* has been produced however in this case all the devices of the BL and of the BR quarters presented semiconductive behaviour with  $4\text{ K}$  RA products in the range  $10^{-3} - 10^{-5}\Omega\text{cm}^2$ .

All these measurements confirm poor control of the fabrication process of the  $Au/YBa_2Cu_3O_7$  ramp type contacts, in fact the repetition of the fabrication process used for sample *CS82* did not produce devices with a comparable  $4\text{ K}$  RA product. This fabrication process is similar to that one used in Twente where ramp type contacts with an RA product in the range  $10^{-7} - 10^{-8}\Omega\text{cm}^2$  have been obtained. The fabrication procedure adopted for the samples *GV06* and *GV08* produced three devices having the desired  $4\text{ K}$  RA product but its repetition did not produce comparable results.

The possible reasons for a poor  $Au/YBa_2Cu_3O_7$  interface, as already reported, are the presence of off-stoichiometric layers and redeposited material on the surface of the  $YBa_2Cu_3O_7$  ramp. The redeposited material seems to be the main issue related to the not reproducible fabrication process in fact the trajectories of the milled material are quite difficult to control. In Twente the in-situ argon ion cleaning process is performed along the film normal in order to minimize redeposited material [11] this is the reason which led to the introduction of the in-situ tiltable heater in our deposition chamber fig. 3.1. In this way a soft and a hard etch along the sample normal can be performed.

### Devices fabricated with the new heater

With the introduction of the new heater, as already reported in chap. D.3, a recalibration of the ablation parameters, necessary to reduce the roughness on the  $SrTiO_3/YBa_2Cu_3O_7$  bilayers, has been done. Private communication with Dr. Andreski [133] revealed that the deposition of the  $YBa_2Cu_3O_7$  interlayer in Twente is performed at a frequency of  $1\text{ Hz}$ , rather than the  $4\text{ Hz}$

value used during the growth of the base electrode. The lower pulse rate should give to the atomic species which arrive on the substrate a longer time for the crystal growth before the arrival of new clusters of atoms. Wördenweber [101], for  $YBa_2Cu_3O_7$  grown by pulsed laser deposition, reported a resident time  $\tau$  equal to 0.2 s. The resident time is defined as:

$$\tau = \frac{\lambda^2}{D_s} \quad (\text{D.32})$$

where  $\lambda$  is the adatom mean migration length on substrate and  $D_s$  is the surface diffusivity coefficient. When a pulse rate of 4 Hz is used, the time interval between two pulses is equal to 250 ms this value is bigger than  $\tau$ , so a reduction of the pulse rate should not produce any significant difference in the growth of the  $YBa_2Cu_3O_7$ . However a sample with an interlayer deposited at 1 Hz has been prepared in order to verify if the reduction of the pulse rate during deposition affects the properties of the  $Au/YBa_2Cu_3O_7$  ramp type contacts.

Two samples have been prepared with the new heater they have been labeled as *GV41* and *GV42*. The bilayers have been grown with the new heater ablation parameters reported in table D.1. The ramp cleaning process and heat treatment have been performed as described in sec. D.3.4. It is important to remark that also the  $YBa_2Cu_3O_7$  interlayer has been ablated at a temperature of 740°C and at a pulse rate of 4 Hz for sample *GV41* and of 1 Hz for the sample *GV42*. The hard and the soft etches have been run with the argon ion beam incident along the normal to the sample.

Fig. D.33a shows the resistance versus temperature measurement of a

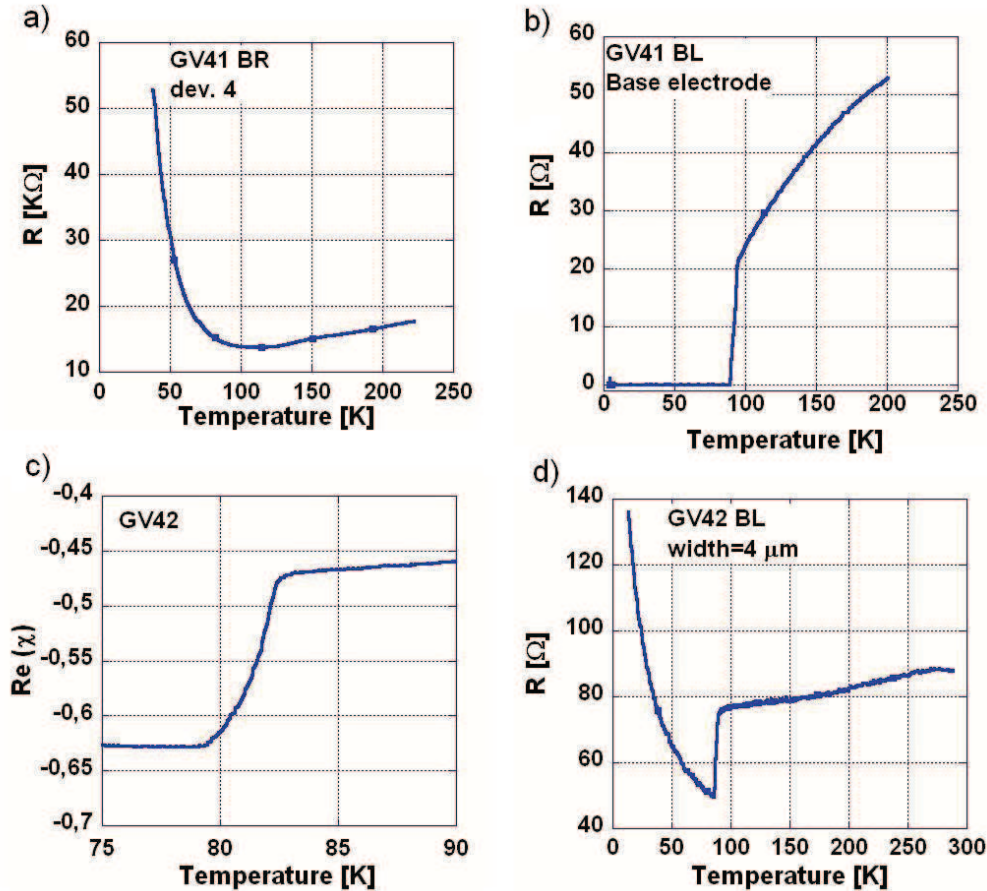


Figure D.33: a) Resistance versus temperature for a  $Au/YBa_2Cu_3O_7$  ramp type contact belonging to the BL quarter of sample GV41, having a width equal to  $10 \mu m$  and a contact area of  $4.2 \mu m^2$ ; b) Resistance versus temperature measurements of the  $YBa_2Cu_3O_7$  base electrode of the BL quarter of sample GV41; c) Susceptibility measurements of the  $SrTiO_3/YBa_2Cu_3O_7$  bilayer of sample GV42; d) Resistance versus temperature for a  $Au/YBa_2Cu_3O_7$  ramp type contact belonging to the BL quarter of sample GV42, having a width equal to  $4 \mu m$  and a contact area of  $1.68 \mu m^2$ .

$Au/YBa_2Cu_3O_7$  ramp type contact belonging to the BR quarter of sample GV41, semiconductive behaviour in this device and in all the devices belonging to the BL and BR quarters of this sample is observed, the measured  $4 K$

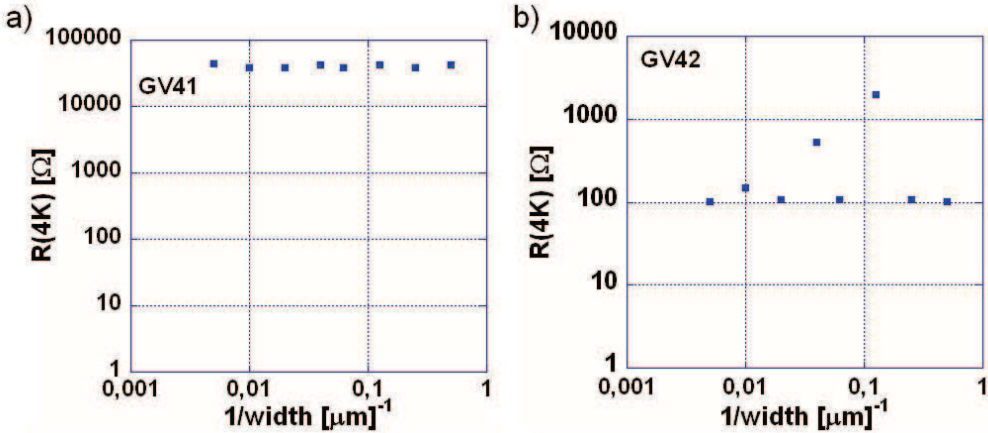


Figure D.34: Resistance of the  $Au/YBa_2Cu_3O_7$  ramp type contacts as function of the inverse of the contact width for the devices belonging to the BL quarter of sample a) *GV41* b) *GV42*.

RA product is in the range  $10^{-4} - 10^{-6} \Omega cm^2$ . The  $4 K$  resistance is larger than the values measured at room temperature. Fig. D.33b shows the resistance versus temperature measurement of the  $YBa_2Cu_3O_7$  base electrode belonging to the BL quarter of sample *GV41*, from this picture it is clear that the  $YBa_2Cu_3O_7$  undergoes the superconductive transition, so the high value of the  $4 K$  RA product is again attributed to an unsuccessful ramp cleaning process.

Fig. D.33 shows a susceptibility measurement after the  $SrTiO_3/YBa_2Cu_3O_7$  bilayer deposition for the sample *GV42*, also in this case the base electrode experiences the superconductive transition but the ramp type contacts of this sample show semiconductive behaviour fig. D.33d, with  $4 K$  RA products in the range of  $10^{-5} - 10^{-6} \Omega cm^2$ .

In both samples no scaling behaviour is observed for the devices belonging

to the respective BL quarters, fig. D.34, this indicates that the soft and the hard etches performed with a beam normal to the surface of the film do not reduce the amount of the redeposited material. In sec. D.3.4 AFM scans performed on the  $YBa_2Cu_3O_7$  ramp after the same ramp treatment, showed that some areas look smooth while other areas present a rough profile fig. D.28. This has been attributed to a lack of control on the redeposited material.

With the new heater, the ramp recovery process is performed by milling onto the ramp surface. As already mentioned in sec. D.3.3, different works [127, 128, 129] state that milling into the ramp should be avoided. Our investigations seem to support this statement however this is in contrast with the fabrication process adopted in Twente [10, 111]. Private communication with Dr. Andreski [133] revealed that at the moment the ramp junction fabrication process performed in Twente is run on sapphire substrate supplied by Theva which already have a  $CeO_2/YBa_2Cu_3O_7$  bilayer on their top. This can explain the different results obtained in Birmingham, however Smilde et al. [10, 111] reported the successfull fabrication of  $Nb/Au/YBa_2Cu_3O_7$  with the fabrication procedure which has been performed during this Phd but it is unknown if they experienced problems on the control of the fabrication process.

The introduction of the new heater necessary to perform the ramp cleaning process adopted in Twente did not produce the expected improvements, in particular resistance measurements as function of the inverse width of the contact do not show scaling behaviour. This means that the redeposited material problem has not been solved and actually the milling perpendicular to

the ramp surface seems to increase damage of the contact area as confirmed by the higher  $4\text{ K}$  RA products of the samples *GV41* and *GV42*.

The reasons of the semiconductive behaviour are again attributed to the redeposited material and to the presence of an amorphous off-stoichiometric layer at the  $\text{Au}/\text{YBa}_2\text{Cu}_3\text{O}_7$  interface.

#### D.4.2 Conclusions

The fabrication process and the electrical measurements on the  $\text{Au}/\text{YBa}_2\text{Cu}_3\text{O}_7$  ramp type contacts have been reported. The challenge associated with the fabrication of these devices is the recovery of the  $\text{YBa}_2\text{Cu}_3\text{O}_7$  crystal structure on the ramp surface. The ramp is fabricated by argon ion beam milling, this creates an amorphous and off-stoichiometric layer on the ramp area. The cleaning process necessary to recover the crystal structure of the ramp is not always effective as redeposited material can evenly or unevenly spread on the contact surface.

Two samples *GV06* and *GV08* contain  $\text{Au}/\text{YBa}_2\text{Cu}_3\text{O}_7$  ramp type contacts with  $4\text{ K}$  RA products similar to those ones reported in literature [10, 111], however the majority of the devices on these samples present  $4\text{ K}$  RA products which are one or two orders of magnitude larger. Devices showing semiconductive behaviour together with devices having a low  $4\text{ K}$  RA products are present on the same sample, showing difficulty in the control of the redeposited material produced during the hard and the soft etches.

The fabrication process adopted in Twente did not produce the expected results, in particular the cleaning of the ramp along the sample normal does

not solve the problem with the redeposited material, furthermore it can not be excluded that the process increases the damage of the  $YBa_2Cu_3O_7$  crystal structure as a consequence of the milling onto the ramp area.

Our investigations show that the lowest RA products have been obtained with a cleaning process performed at  $200^\circ C$  with an argon ion beam parallel to the ramp surface. Respect to room temperature the sticking coefficient of the redeposited material is reduced when the temperature is set at  $200^\circ C$  furthermore milling with a beam parallel to the ramp surface reduces the damages on the  $YBa_2Cu_3O_7$ . A 10 minutes soft etch seems to be more effective than the pulse cleaning adopted in Twente, however the device showing the lowest  $4 K$  RA product has been obtained with a pulse cleaning.

RA products similar to the values reported in literature have been obtained however the fabrication process is difficult to control and it is not always reproducible as testified by samples prepared with equal fabrication process and showing different behaviour, this inconsistency is attributed to the lack of control on the redeposited materials which together with the damages produced by the milling reduce the transparency of the contact.

## Appendix E

# Parallel plate capacitors containing $LaYbO_3$ as dielectric layer

Recently, interlanthanides perovskites such as  $LaLuO_3$  have been investigated [136] as potential candidates to replace  $SiO_2$  as a high-k gate dielectric because of their low leakage current and suitability to be deposited by several thin-film fabrication techniques including pulsed laser deposition [137, 138].

A. Feteira [139] prepared and investigated the crystal structure and the dielectric properties of  $LaYbO_3$  ceramics [140]. These  $LaYbO_3$  ceramic targets have been used to fabricate  $SrRuO_3/LaYbO_3/SrRuO_3$  capacitive structures on (001) oriented  $SrTiO_3$  substrate by using a fabrication process similar to that one discussed in sec. 4.2.

For the  $SrRuO_3$ , the pulsed laser deposition parameters reported in tab. 4.1 have been used. The  $LaYbO_3$  layer has been grown at a temperature of

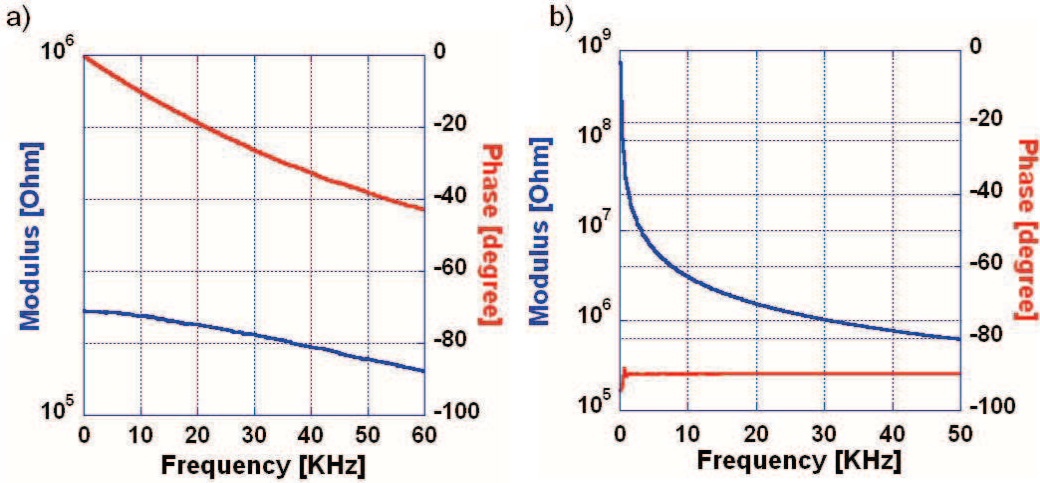


Figure E.1: Impedance measurement of a: a)  $205\ \mu m \times 30\ \mu m$   $SrRuO_3(100nm)/LaYbO_3(300nm)/SrRuO_3(150nm)$  parallel plate capacitor grown on (001) oriented  $SrTiO_3$  substrate. The  $LaYbO_3$  has been grown at  $780^\circ C$  at a pressure of  $40\ Pa\ O_2$ ; b)  $205\ \mu m \times 30\ \mu m$   $SrRuO_3(100nm)/LaYbO_3(580nm)/SrRuO_3(150nm)$  parallel plate capacitor grown on (001) oriented  $SrTiO_3$  substrate. The  $LaYbO_3$  has been grown at  $780^\circ C$  at a pressure of  $0.40\ Pa\ O_2$ .

$780^\circ C$  in oxygen flow. When the  $LaYbO_3$  is grown at a pressure of  $40\ Pa$ , the fabricated capacitive structure present resistive losses as can be seen by the phase of the impedance of one of these capacitors, fig. E.1a. The full capacitive behaviour is recovered for deposition pressures equal to  $0.40\ Pa$  fig. E.1b. This is in agreement with what is reported in chap. 7 for the  $BaTiO_3$  capacitive structures.

Two different procedures have been followed for the fabrication of the  $SrRuO_3/LaYbO_3/SrRuO_3$  capacitors. For the sample labeled as *GV02(D)* first the  $SrRuO_3$  bottom electrode layer is grown and patterned, then the  $SrRuO_3/LaYbO_3$  bi-layer is deposited, the top electrode geometry is defined and finally some windows through the  $LaYbO_3$  layer are opened to

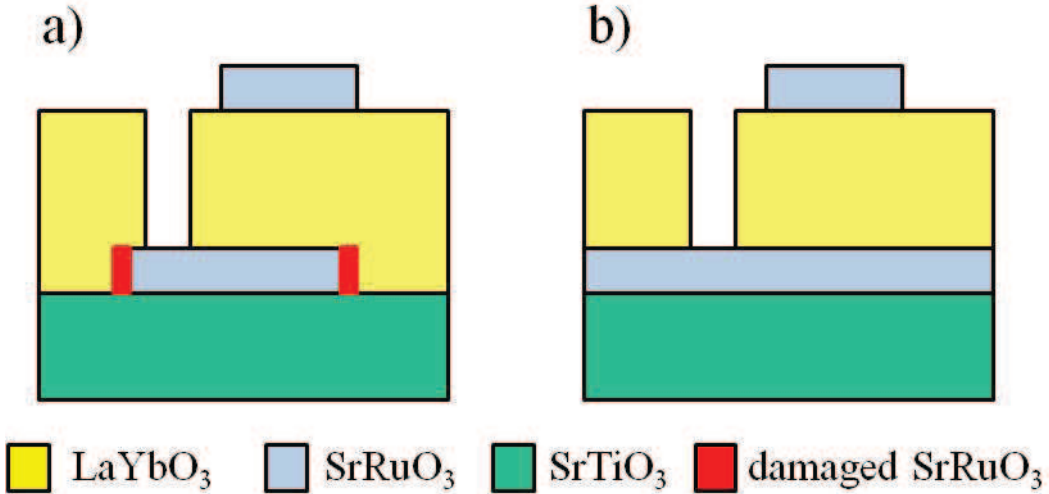


Figure E.2: a) Sideview of a device belonging to the sample *GV02(D)*.  
b) Sideview of a device belonging to the sample *GV03(D)*.

contact the bottom electrode. For the sample labeled as *GV03(D)* the *SrRuO<sub>3</sub>/LaYbO<sub>3</sub>/SrRuO<sub>3</sub>* tri-layer is grown *in situ*, then the top electrode is defined and finally the contact windows are opened through the *LaYbO<sub>3</sub>* film. The sideview of a device belonging to the sample *GV02(D)* is sketched in fig. E.2a while the sideview of a device of the sample *GV03(D)* is sketched in fig. E.2b.

Impedance measurements on the devices of the samples *GV02(D)* and *GV03(D)* indicates good capacitive behaviour as shown by fig. E.2b with constant capacitive values all over the measured frequency range (40 Hz – 50 KHz). The values of the dielectric constant for the grown *LaYbO<sub>3</sub>* films are higher than the value of the *LaYbO<sub>3</sub>* target which is equal to 26 [140]. Fig. E.3 reports the dielectric constant of two devices, one belonging to the sample *GV02(D)* and the other belonging to the sample *GV03(D)*. The open

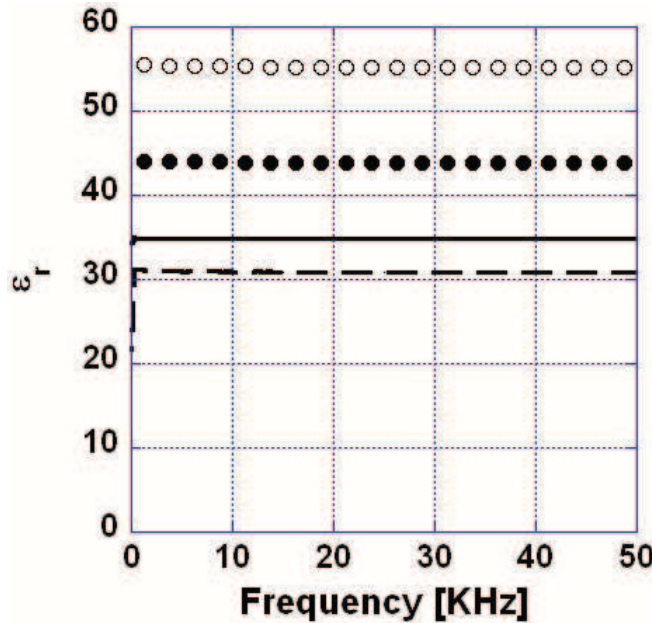


Figure E.3: Dielectric constants as function of frequency for  $SrRuO_3/LaYbO_3/SrRuO_3$  plate capacitors. The open circles ( $\circ\circ$ ), the full circles ( $\bullet\bullet$ ) and the dashed line (—) show the dielectric constant of a capacitor belonging to the sample  $GV02(D)$  after fabrication, 8 hours and 22 hours of annealing at  $500^\circ C$  in oxygen respectively. This capacitor has an area of  $6150 \mu m^2$  and a  $LaYbO_3$  layer which is  $583 nm$  thick. The continuous line (—) shows the dielectric constant of a capacitor belonging to the sample  $GV03(D)$ , this device has an area of  $49350 \mu m^2$  and a  $LaYbO_3$  layer which is  $567 nm$  thick. Sample  $GV03(D)$  has not been annealed.

circles ( $\circ\circ$ ) represent the dielectric constant of the  $LaYbO_3$  layer belonging to a capacitive structure integrated on the sample  $GV02(D)$ , the measured value is around 55 and it is twice the value measured in bulk material. The continuous line is the dielectric constant of the  $LaYbO_3$  layer of a capacitor belonging to the sample  $GV03(D)$  in this case the dielectric constant is around 35 this value is 35% higher than that one measured in bulk material.

The difference between the two samples consists in the patterning by con-

tact photolithography and argon ion beam milling of the bottom electrodes of sample *GV02(D)*. At the edges of the bottom electrodes of this sample the *SrRuO<sub>3</sub>* might be damaged as effect of the argon ion bombardment fig. E.2a. The damaged area is not a good seed layer for the growth of the *LaYbO<sub>3</sub>* film, this is believed to affect the value of the dielectric constant.

Investigation on the *SrTiO<sub>3</sub>* dielectric constant in *YBa<sub>2</sub>Cu<sub>3</sub>O<sub>7</sub>/SrTiO<sub>3</sub>/YBa<sub>2</sub>Cu<sub>3</sub>O<sub>7</sub>* capacitive structures where the *YBa<sub>2</sub>Cu<sub>3</sub>O<sub>7</sub>* bottom electrode has been patterned by contact photolithography and argon ion beam milling, revealed a *SrTiO<sub>3</sub>* dielectric constant higher than that one reported for bulk materials [141]. This behaviour has been attributed to the presence of defects and to the island growth of the *SrTiO<sub>3</sub>* film which lead to space charge polarization in the dielectric layer and results in a high dielectric constant [141].

To repair the eventual defects present at the *LaYbO<sub>3</sub>-SrRuO<sub>3</sub>* bottom electrode interface, sample *GV02(D)* has been annealed in oxygen environment at 500°C. After 8 hours annealing the dielectric constant was reduced to 44 (fig. E.3 full circle line) while after 22 hours annealing its value was around 31 (fig. E.3 dashed line). It is believed that the annealing recrystallize the damaged regions in the tri-layer stack and the dielectric constant approaches that one of the bulk material.

To support this idea X-ray diffraction measurements on the fabricated structures have been run by D. Woodward [142] at the University of Warwick. Fig. E.4 reports the experimental X-ray profiles of two *SrRuO<sub>3</sub>/LaYbO<sub>3</sub>/SrRuO<sub>3</sub>* stacks where the bottom *SrRuO<sub>3</sub>* layer has been patterned by contact photolithography and argon ion beam milling. Fig.

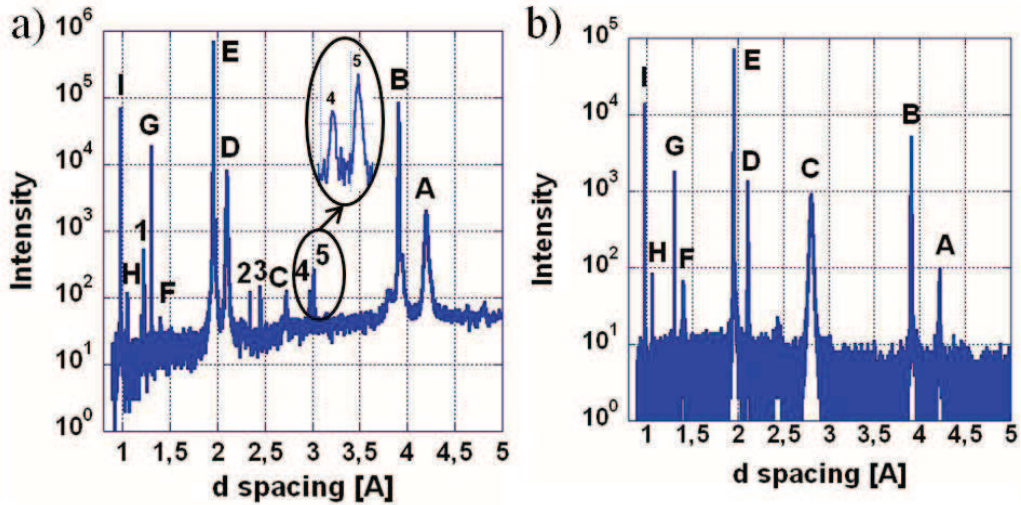


Figure E.4: Experimental X-ray diffraction profile for  $SrRuO_3/LaYbO_3/SrRuO_3$  stack where the bottom  $SrRuO_3$  layer has been patterned by contact photolithography and argon ion beam milling. a) Sample not annealed. b) Sample annealed at  $500^\circ C$  in oxygen flow for 22 hours.

E.4a shows the X-ray profile of a sample which has not been annealed, instead fig. E.4b reports the profile of a sample which has been annealed for 22 hours at  $500^\circ C$  in oxygen.

The peaks labeled with the letters are present before and after annealing while the peaks labeled with the numbers are only present before annealing. On both samples peaks A, D and H indicates epitaxially (001) oriented  $LaYbO_3$  on (001)  $SrRuO_3$  and  $SrTiO_3$  substrate, see tab. E.1.

The  $LaYbO_3$  has an orthorhombic crystal structure with  $a = 5.843 \text{ \AA}$ ,  $b = 6.033 \text{ \AA}$  and  $c = 8.432 \text{ \AA}$ . The  $SrRuO_3$  is treated as a pseudocubic perovskite with lattice constant  $a = 3.93 \text{ \AA}$ .

In the sample which has not been annealed the peaks 1, 2, 3, 4 and 5

<i>Peak label</i>	<i>Material and reflection</i>
A	(002) <i>LaYbO<sub>3</sub></i>
B	(001) <i>SrTiO<sub>3</sub></i> + (001) <i>SrRuO<sub>3</sub></i>
C	(110) <i>SrRuO<sub>3</sub></i>
D	(004) <i>LaYbO<sub>3</sub></i>
E	(002) <i>SrTiO<sub>3</sub></i> + (002) <i>SrRuO<sub>3</sub></i>
F	(220) <i>SrRuO<sub>3</sub></i>
G	(003) <i>SrTiO<sub>3</sub></i>
H	(008) <i>LaYbO<sub>3</sub></i>
I	(004) <i>SrTiO<sub>3</sub></i>
1	(044) <i>LaYbO<sub>3</sub></i>
2	(202) <i>LaYbO<sub>3</sub></i>
3	(022) <i>LaYbO<sub>3</sub></i>
4	(112) <i>LaYBO<sub>3</sub></i>
5	(020) <i>LaYBO<sub>3</sub></i>

Table E.1: Assignment of the diffraction peaks reported in fig. E.4.

show the presence of misoriented grains in the *LaYbO<sub>3</sub>*. We think that they grow on the damaged bottom electrode regions, even if the damaged regions are believed to partially recrystallize during the *SrRuO<sub>3</sub>/LaYbO<sub>3</sub>* bilayer deposition as showed by the peaks labeled as C and F in fig. E.4a and tab. E.1.

After the annealing the misoriented peaks of the *LaYbO<sub>3</sub>* film disappear and the (110) and (220) reflections of the *SrRuO<sub>3</sub>* becomes stronger. This indicates recrystallization in the stack, such recrystallization is believed to repair the damaged regions of the film and the dielectric constant of the *LaYbO<sub>3</sub>* layer approaches that one of the of the bulk material.

The values of the dielectric constant of the sample *GV03(D)* and of the sample *GV02(D)* after the annealing are comprised between 30 and 36. These

values are still higher than the dielectric constant of the bulk, and they might be attributed to an higher permittivity along the (001) axis as Schubert et al. [136] suggested in the case of *LaLuO<sub>3</sub>* films. However the investigation of these structures has not been completed and it will be further developed in the next future.

## **Appendix F**

### **Copies of the publications**

## New Multilayer Architectures for Piezoelectric BaTiO<sub>3</sub> Cantilever Systems

Giuseppe Vasta<sup>1</sup>, Timothy J. Jackson<sup>1</sup>, James Bowen<sup>2</sup> and Edward J. Tarte<sup>1</sup>

<sup>1</sup>School of Electronic Electrical and Computer Engineering, University of Birmingham, B15 2TT Birmingham, United Kingdom

<sup>2</sup>Department of Chemical Engineering, University of Birmingham, B15 2TT Birmingham, United Kingdom

### ABSTRACT

The fabrication and characterization of released cantilevers in new multilayer thin films architectures is reported. In contrast to previous works, the cantilevers are produced without etching of the substrate and are based on lead free piezoelectric materials. The three architectures are: SrRuO<sub>3</sub>/BaTiO<sub>3</sub>/MgO/SrTiO<sub>3</sub>/YBa<sub>2</sub>Cu<sub>3</sub>O<sub>7</sub>, SrRuO<sub>3</sub>/BaTiO<sub>3</sub>/SrRuO<sub>3</sub>/YBa<sub>2</sub>Cu<sub>3</sub>O<sub>7</sub> and SrRuO<sub>3</sub>/BaTiO<sub>3</sub>/SrRuO<sub>3</sub>/SrTiO<sub>3</sub>/YBa<sub>2</sub>Cu<sub>3</sub>O<sub>7</sub>. It is shown that the different architectures allow a choice of the orientation of the polar axis in piezoelectric layers, in plane ( $d_{33}$  mode) or out of plane ( $d_{31}$  mode). Both configurations may be utilized in piezoelectric energy harvesting devices. Released cantilevers with the above layer sequences have been produced with lengths ranging from, 100  $\mu\text{m}$  to 250  $\mu\text{m}$ . The residual stress after the release of the cantilevers produces an upwards bending, the distance between the cantilever tips and the substrate varying between 20  $\mu\text{m}$  and 45  $\mu\text{m}$ . This distance would allow the sufficient vibration amplitude to enable the cantilevers to be used as micro-generators. Measurements of Young Modulus of the cantilevers and of polarization hysteresis loop are reported.

### INTRODUCTION

Energy scavenging from the surrounding environment represents the key towards the building of autonomous micro-systems. Solar power is the most powerful ambient energy source but not always the most convenient. Another interesting way to harvest energy from the environment is represented by the conversion of the parasitic mechanical vibrations into electrical energy.

Piezoelectric materials are the perfect candidate for such conversion because they can efficiently convert mechanical strain into the separation of electrical charge and hence potential difference [1]. Furthermore the simplicity of the piezoelectric micro-generator is particularly attractive for use in MEMS [2].

Studies on energy harvesting devices based on Pb(Zr,Ti)O<sub>3</sub> have been widely performed [1,3,4]. Lead-free piezoelectric materials are increasingly of interest. This paper describes the fabrication and characterization of energy harvesting devices based on thin-film architectures using BaTiO<sub>3</sub> as piezoelectric layers. The properties of BaTiO<sub>3</sub> are well known, making it ideal for exploration of new systems which could then be modified to exploit more recently discovered, higher performance materials. The three multilayer systems investigated were:

SrRuO<sub>3</sub>/BaTiO<sub>3</sub>/MgO/SrTiO<sub>3</sub>/YBa<sub>2</sub>Cu<sub>3</sub>O<sub>7</sub>, SrRuO<sub>3</sub>/BaTiO<sub>3</sub>/SrRuO<sub>3</sub>/YBa<sub>2</sub>Cu<sub>3</sub>O<sub>7</sub> and SrRuO<sub>3</sub>/BaTiO<sub>3</sub>/SrRuO<sub>3</sub>/SrTiO<sub>3</sub>/YBa<sub>2</sub>Cu<sub>3</sub>O<sub>7</sub>. In these multi-layers, SrRuO<sub>3</sub> acts as electrode

layer and the  $\text{YBa}_2\text{Cu}_3\text{O}_7$  is the sacrificial layer used to obtain suspended structures through undercutting.

## EXPERIMENT

The multi-layer films were grown on (100) oriented  $\text{SrTiO}_3$  substrates by Pulsed Laser Deposition using a KrF excimer laser with a wavelength of 248 nm. The distance between the material target and the substrate was set to 5.7 cm. A 4 Hz pulse repetition rate was used, with the laser beam focused to a spot size of  $2.4 \text{ mm}^2$  on the target, providing a fluence on target of  $3.4 \text{ J/cm}^2$ . The films were grown in an oxygen flow producing pressures of 0.15 Torr  $\text{O}_2$  for the  $\text{YBa}_2\text{Cu}_3\text{O}_7$  deposition, 0.2 Torr  $\text{O}_2$  for the  $\text{SrTiO}_3$  and  $\text{MgO}$  depositions, 0.3 Torr  $\text{O}_2$  for the  $\text{SrRuO}_3$  deposition, and either 0.15 and 0.06 Torr  $\text{O}_2$  for the  $\text{BaTiO}_3$  deposition.

The  $\text{YBa}_2\text{Cu}_3\text{O}_7$  deposition was performed at the relatively low temperature of  $740^\circ\text{C}$  in order to avoid outgrowths which may form at higher deposition temperatures [5]. The  $\text{SrRuO}_3$  and the  $\text{BaTiO}_3$  were deposited at a temperature of  $780^\circ\text{C}$ , for the other two layers a deposition temperature of  $740^\circ\text{C}$  was used. After the multi-layer deposition the sample was cooled down in 900mbar of static  $\text{O}_2$  environment. There were dwells of 15 minutes at  $600^\circ\text{C}$  and 30 minutes at  $450^\circ\text{C}$  during cooling to fully oxygenate the  $\text{YBa}_2\text{Cu}_3\text{O}_7$  layer [6].

The films were then patterned by contact photolithography and argon ion beam milling, using a Karl Suss mask aligner and an Oxford Applied Research IM150 Ion milling system respectively. Photoresist was used to protect regions of the sample which would become the cantilevers. Milling through to the substrate through windows developed in the photoresist was used to define the cantilever geometry. Secondary ion mass spectrometry was used to monitor the progress of the milling. Then the photoresist was removed and the cantilevers were released by undercutting the  $\text{YBa}_2\text{Cu}_3\text{O}_7$  film. The undercut was achieved by etching with 0.1%  $\text{HNO}_3$ . The sample was then rinsed in distilled water and dried by using critical point drying. The critical point drying was necessary to avoid the breakage of the suspended structures due to stiction [7]. The uncovered  $\text{YBa}_2\text{Cu}_3\text{O}_7$  is milled rather than wet etched in order to obtain a well defined cantilever geometry, figure 1.

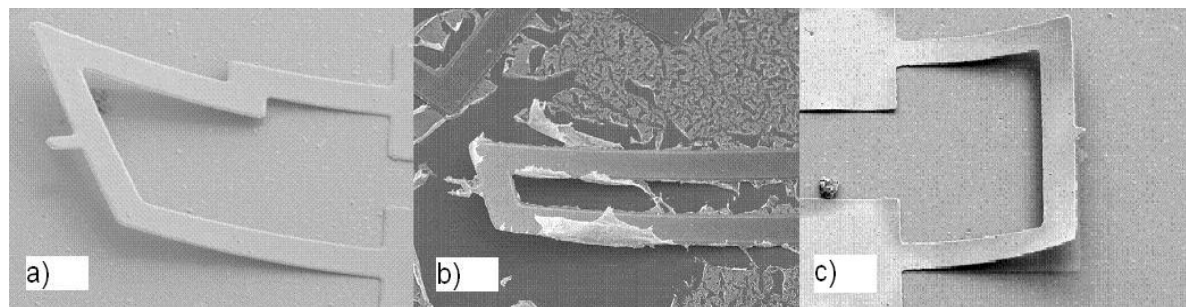


**Figure 1.** a)  $\text{BaTiO}_3(120 \text{ nm})/\text{MgO}(50 \text{ nm})/\text{SrTiO}_3(500 \text{ nm})$ ,  $170 \mu\text{m}$  long u-shape cantilever grown on  $400 \text{ nm}$   $\text{YBa}_2\text{Cu}_3\text{O}_7$ . The cantilever was defined by ion beam milling as described in the text.

- b) BaTiO<sub>3</sub>(120 nm)/SrTiO<sub>3</sub>(500 nm), 300 μm long u-shape cantilever grown on 400 nm YBa<sub>2</sub>Cu<sub>3</sub>O<sub>7</sub>. The YBa<sub>2</sub>Cu<sub>3</sub>O<sub>7</sub> layer in this case was removed by wet etching, rather than ion-beam milling, which has produced a much less well defined cantilever compared with ion milling.  
c) SrRuO<sub>3</sub>(50 nm)/BaTiO<sub>3</sub>(100 nm)/SrRuO<sub>3</sub>(350 nm) 128 μm long u-shape cantilever grown on 400 nm YBa<sub>2</sub>Cu<sub>3</sub>O<sub>7</sub>. The cantilever was defined by ion beam milling as described in the text.

The structure of the films was assessed by X-ray diffraction using a Siemens D5000 X-ray diffractometer. The Young's Modulus was measured by nanoindentation using a NanoTest (Micro Materials, UK) employing a diamond-coated Berkovich indenter. Indentations were performed at depths of 20 nm and greater through the multilayer.

Capacitance and hysteresis loop measurements were performed on SrRuO<sub>3</sub>(100 nm)/BaTiO<sub>3</sub>(400 nm)/SrRuO<sub>3</sub>(150 nm) parallel-plate capacitors. Capacitors with areas of 95 μm x 30 μm, 105 μm x 30 μm, 205 μm x 30 μm and 215 μm x 30 μm were measured. The capacitance measurements were made using an Agilent 4294A Precision Impedance Analyzer, with a source voltage of 1 V over the frequency range of 50 Hz-50 kHz.

Hysteresis loops have been measured by using a custom made Sawyer and Tower circuit. Sinewave voltages with peak to peak amplitude up to 50 V and frequency of 20 kHz have been applied.

## DISCUSSION

BaTiO<sub>3</sub> films sandwiched between two SrRuO<sub>3</sub> electrodes showed resistive behavior when grown in 0.15 Torr O<sub>2</sub>. They showed capacitive behavior when the BaTiO<sub>3</sub> is grown in 0.06 Torr O<sub>2</sub>. The measured capacitance were in the range 100 pF-200 pF.

Resistance measurements were performed on a 100μm long, 10μm wide and 0.12μm high SrRuO<sub>3</sub> line deposited on (100) oriented SrTiO<sub>3</sub> substrate to check that the deposited films have the expected conductive behavior. The room temperature resistivity was 284 μΩcm and at 4 K the resistivity was 31 μΩcm. These values are in agreement with those reported elsewhere [8]. Table I shows the lattice parameters of the deposited BaTiO<sub>3</sub>, in different layer sequences. The BaTiO<sub>3</sub> film was oriented with the polar axis parallel to the surface of the film when grown on MgO. The measured polar lattice parameter of 4.002 Å appears smaller than the bulk value because it is an average value: there are two possible orthogonal orientations when the polar axis is in the plane of the substrate; a non polar axis must also lie in plane. This configuration fits the d<sub>33</sub> energy harvesting mode.

**Table I.** BaTiO<sub>3</sub> film lattice parameters on different layer sequences. Bulk parameters are provided for comparison.

Material [top down layer sequence]	In plane a axis measured [Å] (bulk [Å])	In place b axis measured [Å] (bulk [Å])	Out of plane axis measured [Å] (bulk [Å])
BaTiO <sub>3</sub> [SrRuO <sub>3</sub> (50nm)/BaTiO <sub>3</sub> (100nm)/ SrRuO <sub>3</sub> (350nm)/YBa <sub>2</sub> Cu <sub>3</sub> O <sub>7</sub> (400nm)]	3.951 (3.992)	3.951 (3.992)	4.069 (4.036)
BaTiO <sub>3</sub>	4.002	4.002	3.997

[BaTiO <sub>3</sub> (500nm)/MgO(60nm)/YBa <sub>2</sub> Cu <sub>3</sub> O <sub>7</sub> (400nm)]	(3.992)	(3.992)	(4.036)
BaTiO <sub>3</sub> [BaTiO <sub>3</sub> (126nm)/SrTiO <sub>3</sub> (500nm)/YBa <sub>2</sub> Cu <sub>3</sub> O <sub>7</sub> (400nm)]	3.996 (3.992)	3.996 (3.992)	4.015 (4.036)

When the BaTiO<sub>3</sub> film was grown on a SrRuO<sub>3</sub> or on a SrTiO<sub>3</sub> layer the polar axis was perpendicular to the surface of the film, this configuration fits the d<sub>31</sub> energy harvesting mode. The polar axis of a 100nm thick BaTiO<sub>3</sub> film sandwiched between two SrRuO<sub>3</sub> layers showed an elongation equal to the 0.83% of its length in bulk material, in agreement with observations [9]. In the grown multi-layers the SrTiO<sub>3</sub> film functions as a buffer layer introduced to improve the interface quality between the YBa<sub>2</sub>Cu<sub>3</sub>O<sub>7</sub> and the MgO film. Fig.2 shows secondary ion mass spectroscopy (SIMS) data during the milling of two samples, one with the SrTiO<sub>3</sub> buffer layer and one without. The SrTiO<sub>3</sub>/YBa<sub>2</sub>Cu<sub>3</sub>O<sub>7</sub> interface (figure 2a) is better defined than the MgO/YBa<sub>2</sub>Cu<sub>3</sub>O<sub>7</sub> interface (figure 2b) with a sharp transition between layers evidenced by the SIMS signal. Without a well defined interface was difficult to undercut the YBa<sub>2</sub>Cu<sub>3</sub>O<sub>7</sub> and suspend the beam. The buffer layer can also be introduced between the SrRuO<sub>3</sub> and the YBa<sub>2</sub>Cu<sub>3</sub>O<sub>7</sub> layer in the SrRuO<sub>3</sub>/BaTiO<sub>3</sub>/SrRuO<sub>3</sub>/YBa<sub>2</sub>Cu<sub>3</sub>O<sub>7</sub> structures, in this case the presence of the buffer layer allowed 98% of the structures to be suspended, without buffer layer the yield was reduced to 70%.

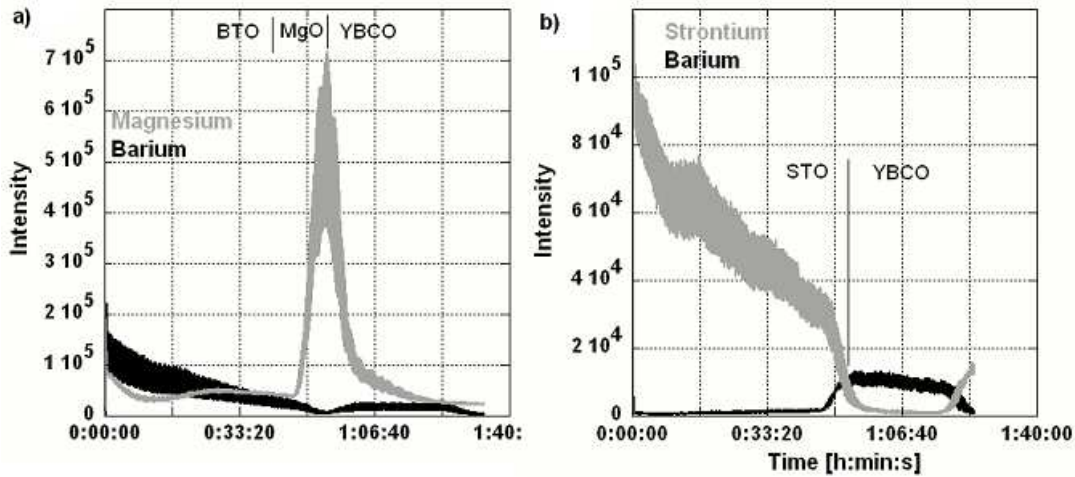


**Figure 2.** Secondary Ion beam spectroscopy of a milling step. a) BaTiO<sub>3</sub>/MgO/YBa<sub>2</sub>Cu<sub>3</sub>O<sub>7</sub> tri-layer. b) SrTiO<sub>3</sub>/YBa<sub>2</sub>Cu<sub>3</sub>O<sub>7</sub> bilayer.

Cantilevers with different layer sequences and a length comprised between 100 µm and 250 µm have been produced, figure 1. Due to the residual stress the cantilever bends upwards after release. Distances in the range 20 µm-45 µm between the substrate and the cantilever free edges were measured. In contrast to the previous works [1,3,4], such a distance can allow the use of these structures as inertial energy harvesting devices without the need to etch the substrate. Table II reports the Young Modulus of the deposited films in different layer combinations. The values reported in the table represent the Young Modulus values averaged over the film thickness over a minimum of 25 measurements. The BaTiO<sub>3</sub> showed a higher Young Modulus

when grown on Mgo, with the polar axis in plane, than when grown on SrRuO<sub>3</sub> and SrTiO<sub>3</sub>, with the polar axis out of plane.

Figure 3 shows the ferroelectric hysteresis behavior of a SrRuO<sub>3</sub>(100 nm)/BaTiO<sub>3</sub>(400 nm)/SrRuO<sub>3</sub>(150 nm) parallel-plate capacitor. The capacitors show a residual polarization between 2.5  $\mu\text{C}/\text{cm}^2$  and 5.35  $\mu\text{C}/\text{cm}^2$ .

**Table II.** Young Modulus of the grown films in different layer sequences.

Top down layer sequence	Material	Young Modulus [GPa]
BaTiO <sub>3</sub> (200 nm)/SrRuO <sub>3</sub> (200 nm)/YBa <sub>2</sub> Cu <sub>3</sub> O <sub>7</sub> (100 nm)	BaTiO <sub>3</sub>	163
	SrRuO <sub>3</sub>	190
BaTiO <sub>3</sub> (200 nm)/MgO(400 nm)	BaTiO <sub>3</sub>	229
	MgO	234
BaTiO <sub>3</sub> (128nm)	BaTiO <sub>3</sub>	134
BaTiO <sub>3</sub> (126 nm)/SrTiO <sub>3</sub> (500 nm)/YBa <sub>2</sub> Cu <sub>3</sub> O <sub>7</sub> (400 nm)	SrTiO <sub>3</sub>	130
	YBa <sub>2</sub> Cu <sub>3</sub> O <sub>7</sub>	147
MgO(150 nm)/YBa <sub>2</sub> Cu <sub>3</sub> O <sub>7</sub> (150 nm)	MgO	231

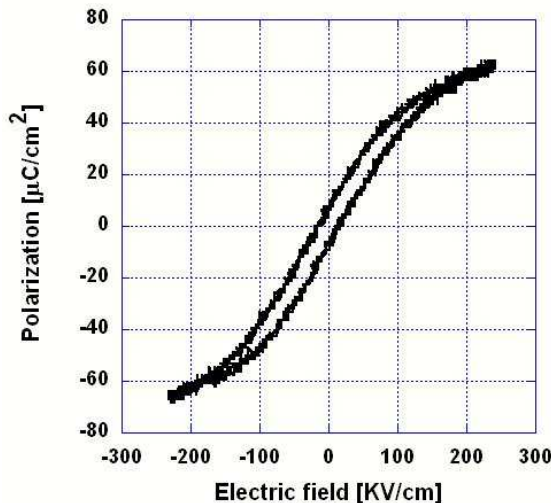


**Figure 3.** Hysteresis loop measurement on a SrRuO<sub>3</sub>(100 nm)/BaTiO<sub>3</sub>(400 nm)/SrRuO<sub>3</sub>(150 nm) parallel plate capacitor of area 95  $\mu\text{m}$  x 30  $\mu\text{m}$ .

## CONCLUSIONS

In energy harvesting applications, piezoelectric cantilevers may use the polar axis in plane (the d<sub>33</sub> mode) or out of plane (the d<sub>31</sub> mode) although the d<sub>33</sub> mode is preferred [3]. Using X-ray diffraction we have found that both modes can be achieved using the multi-layer sequences reported. In particular the SrRuO<sub>3</sub>/BaTiO<sub>3</sub>/MgO/SrTiO<sub>3</sub>/YBa<sub>2</sub>Cu<sub>3</sub>O<sub>7</sub> structure fits the d<sub>33</sub> energy harvesting mode, the SrRuO<sub>3</sub>/BaTiO<sub>3</sub>/SrRuO<sub>3</sub>/YBa<sub>2</sub>Cu<sub>3</sub>O<sub>7</sub> and the

$\text{SrRuO}_3/\text{BaTiO}_3/\text{SrRuO}_3/\text{SrTiO}_3/\text{YBa}_2\text{Cu}_3\text{O}_7$  stacks fit the  $d_{31}$  energy harvesting mode. Cantilever release distances in the range 20-45  $\mu\text{m}$  have been achieved by etching of a sacrificial layer within the multilayer. Release is achieved without the need to etch the substrate; this is different from previous work [1,3,4] where the substrates have always been etched to release the cantilevers.

In the deposited films the high values for the Young's Modulus do not allow to the residual stress to damage the cantilevers after their release. The upward bend is not excessive, and it is beneficial to increase the vibration amplitude.

## ACKNOWLEDGMENTS

The Nanoindenter used in this research was obtained, through Birmingham Science City: Innovative Uses for Advanced Materials in the Modern World (West Midlands Centre for Advanced Materials Project 2), with support from Advantage West Midlands (AWM) and part funded by the European Regional Development Fund (ERDF). The research was funded by the UK EPSRC under grant number EP/E026494/1.

## REFERENCES

1. W. J. Choi, Y. Jeon, J. H. Jeong, R. Sood and S. G. Kim, *J. Electroceram.* **17**, 543-548 (2006).
2. F. Lu, H. P. Lee, and S. P. Lim, *Smart. Matter. Struct.* **13**, 57-63 (2004).
3. Y. B. Jeon, R. Sood, J. H. Jeong, S. G. Kim, *Sensors and Actuators A* **122**, 16-22 (2005).
4. Q. Q. Zhang, S. J. Gross, S. Tadigadapa, T. N. Jackson, F. T. Djuth, S. Trolier-McKinstry *Sensors and Actuators A* **105**, 91-97 (2003).
5. H. Sato, F. J. G. Roesthuis, A. H. Sonnenberg, A. J. H. M. Rijnders, H. Rogalla and D. H. A. Blank, *Supercond. Sci. Technol.* **13**, 522-526 (2000).
6. H. J. H. Smilde, H. Hilgenkamp, G. J. Gerritsma, D. H. A. Blank and H. Rogalla, *IEEE Transactions on Applied Superconductivity* **11**, 501-504 (2001).
7. L. Pellegrino, M. Biasotti, E. Bellingeri, C. Bernini, A. S. Siri and D. Marre` , *Adv. Matter.* **21**, 2377-2381 (2009).
8. X. D. Wu, S. R. Foltyn, R. C. Dye, Y. Coulter and R. E. Muenchausen, *Appl. Phys. Lett.* **62**, 2434-2436 (1993).
9. K. J. Choi, M. Biegalski, Y. L. Li, A. Sharan, J. Schubert, R. Uecker, P. Reiche, Y. B. Chen X. Q. Pan, V. Gopalan, L. Q. Chen, D. G. Schlom, C. B. Eom, *Science* **306**, 1005-1009 (2004).

# Residual stress analysis of all perovskite oxide cantilevers

Giuseppe Vasta · Timothy J. Jackson ·  
Andreas Frommhold · James Bowen ·  
Edward J. Tarte

Received: 4 May 2011 / Accepted: 28 October 2011  
© The Author(s) 2011. This article is published with open access at Springerlink.com

**Abstract** We have used a method to experimentally determine the curvature of thin film multilayers in all oxide cantilevers. This method is applicable for large deflections and enables the radius of curvature of the beam, at a certain distance from the anchor, to be determined accurately. The deflections of the suspended beams are measured at different distances from the anchor point using SEM images and the expression of the deflection curve is calculated for each cantilever. With this expression it is possible to calculate the value of the radius of curvature at the free end of the cantilever. Together with measured values for the Youngs Modulus, this enabled us to determine the residual stress in each cantilever. This analysis has been applied to  $SrRuO_3/BaTiO_3/SrRuO_3$ ,  $BaTiO_3/MgO/SrTiO_3$  and  $BaTiO_3/SrTiO_3$  piezoelectric cantilevers and the results compared to two models in which the stresses are determined by lattice parameter mismatch or differences in thermal expansion coefficient. Our analysis shows that the bending of the beams is mainly due to the thermal stress generated

during the cooling down stage subsequent to the film deposition.

**Keywords** Residual stress · Thermal stress · Cantilever · Thin film stress

## 1 Introduction

There is a wide range of sensors and actuators based on micromachined cantilevers. These devices convert the mechanical vibration of a suspended beam, which may be terminated with a proof mass, into an electrical signal, which may be used to measure acceleration, vibrational frequency or even as a source of electrical power. Usually, the freedom of movement of the cantilever is guaranteed by etching a pit into the substrate and the cantilever is designed so that the curvature is minimized. When a cantilever is fabricated using a multilayer thin film structure, mechanical stresses arise between the layers as a result of a mismatch of lattice constants and thermal expansion coefficients. These result in the beam being curved rather than straight, which is undesirable for some applications. In order to control the curvature of the beam, an understanding of the stresses in the beam is required, which can be obtained from beam theory.

According to beam theory [1], the longitudinal stress in an homogeneous deflected beam, Fig. 1, is:

$$\sigma_x = -\frac{E\delta}{\rho} \quad (1)$$

where  $E$  is the Young's Modulus of the beam,  $\delta$  is the distance from the neutral axis and  $\rho$  is the radius of curvature. So the stress varies linearly along the section

G. Vasta (✉) · T. J. Jackson · E. J. Tarte  
The University of Birmingham, School of Electrical  
Electronic and Computer Engineering, 52 Pritchatts Road,  
Edgbaston, Birmingham, B15 2TT, UK  
e-mail: pipvast@yahoo.it

A. Frommhold  
The University of Birmingham, Nanoscale Physics Research  
Laboratory, School of Physics and Astronomy, Edgbaston,  
Birmingham, B15 2TT, UK

J. Bowen  
The University of Birmingham, School of Chemical  
Engineering, Edgbaston, Birmingham, B15 2TT, UK

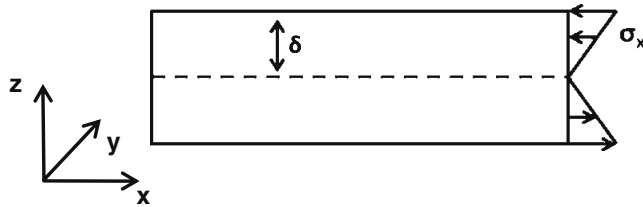


**Fig. 1** Longitudinal stress  $\sigma_x$  along the cross section of an homogeneous beam,  $\delta$  is the distance of a generic fibre from the neutral axis

of the beam. In a multilayer beam, Eq. 1 is valid for each individual layer. The longitudinal stress assumes its maximum value at the bottom and top surface of the cantilever. Previously [2, 3], the radius of curvature  $\rho$  of a deflected beam has been evaluated by measuring the deflection  $\delta$  at the cantilever free end and then the following relation is used:

$$\rho = \frac{L^2}{2\delta} \quad (2)$$

$L$  is the length of the beam. This formula is an approximation valid for small deflections. For larger deflections another method has to be followed. This paper shows a straightforward way to experimentally evaluate the residual stress in released cantilevers and hence determine the residual longitudinal stress in the general case.

We calculated the deflection curve of the cantilever by measuring the deflection of the beam at different distances from the anchor point. This enabled us to evaluate the radius of curvature at the free end of the structure.

The measurement of the deflection profile has been used elsewhere to estimate the curvature of suspended beams containing phase-change materials [4]. In that work the Stoney equation was used to calculate the elastic strain at the interface between a thick cantilever and a thin film grown on its top. Such treatment is only valid if the film thickness is negligible compared with the cantilever thickness [4, 5]. This restriction does not apply to our method and we demonstrate its effectiveness using multilayers to which the Stoney equation would not apply.

In this work the equations of beam theory [1], are used to estimate the residual stress on the top surface of the fabricated cantilevers; we have used this analysis to obtain values for residual stress in all-oxide piezoelectric cantilevers. These consisted of  $SrRuO_3$ / $BaTiO_3/SrRuO_3$  and  $BaTiO_3/MgO/SrTiO_3$  multilayers which are based on lead free materials and have applications as energy harvesting devices. The use of

an all oxide structure allows the layers to be grown epitaxially, which enables us to exploit the anisotropy of piezoelectric oxides in device design. We found that the first structure can be used to produce energy harvesting devices working in the  $d_{31}$  mode because the polar axis is perpendicular to the surface of the film (out of plane), while the second structure can be used for the  $d_{33}$  energy harvesting mode [6, 7] as the polar axis is parallel to the surface of the film (in plane). The maintenance of epitaxy throughout the structure requires us to use an oxide sacrificial layer. Residual stress investigations have been also performed on  $BaTiO_3/SrTiO_3$  cantilevers, these structures were developed at the beginning of the project to investigate the growing conditions and the properties of such material, however they do not find practical applications as energy harvesting devices.

For the analysed structures, the residual stress produces an upward bending of the beam, after their release. We will show how the application of our stress analysis method enables us to identify the dominant sources of stress in our cantilevers and hence illustrate how it may be applied more generally.

The residual stress in a multilayer beam can be predicted given certain key parameters. We have measured the lattice parameter and Youngs modulus for our samples and used these together with published values for Poissons ratio and thermal expansion coefficients to calculate the residual stress in our samples. We compare these to the stresses determined from the curvature of the beam.

## 2 Fabrication and characterization of all oxide cantilevers

We used a KrF excimer laser with a wavelength of 248 nm to grow our films by pulsed laser deposition. A 4 Hz pulse repetition rate is used, the distance between the material target and the substrate is set to 5.7 cm and all the devices were fabricated on (001) oriented  $SrTiO_3$  substrates.

The first layer grown is  $YBa_2Cu_3O_7$  which is used as a sacrificial layer for the release of the beam. This is followed by the  $SrRuO_3/BaTiO_3/SrRuO_3$  (out of plane or OP) or the  $BaTiO_3/MgO/SrTiO_3$  (in plane or IP) stack. The  $BaTiO_3/SrTiO_3$  bilayers (Bi) have been also grown on the top of the sacrificial layer. Our deposition system allows the deposition of only three films in situ, for the Bi structure only three films are necessary so they are grown in situ, for the IP stack first the  $MgO/SrTiO_3/YBa_2Cu_3O_7$  tri-layer is deposited followed by a  $BaTiO_3/MgO$  bilayer, in the case of the

OP structure first the  $BaTiO_3/SrRuO_3/YBa_2Cu_3O_7$  thi-layer is grown followed by a  $SrRuO_3/BaTiO_3$  bilayer. The deposition parameters are reported in Table 1.

In these structures,  $BaTiO_3$  is the piezoelectric layer,  $SrRuO_3$  acts as an electrode for the OP stacks whilst for the IP stacks, the  $MgO$  film is introduced to grow the  $BaTiO_3$  with the polar axis parallel to the surface of the film, and the  $SrTiO_3$  works as buffer layer to improve the interface between the  $YBa_2Cu_3O_7$  and the  $MgO$  film in the IP structure [8].

The IP structure needs the deposition of a gold top electrode. However the gold deposition is performed at room temperature, so it does not influence the thermal stress analysis which will be developed in the next sections. The cantilever geometry is then defined by contact photolithography and argon ion beam milling. To suspend the beam the sample is undercut in 0.1%  $HNO_3$ , rinsed in distilled water and dried using critical point drying in order to avoid stiction problems.

The Young's modulus of the deposited films has been evaluated using nanoindentation measurements. A NanoTest (Micro Materials, UK) employing a diamond-coated Berkovitch indenter has been used, to measure the reduced modulus  $E_r$  of the grown films. The reduced modulus  $E_r$  is calculated according to the following equation:

$$E_r = \frac{1}{2} \frac{1}{dP/dh} + \frac{\pi^{0.5}}{A_p^{0.5}} \quad (3)$$

$dP/dh$  is the compliance of the contact and  $A_p$  is the projected contact area, for a Berkovitch indenter:

$$A_p^{0.5} = 4.896h_c \quad (4)$$

$h_c$  is the contact depth and it is equal to:

$$h_c = h_{\max} - 0.75(h_{\max} - h_r) \quad (5)$$

$h_{\max}$  and  $h_r$  are determined from the loading unloading data [9, 10].

**Table 1** PLD deposition parameters for the deposited films

Material	Fluence [J/cm <sup>2</sup> ]	Deposition temperature [°C]	Deposition pressure [Torr]
$YBa_2Cu_3O_7$	3.4	740	0.15 $O_2$ flow
$SrRuO_3$	3.2	780	0.3 $O_2$ flow
$BaTiO_3$	3.5	740	0.15 $O_2$ flow
$MgO$	3.5	740	0.20 $O_2$ flow
$SrTiO_3$	3.2	740	0.21 $O_2$ flow

The Young's modulus is then calculated from the reduced modulus according to the following equation:

$$\frac{1}{E_r} = \frac{(1 - \nu^2)}{E} \frac{(1 - \nu_i^2)}{E_i} \quad (6)$$

$E$  and  $\nu$  are the Young's modulus and the Poisson's ratio of the specimen under measurements,  $E_i$  and  $\nu_i$  are the same parameters for the indenter, for a Berkovitch indenter the Young's modulus  $E_i$  is equal to 1141 GPa and the Poisson's ratio is equal to 0.07 [10]. The values of the reduced modulus measured near the top surface of the stack or at the interface between two layers have not been used to calculate the Young's modulus of the grown films. Measurements of the reduced modulus reveal that in the first 10 nm or 15 nm from the top surface of the stack, or from the interface between two layers, the reduced modulus assumes values which are not constant and are not compatible with the bulk Young's modulus of the same material. After the first 10 nm or 15 nm the reduced modulus approaches a value compatible with the Young's Modulus measured in the bulk of the same material; such a value is maintained through the thickness of the film until the next interface is reached.

Indentations were performed from the top surface down to the desired depth through the multilayer. The indenter was held at load for 60 s, then retracted from the sample at a rate of 0.5 nm/s. Each indentation was separated by 50  $\mu$ m, to avoid any influence of the previous indentation.

The values reported in Table 2 represent the values of Young's Modulus values averaged over the film thickness over a minimum of 25 measurements. Values obtained from depths near the top surface and near the film interfaces have been rejected, however if such

**Table 2** Thermal expansion coefficient, Poisson's ratio and Young Modulus of the deposited films. The Young Modulus has been measured by nanoindentation technique

Material	Thermal expansion coefficient [10 <sup>-6</sup> 1/K]	Young modulus [GPa]	Poisson ratio
$YBa_2Cu_3O_7$	13.4	129	0.3
$SrRuO_3$	8	190	0.3
$BaTiO_3$ (on $MgO$ or $SrRuO_3$ )	11.3	175	0.35
$BaTiO_3$ (on $SrTiO_3$ )	11.3	79	0.35
$MgO$	8	233	0.18
$SrTiO_3$	9.4	130	0.25

values are considered they alter the final value of the Young's modulus by less than 10%.

X-ray diffraction analysis was performed by using a Siemens D5000 diffractometer. The lattice parameters of the films are reported in Table 3. When the  $BaTiO_3$  film is grown on the  $SrRuO_3$  layer in the OP stack, the lattice parameters are consistent with the longer polar axis being perpendicular to the surface of the film, this orientation would suit the  $d_{31}$  energy harvesting mode. For the IP structures, the in plane lattice parameters are longer than the out of plane ones for  $BaTiO_3$  grown on  $MgO$  which is consistent with the polar axis being parallel to the surface of the film, this orientation suits the  $d_{33}$  energy harvesting mode. In this case the measured polar lattice parameter of  $4.002 \text{ \AA}$  appears smaller than the bulk value because it is an average value, as there are two possible orthogonal orientations for the polar axis in the plane of the substrate, with the non polar axis lying in the perpendicular direction in plane.

The SEM analysis has been performed with a Philips XL30S FEG. Figure 2 shows SEM pictures of three of the devices under investigation. Figure 1(a) shows a  $123 \mu\text{m}$  long,  $20 \mu\text{m}$  wide IP U-shape cantilever, the  $SrTiO_3$  film is  $500 \text{ nm}$  thick, the  $MgO$  layer is  $50 \text{ nm}$  thick and the  $BaTiO_3$  film is  $120 \text{ nm}$  thick. Figure 1(b) shows a  $234 \mu\text{m}$  long,  $20 \mu\text{m}$  wide OP U-shape cantilever, the bottom  $SrRuO_3$  layer is  $350 \text{ nm}$  thick, the  $BaTiO_3$  film is  $100 \text{ nm}$  thick and the  $SrRuO_3$  top layer is  $50 \text{ nm}$  thick. Figure 2(c) shows a  $44 \mu\text{m}$  long,  $10 \mu\text{m}$  wide Bi cantilever, the  $SrTiO_3$  is  $500 \text{ nm}$  thick and the  $BaTiO_3$  is  $120 \text{ nm}$  thick.

When the cantilever is undercut it leaves a trace on the substrate Fig. 3. The deflection of the beam was evaluated by measuring the distance between the trace on the substrate and the top surface of the cantilever.

**Table 3** Lattice constants of the different materials used in the cantilever stack. The lattice parameters have been measured by X-ray diffraction technique

Material	a Measured (a theoretical)	b Measured (b theoretical)	c Measured (c theoretical)
$BaTiO_3$ (on $SrRuO_3$ )	$3.951 \text{ \AA}$ ( $3.992 \text{ \AA}$ )	$3.951$ ( $3.992 \text{ \AA}$ )	$4.069$ ( $4.036 \text{ \AA}$ )
$BaTiO_3$ (on $MgO$ )	$4.002 \text{ \AA}$	$4.002 \text{ \AA}$	$3.997 \text{ \AA}$
$BaTiO_3$ (on $SrTiO_3$ )	$3.996 \text{ \AA}$ ( $3.992 \text{ \AA}$ )	$3.996 \text{ \AA}$ ( $3.992 \text{ \AA}$ )	$4.015 \text{ \AA}$ ( $4.036 \text{ \AA}$ )
$SrRuO_3$ (on $YBa_2Cu_3O_7$ )	$5.519 \text{ \AA}$ ( $5.567 \text{ \AA}$ )	$5.519 \text{ \AA}$ ( $5.530 \text{ \AA}$ )	$7.825 \text{ \AA}$ ( $7.845 \text{ \AA}$ )
$MgO$ (on $SrTiO_3$ )	$4.220 \text{ \AA}$ ( $4.211 \text{ \AA}$ )	$4.220 \text{ \AA}$ ( $4.211 \text{ \AA}$ )	$4.220 \text{ \AA}$ ( $4.211 \text{ \AA}$ )

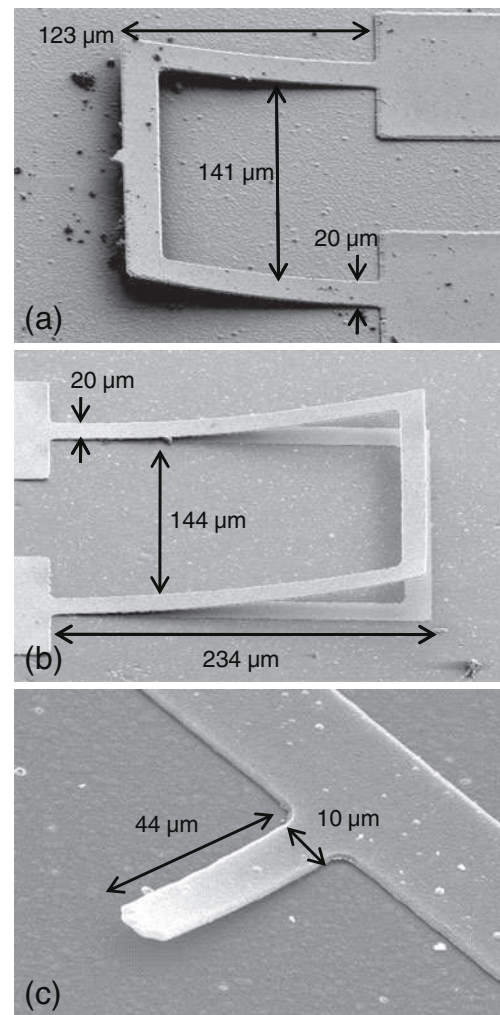


**Fig. 2** SEM pictures of: (a)  $BaTiO_3/MgO/SrTiO_3$   $123 \mu\text{m}$  long,  $20 \mu\text{m}$  wide U-shape cantilever. (b)  $SrRuO_3/BaTiO_3/SrRuO_3$   $234 \mu\text{m}$  long,  $20 \mu\text{m}$  wide U-shape cantilever. (c)  $BaTiO_3/SrTiO_3$   $44 \mu\text{m}$  long,  $10 \mu\text{m}$  wide cantilever

Measurements uncertainties of  $300 \text{ nm}$  in the  $y$  direction and of  $1 \mu\text{m}$  in the  $x$  direction have been estimated.

To validate the SEM measurements, the deflection of the cantilevers was also measured with a MicroXAM2 interferometer (Omniscan, UK). The interferometer was operated in phase mode employing light of wavelength  $510 \text{ nm}$ , and at a magnification of  $100X$ . Interferograms were found to be unreliable, due to differences in the reflectivities of the various materials. Instead, the interferometer was operated manually, employing a motorised  $x, y, z$  stage with  $\pm 0.1 \mu\text{m}$  resolution. The interferometric fringes were focused on the sample surface and the position of peak light intensity was considered to be the  $x, y$  position of interest, whose position could be determined with approximately

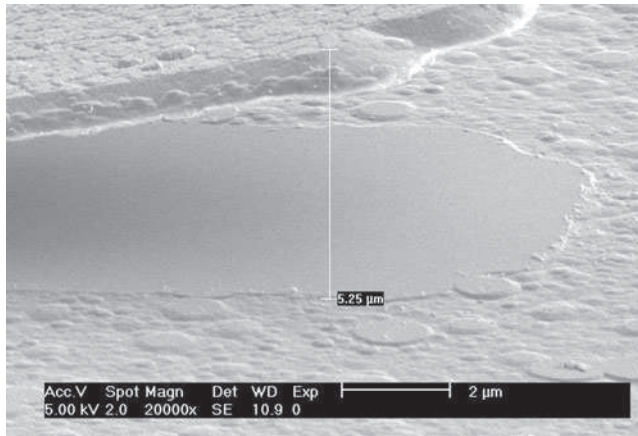


**Fig. 3** SEM pictures showing the measurements of the deflection for a  $\text{BaTiO}_3/\text{SrTiO}_3$  cantilever at 32  $\mu\text{m}$  from the anchor

$\pm 3 \mu\text{m}$  accuracy due to the manual positioning involved. The corresponding  $z$ -position was recorded for each surface location assessed.

### 3 Analysis of the cantilevers

In order to determine the residual stresses in the cantilevers, we must consider the forces distributed over its cross section. These represent a system equivalent to a couple and the resultant of these forces in the  $x$  direction must be equal to zero Fig. 1, [1]. The couple which models the forces along the cross section of the beam generates a moment  $M$ . The differential equation describing the deflection curve can be written as:

$$EI_z \frac{d^2y}{dx^2} = -M \quad (7)$$

where  $I_z$  is the moment of inertia of the cross section of the cantilever [1]. The deflection of the beam is described by a parabola. The U-shape cantilever is mechanically equivalent to a simple cantilever with a beam width equal to twice the real one [11]. So all the relations for the normal beam can be applied to these devices.

The deflections of three example cantilevers (on three different samples), one for each layer sequence, have been measured at five different distances ( $A; B; C; D; E$ ) from the anchors. The data as example of each layer sequence are presented in Table 4. Both the SEM and optical data are shown, together with the equation of the parabola through the first, middle and last points  $A, C$  and  $E$  respectively. Also shown in Table 4 is the radius of curvature for each

**Table 4** Device type, length, width and co-ordinates (x,y) of three example cantilevers (one for each layer sequence);  $x$  is the position of the measurement along the cantilever and  $y$  is the deflection. The parabolic equations describing the deflection of the cantilevers through the points ( $A; C; E$ ) are reported for both the SEM and the interferometer data, the radius of curvatures of each cantilever calculated from Eq. 8 with the parabola obtained from SEM data are also given

Device	Cantilever type	Length [ $\mu\text{m}$ ]	Width [ $\mu\text{m}$ ]	SEM coordinates ( $x[\mu\text{m}], y[\mu\text{m}]$ )	Interferometer coordinates ( $x[\mu\text{m}], y[\mu\text{m}]$ )	SEM Parabola (Interferometer parabola)	Radius of curvature [ $\mu\text{m}$ ]
OP	U-shape	120 $\mu\text{m}$	20 $\mu\text{m}$	(0, 1.74); (20, 3.35); (50, 8.44); (90, 19.5); (118, 30.5); (0, 1.02); (20, 2.3); (50, 5.72); (90, 13.5); (122, 21.6); (2.33, 1.57); (10, 2.23); (20, 3.2); (30, 4.82); (39, 6.68);	(0, 1.5); (20, 3.5); (50, 8.2); (90, 18); (118, 31); (0, 2); (20, 3.6); (50, 5.8); (90, 12.3); (118, 18.6); (0, 1.1); (20, 3.4); (30, 4.5); (44, 7.9)	$y_a = 1620x^2 + 0.053x + 1.74 \cdot 10^{-6}$ $y = 1706x^2 + 0.0487x + 1.5 \cdot 10^{-6}$ $y_b = 1040x^2 + 0.042x + 1.02 \cdot 10^{-6}$ $y = 834x^2 + 0.0343x + 2 \cdot 10^{-6}$ $y_c = 2500x^2 + 0.0339x + 1.51 \cdot 10^{-6}$ $y = 1650x^2 + 0.082x + 1.1 \cdot 10^{-6}$	$403 \pm 7.15$ $551 \pm 37$ $217 \pm 57$
IP	U-shape	120 $\mu\text{m}$	20 $\mu\text{m}$				
Bi	Beam	44 $\mu\text{m}$	10 $\mu\text{m}$				

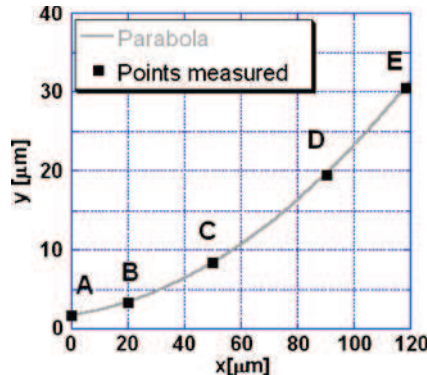


**Fig. 4** Parabola and deflection of the measured points for the 120  $\mu\text{m}$  long, 20  $\mu\text{m}$  wide u-shape cantilever having the OP layer sequence

cantilever, calculated from the parabola by using the following expression [1].

$$\frac{1}{\rho} = \frac{\frac{d^2y}{dx^2}}{\left[1 + \left(\frac{dy}{dx}\right)^2\right]^{\frac{3}{2}}} \quad (8)$$

To evaluate the radius of curvature the parabola obtained from the SEM data has been considered, this because of the higher resolution associated with the SEM measurements.

The parabola describes the deflection of the cantilevers well, as can be seen from Fig. 4 which shows the parabola and the measured points for the analysed OP device. However it has to be emphasized that Eq. 7 is an approximation [1]. A parabola might not be a good approximation generally, in which case an alternative expression should be considered. For the three example devices the deviations in the measured coordinates of *B* and *D* from the parabolic approximation are reported in Table 5. These deviations are in the error range of the SEM coordinates.

As already reported, to validate the method, the deflection of the cantilever has been measured with the interferometer technique. Table 5 also reports the

percentage errors on the parabola coefficients *a* and *b* obtained from the interferometer measurements respect to the parabola coefficients relative to the SEM data. The percentage errors on *a* and *b*,  $e_a$  and  $e_b$  respectively, have been calculated from the following expressions:

$$e_a = \left| \frac{a_{\text{SEM}} - a_{\text{INT}}}{a_{\text{SEM}}} \right| \cdot 100 \quad (9)$$

$$e_b = \left| \frac{b_{\text{SEM}} - b_{\text{INT}}}{b_{\text{SEM}}} \right| \cdot 100 \quad (10)$$

where  $a_{\text{SEM}}$  and  $b_{\text{SEM}}$  are the parabola coefficients calculated from SEM data, while  $a_{\text{INT}}$  and  $b_{\text{INT}}$  are the parabola coefficients obtained from interferometer measurements. The coefficient *c* is not considered as its value does not affect the radius of curvature of the cantilevers.

The longitudinal stress at the free end cross section of each of the three example cantilevers is evaluated by using Eq. 1. The value of the Young's Modulus appropriate for a multilayer system is that of the material with maximum Young's modulus [1]. In fact in a cantilever system with heterogeneous cross section the width of each layer is normalized to the maximum Young Modulus according to transformed section theory Fig. 5 [1].

To evaluate the longitudinal stress at the cantilever top surface, it is necessary to know the position of the neutral axis in order to calculate the distance between the cantilever's top surface and the neutral axis itself. The expression for the position of the neutral axis in a *n*-layer film stack is:

$$h_{\text{neut}} = \frac{\sum_{i=1}^n (t_i b_{i,c}) h_i}{\sum_{i=1}^n (t_i b_{i,c})} \quad (11)$$

$$b_{i,c} = b_i \frac{E_i}{E_{\max}} \quad (12)$$

where  $t_i$  is the thickness of the layer *i*,  $h_i$  is the position of the baricenter of the layer *i*,  $b_{i,c}$  represents the width of the layer *i* normalized to the maximum Young

**Table 5** Errors on the points *B* and *D* consequence of the parabolic approximation used for the deection of the cantilever. Also reported are the percentage errors  $e_a$  and  $e_b$  of the parabola coefficients obtained for the interferometers measurements respect to the SEM data. The reported data are relative to the three example devices

Device	Cantilever type	Length [ $\mu\text{m}$ ]	Width [ $\mu\text{m}$ ]	Error on <i>B</i> for SEM par. [ $\mu\text{m}$ ]	Error on <i>D</i> for SEM par. [ $\mu\text{m}$ ]	$e_a$ SEM-INT	$e_b$ SEM-INT
OP	U-shape	120 $\mu\text{m}$	20 $\mu\text{m}$	+ 0.1	+ 0.22	5.3%	8.11%
IP	U-shape	120 $\mu\text{m}$	20 $\mu\text{m}$	+ 1.22	- 0.28	20%	18.3%
Bi	Beam	44 $\mu\text{m}$	10 $\mu\text{m}$	- 0.13	- 0.04	51.5%	142%

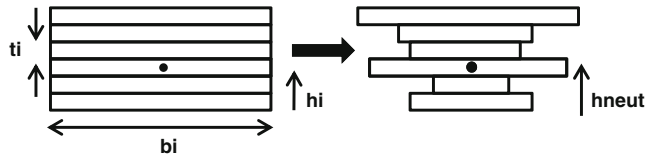


**Fig. 5** Equivalent section model of an heterogeneous multilayer cantilever according to the equivalent section theory;  $b_i$  is the width of the layer  $i$ ,  $t_i$  is the thickness of the layer  $i$ ,  $h_i$  indicates the position of the baricenter of the layer  $i$  and  $h_{\text{neut}}$  indicates the position of the neutral axis in the equivalent section model

modulus and  $E_i$  is the Young Modulus of the layer  $i$ , Fig. 5 [12].

The longitudinal stress at the beam top surface for the example OP cantilever is:

$$\tilde{\sigma}_a = -0.104 \cdot 10^9 \pm 0.002 \cdot 10^9 \left[ \frac{N}{m^2} \right] \quad (13)$$

for the example IP structure the top surface stress is:

$$\tilde{\sigma}_b = -0.131 \cdot 10^9 \pm 0.009 \cdot 10^9 \left[ \frac{N}{m^2} \right] \quad (14)$$

finally for the example Bi device the longitudinal stress at the top surface is:

$$\tilde{\sigma}_c = -0.200 \cdot 10^9 \pm 0.069 \cdot 10^9 \left[ \frac{N}{m^2} \right]. \quad (15)$$

These represent the experimental values of the longitudinal stress at the cantilever top surface.

The same analysis has been performed on other cantilevers belonging to the three analysed samples and having the three layer sequences previously reported. The resulting experimental stresses for all the

devices analysed, together with the theoretical values of the longitudinal stresses (which will be discussed in Section 4) are reported in Table 6.

There are three sources of uncertainty in this analysis. The first source is due to the measurement technique and it is linked to the resolution of the measurement instruments. The second is the curve chosen to approximate the deflection of the beam. The third source of error is due to the fabrication process, this kind of error arises from the undercut and resist resolution.

The uncertainties on the values of the residual stresses  $\tilde{\sigma}_a$ ,  $\tilde{\sigma}_b$  and  $\tilde{\sigma}_c$  have been calculated developing an error analysis on the radius of curvature.

Considering the canonical form of the parabola and Eq. 8, the radius of curvature depends only on the parameters  $a$  and  $b$ , so the uncertainty in the radius of curvature is dependent on the uncertainty in  $a$  and  $b$  but not in  $c$ .

The radius of curvature of each cantilever was calculated at the free end of the structure, so an error on the length of the cantilever also affects its final value. The principle errors on the cantilever lengths is due to the undercut at the anchors points. Undercuts between 9  $\mu\text{m}$  and 20  $\mu\text{m}$  have been measured.

The uncertainty on the radius of curvature has been evaluated using the following formula:

$$(\Delta\rho)^2 = \left( \frac{\partial\rho}{\partial a} \Delta_a \right)^2 + \left( \frac{\partial\rho}{\partial b} \Delta_b \right)^2 + \left( \frac{\partial\rho}{\partial l} \Delta_l \right)^2 \quad (16)$$

where  $\Delta_a$  and  $\Delta_b$  are the standard deviations on the parabola factors  $a$  and  $b$ , they include the instrument and the fitting error;  $\Delta_l$  is the uncertainty on the length

**Table 6** Experimental stress, theoretical thermal stress and theoretical stress due to combined effect of thermal and misfit stress evaluated at the top surface of each cantilever. For each cantilever the device type corresponding to different layer sequence is indicated, also the cantilever shapes and the cantilever lengths and widths are reported

Device	Cantilever type	Length [ $\mu\text{m}$ ]	Width [ $\mu\text{m}$ ]	Experimental stress [ $10^9 \text{ N/m}^2$ ]	Theoretical thermal stress [ $10^9 \text{ N/m}^2$ ]	Theoretical thermal-misfit stress [ $10^9 \text{ N/m}^2$ ]
OP	U-shape	120 $\mu\text{m}$	20 $\mu\text{m}$	$-0.104 \pm 0.002$	-0.051	-0.0013
OP	U-shape	128 $\mu\text{m}$	20 $\mu\text{m}$	$-0.093 \pm 0.009$	-0.051	-0.0013
OP	U-shape	234 $\mu\text{m}$	20 $\mu\text{m}$	$-0.051 \pm 0.026$	-0.051	-0.0013
IP	U-shape	120 $\mu\text{m}$	20 $\mu\text{m}$	$-0.153 \pm 0.011$	-0.145	-7.21
IP	U-shape	122 $\mu\text{m}$	20 $\mu\text{m}$	$-0.131 \pm 0.009$	-0.145	-7.21
IP	U-shape	180 $\mu\text{m}$	20 $\mu\text{m}$	$-0.112 \pm 0.028$	-0.145	-7.21
Bi	Beam	32 $\mu\text{m}$	10 $\mu\text{m}$	$-0.173 \pm 0.136$	-0.071	1.2
Bi	Beam	44 $\mu\text{m}$	10 $\mu\text{m}$	$-0.200 \pm 0.069$	-0.071	1.2
Bi	Beam	55 $\mu\text{m}$	10 $\mu\text{m}$	$-0.190 \pm 0.112$	-0.071	1.2

of the cantilever due to the undercut and to the resolution of the photoresist. The errors on the radius of curvature are reported in Table 4.

The error in the experimental values of the residual stress can be calculated from the error on the radius of curvature, they are reported in Table 6.

#### 4 Theoretical values for the residual stress

Usually vacuum deposited films are in a state of stress. Causes of stress are the mismatch of thermal expansion coefficients between the different layers (thermal stress), the mismatch of lattice constants between the different materials (misfit stress) and the presence of defects in the layers [14]. The theory predicts that an epitaxial layer having a lattice parameter mismatch  $f$  with the underneath layer of less than  $\approx 9\%$  (as in our case), would grow elastically strained to have the same interatomic spacing of the substrate up to some critical film thickness  $d_c$ . Beyond  $d_c$  misfit dislocations are introduced. At this point the initially strained film relaxes because the dislocations release the misfit strain. The critical film thickness  $d_c$  is expressed by

$$d_c = \frac{b}{8\pi(1+\nu)f} \ln\left(\frac{d_c}{b} + 1\right) \quad (17)$$

where  $\nu$  is the Poisson's ratio,  $b$  is the dislocation Burgers vector and  $f$  is the lattice misfit of the film. In a multilayer structure for the layer  $n$  grown on the layer  $n-1$  the lattice misfit is defined as

$$f = \frac{a_{n-1} - a_n}{a_n} \quad (18)$$

where  $a_{n-1}$  and  $a_n$  are the unstrained lattice parameter of the layers  $n$  and  $n-1$ . A positive  $f$  implies that the initial layers of the epitaxial film will be stretched in tension, a negative  $f$  means film compression [15]. To calculate the value of  $d_c$  for each film present in the two stacks rather than the modulus of the Burger vector, to first approximation it is possible to consider the spacing between the (001) planes of the different crystal structures. The values of the Poisson's ratios for the grown films are reported in Table 2 [16–20].

By using the measured lattice parameters we have found that for our layer combinations, the critical thickness is less than 10 nm. The film thicknesses in the two stacks are in the order of hundred of nm, this means that only the thermal stress will be considered in the following stress analysis, as the misfit is released by the generated dislocations. Similar considerations have been also reported in [21].

The deposition of the cantilever films is performed at temperatures of 740°C and 780°C, then the film stack is cooled down to room temperature. The thermal stress will be the result of the differences in the film thermal expansion coefficients.

On a rigid substrate the in plane thermal stress in the layer  $n$  applied by the layer  $n-1$  can be expressed as

$$\sigma_n = \frac{E_n}{1-\nu_n} (\alpha_n - \alpha_{n-1})(T_s - T_a) \quad (19)$$

where  $E_n$  is the Young modulus,  $\nu_n$  is the Poisson's ratio,  $\alpha_n$  and  $\alpha_{n-1}$  are the thermal expansion coefficients of the layers  $n$  and  $n-1$ ,  $T_s$  is the temperature during the deposition and  $T_a$  is the temperature during the measurement. Thin films can be considered as two dimensional systems. Equation 19 is the two dimensional extension of the relation reported in [22].

When the  $YBa_2Cu_3O_7$  is undercut and the beam suspended, the constraint which keeps the multilayer anchored to the substrate is removed. The multilayered structure will bend because of the unbalanced thermal stress present at the film interfaces. Figure 6(a), (b) and (c) show the thermal stresses at the interfaces in the OP, IP and Bi stacks after the  $YBa_2Cu_3O_7$  undercutting. Where  $\sigma_{SRO1-BTO}$  indicates the stress on the  $SrRuO_3$  surface layer applied by the  $BaTiO_3$  film. Similar nomenclature applies to the other layers. The thermal expansion coefficients [23–27] the Poisson's ratio [16–20] and the measured Young Modulus are reported in Table 2.

With these values it is possible to calculate the thermal stress at the interface of each film by using Eq. 19. In the OP multilayer structure each film has to be heated to 780°C during the  $SrRuO_3$  deposition, so  $T_s$  is chosen equal to 780°C. The temperature during the measurement  $T_a$ , is 20°C. In this system the algebraic sum of the thermal stresses at each interface is:

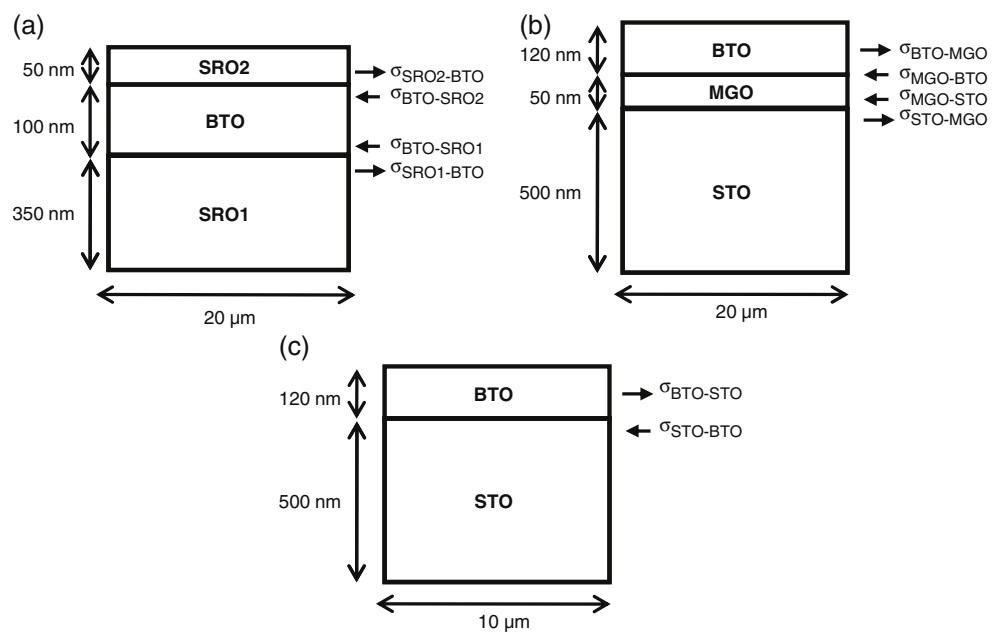
$$\begin{aligned} & \sigma_{SRO1-BTO} + \sigma_{BTO-SRO1} \\ &= \sigma_{BTO-SRO2} + \sigma_{SRO2-BTO} \\ &= -0.0255 \cdot 10^9 \left[ \frac{N}{m^2} \right] \end{aligned} \quad (20)$$

the minus sign indicates a compressive stress.

For the IP multilayer system  $T_s$  is equal to 740°C and  $T_a$  is still 20°C. The algebraic sum of the thermal stresses at each interface is:

$$\sigma_{STO-MGO} + \sigma_{MGO-STO} = -0.111 \cdot 10^9 \left[ \frac{N}{m^2} \right] \quad (21)$$

**Fig. 6** Longitudinal stress at the interface of each film present in the stack, in (a)  $\sigma_{SRO1-BTO}$  indicates the stress on the  $SrRuO_3$  surface layer applied by the  $BaTiO_3$  film, similar nomenclature applies to the other layers. The arrows indicate if the stress in each layer is compressive ( $\leftarrow$ ) or tensile ( $\rightarrow$ )



for the  $SrTiO_3 - MgO$  interface and

$$\sigma_{MGO-BTO} + \sigma_{BTO-MGO} = -0.034 \cdot 10^9 \left[ \frac{N}{m^2} \right] \quad (22)$$

for the  $MgO - BaTiO_3$  interface.

In the case of the Bi device,  $T_s$  is equal to  $740^\circ\text{C}$  while  $T_a$  is  $20^\circ\text{C}$ , the resulting stress at the  $BaTiO_3/SrTiO_3$  interface is:

$$\sigma_{STO-BTO} + \sigma_{BTO-STO} = -0.071 \cdot 10^9 \left[ \frac{N}{m^2} \right] \quad (23)$$

the value of the  $BaTiO_3$  Young's modulus used for the calculations of the stress at the interface of the Bi structures, as suggested by the indentation measurements, is smaller than that one used for the OP and IP devices. This point is further discussed in Section 5.

According to Eq. 1, the longitudinal stress in each layer varies linearly with the film thickness.

The cantilevers under investigation have total thicknesses of 500 nm and 670 nm, widths between 10  $\mu\text{m}$  and 20  $\mu\text{m}$  and lengths between 32  $\mu\text{m}$  and 230  $\mu\text{m}$ . So at a first approximation it is possible to consider each layer in the stack as a two dimensional system, this means that the stress will occur only at the interfaces.

For the OP system shown in Fig. 6(a) it is possible to assume that the stress at the top surface of the beam is equal to the sum of the stresses at the  $SRO_2/BTO$  and at the  $BTO/SRO_1$  interfaces, Eq. 24.

$$\sigma_a = -0.051 \cdot 10^9 \left[ \frac{N}{m^2} \right] \quad (24)$$

This is similar in magnitude to the values determined experimentally for the three OP stacks and in excellent agreement with the experimentally determined stress for one of them, Table 6. For the IP stacks, the stress at the top surface of the beam will be equal to the sum of the stresses at the  $BTO/MGO$  and at the  $MGO/STO$  interfaces, Eq. 25.

$$\sigma_b = -0.145 \cdot 10^9 \left[ \frac{N}{m^2} \right] \quad (25)$$

In this case we have excellent agreement with all the experimentally determined values, Table 6.

For the Bi device the stress at the top surface is assumed equal to the stress at the  $BTO/STO$  interface:

$$\sigma_c = -0.071 \cdot 10^9 \left[ \frac{N}{m^2} \right]. \quad (26)$$

There is a factor 3 between the experimental and the theoretical values, however a large error is present in the experimental stresses and for two devices the theoretical value falls inside the error range, Table 6.

If the contributions coming from the lattice mismatches are considered the stresses at the interfaces of Fig. 6(a) are given by the sum of the thermal stress and of the stress generated by the lattice mismatch. The stress due to the lattice mismatch generated by the layer  $n-1$  on the layer  $n$  is:

$$\sigma_{mis,n} = \frac{E_n}{1-v_n} f \quad (27)$$

where  $f$  is the lattice misfit defined in Eq. 18.

Considering the algebraic sum of the stresses at the interfaces of the OP stack, the theoretical longitudinal stress at the top surface is:

$$\hat{\sigma}_a = -0.0013 \cdot 10^9 \left[ \frac{N}{m^2} \right] \quad (28)$$

this is between five times and one order of magnitude smaller than the experimental values. For the IP devices the introduction of the lattice mismatch in the calculations results in the following top surface stress:

$$\hat{\sigma}_b = -7.21 \cdot 10^9 \left[ \frac{N}{m^2} \right] \quad (29)$$

in this case there are two orders of magnitude between experiment and theory. Finally in the case of the Bi cantilevers the contribution of the misfit stress produces the following theoretical value:

$$\hat{\sigma}_c = 1.2 \cdot 10^9 \left[ \frac{N}{m^2} \right] \quad (30)$$

also in this case a difference of two orders of magnitude between the experimental and the residual stress is present. Furthermore the positive value of the residual stress at the beam top surface indicates a downward bending of the cantilever, in clear contrast with observations. The values of the residual stress calculated with the contributions of the thermal stress and lattice mismatch are reported in Table 6.

When the contributions of the lattice mismatch are included in the calculation of the residual stress there is a clear disagreement between theoretical and experimental values, this is why the residual stress is mainly attributed to the differences in the thermal expansion coefficients between the materials of the different layers.

## 5 Discussion

There are two different techniques used to evaluate the residual stress in thin films. In the first method the curvature of a flat substrate is measured after the film deposition and the residual stress is evaluated using the Stoney formula [4, 7, 14, 29].

The assumptions in this method are: the properties of the film-substrate system are such that the film materials contribute negligibly to the overall elastic stiffness; the change in film stress due to substrate deformation is small; the thickness of the film is small compared to the thickness of the substrate and the curvature of the substrate midplane is spatially uniform [5]. Corrections to the original Stoney formula can be made in the case

of films having a thickness which is not negligible with respect to the thickness of the substrate.

Thus the Stoney formula may not accurately describe the bending of our cantilever, for example the radius of curvature of the fabricated cantilevers is not uniform along the length of the beam and furthermore in multilayer cantilevers all the films contribute to the overall elastic stiffness.

When this method is applied to a multilayer structure grown on a certain substrate it is assumed that the individual layers in the film are added sequentially and that the mismatch strain in each layer depends only on the substrate but not on the order in which the layers are formed [5]. To evaluate the stress in a multilayer the substrate curvature has to be measured before and after each layer deposition [5, 7].

All these assumptions can lead to systematic errors in the evaluation of the local residual stresses.

The second technique involves the measurement of the bending of the multilayer structure when all the constraints are removed [14]. This is the method usually used to evaluate the residual stress in released cantilevers. Under the assumption of small deflections, the deflection of the free end is measured [2, 3], and is used to calculate an approximated value for the radius of curvature (Eq. 2). This is only valid for small deflections of the cantilever free end, and so to calculate a more precise value for the radius of curvature, the method which we proposed can be followed. Measurement of the deflections at different distances from the anchor point is a straightforward way to experimentally evaluate the residual stress in multilayers cantilevers.

For the OP devices, one of the experimentally determined residual stress values is in good agreement with the theoretical value and the other two are of a similar order of magnitude. All of the experimentally determined residual stress values for the IP devices agree well with the theoretical value. The level of agreement between experiment and theory may be somewhat fortuitous, since there is more than one value available in the literature for key parameters such as the thermal expansion coefficients of the materials. In particular for  $MgO$  a different value from that one reported in the table is also found [30].

$$\alpha_{MgO}(300K) = 10.4 \cdot 10^{-6} \left[ \frac{1}{K} \right] \quad (31)$$

Assuming this value for the  $MgO$  thermal expansion coefficient, the value for the theoretical residual stress at the top surface of the IP device is:

$$\sigma_b = -0.072 \cdot 10^9 \left[ \frac{N}{m^2} \right]. \quad (32)$$

In the case of Bi devices the magnitude of the absolute error on the parabolic approximations (error on points *B* and *D*, Table 5) is comparable with the absolute error of the IP and OP structures. The Bi devices experiences deflections which are between three and six times smaller than the deflections experienced by the IP and OP cantilevers, this produces a larger relative error on the parabolic approximation used for the Bi structures. This explains why a bigger error on the residual stress of these cantilevers is present.

For the Bi cantilevers, as already reported in Section 4, the measured value of the Young modulus is smaller than the value measured for  $BaTiO_3$  films grown on  $SrRuO_3$  or on  $MgO$ . This smaller value of 79 GPa is in agreement with that reported in [28]. When the  $BaTiO_3$  is grown on  $MgO$  or on  $SrRuO_3$  its Young's modulus is larger. Further investigation is necessary to understand the origin of such disagreement. It is known that  $MgO$  and  $SrRuO_3$  are stiffer than  $SrTiO_3$  and so an influence of the underlying layer on the Yong's modulus of  $BaTiO_3$  can not be excluded. Furthermore it has to be highlighted that in the Bi structure all the thin films are deposited *in situ* while for the IP and OP stacks this is not possible because our deposition system allows the deposition of only three layers *in situ*. In the IP and OP devices before the deposition of the  $BaTiO_3$  the thin film stacks are heated up in oxygen at the deposition temperature and annealed for about 30 min before the deposition. The annealing step can improves the quality of the top surface of the film stack which acts as a seed for the  $BaTiO_3$  deposition. Alternatively, since it is known that heating and cooling cycles can reduce stresses in ceramics like  $BaTiO_3$  [13], stresses in the Bi structures may be higher than those in the IP and OP because the IP and OP structures were grown with extra heating/cooling steps. Thirdly, the Bi structures are smaller than the IP and OP devices so edges effects might contribute to the total longitudinal stress [5].

Nevertheless for two of the Bi structures the theoretical stress lies with the error range of the experimental value. Therefore we consider that the overall agreement with theory is good and that the mismatch between the thermal expansion coefficients is the main cause of the residual stress in these devices. If instead the lattice mismatches are used to calculate the longitudinal stresses at the top surfaces of the cantilevers, there is a difference of one or two orders of magnitude between theoretical and experimental values. This rules out the lattice mismatch as the cause of residual stress.

We believe that the variation in stress values can arise from variations in deposition parameters, associated with the alignment of the laser ablation plume with

the centre of the substrate. For the sample containing the OP structures, two of the devices were much closer to each other than the third device. If the thickness of each layer deposited on the  $SrTiO_3$  substrate were not uniform all over the sample, this would give errors in the position of the neutral axis and according to Eq. 1 an error on the value of the residual longitudinal stress.

Another potential source of variation is the value of the Young's modulus. Measurements show that the values of the Young modulus are not constant through the film thicknesses with variations up to 10% around the central value across the thickness of each film. Another source of error might be due to the not perfect undercut in fact it is possible that material from the top part of the sacrificial layer might remain attached to the bottom surface of the cantilever. Finally other sources of stress like microscopic voids, incorporation of impurities and recrystallization [5, 15] could be present in the deposited films.

To validate the method, the measurements of the deflection of the cantilevers have been also performed with the interferometry technique. The measured values together with the corresponding parabola are reported in Table 4. Table 5 reports the percentage errors on the parabola coefficients *a* and *b*,  $e_a$  and  $e_b$  respectively, obtained from the interferometer measurements respect to the parabola coefficients relative to the SEM data. For the IP and OP devices errors on the coefficients between 5% and 20% seem to validate the method applied on the SEM measurements. For the Bi devices errors on the coefficients over 50% are reported, this is attributed to the smaller resolution associated with the interferometer measurements. The Bi devices have lengths between 32  $\mu\text{m}$  and 55  $\mu\text{m}$  and experience a maximum deflection of the free end equal to 10  $\mu\text{m}$ . For these small deflections, the resolution of the method as consequence of the manual measurement involved does not allow the application of the method on these data.

The SEM measurements present a better resolution than the interferometers data, this is why the radius of curvature and the values of the residual stresses at the top surface of the cantilevers have been calculated from the SEM measurements.

## 6 Conclusions

We have shown a method to experimentally determine the curvature of thin film multilayer suspended cantilever structures. This method is applicable for beams with large deflections and which do not present a constant radius of curvature. It enables the radius

of curvature at a certain distance from the anchor to be determined accurately. The deflection of the suspended beams is measured at different distances from the anchor point using SEM and interferometer images in this way the expression of the deflection curve is calculated for each cantilever. With this expression it is possible to calculate the value of the radius of curvature at the cantilever free end. Together with measured values for the Youngs Modulus, this enabled us to determine the residual stress in a cantilever. This analysis has been applied to  $SrRuO_3/BaTiO_3/SrRuO_3$  and  $BaTiO_3/MgO/SrTiO_3$  piezoelectric cantilevers. These thin film sequences produce  $BaTiO_3$  layers with polar axes oriented out of plane(OP) or in plane(IP) respectively. The OP structures are suited to energy harvesting applications where the  $d_{31}$  mode is used whilst the IP structures are suited to the  $d_{33}$  mode. Investigations have been also performed on  $BaTiO_3/SrTiO_3$  bilayer cantilevers. The results were compared to two models in which the stresses are determined by lattice parameter mismatch or differences in thermal expansion coefficient. The experimentally determined residual stresses of the IP and OP devices were found to agree with the calculated thermal stresses, suggesting that the latter is the source of the curvature, rather than the lattice mismatch. For the Bi structures the experimental stress is three times bigger than the theoretically calculated thermal stress, however in this case a large uncertainty is associated with the experimental values. For energy harvesting applications, the output power of a cantilever increases when its swinging amplitude increases. So in some cases, the bending up, can be used to increase the swinging amplitude of the released beam. In this way it is possible to have swinging amplitudes in the orders of 20  $\mu\text{m}$  without the need to etch the substrate. Using the methods described in this paper, the upward curvature of such cantilevers can be better understood and even tuned by appropriate selection of oxide layers to enhance their performances.

**Acknowledgements** The Interferometer and Nanoindenter used in this research were obtained, through Birmingham Science City: Innovative Uses for Advanced Materials in the Modern World (West Midlands Centre for Advanced Materials Project 2), with support from Advantage West Midlands (AWM) and part funded by the European Regional Development Fund (ERDF).

This research has been funded by the UK EPSRC under EP/E026494/1 and by The University of Birmingham.

**Open Access** This article is distributed under the terms of the Creative Commons Attribution Noncommercial License which permits any noncommercial use, distribution, and reproduction in any medium, provided the original author(s) and source are credited.

## References

1. S. Timoshenko, *Strength of Materials*, (D. Van Nostrand Company Inc., USA, 1955), pp. 92–97, 136–140, 210–226
2. H. Lakdawala, G.K. Fedder, Analysis of temperature-dependent residual stress gradient in CMOS micromachined structures. *Transducers '99*, 526–529 (1999)
3. J.S. Pulskamp, A. Wickenden, R. Polcawich, B. Piekarski, M. Dubey, Mitigation of residual film stress deformation in multilayer microelectromechanical systems cantilever devices. *J. Vac. Sci. Technol., B*, **21**(6), 2482–2486 (2003)
4. J.A. Kalb, Q. Guo, X. Zhang, Y. Li, C. Sow, C.V. Thompson, Phase-change materials in optically triggered microactuators. *Journal of Microelectromechanical System* **17**(5), 1094–1103 (2007)
5. L.B. Freund, S. Suresh, *Thin Film Materials*, vol. 88 (Cambridge University Press, 2003), pp. 93–95, 125–127
6. W.J. Choi, Y. Jeon, J.H. Jeong, S.G. Kim, Energy harvesting MEMS device based on thin film piezoelectric cantilevers. *J. Electroceram.* **17**, 543–548 (2006)
7. Y.B. Jeon, R. Sood, J.H. Jeong, S.G. Kim, MEMS power generator with transverse mode thin film PZT. *Sens. Actuators, A*, **122**, 16–22 (2005)
8. G. Vasta, T.J. Jackson, J. Bowen, E. Tarte, New Multilayer Architectures for Piezoelectric  $BaTiO_3$  cantilever systems. *MRS Proceedings*, 1325, mrss11-1325-e08-05 (2011). doi:[10.1557/opl.2011.970](https://doi.org/10.1557/opl.2011.970)
9. A.C. Fischer-Cripps, *Nanoindentation* (2nd edn. Springer, New York, 2004), pp. 6–45
10. Micro Materials Ltd. (MML NanoTest manual 2004)
11. L. Latorre, P. Nouet, Y. Bertrand, P. Hazard, F. Pressecq, Characterization and modeling of a CMOS-compatible MEMS technology. *Sens. Actuators* **74**, 143–147 (1999)
12. S. Baglio, S. Castorina, N. Savalli, *Scaling Issues and Design of MEMS*. (John Wiley & Sons LTD, England, 2007)
13. Y. He, Heat capacity thermal conductivity and thermal expansion of barium titanate-based ceramics. *Thermochim. Acta* **419**, 135–141 (2004)
14. S. Huang, X. Zhang, Gradient residual stress induced elastic deformation of multilayer MEMS structures. *Sens. Actuators, A*, **134**, 177–185 (2007)
15. M. Ohring, *The Materials Science of Thin Films* (Academic Press, London, 1992), pp. 314–319
16. E. Bartolome, J.J. Roa, B. Bozzo, M. Segarra, X. Granados, Effective silver-assisted welding of YBCO blocks: mechanical versus electrical properties. *Supercond. Sci. Technol.* **23**, 045013 (6pp) (2010)
17. K. Khamchame, Thesis: Ferroelectric Heterostructures Growth and Microwave Devices. Department of Microelectronics and nanoscience, (Chalmers University of Technology, Goteborg, 2003)
18. A.C. Dent, C.R. Bowen, R. Stevens, M.G. Cain, M. Stewart, Effective elastic properties for unpoled barium titanate. *J. Eur. Ceram. Soc.* **27**, 3739–3743 (2007)
19. C.S. Zha, H.K. Mao, R.J. Hemley, Elasticity of  $MgO$  and a primary pressure scale to 55 GPa. *PNAS* **97**(25), 13494–13499 (2000)
20. T. Suzuki, Y. Nishi, M. Fujimoto, Defect structure in homoepitaxial non-stoichiometric strontium titanate thin films. *Philos. Mag., A*, **80**(3) 621–637 (2000)
21. I.B. Misirlioglu, S.P. Alpay, F. He, B.O. Wells, Stress induced monoclinic phase in epitaxial  $BaTiO_3$  on  $MgO$ . *J. Appl. Phys.* **99**, 104103 (2006)
22. J.A. Thornton, D.W. Hoffman, Stress related effects in thin films. *Thin Solid Films* **171**, 5–31 (1989)

23. AZoM.com, Strontium Titanate ( $\text{SrTiO}_3$ ) - properties and applications, (2004) <http://www.azom.com/Details.asp?ArticleID=2362>. Accessed 5 November 2011
24. J. Kawashima, Y. Yamada, I. Hirabayashi, Critical thickness and effective thermal expansion coefficient of YBCO crystalline film. *Physica C*, **306**, 114–118 (1998)
25. S.N. Bushmeleva, V.Y. Pomjakushin, E.V. Pomjakushina, D.V. Sheptyakov, A.M. Balagurov, Evidence for the band ferromagnetism in  $\text{SrRuO}_3$  from neutron diffraction. *J. Magn. Magn. Mater.*, **305**, 491–496 (2006)
26. Y. He, Heat capacity thermal conductivity and thermal expansion of barium titanate-based ceramics. *Thermochim. Acta*, **419**, 135–141 (2004)
27. SPI supplies, SPI Supplies Brand MgO Magnesium Oxide Single Crystal Substrates, Blocks, and Optical Components, (1999) <http://www.2spi.com/catalog/submat/magnesium-oxide.shtml>. Accessed 5 November 2011
28. B.L. Cheng, M. Gabbay, G. Fantozzi, W.J. Duffy, Mechanical loss and elastic modulus associated with phase transitions of barium titanate ceramics. *J. Alloys Compd.*, **211/212**, 352–355 (1994)
29. Z. Feng, E.G. Lovell, R.L. Engelstad, A.R. Mikkelson, P.L. Reuand Jaewoong Sohn, Film stress characterization using substrate shape data and numerical techniques. *Mat. Res. Soc. Symp. Proc.*, **750**, Y.3.4.1–Y.3.4.6 (2003)
30. O. Madelung, U. Rssler, M. Schulz, Magnesium oxide ( $\text{MgO}$ ) crystal structure, lattice parameters, thermal expansion. The Landolt-Bornstein Database (<http://www.springermaterials.com>), doi:[10.1007/10681719\\_206](https://doi.org/10.1007/10681719_206). vol. III/17B– 22A–41B SpringerMaterials



## Thin Solid Films

journal homepage: [www.elsevier.com/locate/tsf](http://www.elsevier.com/locate/tsf)

# Electrical properties of BaTiO<sub>3</sub> based ferroelectric capacitors grown on oxide sacrificial layers for micro-cantilevers applications

Giuseppe Vasta <sup>\*</sup>, Timothy J. Jackson <sup>1</sup>, Edward Tarte <sup>2</sup>

The University of Birmingham, School of Electrical Electronic and Computer Engineering, 52 Pritchatts road, Edgbaston, Birmingham B15 2TT, UK

---

## ARTICLE INFO

### Article history:

Received 4 August 2011

Received in revised form 7 November 2011

Accepted 8 November 2011

Available online 15 November 2011

---

### Keywords:

Barium titanate

Ferroelectric capacitors

Impedance

Yttrium barium copper oxide

Magnesium oxide

Sacrificial layers

Piezoelectric cantilevers

Pulse laser deposition

---

## ABSTRACT

An investigation of all oxide ferroelectric capacitors based on SrRuO<sub>3</sub>/BaTiO<sub>3</sub>/SrRuO<sub>3</sub> multi-layers grown on sacrificial oxide layers of YBa<sub>2</sub>Cu<sub>3</sub>O<sub>7</sub> and MgO for Micro-Electro-Mechanical systems applications is reported. By insertion of additional MgO or SrTiO<sub>3</sub> buffer layers the orientation of the BaTiO<sub>3</sub> film can be controlled allowing the fabrication of suspended cantilevers using the 31 and the 33 piezoelectric modes. The electrical properties of SrRuO<sub>3</sub>/BaTiO<sub>3</sub>/SrRuO<sub>3</sub> capacitors are changed compared with those grown directly on a single crystal substrate by the introduction of sacrificial layers. Circuit modeling of the electrical characteristics of these devices shows that a reduction of the deposition pressure for BaTiO<sub>3</sub> produces a decrease of the parasitic shunting conductance (modeled with a resistor in parallel to the capacitance of the device) which reduces the resistive losses present in the BaTiO<sub>3</sub> film. However for extremely low deposition pressure the quality of the polarization hysteresis loops is compromised. Particulates present on the surface of the YBa<sub>2</sub>Cu<sub>3</sub>O<sub>7</sub> increase the parasitic conductance at low frequency in the capacitive structure grown on this sacrificial layer. Good electrical properties are obtained for the capacitive structures grown on top of the MgO sacrificial layers at pressures equal or lower than 8 Pa.

G. Vasta, T. J. Jackson, E. Tarte

Electrical properties of BaTiO<sub>3</sub> based ferroelectric capacitors grown on oxide sacrificial layers  
for microcantilevers applications

Thin Solid Films  
520 (2012) 3071–3078

DOI: 10.1016/j.tsf.2011.11.032

This is the author's version of a work that was accepted for publication in *Thin Solid Films*. Changes resulting from the publishing process, such as editing, corrections, structural formatting, and other quality control mechanisms may not be reflected in this document. A definitive version was subsequently published in the reference given above. The DOI number of the final paper is also given above.

# **Electrical properties of BaTiO<sub>3</sub> based ferroelectric capacitors grown on oxide sacrificial layers for micro-cantilevers applications**

Giuseppe Vasta <sup>a</sup>, Timothy J. Jackson <sup>b</sup>, Edward Tarte <sup>c</sup>

*The University of Birmingham, School of Electrical Electronic and Computer Engineering, 52*

*Pritchatts road, Edgbaston, Birmingham B15 2TT UK*

<sup>a</sup> email: [pipvast@yahoo.it](mailto:pipvast@yahoo.it); tel: (+44) (0)1214144348 (corresponding author)

<sup>b</sup> email: [T.J.Jackson@bham.ac.uk](mailto:T.J.Jackson@bham.ac.uk); tel: (+44) (0)121414 4291

<sup>c</sup> email: [tartee@adf.bham.ac.uk](mailto:tartee@adf.bham.ac.uk); tel: (+44) (0)121414 4301

## **Abstract:**

An investigation of all oxides ferroelectric capacitors based on SrRuO<sub>3</sub>/BaTiO<sub>3</sub>/SrRuO<sub>3</sub> multi-layers grown on sacrificial oxide layers of YBa<sub>2</sub>Cu<sub>3</sub>O<sub>7</sub> and MgO for Micro-Electo-Mechanical systems applications is reported. By insertion of additional MgO or SrTiO<sub>3</sub> buffer layers the orientation of the BaTiO<sub>3</sub> film can be controlled allowing the fabrication of suspended cantilevers using the 31 and the 33 piezoelectric modes. The electrical properties of SrRuO<sub>3</sub>/BaTiO<sub>3</sub>/SrRuO<sub>3</sub> capacitors are changed compared with those grown directly on a single crystal substrate by the introduction of sacrificial layers. Circuit modeling of the electrical

characteristics of these devices shows that a reduction of the deposition pressure for BaTiO<sub>3</sub> produces a decrease of the parasitic shunting conductance (modeled with a resistor in parallel to the capacitance of the device) which reduces the resistive loss present in the BaTiO<sub>3</sub> film. However for extremely low deposition pressure the quality of the polarization hysteresis loops is compromised.

Particulates present on the surface of the YBa<sub>2</sub>Cu<sub>3</sub>O<sub>7</sub> increases the parasitic conductance at low frequency in the capacitive structure grown on this sacrificial layer. Good electrical properties are obtained for the capacitive structures grown on top of the MgO sacrificial layers at pressures equal or lower than 8 Pa.

*Keywords:* *BaTiO<sub>3</sub> ferroelectric capacitor; impedance measurement; ,YBa<sub>2</sub>Cu<sub>3</sub>O<sub>7</sub> and MgO sacrificial layer;, piezoelectric cantilevers.*

## 1 Introduction

In recent years investigations of piezoelectric materials with a perovskite structure and containing lead, have been widely performed for applications such as Micro-Electro-Mechanical systems (MEMS) energy harvesting devices [1,2] or sensors and actuators [3,4,5,6]. Lead containing piezoelectric-perovskite materials provide high strain-charge displacement conversion, but the environmental problems associated with lead have stimulated recent work focusing on the use of lead free piezoelectric materials [7].

$\text{BaTiO}_3$  is a lead free piezoelectric material whose growth has been investigated on a range of substrates [8,9,10,11]. A number of studies have reported the performance of  $\text{BaTiO}_3$  based ferroelectric capacitors [12] which can find applications also in the field of memories [6]. This work focuses on the properties of  $\text{BaTiO}_3$  thin films in MEMS device like micro-cantilevers with a view to applications as sensors, actuators and energy harvesting devices. Sacrificial layers on which a multi-layer stack can be grown are necessary to fabricate micro-cantilevers. The properties of  $\text{BaTiO}_3$  capacitors grown on different multi-layers are expected to differ from the properties of the thin films directly deposited on the substrate.

We have recently shown that it is possible to suspend multilayer cantilevers containing a  $\text{BaTiO}_3$  film grown on  $\text{YBa}_2\text{Cu}_3\text{O}_7$  sacrificial layers [7]. The advantage of using  $\text{YBa}_2\text{Cu}_3\text{O}_7$  as sacrificial layer is the ease with which it can be etched in weak  $\text{HNO}_3$  solutions. In addition its perovskite-based structure allows the growth on its surface of epitaxial multi-layers of  $\text{SrRuO}_3/\text{BaTiO}_3/\text{SrRuO}_3$  and  $\text{SrRuO}_3/\text{BaTiO}_3/\text{SrRuO}_3/\text{SrTiO}_3$  which can be used as a 31 mode energy harvester, or  $\text{SrRuO}_3/\text{BaTiO}_3/\text{MgO}/\text{SrTiO}_3$  which can be used as a 33 mode energy harvester [7]. In our previous work [7], the electrical properties of these capacitive structures grown on a (001) oriented  $\text{SrTiO}_3$  substrate were reported. However as we will show, when these capacitors are grown on thick (over 400 nm)  $\text{YBa}_2\text{Cu}_3\text{O}_7$  or  $\text{MgO}$  sacrificial layers the electrical properties of the  $\text{BaTiO}_3$  change. This article describes the results of a study of the electrical properties of these structures as function of the deposition conditions.

## 2 Experimental procedure

Multi-layer thin films were grown on **(001)** oriented SrTiO<sub>3</sub> substrates by Pulsed Laser Deposition using a KrF excimer laser with a wavelength of 248 nm. A 4 Hz repetition rate was used with the laser beam focused to a spot size of 2.4 mm<sup>2</sup> on the target providing a fluence of 3.4 J/cm<sup>2</sup>. The distance between the SrTiO<sub>3</sub> substrate and the target material was set to 5.7 cm. All the films were grown in an oxygen flow environment at pressures of 20 Pa for the YBa<sub>2</sub>Cu<sub>3</sub>O<sub>7</sub>, 40 Pa for the SrRuO<sub>3</sub>, 26.66 Pa for the MgO, 8 Pa, 0.40 Pa and 0.013 Pa for the BaTiO<sub>3</sub> and 28 Pa for the SrTiO<sub>3</sub>.

The YBa<sub>2</sub>Cu<sub>3</sub>O<sub>7</sub> film were deposited at a temperature of 740 °C in order to reduce the number of outgrowths which usually form at higher deposition temperatures [13], all the other layers were grown at the temperature of 780 °C. After the deposition, the multi-layers were cooled in 900 mbar O<sub>2</sub> static environment, with dwells of 15 minutes at 600 °C and of 30 minutes at 450 °C during cooling to fully oxygenate the YBa<sub>2</sub>Cu<sub>3</sub>O<sub>7</sub> layer [14]. The dwells were maintained also in the case of stacks of thin films which did not contain the YBa<sub>2</sub>Cu<sub>3</sub>O<sub>7</sub> in order to maintain consistency for oxygenation of the BaTiO<sub>3</sub> layer [8]. Compared to the other oxide films, the BaTiO<sub>3</sub> was grown to a relatively low pressure.

The thin films were patterned by contact photolithography and argon ion beam milling, using a Karl Suss mask aligner and an Oxford Applied Research IM150 ion milling system. Photoresist was used to protect the regions of the sample which would become the cantilevers. Milling through windows developed in the photoresist, was used to define the cantilever geometry. The cantilevers were released by undercutting the sacrificial layer in HNO<sub>3</sub> solutions. A concentration of 0.1% was used to undercut the YBa<sub>2</sub>Cu<sub>3</sub>O<sub>7</sub> sacrificial layer while a concentration of 20% was needed to undercut the MgO sacrificial layer. The sample was then

rinsed in distilled water and dried by using critical point drying in order to avoid the breakage of the suspended structures due to stiction [15].

In the case of the 31 piezoelectric capacitors, the  $\text{YBa}_2\text{Cu}_3\text{O}_7$  or the  $\text{MgO}$  sacrificial layer together with a thin  $\text{SrTiO}_3$  film and a  $\text{SrRuO}_3$  conductive layer were grown first and then the bottom electrodes and their contact pads were patterned by contact photolithography and argon ion beam milling. The sample was then returned to the deposition chamber, 15 minutes of annealing at the  $\text{BaTiO}_3$  deposition temperature was performed, to repair the regions damaged by the milling, followed by deposition of the  $\text{BaTiO}_3$  piezoelectric film and the  $\text{SrRuO}_3$  film. Finally the top electrode was patterned and some windows, necessary to contact the bottom electrode layer, were opened through the  $\text{BaTiO}_3$ .

In the case of the 33 piezoelectric capacitors the  $\text{YBa}_2\text{Cu}_3\text{O}_7$  sacrificial layer was first grown followed by the deposition of a  $\text{SrTiO}_3$  and of a  $\text{MgO}$  thin film. The vacuum was then broken (our deposition system allows the deposition *in situ* of only three films) and then another thin  $\text{MgO}$  layer, the  $\text{BaTiO}_3$  and the  $\text{SrRuO}_3$  were deposited. Finally the top electrodes and their contact pads were patterned. In the case of an  $\text{MgO}$  sacrificial layer, the  $\text{MgO}$ , the  $\text{BaTiO}_3$  and the  $\text{SrRuO}_3$  can be grown *in situ* and then the top electrode can be patterned.

Atomic Force Microscope (AFM) measurements on the surface of the deposited film were performed in contact mode on an area of  $10 \mu\text{m} \times 10 \mu\text{m}$  at a frequency of 0.4 Hz. The measurements system consists of a Veeco autoprobe CB based unit AP0100 controlled by a data acquisition software supplied by Veeco.

The structure of the films was assessed by using X-ray diffraction. The measurements were performed using the CuK $\alpha_1$  radiation (1.54056 Å) of a four circle Siemens D5000 diffractometer, the symmetrical Bragg-Brentano configuration has been used.

The diffractometer software allows the angles at which diffraction peaks are expected to be determined. The detector is then moved to the indicated positions and a scan is run. If the diffraction peak is found in the indicated position, further scans allow a refinement in the evaluation of the diffraction angle.

Capacitance measurements were performed on both the 31 and the 33 structures by means of an Agilent 4294A precision impedance analyzer with a source voltage of 1 V over the frequency range of 50 Hz – 50 kHz.

Hysteresis loop measurements were run on the 31 structures by using a custom made Sawyer and Tower circuit and applying sinewave voltages with peak to peak amplitude up to 50 V and frequency of 20 kHz.

### **3 Device description and modeling**

The scope of this article is the investigation of multi-layer cantilevers, containing a BaTiO<sub>3</sub> based capacitive structure for use as energy harvesting devices. These devices convert the mechanical vibrations of suspended beams, which may be terminated with a proof mass, into an electrical signal, which may be used as a source of electrical power.

There are two piezoelectric modes which are commonly used in piezoelectric transducers, they are the 33 and the 31 modes, fig 1 [1,2]. In a 31 mode device the input stress  $\sigma_{xx}$  is perpendicular

to the developed electric field and the mechanical strain is converted into the separation of charge by using a parallel plate capacitor.

In a 33 mode device the input stress  $\sigma_{xx}$  is parallel to the developed electric field and the mechanical strain is converted into charges by using an interdigitated capacitor.

The generated output voltage can be expressed as [1,2]:

$$V_{3i} = \sigma_{xx} g_{3i} t \quad (1)$$

where  $g_{3i}$  [Vm/N] is the piezoelectric constant, and  $t$  is the electrode spacing. The output voltage is expected to be larger in the 33 mode because the BaTiO<sub>3</sub> piezoelectric constant  $g_{33}$  is larger than the  $g_{31}$  piezoelectric constant [16], furthermore the electrode spacing is bigger in the 33 mode.

In our case the 31 mode devices are given by the following layer sequences:

SrRuO<sub>3</sub>/BaTiO<sub>3</sub>/SrRuO<sub>3</sub> and SrRuO<sub>3</sub>/BaTiO<sub>3</sub>/SrRuO<sub>3</sub>/SrTiO<sub>3</sub> grown on a MgO or on a YBa<sub>2</sub>Cu<sub>3</sub>O<sub>7</sub> sacrificial layer respectively. For the 33 mode devices the stack SrRuO<sub>3</sub>/BaTiO<sub>3</sub>/MgO/SrTiO<sub>3</sub> can be grown on a YBa<sub>2</sub>Cu<sub>3</sub>O<sub>7</sub> sacrificial layer, alternatively a SrRuO<sub>3</sub>/BaTiO<sub>3</sub> bi-layer can be grown on a MgO sacrificial layer. The reason for the choice of such layer sequences will be explained in the subsection 4.1.

The model which has been adopted to describe the fabricated capacitors is that one depicted in fig. 2 where C represents the capacitance of the device, R is a parallel resistor modeling the parasitic shunting conductance representing the losses present in the BaTiO<sub>3</sub> film [17], and R<sub>L</sub> is the series resistance which models the resistive contribution of the SrRuO<sub>3</sub> lines connecting the device to the contact pads. When a dc voltage is applied to the circuit of fig. 2 the capacitor is an

open circuit, in this way the sum of the parallel and of the series resistor can be estimated. Current versus voltage measurements on SrRuO<sub>3</sub> lines reveals a SrRuO<sub>3</sub> resistivity of 2.84 Ωμm, in agreement with values reported in [18], and this value can be used to estimate the series resistance so that the parallel resistor can be calculated by subtracting the series resistance from the measured dc resistance.

The impedance of the circuit shown in fig. 2 has the following expression:

$$z(j\omega) = R_L + R / [1+(\omega CR)^2] - j \omega C(R)^2 / [1+(\omega CR)^2] \quad (2).$$

The value of the capacitance can be estimated by equating the measured imaginary part of the impedance to the imaginary part of the right hand side of equation 2. This gives rise to quadratic equation, the root that is inconsistent with the real part of the impedance obtained using the series and parallel resistances as described above is rejected.

This can be repeated at different frequencies and finally the estimated capacitance can be chosen equal to the average of the calculated values. Once that the parameters R, R<sub>L</sub> and C have been estimated, their value have been refined by minimizing the quantity:

$$[Re(z)_m - Re(z)_p]^2 + [Im(z)_m - Im(z)_p]^2 \quad (3)$$

where Re(z)<sub>m</sub> is the measured real part of the impedance and Re(z)<sub>p</sub> is the real part of the impedance calculated by assuming the lumped element model of fig. 2, similar nomenclature has been used for the imaginary part of the impedance.

## 4 Results and discussion

As previously stated the  $\text{YBa}_2\text{Cu}_3\text{O}_7$  was chosen as the sacrificial layer because it is easy to etch in weak  $\text{HNO}_3$  solutions. Furthermore it allows the subsequent epitaxial growth of thin films like  $\text{BaTiO}_3$ ,  $\text{SrRuO}_3$ ,  $\text{SrTiO}_3$  and  $\text{MgO}$ .

Fig. 3 shows a  $\text{SrRuO}_3/\text{BaTiO}_3/\text{SrRuO}_3$  u-shape cantilever with a simple beam connected in series, the three-layer were grown on a  $\text{YBa}_2\text{Cu}_3\text{O}_7$  sacrificial layer which was removed by undercutting. The  $\text{SrRuO}_3$  works as an electrode layer for the ferroelectric capacitor and the  $\text{BaTiO}_3$  is the piezoelectric material.

Alternatively  $\text{MgO}$  can be chosen as sacrificial layer, however in this case stronger  $\text{HNO}_3$  solutions are necessary for its undercut

#### **4.1 X-ray diffraction analysis**

X-ray diffraction measurements performed on different thin film stacks grown on  $\text{YBa}_2\text{Cu}_3\text{O}_7$  sacrificial layers showed that the  $\text{BaTiO}_3$  grows with the polar axis perpendicular to the plane of the film on  $\text{SrTiO}_3$  and on  $\text{SrRuO}_3$ , while it grows with the polar axis parallel to the plane of the film on  $\text{MgO}$ , as summarized in Table 1. This may be due to the smaller lattice mismatch between the  $\text{BaTiO}_3$  polar axis and the lattice constant of  $\text{MgO}$  [8].

In the case of  $\text{BaTiO}_3$  grown on a  $\text{MgO}$  film the measured polar lattice parameter of  $4.002 \text{ \AA}$  appears smaller than the bulk value because it is an average value. There are two possible orthogonal orientations when the polar axis is in the plane of the substrate and a non polar axis must also lie in plane [7]. For a  $100 \text{ nm}$  thick  $\text{BaTiO}_3$  film sandwiched between two  $\text{SrRuO}_3$  layers, see Table 1, the polar axis showed an elongation equal to the  $0.83\%$  of its length in bulk material, in agreement with observations [12].

When the polar axis is perpendicular to the plane of the film, the polarization can be easily accessed by a parallel plate capacitor, so a three-layer SrRuO<sub>3</sub>/BaTiO<sub>3</sub>/SrRuO<sub>3</sub> parallel plate capacitor grown on the top of a YBa<sub>2</sub>Cu<sub>3</sub>O<sub>7</sub> film works as a 31 device (SBSY device). To improve the interface between the YBa<sub>2</sub>Cu<sub>3</sub>O<sub>7</sub> and the SrRuO<sub>3</sub> and to achieve a better undercut of the sacrificial layer, a SrTiO<sub>3</sub> buffer layer can be introduced between the sacrificial layer and the bottom electrode [7]. The layer sequence which has to be deposited to produce a 31 device is then: SrRuO<sub>3</sub>/BaTiO<sub>3</sub>/SrRuO<sub>3</sub>/SrTiO<sub>3</sub>/YBa<sub>2</sub>Cu<sub>3</sub>O<sub>7</sub> (SBSSY device).

When the polar axis is parallel to the surface of the film, the polarization can be accessed by using an interdigitated capacitor. In this case a SrRuO<sub>3</sub>/BaTiO<sub>3</sub>/MgO/YBa<sub>2</sub>Cu<sub>3</sub>O<sub>7</sub> (SBMY device) stack can be used. The MgO layer changes the growth orientation of the BaTiO<sub>3</sub> (and it is not used as sacrificial layer in this sequence), the consequence is that the polar axis will be parallel to the surface of the film. Again to achieve a more efficient undercut a SrTiO<sub>3</sub> buffer layer can be introduced between the MgO and the YBa<sub>2</sub>Cu<sub>3</sub>O<sub>7</sub> [7]. So the layer sequence to use in the case of a 33 device is: SrRuO<sub>3</sub>/BaTiO<sub>3</sub>/MgO/SrTiO<sub>3</sub>/YBa<sub>2</sub>Cu<sub>3</sub>O<sub>7</sub> (SBMSY device). If an MgO sacrificial layer is used the sequence becomes SrRuO<sub>3</sub>/BaTiO<sub>3</sub>/MgO (SBM device).

In the case of a MgO sacrificial layer, the stacks to use as 31 devices are SrRuO<sub>3</sub>/BaTiO<sub>3</sub>/SrRuO<sub>3</sub>/MgO (SBSM device) and SrRuO<sub>3</sub>/BaTiO<sub>3</sub>/SrRuO<sub>3</sub>/SrTiO<sub>3</sub>/MgO (SBSSM device). For the SBSSM device the use of the SrTiO<sub>3</sub> layer allows the growth of BaTiO<sub>3</sub> with the polar axis out of plane all over the sample after the patterning and the milling of the SrRuO<sub>3</sub> bottom electrode.

The use of the MgO sacrificial layer presents the advantage of dealing with a simple tri-layer, however the undercut of the MgO requires a wet etching of several hours in 20% HNO<sub>3</sub>. When

the  $\text{YBa}_2\text{Cu}_3\text{O}_7$  is used, a wet etch of few minutes in 0.1%  $\text{HNO}_3$  is necessary to suspend the structures.

#### **4.2 Impedance measurements and AFM investigation**

Impedance measurements showed that  $\text{SrRuO}_3(100 \text{ nm})/\text{BaTiO}_3(400 \text{ nm})/\text{SrRuO}_3(150 \text{ nm})$  and  $\text{SrRuO}_3(100)/\text{BaTiO}_3(300 \text{ nm})/\text{MgO}(60 \text{ nm})$  structures grown on  $\text{SrTiO}_3$  substrates have capacitive behavior when the  $\text{BaTiO}_3$  is deposited in oxygen flow at a pressure equal or lower than 8 Pa. This is shown by the value of the impedance phase. Fig. 4 shows the modulus and the phase of the impedance for a  $\text{SrRuO}_3/\text{BaTiO}_3/\text{SrRuO}_3$  device. Its phase varies between -85° and -82° in the frequency range 40Hz-40 kHz revealing a clear capacitive behavior. When the  $\text{BaTiO}_3$  was deposited in oxygen flow at a pressure of 20 Pa these structures exhibited resistive behavior [7].

With the introduction of an oxide sacrificial layer under the multi-layer capacitive structures the electrical properties of the  $\text{BaTiO}_3$  change.

For  $\text{YBa}_2\text{Cu}_3\text{O}_7$  used as sacrificial layers, SBSSY 31 mode and SBMSY 33 mode structures have been investigated.

The  $\text{BaTiO}_3$  films were grown at pressures of 8 Pa. These devices presented poor capacitive behavior. Fig.5 shows the impedance measurement on a SBSSY 31 device with the  $\text{BaTiO}_3$  layer deposited at a pressure of 8 Pa. In this case the impedance is mainly resistive, around 20 kHz some capacitive effect starts to be visible, at 50 kHz the impedance phase is around -23°. Our impedance analyzer allows a minimum measurement frequency of 40Hz, at which frequency the

phase of the impedance is equal to -0.1 so the impedance can be considered as pure resistive and the parallel and the series resistances can be calculated.

The parallel resistance is estimated equal to 1.4 K $\Omega$  resulting in a resistance area (RA) product of  $44.1 \times 10^5 \Omega \mu\text{m}^2$ . The calculated series resistance has a value of 1.086 K $\Omega$  and the estimated capacitance is equal to 1.98 nF resulting in a capacitance per unit area (C/A) of  $6.28 \times 10^{-13} \text{ F}/\mu\text{m}^2$ .

Fig. 5 also shows a fit to the data obtained using the lumped element model, illustrating the good agreement between the model and the measured data. This device shows poor capacitive behavior to the extent that the low value of the parallel resistance dominates the parallel capacitor. Despite this, X-ray measurements on stacks grown on YBa<sub>2</sub>Cu<sub>3</sub>O<sub>7</sub> sacrificial layers, revealed the presence of a crystal structure in the BaTiO<sub>3</sub> films.

Studies on the pulsed laser deposition of YBa<sub>2</sub>Cu<sub>3</sub>O<sub>7</sub> films reported the presence of different types of particulates on their surface [19]. It is likely that such particulates degrade the quality of the layers deposited on their surface, by creating resistive paths through the capacitive structures which might be responsible for the low value of the RA product.

In order to investigate this, an Atomic Force Microscope was used to examine the surface of the deposited YBa<sub>2</sub>Cu<sub>3</sub>O<sub>7</sub> films. Fig. 6a shows an AFM scan on the surface of a 150 nm YBa<sub>2</sub>Cu<sub>3</sub>O<sub>7</sub> layer, on whose surface it is possible to see an outgrowth with a height comparable to the film thickness, despite the relatively low deposition temperature. Such outgrowths are also present after the deposition of a 100 nm SrTiO<sub>3</sub> layer as shown in, fig. 6b. The effect of such outgrowths on the upper layers can be reduced using a thicker SrTiO<sub>3</sub> layer. Fig. 6c shows an AFM scan on a SrTiO<sub>3</sub>(500 nm)/ YBa<sub>2</sub>Cu<sub>3</sub>O<sub>7</sub>(400 nm) bi-layer which confirms that the particulates present on the surface of the film are fewer in number and generally smaller.

Fig. 7 reports the impedance measurements of a SBSSY device with a 1  $\mu\text{m}$  thick SrTiO<sub>3</sub> film on the YBa<sub>2</sub>Cu<sub>3</sub>O<sub>7</sub> sacrificial layer. The oxygen pressure during deposition of the BaTiO<sub>3</sub> was equal to 8 Pa. Also in this case the impedance is not fully capacitive, at 40 Hz the impedance phase is equal to -0.5°, again at such frequency the impedance is considered as purely resistive and so the parallel and the series resistances can be estimated. The series resistance is equal to 1.086 K $\Omega$ , the parallel resistance has a value of 31.78 K $\Omega$  resulting in a RA product of  $19.54 \times 10^7$   $\Omega\mu\text{m}^2$  and the capacitance is equal to 480 pF, giving a C/A of  $7.8 \times 10^{-14}$  F/ $\mu\text{m}^2$ .

The lines in figs. 7 represent the modulus and the phase for the impedance of the lumped element model, the points are the measured values. The impedance modulus of the lumped element model agrees quite well with the measured data while an error of 8% is present in the value of the impedance phase over 20 kHz.

The introduction of a thicker SrTiO<sub>3</sub> buffer layer reduces the parasitic shunting conductance and so the losses which are present in the BaTiO<sub>3</sub> film due to the outgrowths on the surface of the YBa<sub>2</sub>Cu<sub>3</sub>O<sub>7</sub> sacrificial layer. This is illustrated by the higher value of the RA product, however the quality of these devices is still not satisfactory especially at low frequencies where the resistive part of the impedance dominates.

In the case of capacitors grown directly on the substrate it has been demonstrated that the reduction of the BaTiO<sub>3</sub> deposition pressure reduces the parasitic shunting conductance and so losses present in the film [7]. When a YBa<sub>2</sub>Cu<sub>3</sub>O<sub>7</sub> sacrificial layer is used a further reduction of the BaTiO<sub>3</sub> deposition pressure is not possible as there would be dissociation of the sacrificial layer at the BaTiO<sub>3</sub> deposition temperature [20].

Another solution is to use an MgO sacrificial layer, as this material can still be etched in HNO<sub>3</sub> although a high acid concentration and longer etching time are necessary. The advantage of the MgO sacrificial layer is that it does not dissociate at low pressures at the BaTiO<sub>3</sub> deposition temperature.

Fig. 8 shows the impedance measurement on a SBSSM device. Assuming for this device the model of fig. 2, the resistance of the lines R<sub>L</sub> is 1.17 KΩ, the parallel resistor R is equal to 1.966 MΩ resulting in a RA product of 61.93\*10<sup>8</sup> Ωμm<sup>2</sup>. The capacitance is equal to 95.66 pF, giving a C/A of 3.04\*10<sup>-14</sup> F/μm<sup>2</sup>. The plots show a good agreement between the model and the measured data.

There is a difference of one order of magnitude between the RA product of this device and that one of the device using a 1μm thick SrTiO<sub>3</sub> buffer layer on a YBa<sub>2</sub>Cu<sub>3</sub>O<sub>7</sub> sacrificial layer. Compared to that case, this high value of the RA product makes the capacitive part of the impedance dominate at much lower frequencies. At 5.5 kHz the phase of the total impedance is equal to -80°, the capacitive part of the impedance is roughly 7 times smaller than the parallel resistance and 250 times bigger than the series resistance, so over 5.5 kHz the device can be approximated as a pure capacitor.

If the BaTiO<sub>3</sub> deposition pressure is further reduced to 0.013 Pa the losses are eliminated also at low frequency, this is shown in fig. 9, and an impedance phase of 88° is already present at 50Hz. Due to the high value of the impedance phase at low frequencies, the parallel resistor can be approximated as an open circuit and the equivalent model of the device is given by the resistor R<sub>L</sub> in series with the capacitor C. For this device the series resistance was estimated equal to 1.086 KΩ while the capacitance is equal to 55.57 pF resulting in a C/A of 1.76\*10<sup>-14</sup> F/μm<sup>2</sup>. By

using these values in the lumped element model good agreement is obtained with the measured data, fig. 9. This demonstrates that a reduction of the BaTiO<sub>3</sub> deposition pressure reduces the parasitic shunting conductance and so the resistive losses present in the film. Furthermore in this case the approximation of the parallel resistor with an open circuit works quite well and the behavior of the device can be approximated as purely capacitive.

The reduction of the BaTiO<sub>3</sub> deposition pressure also produces a reduction in the value of the parallel capacitance. Figs. 8 and 9 report the impedance measurements of two devices with the same faced area and the same BaTiO<sub>3</sub> thickness. For a BaTiO<sub>3</sub> deposition pressure of 8 Pa a C/A of  $3.04 \times 10^{-14}$  F/ $\mu\text{m}^2$  was measured while for a BaTiO<sub>3</sub> deposition pressure of 0.013 Pa the C/A was reduced to  $1.76 \times 10^{-14}$  F/ $\mu\text{m}^2$ . It was reported that in SrTiO<sub>3</sub>/BaTiO<sub>3</sub> systems grown by Pulsed Laser Deposition the dielectric constant increases when the oxygen deposition pressure increases [21]. If the oxygen pressure during the growth of the thin films is low it is more favorable to form oxygen vacancies in the oxide films during the process which results in a decrease of the dielectric constant [21].

The layer sequences, the RA products, the C/A and the BaTiO<sub>3</sub> deposition pressures for the investigated devices are summarized in table 2.

#### 4.3 Hysteresis measurements

The disadvantage of extremely low BaTiO<sub>3</sub> deposition pressures is the degradation of the hysteresis loop of the ferroelectric capacitors. Fig. 10a represents the hysteresis loop of a SrRuO<sub>3</sub>/BaTiO<sub>3</sub>/SrRuO<sub>3</sub> capacitor grown on the SrTiO<sub>3</sub> substrate at a pressure of 8 Pa, in this case the residual polarization is equal to 5.3  $\mu\text{C}/\text{cm}^2$ . Fig. 10b shows the hysteresis loop of a SBSSM device containing a BaTiO<sub>3</sub> at a pressure of 8 Pa, the residual polarization is equal to 2.5

$\mu\text{C}/\text{cm}^2$ . Finally fig. 10c shows the hysteresis loop of a SBSM device having a BaTiO<sub>3</sub> film grown at a pressure of 0.013 Pa. In this case the hysteresis behavior is not clear and the loop seems to be degraded into a double loop.

The presence of defects in the BaTiO<sub>3</sub> film can produce a distorted loop as that one reported in fig. 10c [22]. Oxygen vacancies produce a lower dielectric constant in BaTiO<sub>3</sub> films grown at low pressure, so we believe that the degradation of the hysteresis loops arises from defects due to oxygen deficiency in the BaTiO<sub>3</sub> film.

#### 4.4 Discussion

The performances of BaTiO<sub>3</sub> based ferroelectrics capacitors grown on MgO and YBa<sub>2</sub>Cu<sub>3</sub>O<sub>7</sub> sacrificial layers have been assessed. These sacrificial layers allow the epitaxial growth of thin film stacks containing BaTiO<sub>3</sub>, SrRuO<sub>3</sub> and SrTiO<sub>3</sub>.

In both cases in order to produce a capacitive structure the oxygen pressure used for deposition of the BaTiO<sub>3</sub> should be equal to or lower than 8 Pa.

For PLD deposition depending on the surface mobility of the atoms, the growth of the film may be accompanied by the formation of stacking faults and amorphous and void like grain boundaries [23]. The surface mobility of the atoms is influenced by the deposition pressure, the substrate temperature and the laser energy.

Our investigations show that a reduction of the BaTiO<sub>3</sub> deposition pressure reduces the losses present in the fabricated capacitors, this happens either in the case of capacitors grown on the substrate or on the sacrificial layer. Higher deposition pressures imply a larger number of

collisions in the path between the material target and the substrate. The energy lost in the ablation path produces a lower mobility of the atomic species on the substrate [19].

In the case of multi-layers grown on the top of SrTiO<sub>3</sub>(250 nm)/YBa<sub>2</sub>Cu<sub>3</sub>O<sub>7</sub>(500 nm) bi-layers, the presence of outgrowths on the surface of the YBa<sub>2</sub>Cu<sub>3</sub>O<sub>7</sub> sacrificial layer, produces a low value of the parallel resistance which dominates the parallel capacitance.

With the introduction of a thicker SrTiO<sub>3</sub> buffer layer the effect of the YBa<sub>2</sub>Cu<sub>3</sub>O<sub>7</sub> outgrowths on the fabricated capacitor is reduced and this is testified by an increase of the RA product.

However a further reduction of the film losses which correspond to an increase of the RA product and to a decrease of the parasitic shunting conductance is desirable. To reduce the losses present in the BaTiO<sub>3</sub> film its deposition pressure can be reduced, however for multi-layers containing YBa<sub>2</sub>Cu<sub>3</sub>O<sub>7</sub> the minimum BaTiO<sub>3</sub> deposition pressure is limited by the dissociation of the sacrificial layer.

The structures grown on the MgO sacrificial layer show a value of the resistance area product which is at least one order of magnitude bigger than that one of the devices using the YBa<sub>2</sub>Cu<sub>3</sub>O<sub>7</sub> sacrificial layer. Furthermore the RA product increases with the reduction of the BaTiO<sub>3</sub> deposition pressure this produce structures approaching the behavior of a pure capacitor. However with the reduction of the deposition pressure the value of the capacitance per unit area decreases and the quality of the hysteresis loop downgrades. This may be due to the oxygen vacancies present in BaTiO<sub>3</sub> grown at low pressures.

To increase the mobility of the atomic species on the substrate, a higher BaTiO<sub>3</sub> deposition temperature rather than a low deposition pressure can be used. Stacks containing a BaTiO<sub>3</sub> layer grown at temperatures of 850 °C and at a pressure of 8 Pa, show the presence of holes on the top

surface of the stack which can be due to thermal stresses produced during the cooling down of the multi-layers. Furthermore some layers peel off during the wirebonding of the pads of the capacitors, necessary for the electrical characterization of the devices.

Another parameter which can be used to increase the mobility on the substrate of the incoming atoms is the laser energy, however the deposition energy is very near to the maximum achievable with our apparatus.

## 5 Conclusions

All oxide multi-layer structures containing BaTiO<sub>3</sub> can find applications as MEMS devices in the field of energy harvesting or as components of sensors and actuators. Layers sequences like SrRuO<sub>3</sub>/BaTiO<sub>3</sub>/SrRuO<sub>3</sub>/SrTiO<sub>3</sub>/YBa<sub>2</sub>Cu<sub>3</sub>O<sub>7</sub> (SBSSY device), SrRuO<sub>3</sub>/BaTiO<sub>3</sub>/SrRuO<sub>3</sub>/SrTiO<sub>3</sub>/MgO (SBSSM device), SrRuO<sub>3</sub>/BaTiO<sub>3</sub>/MgO/SrTiO<sub>3</sub>/YBa<sub>2</sub>Cu<sub>3</sub>O<sub>7</sub> (SBMSY device) and SrRuO<sub>3</sub>/BaTiO<sub>3</sub>/SrTiO<sub>3</sub>/MgO(SBSM device) allow the use of both the 31 and the 33 piezoelectric modes.

The YBa<sub>2</sub>Cu<sub>3</sub>O<sub>7</sub> is easily etched in weak acids like 0.1% HNO<sub>3</sub> however the structures grown on top do not behave as pure capacitors but present losses.

The stacks grown on the MgO sacrificial layer show a value of the resistance area product which is at least one order of magnitude bigger than that one of the devices using the YBa<sub>2</sub>Cu<sub>3</sub>O<sub>7</sub> sacrificial layer. Furthermore the RA product increases with the reduction of the BaTiO<sub>3</sub> deposition pressure but the quality of the hysteresis loop downgrades.

A good compromise is reached for the BaTiO<sub>3</sub> deposition pressure of 8 Pa.

Future developments for these kind of structures consist in the reduction of the resistive losses for the stacks containing YBa<sub>2</sub>Cu<sub>3</sub>O<sub>7</sub> and in the recovery of the capacitive behavior at low frequencies.

For the stacks using the MgO sacrificial layer, and for BaTiO<sub>3</sub> growth pressures equal to 8 Pa, a reduction of the resistive losses below 1 kHz it is necessary. Alternatively an improving of the hysteresis loop can be reached for the multi-layers containing BaTiO<sub>3</sub> grown at pressures below 8 Pa.

## Acknowledgements

This research has been funded by the UK EPSRC under EP/E026494/1 and by The University of Birmingham.

## References

- 1 Y. B. Jeon, R. Sood, J. H. Jeong, S. G. Kim, Sensor Actuat. A-Phys. 122 (2000) 16
- 2 J. W. Choi, Y. Jeon, J. H. Jeong, R. Sood, S. G. Kim, J. Electroceram. 17 (2006) 543
- 3 Q. Q. Zhang, S. J. Gross, S. Tadigadapa, T. N. Jackson, F. T. Djuth, S. T. McKinstry, Sensor Actuat. A-Phys. 105 (2003) 91
- 4 F. F. C. Duval, S. A. Wilson, G. Ensell, N. M. P. Evanno, M. G. Cain, R. W. Whatmore, Sensor Actuat. A-Phys. 133 (2007) 35
- 5 F. F. C. Duval, R. A. Dorey, R. W. Wright, Z Huang, R. W. Whatmore, IEEE Trans. Ultrason., Ferroelectr., Freq. Control 51(2004) 1255

6 N. Setter, D. Damjanovic, L. Eng, G. Fox, S. Gevorgian, S. Hong, A Kingon, H. Kohlstedt, N. Y. Park, G. B. Stephenson, I. Stolitchnov, A. K. Tagantsev, D. V. Taylor, T. Yamada, S Streiffer, J. Appl. Phys. 100 (2006) 051606-1

7 G. Vasta, T. J. Jackson, J. Bowen, E. Tarte, New multilayer architecture for piezoelectric BaTiO<sub>3</sub> cantilever systems, MRS Proc. 1325 (2011) e08-05

8 F. X. Wang, W. Li, F. Lu, H. Hu, K. M. Wang, Z. G. Liu, Y. Zhu, Nucl. Instr. Meth. Phys. Res. B 191 (2002) 778

9 K. Sato, M. Takahashi, N. Matsunami, Y. Takai, Supercond. Sci. Tech. 9 (1996) A156

10 D. H. Kim, H. S. Kwok (1995), Appl. Phys. Lett. 67 (1995) 1803

11 Y. Yang, Z. Wang , J. F. Li, D. Viehland, J. Nanomater. 2010 (2010) 756319

12 K. J. Choi, M. Biegalski, Y. L. Li, A. Sharan, J. Schubert, R. Uecker, P. Reiche, Y. B. Chen, X. Q. Pan, V. Gopalan, L. Q. Chen, D. G. Schlom, C. B. Eom, Science 306 (2004) 1005

13 H. Sato, F. J. G. Roesthuis, A. H. Sonnenberg, A. J. H. M.Rijnders, H. Rogalla, D. H. A. Blank, Supercond. Sci. Tech. 13 (2000) 522

14 H. J. H. Smilde, H. Hilgenkamp, G. J. Gerritsma, D. H. A. Blank, H. Rogalla, IEEE Trans Appl. Supercond. 11 (2001) 501

15 L. Pellegrino, M. Biasotti, E. Bellingeri, C. Bernini, A. S. Siri, D. Marre` , Adv. Mater. 21 (2009) 2377

16 D. Berlincourt, H. Jaffe, Phys. Rev. 111 (1958) 143

17 E. J. Abram, D. C. Sinclair, A. R. West, J. of Electroceram. 10 (2003) 165

18 X. D. Wu, S. R. Folty, R. C. Dye, Y. Coulter, R. E. Muenchausen, Appl. Phys. Lett. 62 (1993) 2434

19 S. Proyer, E. Stangl, M. Borz, B. Hellebrand, D. Bauerle, Physica C 257 (1996) 1

20 R. Wordenweber, Supercond. Sci. Tech. 12 (1999) R86

21 B. R. Kim, T. U. Kim, W. J. Lee, J. H. Moon, B. T. Lee, H. S. Kim, J. H. Kim, Thin Solid Films 515 (2007) 6438

22 M. E. Lines, A. M. Glass, Principles and applications of ferroelectrics and related materials, Clarendon Press Oxford 1977

23 D. Su, T. Yamada, R. Gysel, A. K. Tagantsev, P. Murat N. Setter, N Jiang, J. Mater. Res. 26 ( 2011) 770

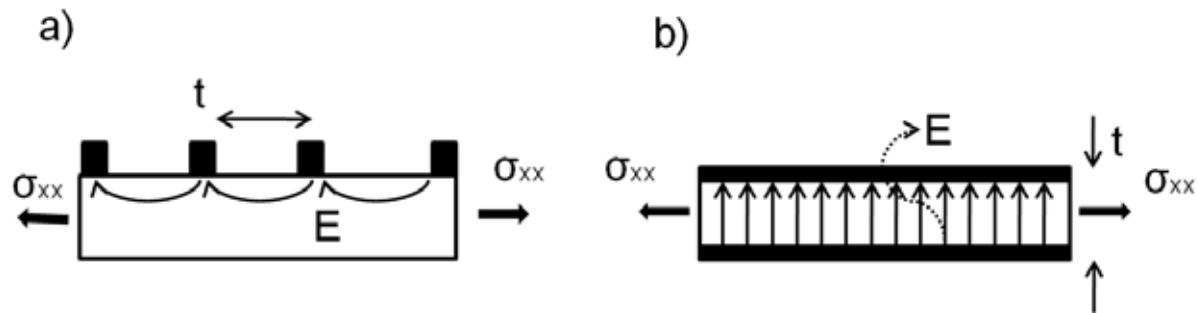


Fig. 1 a) 33 piezoelectric conversion mode,  $\sigma_{xx}$  is the applied external stress,  $t$  is the spacing between the fingers of the electrode and  $E$  is the electric field sensed by the electrodes. b) 31 piezoelectric conversion mode,  $\sigma_{xx}$  is the applied external stress,  $t$  is the spacing between the top and the bottom electrode and  $E$  is the electric field sensed by the electrodes.

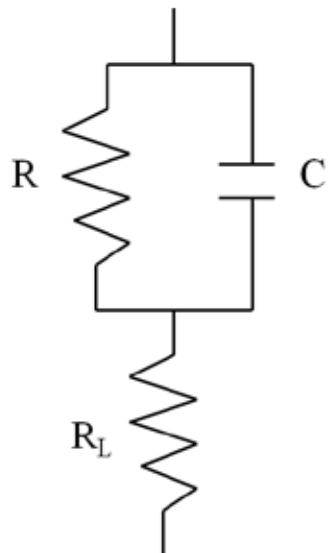


Fig. 2 Equivalent model for  $\text{SrRuO}_3/\text{BaTiO}_3/\text{SrRuO}_3$  structures showing resistive impedance at low frequency and capacitive impedance at high frequency. The resistor  $R_L$  models the resistance of the lines, the resistor  $R$  in parallel with the capacitor  $C$  models the  $\text{BaTiO}_3$  film.

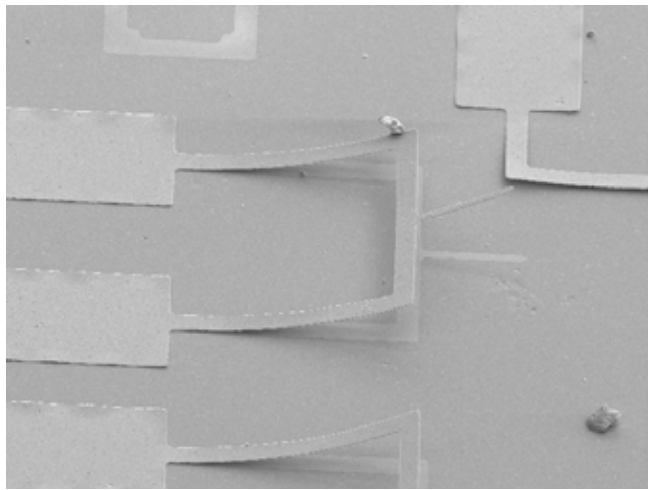


Fig. 3 SrRuO<sub>3</sub>/BaTiO<sub>3</sub>/SrRuO<sub>3</sub> u-shape cantilever with a simple beam connected in series. The total length of the structure is equal to 260  $\mu\text{m}$ . The tri-layer was grown on a YBa<sub>2</sub>Cu<sub>3</sub>O<sub>7</sub> sacrificial layer.

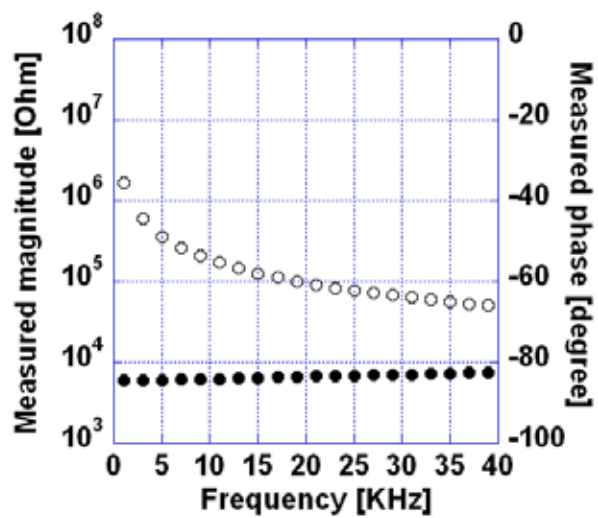


Fig. 4 Impedance measurements on a 105  $\mu\text{m} \times 30 \mu\text{m}$  SrRuO<sub>3</sub>(100 nm)/BaTiO<sub>3</sub>(400 nm)/SrRuO<sub>3</sub>(150 nm) parallel plate capacitor grown on a (001) oriented SrTiO<sub>3</sub> substrate. The BaTiO<sub>3</sub> was grown at 780 °C at a pressure of 0.06 Torr O<sub>2</sub>. Impedance measurements were performed with an input signal amplitude of 1 V. The open circles (○○) show the modulus of the measured impedance, while the full circles (●●) show the measured impedance phase of the structure.

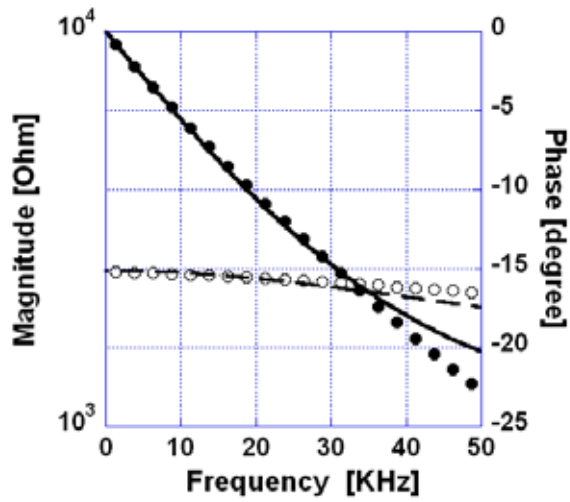


Fig. 5 Impedance measurements on a  $105 \mu\text{m} \times 30 \mu\text{m}$   $\text{SrRuO}_3(100 \text{ nm})/\text{BaTiO}_3(300 \text{ nm})/\text{SrRuO}_3(150 \text{ nm})$  parallel plate capacitor grown on a  $\text{SrTiO}_3(250 \text{ nm})/\text{YBa}_2\text{Cu}_3\text{O}_7(500 \text{ nm})$  bi-layer. The  $\text{BaTiO}_3$  was grown at  $780^\circ\text{C}$  at a pressure of 0.06 Torr  $\text{O}_2$ . Impedance measurements were performed with an input signal amplitude of 1 V. The dashed line (---) represents the modulus of the impedance for the lumped element model, while the open circles (○○) show the modulus of the measured impedance. The continuous black line (—) line represents the impedance phase of the circuit used to model the device, while the full circles (●●) indicate the measured impedance phase of the structure.

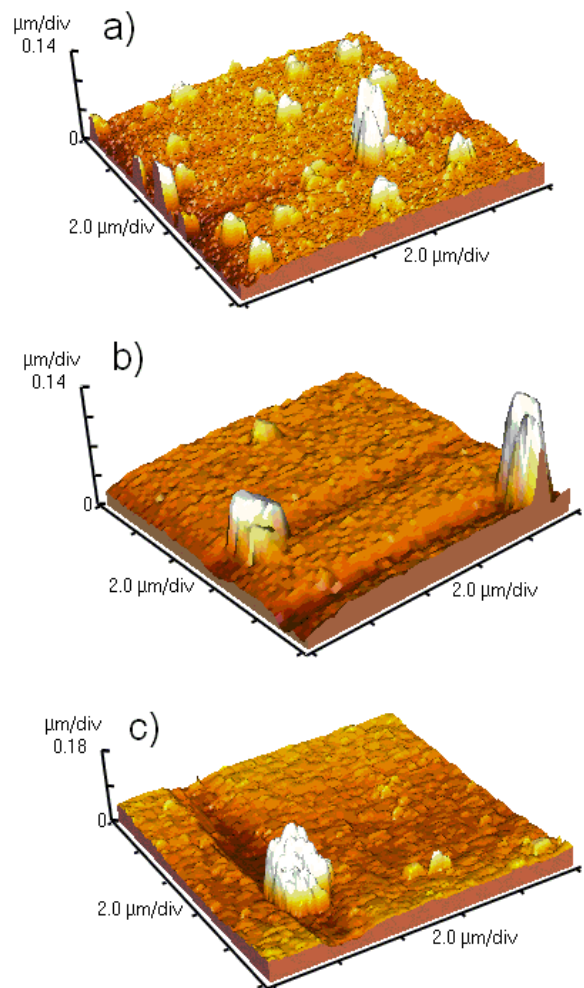


Fig. 6 AFM scan of a 10  $\mu\text{m}$  x 10  $\mu\text{m}$  area of: a) 150 nm  $\text{YBa}_2\text{Cu}_3\text{O}_7$  film, b) SrTiO<sub>3</sub>(100 nm)/ $\text{YBa}_2\text{Cu}_3\text{O}_7$ (150 nm) bi-layer, c) /SrTiO<sub>3</sub>(500 nm)/ $\text{YBa}_2\text{Cu}_3\text{O}_7$ (400 nm) bi-layer.

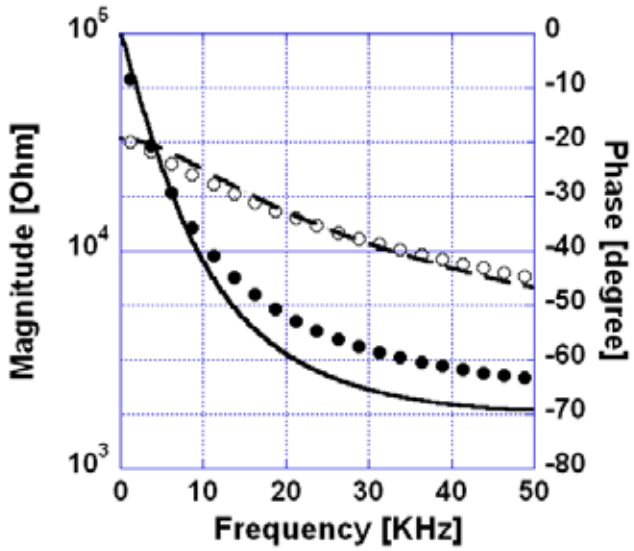


Fig. 7 Impedance measurements of a  $205\text{ }\mu\text{m} \times 30\text{ }\mu\text{m}$   $\text{SrRuO}_3(100\text{ nm})/\text{BaTiO}_3(300\text{ nm})/\text{SrRuO}_3(150\text{ nm})$  parallel plate capacitor grown on a  $\text{SrTiO}_3(1\text{ }\mu\text{m})/\text{YBa}_2\text{Cu}_3\text{O}_7(500\text{ nm})$  bi-layer. The  $\text{BaTiO}_3$  was grown at  $780\text{ }^\circ\text{C}$  at a pressure of  $0.06\text{ Torr O}_2$ . Impedance measurements were performed with an input signal amplitude of  $1\text{ V}$ . The dashed line (--) shows the modulus of the impedance for the lumped element model, while the open circles (○○) show the modulus of the measured impedance. The continuous black line (—) line shows the impedance phase of the circuit used to model the device, while the full circles (●●) indicate the measured impedance phase of the structure.

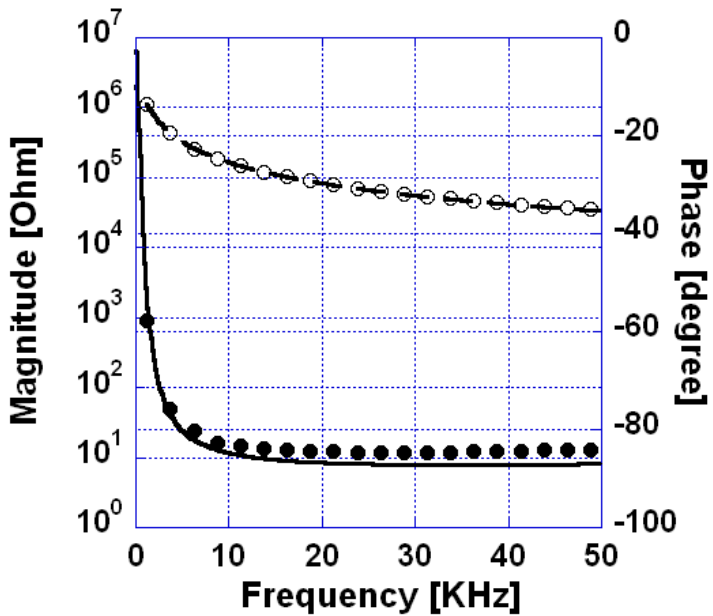


Fig. 8 Impedance measurement of a  $105 \mu\text{m} \times 30 \mu\text{m}$  SrRuO<sub>3</sub>(100 nm)/BaTiO<sub>3</sub>(300 nm)/SrRuO<sub>3</sub>(150 nm) parallel plate capacitor grown on a SrTiO<sub>3</sub>(250 nm)/MgO(400 nm) bi-layer. The BaTiO<sub>3</sub> was grown at 780 °C at a pressure of 0.06 Torr O<sub>2</sub>. Impedance measurements were performed with an input signal amplitude of 1 V. The dashed line (---) shows the modulus of the impedance for the lumped element model, while the open circles (○○) show the modulus of the measured impedance. The continuous black line (—) line shows the impedance phase of the circuit used to model the device, while the full circles (●●) indicate the measured impedance phase of the structure.

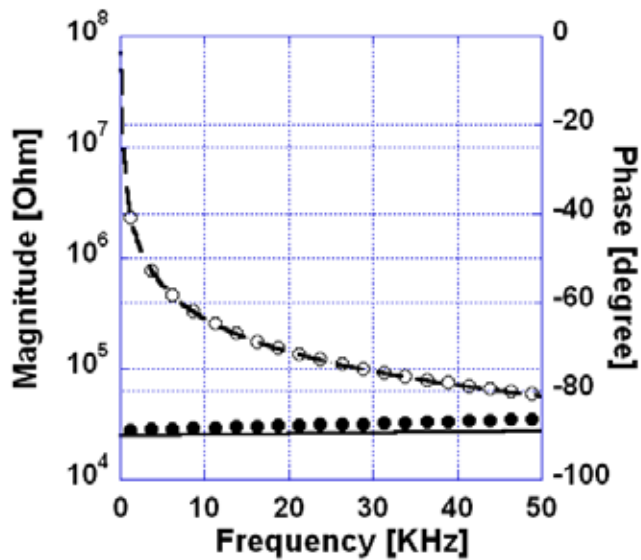


Fig. 9 Impedance measurement of a  $105 \mu\text{m} \times 30 \mu\text{m}$  SrRuO<sub>3</sub>(100 nm)/BaTiO<sub>3</sub>(300 nm)/SrRuO<sub>3</sub>(150 nm) parallel plate capacitor grown on a MgO(400 nm) sacrificial layer. The BaTiO<sub>3</sub> was grown at 780 °C at a pressure of 0.1 mTorr O<sub>2</sub>. Impedance measurements were performed with an input signal amplitude of 1 V. The dashed line (---) shows the modulus of the impedance for the lumped element model, while the open circles (○○) show the modulus of the measured impedance. The continuous black line (—) line shows the impedance phase of the circuit used to model the device, while the full circles (●●) indicate the measured impedance phase of the structure.

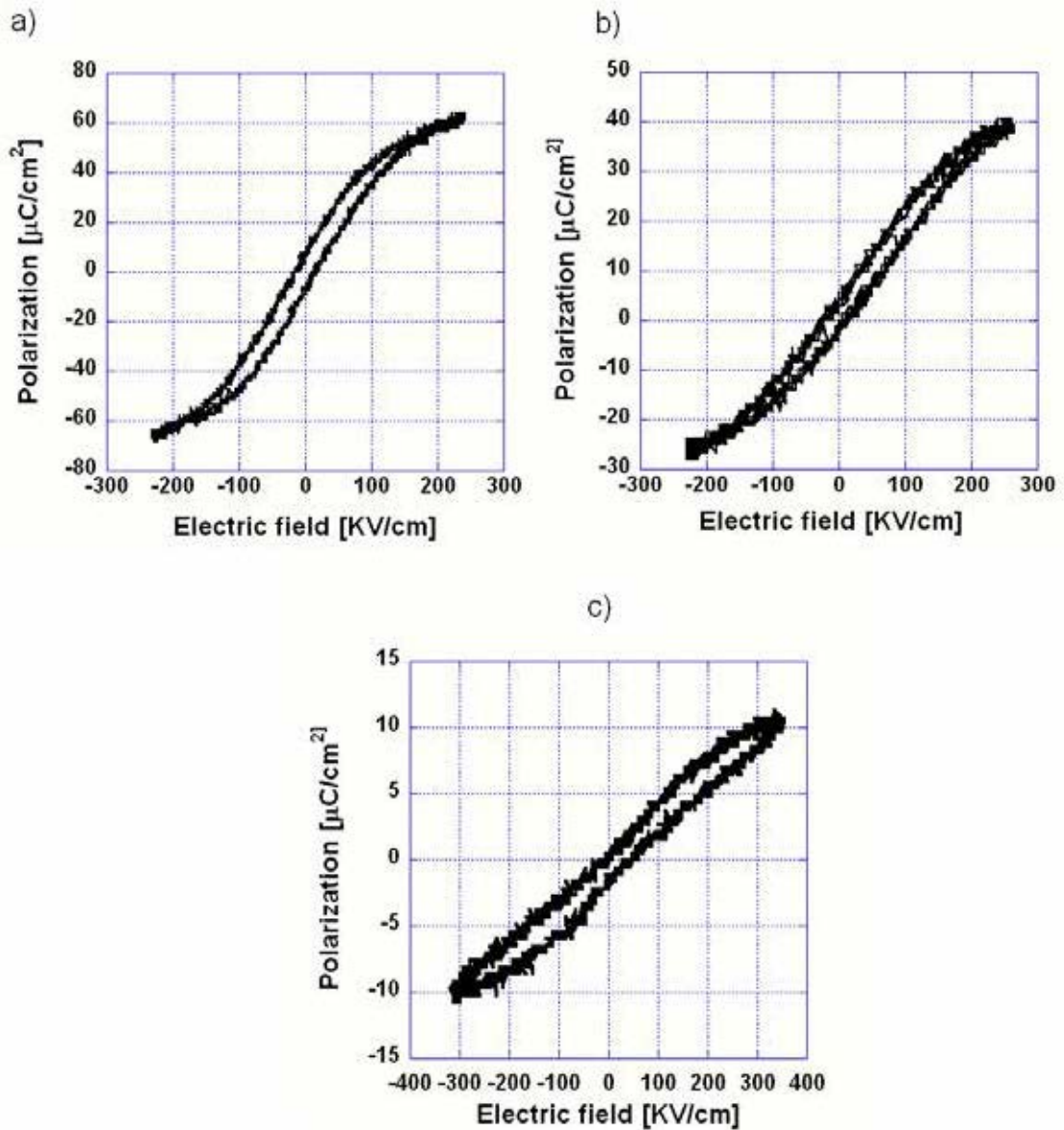


Fig. 10 a) Hysteresis loop measurements on a SrRuO<sub>3</sub>(100 nm)/BaTiO<sub>3</sub>(400 nm)/SrRuO<sub>3</sub>(150 nm) parallel plate capacitor directly deposited on the SrTiO<sub>3</sub> substrate. The BaTiO<sub>3</sub> film was grown at a pressure of 0.06 Torr. b) Hysteresis loop measurements on a SrRuO<sub>3</sub>(100 nm)/BaTiO<sub>3</sub>(300 nm)/SrRuO<sub>3</sub>(150 nm) parallel plate capacitor deposited directly on a SrTiO<sub>3</sub>(250nm)/MgO(400 nm) bi-layer. The BaTiO<sub>3</sub> film was grown at a pressure of 0.06 Torr. c) Hysteresis loop measurements on a SrRuO<sub>3</sub>(100 nm)/BaTiO<sub>3</sub>(300 nm)/SrRuO<sub>3</sub>(150 nm) parallel plate capacitor deposited on a 400 nm thick MgO layer, the BaTiO<sub>3</sub> film was grown at a pressure of 0.1 mTorr.

<b>Material [top down layer sequence]</b>	<b>In plane a axis measured [Å] (bulk [Å])</b>	<b>In place b axis measured [Å] (bulk [Å])</b>	<b>Out of plane axis measured [Å] (bulk [Å])</b>
BaTiO <sub>3</sub> [SrRuO <sub>3</sub> (50nm)/BaTiO <sub>3</sub> (100nm)/ SrRuO <sub>3</sub> (350nm)/YBa <sub>2</sub> Cu <sub>3</sub> O <sub>7</sub> (400nm)]	3.951 (3.992)	3.951 (3.992)	4.069 (4.036)
BaTiO <sub>3</sub> [BaTiO <sub>3</sub> (500nm)/MgO(60nm)/ YBa <sub>2</sub> Cu <sub>3</sub> O <sub>7</sub> (400nm)]	4.002 (3.992)	4.002 (3.992)	3.997 (4.036)
BaTiO <sub>3</sub> [BaTiO <sub>3</sub> (126nm)/SrTiO <sub>3</sub> (500nm)/ YBa <sub>2</sub> Cu <sub>3</sub> O <sub>7</sub> (400nm)]	3.996 (3.992)	3.996 (3.992)	4.015 (4.036)
Table 1: BaTiO <sub>3</sub> film lattice parameters on different layer sequences. Bulk parameters are provided for comparison.			

<b>Device (fig)</b>	<b>Top down layer sequence</b>	<b>BaTiO<sub>3</sub> deposition pressure [Pa]</b>	<b>RA product [Ωμm<sup>2</sup>]</b>	<b>C/A ratio [F/μm<sup>2</sup>]</b>
SBSSY (fig. 5)	SrRuO <sub>3</sub> (100nm)/BaTiO <sub>3</sub> (300nm)/ SrRuO <sub>3</sub> (150nm)/SrTiO <sub>3</sub> (250nm)/ YBa <sub>2</sub> Cu <sub>3</sub> O <sub>7</sub> (500nm)	8	44.1*10 <sup>5</sup>	6.28*10 <sup>-13</sup>
SBSSY (fig. 7)	SrRuO <sub>3</sub> (100nm)/BaTiO <sub>3</sub> (300nm)/ SrRuO <sub>3</sub> (150nm)/SrTiO <sub>3</sub> (1000nm)/ YBa <sub>2</sub> Cu <sub>3</sub> O <sub>7</sub> (500nm)	8	19.54*10 <sup>7</sup>	7.8*10 <sup>-14</sup>
SBSSM (fig. 8)	SrRuO <sub>3</sub> (100nm)/BaTiO <sub>3</sub> (300nm)/ SrRuO <sub>3</sub> (150nm)/ SrTiO <sub>3</sub> (250nm)/ MgO(400 nm)	8	61.93*10 <sup>8</sup>	3.04*10 <sup>-14</sup>
SBSM (fig. 9)	SrRuO <sub>3</sub> (100nm)/BaTiO <sub>3</sub> (300nm)/ SrRuO <sub>3</sub> (150nm)/MgO(400 nm)	0.013	$\approx \infty$	1.76*10 <sup>-14</sup>
Table 2: Top down layer sequences, BaTiO <sub>3</sub> deposition pressure, RA product and C/A ratio of the structures under investigation, the figure numbers showing the impedance measured of each device are reported.				

## Part II

# Bibliography

# Bibliography

- [1] W. J. Choi, Y. Jeon, J. H. Jeong, R. Sood, S. G. Kim, "Energy harvesting MEMS device based on thin film piezoelectric cantilevers", *J. Electroceram.* 17, 543-548 (2006)
- [2] S. Roundy, P K. Wright, J Rabaey, "A study of low level vibrations as a power source for wireless sensor nodes" *Computer Communications* 26 11311144 (2003)
- [3] F. Lu, H. P. Lee, S. P. Lim, "Modeling and analysis of micro piezoelectric power generator for micro-electromechanical-systems applications" *Smart. Matter. Struct.* 13, 57-63, (2004)
- [4] Y. B. Jeon, R Sood, J. H. Jeong, S. G. Kim, "MEMS power generator with transverse mode thin film PZT" *Sensors and Actuators A* 122, 16-22 (2005)
- [5] S. P. Beeby, M. J. Tudor, N. M. White, "Energy harvesting vibration sources for microsystems applications", *Meas. Sci. Technol.* 17, R175-R195 (2006)

- [6] D. Berlincourt, H. Jaffe, "Elastic and Piezoelectric Coefficients of Single-Crystal Barium Titanate", Phys. Rev. 111, 143-148 (1958)
- [7] S. Zhang, R. Xia, T. R. Shrout, "Lead-free piezoelectric ceramics vs. PZT?" J Electroceram 19, 251257 (2007)
- [8] X. Du, J. Zheng, U. Belegundu, K. Uchino, "Crystal orientation dependence of piezoelectric properties of lead zirconate titanate near the morphotropic phase boundary" Appl. Phys. Lett., Vol. 72, 19, 2421-2423 (1998)
- [9] "Directive 2002/95/EC of the European Parliament and of the Council of 27 January 2003 on the restriction of the use of certain hazardous substances in electrical and electronic equipment" Official Journal L 037, P. 0019 - 0023, 13/02/2003
- [10] H. J. H. Smilde, H. Hilgenkamp, G. J. Gerritsma, D. H. A. Blank, H. Rogalla, "Y - Ba - Cu - O/Au/Nb Ramp-type Josephson Junctions" IEEE Transactions on applied superconductivity 11, 501-504 (2001)
- [11] C. Schuppler, "Ramp-type Nb/Au/YBCO Josephson junctions for potential qubit application" thesis, The University of Birmingham, School of Physics and Astronomy April 2009.
- [12] H. Lakdawala, G. K. Fedder, "Analysis of temperature-dependent residual stress gradient in CMOS micromachined structures", IEEE Transducers '99, pp 526-529 (1999)

- [13] J. S. Pulskamp, A. Wickenden, R. Polcawich, B. Piekarski, M. Dubey, "Mitigation of residual film stress deformation in multilayer microelectromechanical systems cantilever devices", *J. Vac. Sci. Technol. B*, 21(6), 2482-2486 (2003)
- [14] J. A. Kalb, Q. Guo, X. Zhang, Y. Li, C. Sow, C. V. Thompson, "Phase-Change Materials in Optically Triggered Microactuators", *Journal of Microelectromechanical System* 17, 5, 1094-1103 (2007)
- [15] L. B. Freund, S. Suresh, "Thin Film Materials", 88, 93-95, 125-127 Cambridge University Press (2003)
- [16] F. Jona, G. Shirane, "Ferroelectric crystals" Dover publications, inc. New York (1993)
- [17] S.L. Miller, R.D. Nasby, J.R. Schwank, M.S. Rodgers, P.V. Dressendorfer, "Device modeling of ferroelectric capacitors" *J. Appl. Phys.* 68 (12), 1990
- [18] V. Z. Parton, B. A. Kudryavtsev, "Electromagnetoelasticity" Gordon and Breach Science Publishers (1988).
- [19] M. E. Lines, A. M. Glass, "Principles and applications of ferroelectrics and related materials" Clarendon Press Oxford (1977)
- [20] T. Ikeda, "Fundamentals of Piezoelectricity" Oxford University Press (1996)
- [21] The A to Z of materials, "Barium titanate ( $BaTiO_3$ )-Properties and Applications" <http://www.azom.com/article.aspx?ArticleID=4154>

- [22] K. J. Choi, M. Biegalski, Y. L. Li, A. Sharan, J. Schubert, R. Uecker, P. Reiche, Y. B. Chen, X. Q. Pan, V. Gopalan, L. Q. Chen, D. G. Schlom, C. B. Eom, "Enhancement of Ferroelectricity in Strained BaTiO<sub>3</sub> Thin Films", Science 306, 1005-1008 (2004)
- [23] Q. Q. Zhang, S. J. Gross, S. Tadigadapa, T. N. Jackson, F. T. Djuth, S. Troiler-McKinstry, "Lead zirconate titanate films for d<sub>33</sub> mode cantilever actuators", Sensors and Actuators A 105, 91-97 (2003).
- [24] M. R. Levy, "Crystal Structure and Defect Property Predictions in Ceramic Materials", thesis, Department of Materials, Imperial College of Science Technology and Medicine, University of London (2005)
- [25] K. Khamchane, "Ferroelectric Heterostructures: Growth and Microwave Devices", thesis, Department of Microelectronics and Nanoscience, Chalmers University of Technology, Goteborg University (2003)
- [26] O. Madelung, U. Rossler, M. Schulz, "Magnesium Oxide MgO crystal structure, lattice parameters, thermal expansion", volumes III/17B – 22A – 41B, SpringerMaterials - The Landolt-Bornstein Database (<http://www.springermaterials.com>). DOI: 10.1007/10681719\_06
- [27] M. Causa', R. Dovesi, C. Pisani, C. Roetti, "Electronic Structure and stability of different crystal phases of magnesium oxide", Physical Review B, vol. 33, n. 2 (1986)
- [28] L. Latorre, P. Nouet, Y. Bertrand, P. Hazard, F. Pressecq, "Characterization and modeling CMOS-compatible MEMS technology" Sensors and Actuators 74 (1999) 143-147

- [29] P. D. Mitcheson, T. C. Green, M. Yeatman, A. S. Holmes, "Architectures for Vibration-Driven Micropower Generators" Journal of Microelectromechanical Systems, vol. 13, n. 3, 429-440, June (2004)
- [30] S. Baglio "Sistemi integrati di misura" master degree course at Universita' di Catania 2005-2006
- [31] M. Dardalhon, V. Beroullie, L. Latorre, P. Nouet, G. Perez, J. M. Nicot, C. Oudea, "Reliability analysis of CMOS MEMS structures obtained by Front Side Bulk Micromachining" Microelectronics Reliability, 42, 1777-1782, (2002)
- [32] S. Timoshenko, "Strength of Materials" D. Van Nostrand Company, third edition (1955)
- [33] S. Baglio, S. Castorina, N. Savalli, "Scaling Issues and Design of MEMS" Wiley (2007)
- [34] W. T. Thomson, "Theory of Vibration with Applications" George Allen & UNWIN LTD, second edition (1981)
- [35] C. B. Williams, R. B. Yates, "Analysis of a micro-electric generator for microsystems" Sensors and Actuators A, 52 8-11, (1996)
- [36] S. G. Kim, "Multiscale Systems Design & Manufacturing" MIT course 2-76Fall (2004)
- [37] J. D'Azzo, C. H. Houpis, "Linear Control System Analysis and Design" McGraw-Hill, fourth edition (1995)

- [38] P. Bolzern, R. Scattolini, N. Schiavoni, "Fondamenti di controlli automatici" McGraw-Hill (1998)
- [39] The A to Z of Materials. "Strontium Titanate ( $SrTiO_3$ )- Properties and applications" <http://www.azom.com/article.aspx?ArticleID=2362>
- [40] SPI Supplies Brand, "MgO Datasheet" <http://www.2spi.com/catalog/submat/magnesium-oxide.shtml>
- [41] Mineralogy Database "Gold Mineral Data" <http://webmineral.com/data/Gold.shtml>
- [42] C. A. Desoer, E. S. Kuh, "Fondamenti di teoria dei circuiti" McGraw-Hill Inc., New York, N.Y. - USA 18a edizione (1995)
- [43] T. D. Rossing, D. A. Russel, D. E. Brown, "On the acoustics of tuning forks" Am. J. Phys. 60 (7), 620-626 (1992)
- [44] A. Morimoto, T. Shimizu, "Laser Ablation" Handbook of Thin Film Process Technology, 1995 IOP Publishing Ltd.
- [45] J. Cheung, J. Horwitz, "Pulsed laser deposition history and laser-target interactions" MRS Bulletin February 1992.
- [46] D. Dijkkamp, T. Venkatesan, X. D. Wu, S. A. Shaheen, N. Jisrawi, Y. H. Min-Lee, W. L. McLean, M. Croft, "Preparation of  $Y - Ba - Cu$  oxide superconductor thin films using pulsed laser evaporation from high  $T_c$  bulk materials" Appl. Phys. Lett. 51 619.
- [47] C. Hammond "The basics of crystallography and Diffraction" second edition, Oxford university press.

- [48] A. Krupowski, "X-ray texture tomography of near-surface area" Progress in Material Science 51 (2006) 61-149.
- [49] Bruker D5000 4-circle X-ray diffractometer, manual (1997-2007).
- [50] Microposit S1800 series photo resists, Shipley.
- [51] N. Maluf, K. Williams, "An introduction to Microelectromechanical Systems Engineering" Artech House, Inc., second edition (2004)
- [52] Radian Technologies, Inc., Application Note AN0701-RTI.
- [53] J. F. Scott "Ferroelectrics go bananas" J Phys. Condens. Matter 20 (2008).
- [54] B. Beake, S. Goodes, S. Jones, R. Parkinson, N. Pickford, J Smith, "Nano Test manual" Micro Materials LTD (2004)
- [55] W. C. Oliver, G. M. Pharr, "An improved technique for determining hardness and elastic modulus using load and displacement sensing indentation experiments" J. Mater. Res. 7, 6, 1564-1583 (1992)
- [56] Dr. James Bowen School of Chemical Engineering The University of Birmingham
- [57] F. K. Shokoohi, L. M. Schiavone, C. T. Rogers, A. Inam, X. D. Wu, L. Nazar, T. Venkatesan, "Wet chemical etching of high-temperature superconducting Y-Ba-Cu-O films in ethylenediaminetetraacetic acid" Appl. Phys. Lett. 55 25, 2661-2663 (1989)
- [58] Crystal GmbH, Ostendstrae 25, Haus 4, D-12459 Berlin

- [59] Praxair, Electronic Materials, Specialty Ceramics,  
<http://www.praxair.com> (last access January 2012)
- [60] Timothy J. Jackson Senior lecturer at the School of Electrical Electronic and Computer Engineering of The University of Birmingham, private communication (2008)
- [61] D. B. Chrisey, G. K. Hubler, "Pulsed Laser Deposition of Thin Films" John Wiley & Sons, Inc. (1994)
- [62] H. Sato, F. J. G. Roesthuis, A. H. Sonnenberg, A. J. H. M. Rijnders, H. Rogalla, D. H. A. Blank, "Investigation of the microstructure of ramp-type  $YBa_2Cu_3O_{7-\delta}$  structures" Supercond. Sci. Technol. 13, 522-526 (2000)
- [63] Shipley, "Microposit S1800 series photo resists" datasheet.
- [64] A. Frommhold, The University of Birmingham, Nanoscale Physics Research Laboratory, School of Physics and Astronomy, Edgbaston, Birmingham, B15 2TT, UK
- [65] Y. Yang, Z. Wang, J. F. Li, D. Viehland, "Pulsed Laser Deposition of  $BaTiO_3$  Thin Films on Different Substrates" Journal of Nanomaterials vol. 2010, ID 756319, 5 pages (2010)
- [66] D. H. Kim, H. S. Kwok, "Pulsed laser deposition of  $BaTiO_3$  thin films and their optical properties" Appl. Phys. Lett. 67, 13, 1803-1805 (1995)
- [67] F. X. Wang, W. Li, F. Lu, H. Hu, K. M. Wang, Z. G. Liu, Y. Zhu, " $BaTiO_3$  film optical-waveguide prepared by pulsed laser deposition"

- Nuclear Instruments and Methods in Physics Research B 191, 778-782 (2002)
- [68] L. Pellegrino, M. Biasotti, E. Bellingeri, C. Bernini, A. S. Siri, D. Marre', "All-Oxide Crystalline Microelectromechanical Systems: Bending the Functionalities of Transition-Metal Oxide Thin Films" Adv. Mater. 21, 2377-2381 (2009)
- [69] Y. Wu, Z. Hao, Y. Enomoto, K. Tanabe, "Atomic configurations of  $YBa_2Cu_3O_7/MgO$  interfaces" Physica C 371, 309314 (2002)
- [70] K. Sangwal, T. C. Patel, "Etching Behaviour to  $MgO$  Crystals in Relation to Chemical Reactions" Kristall und Technik 13, 12, 1407-1412 (1978)
- [71] J. I. Langford, "LAPOD Unit Cell Refinement Software" The University of Birmingham (1999) <http://www.ccp14.ac.uk/ccp/web-mirrors/lapod-langford/>
- [72] M. Ohring, The Materials Science of Thin Films, Academic Press, London (1992)
- [73] I. B. Misirlioglu, S. P. Alpay, F. He, B. O. Wells, "Stress induced monoclinic phase in epitaxial  $BaTiO_3$  on  $MgO$ ", Journal of Applied Physics 99, 104103 (2006)
- [74] E. Bartolome', J. J. Roa, B. Bozzo, M. Segarra, X. Granados, "Effective silver-assisted welding of YBCO blocks: mechanical versus electrical properties", Supercond. Sci. Technol., 23, 045013 (6pp) (2010)

- [75] A. C. Dent, C. R. Bowen, R. Stevens, M. G. Cain, M. Stewart, "Effective elastic properties for unpoled barium titanate", Journal of the European Ceramics Society 27, 3739-3743 (2007)
- [76] C. S. Zha, H. K. Mao, R. J. Hemley, "Elasticity of MgO and a primary pressure scale to 55 GPa", PNAS vol.97 no.25 13494-13499 (2000)
- [77] T. Suzuki, Y. Nishi, M. Fujimoto, "Defect structure in homoepitaxial non-stoichiometric strontium titanate thin films, Philosophical Magazine A, vol.80 no.3 621-637 (2000)
- [78] G. Chern, "Incommensurate growth and interface stability in MgO/SrTiO<sub>3</sub>(001)", Surface Science 387, 183-191 (1997)
- [79] B. R. Kim, T. U. Kim, W. J. Lee, J. H. Moon, B. T. Lee, H. S. Kim, J. H. Kim, "Effects of periodicity and oxygen partial pressure on the crystallinity and dielectric property of artificial SrTiO<sub>3</sub>/BaTiO<sub>3</sub> superlattices integrated on Si substrates by pulsed laser deposition method", Thin Solid films 515, 6438-6441 (2007)
- [80] D. E. Daush, G. H. Haertling, "Bulk vs. thin film PLZT ferroelectrics", IEEE 8th Int. Symp. Application of Ferroelectrics, 297-300 (1992)
- [81] B. L. Cheng, M Gabbay, G. Fantozzi, W. J. Duffy, Mechanical loss and elastic modulus associated with phase transitions of barium titanate ceramics, Journal of Alloys and Compounds 211/212, 352-355, (1994)

- [82] The Landolt Börnstein Database "substance: magnesium oxide ( $MgO$ ), property: Young's, shear and bulk moduli, Poisson's ratio" Springer, [http://www.springermaterials.com/docs/pdf/10681719\\_10.html](http://www.springermaterials.com/docs/pdf/10681719_10.html)
- [83] S. Yamanaka, T. Maekawa, H. Muta, T. Matsuda, S. Kobayashi, K. Kurosakia, "Thermophysical properties of  $SrHfO_3$  and  $SrRuO_3$ " Journal of Solid State Chemistry 177, 3484-3489 (2004)
- [84] T. Suzuki, Y. Nishi, M. Fujimoto, "Defect structure in homoepitaxial non-stoichiometric strontium titanate thin films" Philosophical Magazine A, 80, 3, 621-637 (2000)
- [85] "The A to Z of materials, Strontium Titanate properties and applications", <http://www.azom.com/Details.asp?ArticleID=2362>
- [86] J. Kawashima, Y. Yamada, I. Hirabayashi, "Critical thickness and effective thermal expansion coefficient of  $YBCO$  crystalline film", Physica C, 306, 114-118 (1998)
- [87] S. N. Bushmeleva, V. Y. Pomjakushin, E. V. Pomjakushina, D. V. Sheptyakov, A. M. Balagurov, "Evidence for the band ferromagnetism in  $SrRuO_3$  from neutron diffraction", Journal of Magnetism and Magnetic Materials, 305, 491-496 (2006)
- [88] Y. He, "Heat capacity thermal conductivity and thermal expansion of barium titanate-based ceramics", Thermochimica Acta, 419, 135-141 (2004)

- [89] SPI Supplies Brand, " *MgO substrate datasheet*" ,  
<http://www.2spi.com/catalog/submat/magnesium-oxide.shtml>
- [90] S. Huang, X. Zhang, " *Gradient residual stress induced elastic deformation of multilayer MEMS structures*" Sensors and Actuators A, 134, 177-185 (2007)
- [91] J. H. Lee, K. S. Hwang, T. S. Kim, " *The Microscopic Origin of Residual Stress for Flat Self-actuating Piezoelectric Cantilevers*" Nanoscale Research Letters, 6:55, doi:10.1007/s11671-010-9810-z (2010)
- [92] D. Su, T Yamada, R. Gysel, A. K. Tagantsev, P. Muralt, N. Setter, N. Jiang, *Growth-mode induced defects in epitaxial SrTiO<sub>3</sub> thin films grown on single crystal LaAlO<sub>3</sub> by a two-step PLD process* J. Mater. Res., 26, 6, 770-774 (2011)
- [93] J. A. Thornton, D.W. Hoffman, " *Stress related effects in thin films*" , Thin Solid Films, 171, 5-31 (1989)
- [94] Z. Feng, E. G. Lovell, R. L. Engelstad, A. R. Mikkelson, P. L. Reuand Jaewoong Sohn, " *Film Stress Characterization Using Substrate Shape Data and Numerical Techniques*" , Mat. Res. Soc. Symp. Proc., Vol. 750, Y.3.4.1-Y.3.4.6 (2003)
- [95] X. D. Wu, S. R. Foltyn, R. C. Dye, Y. Coulter, R. E. Muenchausen, " *Properties of epitaxial SrRuO<sub>3</sub> thin films*" , Applied Physics Letters 62, 2434-2436 (1993)

- [96] E. J. Abram, D. C. Sinclair, A. R. West, "A Strategy for Analysis and Modeling of Impedance Spectroscopy Data of Electroceramics: Doped Lanthanum Gallate" Journal of Electroceramics, 10, 165-177 (2003)
- [97] J. K. Sinha, "Modified Sawyer and Tower circuit for the investigation of ferroelectric samples" J. Sci. Instrum., 42, 696-698 (1965)
- [98] S. Proyer, E. Stangl, M. Borz, B. Hellebrand, D. Bäuerle, "Particulates on pulsed-laser deposited Y-Ba-Cu-O films" Physica C, 257, 1-15 (1996)
- [99] K. Sato, M. Takahashi, N. Matsunami, Y. Takai, "Pulsed laser deposition of BaTiO<sub>3</sub>" Supercond. Sci. Technol. 9, A156-A160 (1996)
- [100] K. Abe, N. Yanase, T. Kawakubo, "Bistable States of Ferroelectric Hysteresis Loops in a Heteroepitaxial BaTiO<sub>3</sub> thin film capacitor" Jpn. J. Appl. Phys. 40, 2367-2371 (2001)
- [101] R. Wördenweber, "Growth of high-T<sub>c</sub> thin films" Supercond. Sci. Technol. 12, R86-R102, (1999)
- [102] P. Mazzoldi, M. Nigro, C. Voci, "Fisica vol. II" Seconda Edizione, EdiSES (1998)
- [103] W. Buckel, R. Kleiner, "Superconductivity Fundamentals and Applications" Second edition, WILEY-VCH Verlag GmbH & Co. KGaA
- [104] T. P. Orlando, K. A. Delin, "Foundations of applied superconductivity" Wokingham : Addison-Wesley, (1991)
- [105] H. Hilgenkamp, "Pi-phase shift Josephson structures" Supercond. Sci. Technol. 21 (2008) 034011 (5pp)

- [106] G. Wendum, V. S. Shumeiko, "Quantum bits with Josephson junctions" Low Temp.Phys. 33, p. 724 (2007)
- [107] J. Clarke, "Flux qubit completes the hat trick" Science 299, p. 1850 (2003)
- [108] G. Wendum, V. S. Shumeiko, "Superconducting Quantum Circuits, Qubits and Computing" arXiv:cond-mat/0508729 v1 (2005)
- [109] C. Schuppler, "HTSC phase qubit with implemented ramp type Josephson junctions" Midterm report, University of BirminghamPhysics and Astronomy Condensed Matter Group, 11<sup>th</sup> of October 2006.
- [110] M. H. S. Amin, A. Y. Smirnov, A. M. Zagoskin, T. Lindstroem, S. A. Charlebois, T. Claeson, A. Y. Tzalenchuk, "Silent phase qubit based on d-wave Josephson junctions" Physical Review B 71, p. 064516 (2005)
- [111] H. J. H. Smilde, H. Hilgenkamp, G. Rijnders, H. Rogalla, "Enhanced transparency ramp-type Josephson contacts through interlayer deposition" Applied Physics Letters 80, 24, 4579-4581 (2002)
- [112] J. Ekin, "Superconducting Contacts", Bristol and Philadelphia: Institute of Physics, David A Cardwell and David S Ginley, 2003.
- [113] R. Gross, B. Mayer, "Transport processes and noise in  $YBa_2Cu_3O_{7\delta}$  grain boundary junctions", Physica C, vol. 180, 235-242, (1991)
- [114] M. F. Yan, R. L. Barns, H. M. O'Bryan, P. K. Gallagher, R. C. Sherwood, S. Jin, "Water interaction with the superconducting  $YBa_2Cu_3O_7$  phase", Appl. Phys. Lett., vol. 51, p. 532, (1987)

- [115] D. H. A. Blank, H. Rogalla, "The effect of ion milling on the morphology of ramp-type Josephson junctions" J. Mater. Res. 12, 11, 2952-2957 (1997)
- [116] Z. H. Gong, F. Vassenden, R. Faberberg, J. K. Grebstad, A. Bardal, R. Hoier, "Processing dependence of the interfacial microstructure of Ag contacts to  $YBa_2Cu_3O_{7+\delta}$  thin films", Appl. Phys. Lett., vol. 63, p. 836, (1993)
- [117] Y. Soutome, R. Hanson, T. Fukazawa, K. Saitoh, A. Tsukamoto, Y. Tarutani, K Takagi, "Investigation of Ramp-type Josephson Junctions with Surface-modifies Barriers" IEEE Trans. on Appl. Supercond. 11, 1, 163-166 (2001)
- [118] U. Schoop, M. Schonecke, S. Thienhaus, S. Schymon, L. Alff, R. Gross, "Role of ion beam etching in the fabrication of ramp-type junctions" Physica C 351, 200-214 (2001)
- [119] Veeco Instruments, "ProScan Data Acquisition Software Reference" User's Guide to AutoProbe CP and M5 part III 48-101-1101, Rev. E (2004)
- [120] M. Nikolo, "Superconductivity: A guide to alternating current susceptibility measurements and alternating current susceptometer design" Am. J. Phys. 63, 1, 57-65 (1995)
- [121] Stanford research systems, "About lock-in Amplifiers" Application note # 3, [www.thinkSRS.com](http://www.thinkSRS.com)

- [122] PerkinElmer Instruments, "What is a lock in Amplifier?" Technical Note TN 100 (2000)
- [123] National Instruments, "*Labview data acquisition basic manual*" January 1998 edition
- [124] Edward Tarte, lecturer at the School of Electrical Electronic and Computer Engineering of The University of Birmingham, private communication (2008)
- [125] Ariando, "*Josephson junction arrays with d-wave-induced  $\pi$ -phase-shifts*", PhD thesis, University of Twente, Holland, (2005)
- [126] Twente Solid State Technology, P.O. Box 256, 7500 AG ENSCHEDE, The Netherlands
- [127] C. L. Jia, M. I. Faley, U. Poppe, K. Urban, "*Effect of chemical and ion-beametching on the atomic structure of interfaces in  $YBa_2Cu_3O_{7-\delta}/PrBa_2Cu_3O_7$  Josephsonjunctions*", Appl. Phys. Lett., vol. 67, 3635-3637 (1995)
- [128] Y. Li, S. Linzen, F. Machalett, F. Schmidl, P. Seidel, "*Recovery of superconductivity and recrystallization of ion-damaged  $YBa_2Cu_3O_{7-x}$  films after thermal annealing treatment*", Physica C, vol. 243, 294-302 (1995)
- [129] G. J. Clark, A. D. Marwick, R. H. Koch, R. B. Laibowitz, "*Effects of radiation damage in ion-implanted thin films of metal-oxide superconductors*" Applied Physics Letter, vol. 51, 139-141 (1987)

- [130] M. Q. Huang, Z. G. Ivanov, P. V. Komissinski, T. Claeson, "Fabrication and properties of high- $T_c$  ramp junctions with manganite barriers" Physica C 326-327, 79-82 (2009)
- [131] M. Q. Huang, Z. G. Ivanov, P. V. Komissinski, P. B. Mozhaev, T. Claeson, "High- $T_c$  Ramp-Type Josephson Junctions for Rapid Single Flux Quantum Circuits" Journal of Low Temperature Physics 117, 587-591 (1999)
- [132] H. J. Smilde, "Josephson contacts between high- $T_c$  and low - $T_c$  superconductors", PhDthesis , University of Twente , Holland, (2001)
- [133] A. Andreski Faculty of Science & Technology University of Twente Holland
- [134] J. G. Wen, N. Koshizuka, S. Tanaka, T. Satoh, M. Hidaka, S. Tahara, "Atomic structure and composition of the barrier in the modified interface high- $t_c$  Josephson junction studied by transmission electron microscopy" Appl. Phys. Lett., vol. 75, 2470-2472, 1999.
- [135] B. D. Hunt, M. G. Forrester, J. Talvacchio, J. D. McCambridge, R. M. Young, High- $T_c$  superconductor/normal-metal/superconductor edge junctions and SQUIDs with integrated groundplanes" Appl. Phys. Lett., 68, 3805-3807, 1996.
- [136] J. Schubert, O. T. Veesak, W. Zander, M. Roeckerath, T. Heeg, H. Y. Chen, C. L. Jia, D. G. Schlom, "Characterization of epitaxial lanthanum lutetium oxide thin films prepared by pulsed-laser deposition" Applied Physics A 90, 577-579 (2008)

- [137] D. H. Triyosoa, D. C. Gilmera, J. Jianga, R. Droopad, "Characteristics of thin lanthanum lutetium oxide high-*k* dielectrics" Microelectronic Engineering 85, 1732-1735 (2008)
- [138] J. M. J. Lopes, M. Roeckerath, T. Heeg, U. Littmark, J. Schubert, S. Mantl, Y. Jia, D. G. Schlom, "La-based ternary rare-earth oxides as alternative high-*k* dielectrics" Microelectronic Engineering 84, 1890-1893 (2007)
- [139] A. Feteira, School of Chemistry, University of Birmingham, Edgbaston Birmingham B15 2TT UK
- [140] A. Feteira, L. J. Gillie, R. Elsebrock, D. C. Sinclair, "Crystal Structure and Dielectric Properties of LaYbO<sub>3</sub>" Journal of the American Ceramic Society 90, 1475-1482 (2007)
- [141] B. Prijamboedi, H. Takashima, R. Wanga, A. Shoji, M. Itoh, "Dielectric properties of SrTiO<sub>3</sub> thin film prepared in a mixture of <sup>18</sup>O<sub>2</sub> and <sup>16</sup>O<sub>2</sub> gas" Journal of Alloys and Compounds 449, 4851 (2008)
- [142] David Woodward Department of Physics, University of Warwick, Coventry, CV4 7AL